Study of correlations of heavy quarks in heavy ion collisions and their role in understanding the mechanisms of energy loss in the quark gluon plasma

Martin Rohrmoser

To cite this version:

Martin Rohrmoser. Study of correlations of heavy quarks in heavy ion collisions and their role in understanding the mechanisms of energy loss in the quark gluon plasma. Plasma Physics [physics.plasm-ph]. Ecole nationale supérieure Mines-Télécom Atlantique, 2017. English. NNT : 2017IMTA0015 . tel-01596015

HAL Id: tel-01596015
https://tel.archives-ouvertes.fr/tel-01596015

Submitted on 27 Sep 2017

UNIVERSITE
BRETAGNE
LOIRE

IMT Atlantique
Bretagne-Pays de la Loire
École Mines-Télécom

Thèse de Doctorat

Martin ROHRMOSER

Mémoire présenté en vue de l'obtention du
grade de Docteur de l'IMT ATLANTIQUE
sous le sceau de L'Université Bretagne Loire

École doctorale : 500 (3MPL)

Discipline : Physique
Spécialité : Constituants élémentaires et physique théorique
Unité de recherche : SUBATECH UMR6457

Soutenue le 05 Avril 2017 à Nantes
Thèse N° : 2017IMTA0015

Study of correlations of heavy quarks in heavy ion collisions and their role in understanding the mechanisms of energy loss in the quark gluon plasma

JURY

Rapporteurs :	**Néstor ARMESTO**, Professeur, Universidade de Santiago de Compostela **Ingo SCHIENBEIN**, Maître de Conférences HDR, Université Joseph Fourier Grenoble
Examinateurs :	**Wolfgang CASSING**, Professeur, Justus-Liebig Universität Gießen **Matthew NGUYEN**, Chargé de Recherche (1e classe), Ecole Polytechnique **Ingo SCHIENBEIN**, Maître de Conférences HDR, Université Joseph Fourier Grenoble
Directeur de Thèse :	**Pol-Bernard GOSSIAUX**, Professeur, IMT Atlantique
Co-directeur de Thèse :	**Thierry GOUSSET**, Professeur, Université de Nantes **Joerg AICHELIN**, Professeur, Université de Nantes

Für meine Eltern Hans und Christine,
und meinen Bruder Fabian Rohrmoser

Résumé en français :

Contexte : La chromodynamique quantique (CDQ), théorie de l'interaction forte, prédit un nouvel état de la matière, le plasma de quarks et de gluons (PQG) dont les degrés de liberté fondamentale, les quarks et les gluons, peuvent bouger quasi-librement. Les hautes températures et densités de particules, qui sont nécessaires, sont supposées être les conditions de l'univers dans ses premiers moments ou dans les étoiles à neutrons. Récemment elles ont été recrées par des collisions de noyaux d'ions lourdes à hautes énergies. Ces expériences étudient le PQG par la détection des particules de hautes énergies qui traversent le milieu, notamment, les quarks lourds. Les mécanismes de leur perte d'énergie dans le PQG ne sont pas compris complètement. Particulièrement, ils sont attribués aux processus soit de radiation induite par le milieu, soit de collisions de particules de type 2 vers 2, ou des combinaisons.

Méthodes : Afin de trouver de nouvelles observables pour pouvoir distinguer les mécanismes de la perte d'énergie, on a implémenté un algorithme Monte-Carlo, qui simule la formation des cascades des particules à partir d'une particule initiale. Pour traiter le milieu, on a introduit des interactions PQG-jets, qui correspondent aux processus collisionnels et radiatifs. Les corrélations entre deux particules finales des cascades, dont une représente un quark trigger, ont été examinées comme moyen pour distinguer les modèles.

Résultats : La dépendance de l'ouverture angulaire pour des corrélations entre deux particules en fonction des énergies des particules peut servir comme moyen pour séparer les mécanismes collisionnels et radiatifs de la perte d'énergie dans le milieu.

Mots clés:

Plasma des Quarks et des Gluons, Collisions d'ions lourds, Corrélations angulaires, Corrélations à deux particules, jets, fragmentations, Simulations Monte-Carlo

Summary in English:

Context: Quantum chromodynamics (QCD), the theory of the strong interactions, predicts a new state of matter, the quark-gluon plasma (QGP), where its fundamental degrees of freedom, the quarks and gluons, behave quasi-freely. The required high temperatures and/or particle densities can be expected for the early stages of the universe and in neutron stars, but have lately become accessible by highly energetic collisions of heavy ion cores. Commonly, these experiments study the QGP by the detection of hard probes, i.e. highly energetic particles, most notably heavy quarks, that pass the medium. The mechanisms of their energy-loss in the QGP are not yet completely understood. In particular, they are attributed to processes of either additional, medium induced radiation or 2 to 2 particle scattering, or combinations thereof.

Methods: In a theoretical, phenomenological approach to search for new observables that allow discriminating between these collisional and radiative energy-loss mechanisms a Monte-Carlo algorithm that simulates the formation of particle cascades from an initial particle was implemented. For the medium, different types of QGP-jet interactions, corresponding to collisional and/or radiative energy loss, were introduced. Correlations between pairs of final cascade particles, where one represents a heavy trigger quark, were investigated as a means to differentiate between these models.

Findings: The dependence of angular opening for two-particle correlations as a function of particle energy may provide a means to disentangle collisional and radiative mechanisms of in-medium energy loss.

Key Words:
Quark Gluon Plasma, Heavy Ion Collisions, Angular Correlations, Two-Particle Correlations, Parton-Energy Loss, Jets, Fragmentation, Monte-Carlo Simulations

Remerciements :

Je veux remercier beaucoup de personnes pour leur aide pendant la thèse :

Merci à Prof. Pol-Bernard Gossiaux, Prof. Thierry Gousset, et Prof. Jörg Aichelin pour votre encadrement : Votre encouragement et les discussions scientifiques fructueuses qu'on à mêné m'ont beaucoup aidé et j'en suis très réconnaissant! Je vous remercie également pour votre vigueur pédagogique avec laquelle vous m'avez enseigné des méthodes en pQCD et des méthodes numériques.

Merci à Prof. Ingo Schienbein et Prof. Wolfgang Cassing pour m'aider comme membre de mon comité de suivi de thèse. Je veux remercier également Profs. Aichelin, Cassing, Gossiaux, Gousset, et Schienbein, ainsi que Profs. Néstor Armesto et Matthew Nguyen de participer comme membre de Jury de ma thèse et Profs. Armesto et Schienbein de corriger ma thèse.

Merci à tous les personnes qui m'ont enseigné dans le passé, en particulier Prof. Willibald Plessas, Prof. Wolfgang Schweiger.

En particulier je veux remercier mes parents Hans et Christine Rohrmoser et mon frère Fabian pour m'avoir encouragé et motivé pendant la thèse (et dehors de la thèse aussi) ! Sans votre aide, cette thèse n'aurait pas été possible !

Merci également à mes collègues et amis,
MSc. Benjamin Audurier, Dr. Hamza Berrehrah, Dr. José Briz-Monago, Mag. Monika Böck,
MSc. Florian Cougoulic, Dr. Charlotte Duchemin, MSc. Audrey Francisco, Dr. Lucia Gallego-Manzano, Dr. Daniel Garcia-Fernandez, Dr. Florian Gaté, Dr. Benjamin Guiot, Mag. Sebastian Guttenbrunner, Dr. Maxime LeCalloch, Dr. Roland Katz, Dr. Jennifer Maller, Dr. Javier Martin, MSc. Kevin Micheneau, MSc. Alexandre Parent du Chatêlet, Emanuel Rušec Bakk. , Dr. Benjamin Sintes, MSc. Gabriel Sophys, Sebastian Straßmeier, et MSc. Loïck Virone.

Contents

Chapter 1

Introduction: heavy quark production in heavy ion collisions

1.1 Heavy Ion collisions as probes for hot and dense hadronic matter

1.1.1 Description of strong interaction via QCD

In an attempt to search for the fundamental degrees of freedom of matter, it was discovered that atoms are bound states of electrons e and a nuclear core formed by the nucleons: the protons p and the neutrons n. Later on, numerous additional particles were found and one learned that they belong to larger classes of particles, ordered by the considerably different mass-scales of their constituents: The leptons (from Greek ”leptos” for light; examples are the e with ≈ 0.5 MeV rest-mass), the baryons (from Greek ”barys” for heavy; the lightest baryons, and only known stable states, are the nucleons of ≈ 940 MeV rest-mass) and the mesons (from the Greek ”mesos” for ”in the middle”; e.g.: the π of ≈ 140 MeV rest-mass). Baryons and mesons are also called hadrons. The interactions – and, thus, also the bound-states – between hadrons and/or leptons were found to be mediated by exchange bosons: The photons γ for electromagnetic forces and the W^+, W^-, and Z bosons for the weak interactions. To each of the leptons and hadrons antiparticles with the same mass exists. Particles can annihilate with the corresponding antiparticles[1] and create, in an intermediate state, one of the exchange-bosons in these interactions.

However, it was discovered that hadrons do not represent elementary particles either: Instead it was found that they are bound states of three ”valence” quarks q in case of the baryon[2] or a $q\bar{q}$ pair in case of the meson. Experiments allowed to demonstrate that quarks appear in six so called 'flavors', up (u), down (d), strange (s), charm (c), bottom (b), and top (t), with different electrical charges and masses.

Quarks also possess the property of 'color', a name that refers to the fact that a number of $N_c = 3$ possible colors – red, green, and blue – exist and hadrons form color-neutral or 'white' bound states through a combination of several quarks in various color states. The confinement of quarks within hadrons is attributed to the strong interaction, a force that is mediated by the exchange of gluons G[3]. These bosons transport the color charge

---

[1] In the remainder of this thesis one will adopt for antiparticles the notation of a bar over the corresponding particles, e.g.: $\bar{p}$ for the antiproton.

[2] Due to the nature of the underlying theory (that is outlined shortly) spontaneous production and annihilation processes of $q\bar{q}$ pairs –called sea quarks– are always possible.

[3] In a first stage quarks and gluons were both understood as partons, before their individual existence has been understood. This terminology has survived.

between emitting and absorbing quarks, but also between themselves.

Quantum Chromodynamics (QCD; cf. Greek "Chroma" for color) is the quantum field theory that describes the strong interaction between partons [1] (cf. textbooks for a review, e.g.: Ref. [2]). It is a gauge theory, i.e.: it is based on the fundamental assumption that if all colors in a system are simultaneously changed, this does not affect the interactions within the system (a principle referred to as gauge invariance or invariance under gauge transformations). More precisely, systems in QCD are even invariant under gauge transformations that depend on positions in space and time. This assumption is referred to as local gauge invariance, and, thus, QCD is called a local gauge theory.

Mathematically, this notion is expressed by first introducing complex fields ψ_i for each quark and each color $i = 1 \ldots N_c$. The gauge transformations are then expressed as rotations (or rather SU(N_c) transformations) in this N_c dimensional color space acting on the quark fields, i.e.:

$$\psi_k \mapsto \psi'_j = e^{i\theta_a t^a_{jk}} \psi^k \, , \tag{1.1}$$

where t^a_{jk} with $a = 1 \ldots N_C^2 - 1$ are hermitean generators of the unitary transformations and the θ_a are, thus, real fields. Thus, the theory of QCD satisfies gauge invariance if its Lagrangian density $\mathcal{L}$ is invariant under the transformations in Eq. (1.1). Starting from a Lagrangian density for a freely moving quark, one can obtain a gauge invariant version by replacing derivatives with covariant derivatives, i.e.: $\partial_\mu \mapsto D_\mu = \partial_\mu - i g_s A^a_\mu t_a$ with the coupling strength g_s and the gluon field A^μ_a, which transforms differently under gauge transformations Eq. (1.1), cf. Refs. [2, 3] for a more detailed description. For the gluon field a gauge invariant Lagrangian density needs to be introduced as well. Finally, one, thus, arrives at the Lagrangian density of QCD,

$$\mathcal{L} = \bar{\psi} \left(i\gamma^\mu \left(\partial_\mu - i g_s A^a_\mu t_a \right) - m \right) \psi - \frac{1}{4} F^a_{\mu\nu} F^{\mu\nu}_a \, . \tag{1.2}$$

The first term on the right hand side considers the quark parts of the theory: It contains the Lagrangian of the free quark and, thus, describes its free propagation in the vacuum, but furthermore also a term that describes the quark-gluon interaction. The second term on the right hand side represents a purely gluonic part. The tensors $F^{\mu\nu}_a$ used in Eq. (1.2) are defined as

$$F^{\mu\nu}_a = \partial^\mu A^\nu_a - \partial^\nu A^\mu_a - g_s f^{bc}_a A^\mu_b A^\nu_c \, , \tag{1.3}$$

with the structure constants f_{abc} defined as

$$[t_a, \, t_b] = i f_{abc} t^c \, . \tag{1.4}$$

Analogues to the first two terms on the right hand side of Eq. (1.3) exist also in Abelian gauge theories like quantum electrodynamics (QED): In both cases these expressions result in contributions to the Lagrangian densities that depend on two gluon (photon) fields and represent the free propagation of the corresponding boson. However, in the case of QCD, there exists a third term in Eq. (1.3), which results from the non-Abelian algebra of the generators t_a. Its contribution to the QCD Lagrangian density stems from either mixed products with the first two terms and yield interactions between three gluon fields, or the squares of the third term, which result in the interactions of four gluon fields. The fundamental interactions of QCD can be symbolized by Feynman diagrams via the vertices shown in Fig. 1.1. The fact that gluons carry color charge and can, thus, interact with themselves (as manifested in the corresponding three and four gluon vertices shown in Fig. 1.1 or also in textbooks, such as e.g.: Ref. [2]) is strongly conjectured to give rise to a strong confinement force between partons. Phenomenologically, one could express

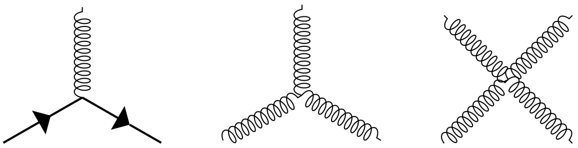

Figure 1.1: Fundamental interaction vertices of QCD: straight lines are quarks, curly lines are gluons. The direction of time has not been specified in these diagrams, i.e.: anyone of the possibilities of incoming or outgoing particles is allowed

the confinement of partons within hadrons by a potential that rises approximately linear with the distance between the partons involved.

After renormalization, the corresponding coupling $\alpha_s = \frac{g_s^2}{4\pi}$ is not a constant: Rather, it is very large in interactions between partons of small (relative) momentum scales. The respective processes occur over large time scales and spatial distances and correspond to the formation of hadronic bound states, or reactions within hadrons.

On the other hand, for partons that are subjected to large momentum transfers $\|\Delta\vec{p}\|$ the coupling α_s becomes small. In the limit $\|\Delta\vec{p}\| \to \infty$ one observes the asymptotic behavior $\alpha_s \to 0$, which is also called asymptotic freedom. For processes involving partons at large momentum and, thus, small time scales and spatial distances, the coupling is sufficiently small that a perturbative treatment (pQCD) is suitable: The corresponding cross sections (and squared matrix elements) can be expanded into a perturbative series of α_s, where the contributions of higher orders in α_s are small compared to contributions of smaller orders in α_s [4] .

1.1.2 Exploration of the QCD phase diagram via heavy ion collisions

In QCD color charges are confined within color-neutral bound-states and cannot be observed freely – in contrast to QED, where free electric charges are possible. However, analogous to electromagnetic plasma, QCD allows for collective states of (quasi-)free partons. This motivates the question, whether such states of matter exist in nature, and/or whether they can be recreated experimentally out of hadronic bound-states. Thus, it is meaningful to study the phase-diagram of QCD, cf. Fig. 1.2 for illustration.

For small temperatures T and particle densities (the latter represented in Fig. 1.2 by the chemical potential μ) quarks and gluons are confined in the bound states of hadrons, either in nucleon cores or hadronic gases. Creating states of very high temperatures would –supposedly– allow to recreate the conditions for matter at early stages of the universe, where it is expected that energy densities were very large. On the other hand, states of high chemical potential are supposed to exist, e.g. in neutron stars, due to the large gravitational pressure.

By studying systems of larger and larger T and/or μ one simultaneously approaches systems of high baryon number densities and energy densities, where partons can no longer be described as being confined within hadronic bound states. Thus, it is expected that at sufficiently high T and μ a phase transition or a cross-over to a new state of

---

[4] The quark-gluon and three-gluon vertices shown in Fig. 1.1 are both of order $\mathcal{O}(g_s)$; the four-gluon vertex of order $\mathcal{O}(g_s^2)$. Chap. 2 describes a probabilistic approximation to processes in QCD. Therein the creation of partons from incoming partons are sub-processes that can be decoupled from the rest of the process – and their individual probabilities can be calculated. This thesis considers only the contributions to these probabilities that are of leading order $\mathcal{O}(\alpha_s)$ in the coupling constant. Therefore, contributions from the four-gluon vertex will be neglected in Chap. 2, while contributions from the other two vertices will be considered.

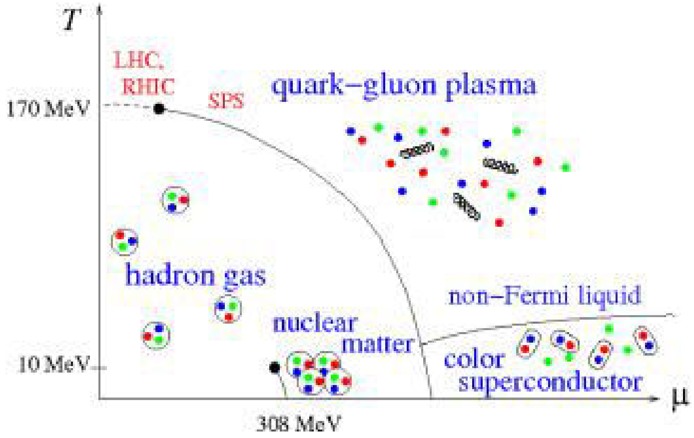

Figure 1.2: Sketch of the QCD phase diagram. At low temperatures T and baryon chemical potentials μ partons exist only in colorless hadronic bound-states, at high T and/or μ as deconfined quark-gluon plasma (QGP). The phase transition is expected to be a cross-over (dashed line) at small μ (with a critical temperature of $T_c \sim 170$ MeV for $\mu = 0$), up to a critical point (black dot) and a first order phase transition for higher μ values (solid line). Several experiments (red texts) have explored the phase diagram, in particular for large T ranges at $\mu \approx 0$ (LHC) and around the expected critical point at small μ values at $T \sim T_c$. At very large μ further states of matter, e.g. color superconducting phases are believed to exist. Figure taken from Ref. [4].

matter occurs. This new phase represents a collective state of a large number of partons that can move freely over distances d much larger than the typical length scales of their hadronic bound states, i.e.: $d \gg \Lambda_{\mathrm{QCD}}^{-1}$, perturbed only by scatterings with other quarks and gluons. This phase is commonly known as quark gluon plasma (QGP). The medium itself – rather than a mere collection of hadron bound-states – is expected to behave like a fluid of a large number of particles, quarks and gluons in this case. Thus, at large timescales after the QGP is created, one should observe the entire medium at thermal equilibrium. At smaller timescales, where the medium itself is still evolving, one can also expect phenomena like a collective flow of partons within the medium. One can also define locally thermal equilibrium and, thus, temperature within the QGP. Particles that enter the QGP experience forces of drag and (stochastic) deflection (cf. Sec. 1.2 for an overview of corresponding observables of incident heavy quarks).

In order to recreate the QGP experimentally, collisions between heavy ions (i.e., here: atoms of a high mass number, stripped of all the electrons) were performed. Cu-Cu, Au-Au, and Pb-Pb collisions with center of momentum energies up to $\sqrt{s} = 200$ GeV were performed at the RHIC experiment. At the LHC Pb cores were collided at $\sqrt{s} = 2.76$, and 5.02 TeV.

One crucial question is, how the QGP phase, once produced, can be accessed experimentally, since this state is very short lived and subsequently decays into multiple hadrons. Charm and bottom quarks (in the remainder of this thesis also referred to as ”heavy quarks”)[5] together with the resulting hadrons provide interesting probes of the QGP medium: Due to their large masses heavy quarks are most likely produced in the initial hard collisions of the incoming nucleons. Therefore, it can be assumed that they are created before the formation of the QGP, and pass through the entire medium. Be-

---

[5] Top quarks cannot be considered in the same way for the study of QGP: Their masses are even larger, but consequently, they rapidly undergo leptonic decays, before they can pass the medium. Strange quarks on the other hand do not have a sufficiently high mass: It can be expected that they are produced – and may even thermalize – within the medium.

cause of their large masses they also have large inertia compared to light partons, and are therefore less likely to thermalize within the medium. Nevertheless, since they are colored particles as well, heavy quarks can interact with partons of the medium.

Heavy quarks experience forces of drag and diffusion, when passing the QGP-medium. Therefore, an interesting observable for the study of the QGP is the in-medium energy-loss of heavy quarks, which is briefly discussed in the next section 1.2.

Finally, also light partons of sufficiently large momenta will not thermalize within the medium. Thus, in addition to heavy quarks also hard partons or even parton cascades radiated from heavy quarks provide suitable probes of the QGP, for the same reasons, and will be discussed later on.

1.1.3 Hard Probes for QGP

The QGP is a thermalized medium. Therefore, color charged particles that enter the QGP can thermalize with the medium as well, i.e.: lose as much of its initial information such as their four-momentum that they become indistinguishable from medium particles. Thus, sensitive probes of the QGP need not only to be able to interact with medium particles (in order to allow to investigate processes within the medium). They also need to be chosen in such a way that these interactions with the medium cannot be expected to lead to a thermalization of the probe itself.

These two requirements are fulfilled by so called hard probes: They consist of strongly interacting particles that possess sufficiently high energy, much larger than the temperature of the QGP-medium, so that they do not thermalize. Due to these high energy scales it can be expected that they are created in the hard collisions at the early stages of heavy ion collisions. This property makes hard probes particularly useful for studies of the space-time evolution of the QGP as well as of cumulative medium effects on the propagation of the hard probe. At least the following types of hard probes can be identified:

1. charged (light) partons at high energies that result in light hadrons,
2. heavy quarks and the resulting heavy hadrons,
3. jets, i.e.: multiple highly energetic heavy and/or light particles (described below).

While light partons can be produced anywhere in the medium, heavy quarks can only be produced at energies above a threshold of twice the quark masses: The charm and bottom quark masses correspond to so called pole masses of $m_c = 1.67 \pm 0.07$ GeV and $m_b = 4.78 \pm 0.06$ GeV, respectively (values taken from Ref. [5], p. 804-806). The high energy densities necessary for heavy quark productions are provided in the early stages of heavy ion collisions.[6]

Jets: Within pp or heavy ion collisions hard subprocesses occur, which emit large numbers of hard particles that propagate strongly collimated around a specific direction. These sets are called jets in order to distinguish them from the thermalized particles of the medium and remnants of the colliding particles.

Given a set of final particles in an experiment, one needs a precise definition of a jet that allows to establish a criterion to identify jet particles and construct the corresponding

---

[6] This argument works for QGP-media with temperatures T in the range $T_c \leq T < 2m_c$, $2m_b$. Since $T_c \ll m_c$, m_b ($T_c \sim 170$ MeV, cf. subsection 1.1.2) there exists a large range of temperatures and, thus, different QGP media that can be studied with heavy quark probes, as described in this section.

jets. There exist different definitions and, thus, different algorithms that allow to identify jets among the final particles of a heavy ion collision in experiment/in a simulation, such as, e.g., the k_t algorithm [6, 7], anti-k_t algorithm [8], the Cambridge-Aachen algorithm [9, 10], the clustering algorithm of the JADE-collaboration [11], the SISCone algorithm [12], or the cone algorithm of Ref. [13].

The production of jets can be attributed to the emission of hard partons in heavy ion collisions, which then generate a cascade of particles, both via emission of bremsstrahlung (which can happen in the medium as well as in the vacuum) as well as interactions with the medium (in the remainder referred to as jet-medium interactions).

The study of heavy quark jets (i.e. jets containing heavy quarks), instead of the study of individual heavy quarks, can provide additional information about jet-medium interactions and QGP evolution: Heavy quarks radiate light partons. Thus, correlated pairs of heavy and light particles are produced within heavy quark jets. The initial correlations of these particle pairs are, however, affected by subsequent jet-medium interactions.

For the work of this thesis two-particle correlations were calculated from the particles obtained from parton showers, which are simulated in the vacuum by means of Monte-Carlo simulations of the so called DGLAP equations (cf. Chap. 2). Some modifications for jets in the medium are introduced later on in Chap. 3. The finally obtained two-particle correlations – for the vacuum as well as for the medium – are presented in Chap. 4.

In the current chapter, Sec. 1.2 focuses on the observables and theoretical approaches concerning individual heavy quarks (and the resulting hadrons). Sec. 1.3 introduces two-particle correlations as promising alternative observables. In order to construct them, it is however necessary to describe the production of multiple particles in heavy ion collisions, in particular jets, and Sec. 1.4 will describe some theoretical approaches (in particular the DGLAP equations in subsection 1.4.2). Sec. 1.5 summarizes this short overview on the phenomenology of heavy-ion collisions and introduces the structure of the remaining part of this thesis.

1.2 Heavy-quark-energy loss in a medium

1.2.1 Nuclear modification factor

Particles passing through a medium with high momenta can lose part of their energy and 3-momenta due to interactions with medium particles. By consequence, some of those particles may remain inside the medium. On the other hand, particle suppression can indicate whether a QGP medium is produced in processes involving high temperatures or particle densities, e.g., in particular heavy ion collisions. One can quantify this suppression of the number of particles[7]experimentally by means of the so called nuclear modification factor. In case of heavy ion collisions (AA) this is the ratio of the production yield N_{AA} for a particular type of hadrons (e.g.: pions, open heavy flavor mesons, quarkonia) in heavy ion collisions and the corresponding production yield in proton-proton (pp) collisions, where supposedly the particles do not pass a medium.[8] Thus, the nuclear modification

---

[7] Phenomena like the Cronin-effect or heavy quark productions in a QGP-medium can also account for an enhancement of the number of particles. These effects are visible in the nuclear modification factor as well, e.g.: in cases, where $R_{\mathrm{AA}} > 1$.

[8] An analogous ratio R_{pA} for heavy ion collisions with protons (pA) or deuterons (dA) is also measured experimentally. This ratio can quantify the effects of the interactions between the hard probes and the nucleon remnants of the heavy ion, which is often referred to as cold nuclear matter (CNM) effects. Another observable that reflects these phenomena is given via the forward to backward ratio R_{FB} (cf., e.g., Ref. [14] for J/Ψ results).

factor can be defined in the following form

$$R_{\mathrm{AA}} = \frac{N_{\mathrm{AA}}}{\langle T_{\mathrm{AA}}\rangle \sigma_{PP}}\,, \tag{1.5}$$

where $\langle T_{AA}\rangle$ [15] is the nuclear overlap function and σ_{PP} is the cross-section for pp collisions that yield the corresponding particles. Eq. (A.1) represents a general definition of the nuclear modification factor. Actual experimental data, however, specify the nuclear modification factor as functions of the particle 3-momentum components orthogonal to the beam axis of pp or heavy ion collisions, p_T, or as functions of either both p_T and rapidity y for heavy particles or of p_T together with pseudorapidity $\eta = -\ln(\tan(\theta/2))$ (where, here, θ is the polar angle with the beam axis), for charged (light) particles. In those cases, the production yield and the cross-section differentiated with regard to p_T (and η) replace the corresponding quantities in Eq. (A.1), cf. the definitions given in Refs. [16] and [17]. Furthermore, in order to study the dependence of particle suppression on particle density in the medium (and, thus, further explore the QGP phase-diagram), it is interesting to specify R_{AA} with regard to the number of nucleons that participate in the heavy ion collisions. A related quantity is the centrality $\mathcal{C}$, which is given via the overlap area of the incident heavy ions, cf. Ref. [18] for a definition. Then, the nuclear modification factor can be calculated individually for different centrality classes, cf. the definition in Sec.$\tilde{3}$ of Ref. [19]. Alternatively, the number of participants N_{part} can be deduced from the centrality of the collision. Consequently, the nuclear modification factor can also be studied as a function of N_{part}. Fig. 1.3 shows experimental data on R_{AA} as a function

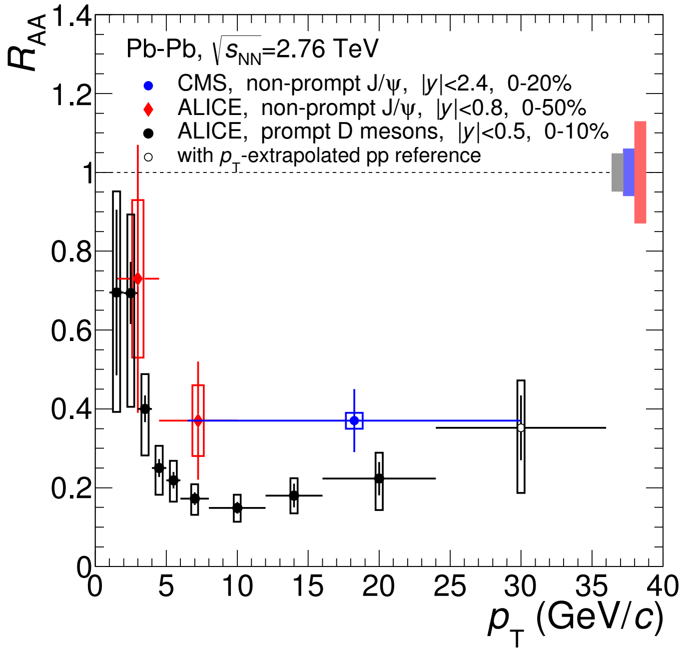

Figure 1.3: Nuclear modification factor R_{AA} as a function of p_T obtained from ALICE [20] and CMS [21] data on non-prompt J/Ψ-meson production, and from ALICE data on prompt D-meson production [22]. Figure taken from Ref. [17].

of p_T for both, the charmonium J/Ψ (which are a good proxy for B mesons; see discussion below) as well as D mesons. While the so-called prompt mesons – in Fig. 1.3 these are the D-mesons – are directly produced by the hadronization of their parton content, non-prompt mesons are the decay products of other hadrons. The non-prompt J/Ψ are weak decay products of an intermediate B-meson, which is created by the hadronization of b quarks. Due to the long life-time of the B meson, it can be assumed that its decay happens outside of a tentative QGP medium. Thus, the R_{AA} values for non-prompt J/Ψ represent an estimate for the suppression of b-quarks due to interactions with the medium, while the suppression of c (and also $\bar{c}$) quarks can be studied by the R_{AA} values of the prompt D mesons.

In general, maximal R_{AA} values can be observed at small p_T – below 5 GeV in the concrete example. With increasing values of p_T, particle suppression strongly increases, e.g. D meson production undergoes a minimum at $p_T \approx 10$ GeV in Fig. 1.3. This kind of behavior can be expected, if the incident hard particles undergo additional processes of energy loss in the medium: Then, compared to the particle production outside of a medium, more particles will be found at small p_T and fewer at higher p_T. For even higher p_T values R_{AA} slowly increases again, which is clearly visible in the case of D-mesons above 1 GeV, while for the J/Ψ this situation is not so clear cut in Fig. 1.3, due to insufficient amounts of experimental data. Studies of the R_{AA} of charged particles by CMS [23] found that for high p_T values, up to 100 GeV, the nuclear modification factor rises strongly and approaches 1 in some cases. An asymptotic behavior $R_{\mathrm{AA}} \to 1$ for high p_T values has also been found theoretically [24].

The R_{AA} data shown in Fig. 1.3 was obtained for collisions in the centrality classes $0-20\%$ and $0-50\%$ for the J/ψ and $0-10\%$ for the D-mesons. Comparisons with values of R_{AA} for less central collisions, as they were performed, e.g. in Ref. [22], show that the D mesons are more suppressed in central collisions. Ref. [17] also shows the corresponding R_{AA} values as a decreasing function of N_{part}. This behavior corresponds well to the picture that the number of interactions of the corresponding heavy quark with the medium increase for a denser phase of a medium (i.e.: when N_{part} is larger). Ref. [17] concludes to an effect of the quark masses, since the mesons originating from b quarks appear to be less suppressed, as those stemming from c quarks. However, it is also noted therein that a definitive conclusion can not be drawn at the moment, due to the large error bars of the R_{AA} values.

1.2.2 Azimuthal anisotropy and Elliptic flow

A tentative QGP medium created in heavy ion collisions does not necessarily have to be spherically symmetric in space. In particular, spatial anisotropy is to be expected for more peripheral collisions, where already the overlap of the incident heavy ions is of lenticular shape, with its largest extension orthogonal to the event plane (which is defined by the directions of the impact parameter and the beam axis). For heavy quarks (the same is true for jets) it can be assumed that they are created directly in the heavy ion collision, due to the high energy threshold necessary for their production. Thus, they travel through the entire medium. Therefore, it can be expected that this kind of spatial anisotropy translates into an anisotropy in their final state momenta. A study of these anisotropies represents an interesting tool in order to quantify the relative importance of different mechanisms of in-medium energy loss: As Ref. [19] notes, theoretical approaches predict that parton-energy loss depends linearly on the in-medium path-length for collisional processes, and quadratically for radiative processes (cf. also subsection 1.2.3.3).

In order to access the corresponding azimuthal anisotropy experimentally, one can study the distribution $\frac{d^2N}{dp_T d\phi}$, where p_T are particle-momentum components transverse to the beam axis with azimuthal angle ϕ, and, in particular, its Fourier expansion with regard to ϕ (For a definition in form of the corresponding equation cf., e.g.: Ref. [25]). Thus, this Fourier expansion is given as the sum of a uniform distribution over the azimuthal angle ϕ and corrections to this isotropic radiation from higher order coefficients v_n. For non-central heavy ion collisions, the second Fourier coefficient v_2, the so called elliptic flow, is the dominant contribution of all the deviations from the isotropic behavior.

Positive v_2 values can be attributed to different phenomena: Mostly at low p_T scales they also reflect collective phenomena of the QGP-medium, such as, e.g. its anisotropic expansion. However, at high p_T scales, positive v_2 values can be interpreted as a result of azimuthally anisotropic energy loss.[9]

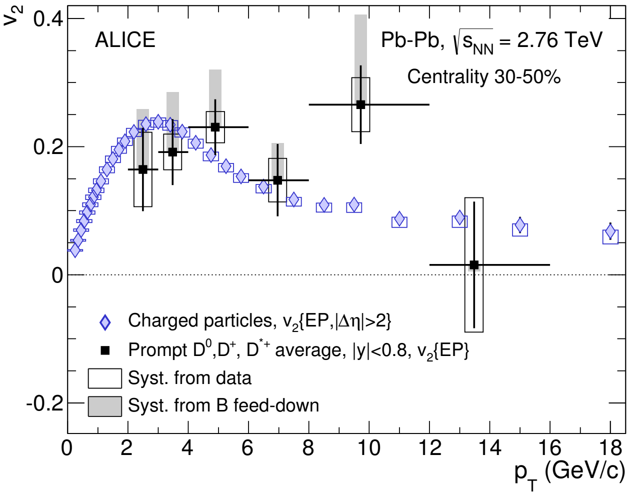

Figure 1.4: ALICE data [25, 26] on elliptic flow v_2 for Pb-Pb collisions in the 30 to 50 % centrality class at $\sqrt{s_{\text{NN}}} = 2.76$ TeV as a function of p_T obtained from charged particles and prompt D-mesons. This figure was taken from Ref. [19].

As an example Fig. 1.4 shows elliptic flow data for prompt D mesons as well as for charged particles both created in semi-peripheral Pb-Pb collisions at $\sqrt{s_{\text{NN}}} = 2.76$ TeV. The data for charged particles strongly increases at small p_T values and reaches a maximum of $v_2 \approx 0.3$ around $p_T \approx 3$ GeV, but falls off for higher p_T values. However, it decreases only slowly for p_T values above 7 GeV and, thus, retains a residual positive v_2 value at higher p_T scales. While there are fewer experimental values available for the case of D mesons, data also agrees in that case with comparable v_2 values around $v_2 \approx 0.2$ at similar p_T scales.

Fig. 1.4 confirms in almost all cases the expectation of a positive, non-vanishing v_2. Thus, the image that in directions of the event plane (in-plane) parton propagation is less suppressed than out-of-plane. In general small positive v_2 values were observed (at least for small p_T) in several different systems, e.g. in heavy ion collisions of $\sqrt{s_{\text{NN}}} = 200$ GeV at the RHIC experiments STAR and PHENIX (while for smaller energy scales of $\sqrt{s_{\text{NN}}} = 62.4$ GeV and $\sqrt{s_{\text{NN}}} = 39$ GeV values compatible to 0 or even slightly negative can be observed as well.). Elliptic flow values obtained from both, RHIC as well as ALICE data, are larger for more peripheral collisions – At least this behavior is true up to semi-peripheral centrality classes, where the RHIC data exhibit the maximal v_2 values.

---

[9] Alternatively, azimuthal anisotropy can also be studied by means of a comparison of 2 different nuclear modification factors: One obtained from particles that travel in the direction of the event plane and another one for particles propagating orthogonal to the event plane. A difference in these 2 modification factors corresponds to azimuthal anisotropy and is directly correlated to a non-vanishing value of the elliptic flow, as Ref. [19] notes.

1.2.3 Theoretical approaches to energy loss of individual particles

On the one hand, this subsection is intended to give an overview of some of the theoretical approaches to parton energy loss in the medium, in particular heavy quark energy loss. On the other hand, its first part, sub-subsection 1.2.3.1, serves also as a basis for the effective models of parton-medium interactions presented in Chap. 3.

Sub-subsection 1.2.3.1 introduces the notion of transport equations, but focuses almost exclusively on the Langevin-equations (since the models of Chap. 3, in particular the one outlined in Sec. 3.2, can be understood in this context). Thus, it should be noted here, that there exist other forms of transport equations, such as the more general Boltzmann- and Fokker-Planck equations. Furthermore, these transport-equations are also used by theoretical approaches to in-medium energy loss, e.g. the one of Refs. [27, 28], which reproduced for open heavy flavors the shapes of the R_{AA} and v_2 data from RHIC reasonably well in Ref. [27] and gave predictions for LHC data in Ref. [28].

In order to demonstrate the usefulness of transport equations, in particular the Langevin-equations, sub-subsection 1.2.3.2 cites an example of an approach based on this framework, together with a complementary approach, both however within the framework of QCD. An important interference effect for medium-induced parton radiation, the so-called BDMPS effect is then introduced in sub-subsection 1.2.3.3. While this effect was originally found for the propagation of individual particles in the medium, it also plays a role for the propagation of jet-particles, where an analogous description can be found. The BDMPS effect will, thus, also be discussed in Sec. 1.4. Approaches that consider in particular the effects of a strong QCD-coupling and go beyond pQCD, are outlined in sub-subsections 1.2.3.4 and 1.2.3.5. Sub-subsection 1.2.3.6 gives a summary on this subsection.

1.2.3.1 Summary on transport equations

A general analytic framework to describe particle energy-loss in a medium relies on transport equations. In these kind of approaches the interactions between an incident particle and the thermalized medium it traverses are represented by effective forces (encoded by the transport coefficients) acting on the incident particle.

Transport equations approximate the interaction of the medium with the incident particle as continuous force fields. Thus, these kind of approaches are valid, if the time after which the Brownian particle is at thermal equilibrium, the relaxation times τ_Q, are much larger than the duration of the interaction τ_0, i.e.: $\tau_Q \gg \tau_0$. One can use the estimate $\tau_Q \simeq \frac{m}{T}\tau_{eq}$, as Ref. [17] notes, where m is the mass of the incident particle, T is the medium temperature, and τ_{eq} its equilibration time. Thus, for heavy quarks produced in heavy-ion collisions [17] with large heavy quark masses (and temperature scales of the order of several 100 MeV) , the relaxation time can be estimated to be larger although not much larger than typical values of τ_0 (estimated here to be of the order of $\sim \frac{1}{T}$).

Langevin equations take the following form

$$\frac{dp^i}{dt} = -\eta_D p^i + \xi^i(t)\,, \tag{1.6}$$

where p^i are the components of the Brownian particle three momentum $\vec{p}$. Thus, the forces described by Eq. (1.6) consist of a drag force acting in the opposite direction of the incident parton momentum as well as a stochastic force $\vec{\xi}$. The strength of the drag force is given by the transport coefficient η_D. The stochastic force $\vec{\xi}$ represent the random collisions that the Brownian particle undergoes when passing a thermal medium. Thus, the values of $\vec{\xi}$ are random. However, their distribution over time has to obey the condition

$$\left\langle \xi^i(t)\xi^j(t')\right\rangle = b^{ij}\delta(t-t')\,, \tag{1.7}$$

with $b^{ij} = \kappa\delta^{ij}$ for non-relativistic particles in a locally isotropic medium and $b^{ij} = \kappa_L\frac{p^ip^j}{\|\vec{p}\|^2} + \kappa_T\left(\delta^{ij} - \frac{p^ip^j}{\|\vec{p}\|^2}\right)$ for a relativistic particle in the same type of medium. κ, or, respectively κ_L and κ_T are called diffusion coefficients. For a medium at rest, one has to demand furthermore that $\langle\xi^i(t)\rangle = 0$ for all i.

For media at thermal equilibrium the drag and diffusion coefficients can be related by means of the Einstein relation. For non-relativistic particles one obtains

$$\kappa = m\eta_D T\,, \tag{1.8}$$

and for relativistic particles (cf. Refs. [29, 30])

$$\eta_D(\vec{p}) = \frac{\kappa_L(\vec{p})}{2Tp_0} + \mathcal{O}\left(\frac{1}{\|\vec{p}\|}\right)\,. \tag{1.9}$$

1.2.3.2 pQCD based energy loss descriptions

Two particular approaches to the calculation of heavy quark in-medium energy-loss are briefly explained. Both of them describe the interactions between the heavy quark and the medium particles in the framework of pQCD, but attribute the energy loss to different processes: The first one calculates the transport coefficients κ_L, κ_T and η_D that were discussed in the previous sub-subsection 1.2.3.1 from processes of collisional energy loss. The second one considers both collisional as well as radiative energy loss, but only a single scattering that represents the interaction with a very dilute medium.

Parton energy loss can be calculated from the changes of heavy quark momenta over time described by transport equations. Ref. [31, 32] calculates the $\kappa_{L/T}$ of incident heavy quarks as the average momentum transferred per time in longitudinal/transverse direction from the medium to the heavy quark from the matrix elements of elastic 2-2 collisions (neglecting radiative collisions) with quarks and gluons in pQCD. The average number of these collisions per time step is given by either a Bose-Einstein or a Fermi-Dirac distribution, as the QGP-medium is assumed at thermal equilibrium. For small momentum transfers, gluons, exchanged with the heavy quark, have long wavelengths. Thus, medium effects need to be resummed at these scales. Ref. [32] considers the transport coefficients $\kappa_{L/T}$ as the sum of a contribution from collisions with hard intermediate particles, where the matrix elements of 2-2 scattering are obtained from the corresponding diagrams in pQCD, and a contribution from collisions with soft gluon exchange, where the matrix elements are resummed in the Hard Thermal Loop (HTL) approximation [33]. The drag coefficient η_D is obtained from $\kappa_{L/T}$ via the Einstein relation Eq. (1.9) [29, 30].

Refs. [33–40] describe collisional as well as radiative in-medium energy loss in a dilute QGP medium in thermal equilibrium. Thus, the interactions with the medium are – at leading order – considered as the interaction of the incident particle with a single medium parton as scattering center, which leads, in case of radiative energy loss, to the radiation of a single gluon. For the description of intermediate gluons HTL propagators are used in order to resum soft medium effects. From the matrix elements of the interaction the spectrum of the energy lost by the incident particle can be calculated, and, thus, the fractional energy loss $\Delta E/E$. In comparison to the static DGLV approach [34, 35] the approach of Refs. [36, 37] represents an extension to a dynamical QCD-medium. Therein, recoil effects were studied for an optically thin medium. Finite size effects (i.e.: consequences of the finite extension of the QGP medium.) and magnetic mass effects are considered as well.

1.2.3.3 BDMPS formalism

The Landau Pomeranchuk Migdal (LPM) [41, 42] effect refers to the suppression of medium induced radiation for a highly energetic particle that interacts with the medium via multiple scattering. Baier, Dokshitzer, Müller, Peigné, and Schiff (BDMPS) explain this kind of behavior by interferences between the different possible processes of interactions between the incident particle and the medium (examples are depicted in Fig. 1.5). This description was first used to describe photon radiation from an electron antenna in a QED medium in Ref. [43] and then for gluon radiation in a hot and dense QCD medium in Ref. [44].

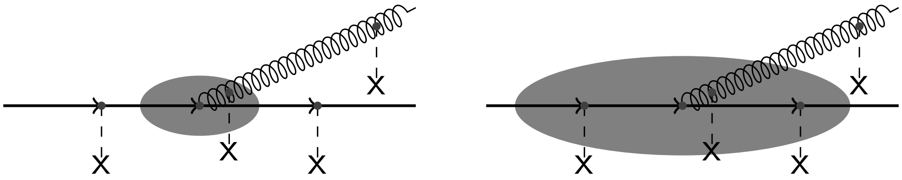

Figure 1.5: Diagrammatic depiction of gluon radiation of a quark line in the medium. Both gluon (curly line) and quark (arrows) undergo scatterings off medium particles (X symbol). The gray oval represents the formation time of the gluon. Left panel: BH-regime of radiation; Right panel: coherent radiation from 3 scattering centers.

Ref. [44] calculates in pQCD the radiation intensities $\omega\frac{dI}{d\omega}$ for the emission of a single gluon from a quark that scatters from N static scattering centers before it leaves the medium after a length L. The formalism is based on the assumption that the radiated particles is sufficiently soft to allow for the factorization of the scattering and the radiation parts in the matrix element. In order to decide whether interference effects (from multiple amplitudes for radiations between different scattering centers) play a role, the formation time t_{form} of the gluon was compared to the mean free path length $\lambda = \frac{L}{N}$ of the quark. In case $t_{\text{form}} < \lambda$ the Bethe-Heitler (BH) regime of independent radiation is obtained. Otherwise, if $t_{\text{form}} > \lambda$, the formation of the gluon happens simultaneously to the scattering from a certain number ν (estimated in Refs. [45, 46]) of scattering centers, which is ω-dependent. In this LPM regime of coherent radiation, interferences between the ν corresponding amplitudes suppress induced radiation. BDMPS identified the BH and LPM regime by introduction of a dimensionless parameter (here for the QCD case)

$$\kappa = \frac{\lambda\mu^2}{2\omega}\,, \tag{1.10}$$

where μ is the Debye mass of the medium. If $\kappa > 1$ the BH behavior applies, in case $\kappa \ll 1$ the LPM effect. BDMPS also specify a further, different radiation behavior for gluons that are radiated above a certain energy scale ω_{fact}, i.e.: $\omega > \omega_{\text{fact}}$, the factorization limit. In this regime $\lambda > L$ and, thus, the gluon is radiated coherently from all N scattering centers, i.e.: $\nu = N$. Summarizing, one finds, with regard to the energy of the emitted gluon ω, 3 different energy intervals that correspond to the 3 different radiation behaviors: $\omega < \omega_{\text{BH}} \sim \lambda\mu^2$ for the BH regime, $\omega_{\text{BH}} < \omega < \omega_{\text{fact}} \sim \frac{\mu^2 L^2}{\lambda}$ for the LPM regime, $\omega > \omega_{\text{fact}}$ for radiation above the factorization limit.

In order to quantify the LPM suppression BDMPS showed for the QED case [43], that in the LPM regime induced radiation is produced by ν scattering centers instead of a single one, as in the BH case (illustrated in Fig. 1.5). Thus, they found the following relation between the corresponding radiation densities

$$\left(\omega\frac{dI}{d\omega dz}\right)_{\text{LPM}} \approx \frac{1}{\nu}\left(\omega\frac{dI}{d\omega dz}\right)_{\text{BH}}\,, \tag{1.11}$$

where z represents in this particular case the distances along the path of the electron propagation. BDMPS found an analogous behavior for the LPM radiation density in the QED and QCD cases, which, for the QCD case, reads, for $\omega_{\text{BH}} < \omega < \omega_{\text{fact}}$, as

$$\left(\omega \frac{dI}{d\omega dz}\right)_{\text{BDMPS}} = \frac{3\alpha_s}{2\pi}\frac{C_R}{\lambda_g}\sqrt{\tilde{\kappa}\ln\left(\frac{1}{\tilde{\kappa}}\right)} \qquad \text{with } \tilde{\kappa} = \frac{2C_F}{N_C}\kappa\,, \tag{1.12}$$

and where $\lambda_g = \lambda \frac{C_F}{N_c}$ is the gluon mean free path length. This behavior leads to a total in-medium energy loss proportional to L^2 for all energies of the incident quark above a critical value $\omega_{\text{fact}} = \frac{L^2\mu^2}{\lambda}$, the factorization limit. Below this scale, the energy loss increases linearly with L.

If one wants to describe the propagation of heavy quarks, one has to take into account that the large heavy quark mass m_Q leads to sizable additional phenomenological consequences. A prominent feature is the so called dead-cone effect [47]:This is the phenomenon that heavy quarks of energy E can only radiate gluons at branching angles $\theta > \frac{m_Q}{E}$ or larger – outside the so called 'dead-cone'. This statement holds for heavy quark fragmentation in the vacuum. However, the interplay of the dead-cone effect with medium induced radiation, as described by the BDMPS formalism, may give rise to additional effects. Thus, it has been argued that interactions with the medium can lead to radiation inside the dead-cone [48].

1.2.3.4 T-matrix approach

In contrast to the methods described in the previous two subsections the T-matrix approach [49–51] goes beyond pQCD calculations. It approximates the interactions of a heavy quark with the medium via scatterings within an effective potential $V(\vec{p}\,', \vec{p})$ with the ingoing (outgoing) heavy quark momenta $\vec{p}(\vec{p}\,')$ in the center of mass frame. The T-matrix approach is well suited to describe also non-perturbative effects, since the effective potential $V(\vec{p}\,', \vec{p})$ can be modeled accordingly.

The T-matrix for the two-body interaction is calculated by means of a Lippmann-Schwinger equation (cf. Eq. (15) of Ref. [49]) of the form,

$$T(E, \vec{p}\,', \vec{p}) = V(\vec{p}\,', \vec{p}) - \int \frac{d^3k}{(2\pi)^3} V(\vec{p}\,', \vec{k}) G_2(E, \vec{k}) T(E, \vec{k}, \vec{p})\,[1 - 2f_k]\;, \tag{1.13}$$

with the center of mass energy E, the two-particle propagator G_2 in the medium and the Pauli-blocking factor f_k. For $V(\vec{p}\,', \vec{p})$ the so called Cornell potential for quarkonia [52, 53] (which can be changed in order to model open heavy flavor states) was used. It is essential for the T-matrix approach to be able to describe the medium modifications of the potential, a problem that has not yet been fully resolved. As Ref. [19] notes, the heavy quark free and internal energies calculated in lattice QCD have been used previously as limits for the potential $V(\vec{p}\,', \vec{p})$.

Once the T-matrix is obtained from the Lippmann-Schwinger equation, one can calculate the drag and diffusion coefficients of the medium. They were found to approach the perturbative results at high momentum scales.

The T-matrix approach is particularly suitable for the treatment of the interactions of the heavy quark with the medium at non-perturbative scales. As Ref. [19] notes, it can be used to describe both open and hidden heavy flavor systems, in their scattering as well as bound states: A large contribution to heavy quark in-medium energy-loss stems from the creation of intermediate excited heavy meson states (e.g.: D-meson resonances in the case of incident c-quarks), which are formed while the corresponding heavy quark passes the medium (represented by the effective potential). Pure pQCD calculations do not contain this type of contribution to heavy quark energy loss. On the other hand, since processes of heavy quark energy loss are summarized in an effective potential, it is not immediately evident how one can identify contributions from collisional or radiative processes within the T-matrix approach. While such a distinction might not be necessary in order to describe the energy loss of a single heavy particle, it is important for the description of (heavy quark) jets (cf. Sec. 1.4).

1.2.3.5 AdS/CFT correspondence

The Anti-de Sitter (AdS)/Conformal field theory (CFT) correspondence, first indroduced in Ref. [54], conjectures that string theories that are defined on an $n+1$ dimensional Anti-de Sitter space[10] are linked to a field theory in n spatial dimensions, via a holographic principle [55]. In particular, if one of the two theories is strongly coupled, the other one involves only a weak coupling and vice versa. This property makes the AdS/CFT correspondence a very valuable tool, since the temperatures of the tentative QGP media produced in LHC or RHIC experiments are of the order of a few times Λ_{QCD}. Therefore, it can be expected that non-perturbative effects of strongly coupled QCD play still a considerable role in the interactions of the medium particles.

When the AdS/CFT correspondence is applied to a description of heavy quark energy-loss an $\mathcal{N} = 4$ super-Yang-Mills (SYM) theory is used instead of QCD as the CFT side of the correspondence, since no exact dual to QCD has been found yet, while the Type IIB string theory is the dual to the $\mathcal{N} = 4$ SYM theory [56, 57]. Ref. [58] notes that both theories allow for plasma-media at non-vanishing temperatures which show similar phenomenological behaviors.

A heavy quark that is propagating through a medium (on the CFT side of the correspondence) is represented in the five dimensional AdS space via the following system: First, a so called brane is introduced. By definition, this object extends into four dimensions – which leaves open the possibility that further objects are placed along the remaining fifth dimension. The heavy quark is represented via a string extending in the fifth dimension with one endpoint close to the brane. The other endpoint is the horizon of a black hole, which corresponds to the thermal medium. If the endpoint close to the brane moves, part of its momentum is transferred towards the black hole. Thus, Refs. [56, 57] obtain a drag-like behavior $\dot{p} = -\eta_D p$. Calculations of Refs. [59, 60] describe scenarios corresponding to thermal fluctuations. Thus, they obtain also the longitudinal and transverse diffusion coefficients κ_L and κ_T, respectively.

1.2.3.6 Conclusions on theoretical approaches

This subsection briefly introduced some of the many qualitatively different theoretical approaches towards the mechanisms of in-medium parton energy loss: Already in the framework of pQCD there exist different approaches that describe the energy-loss in the medium either via collisional processes alone, or via a combination of collisional and radiative processes. The energy spectrum of the radiated gluons in the medium can largely be affected by interference effects, cf. sub-subsection 1.2.3.3. Other models (cf. sub-subsections 1.2.3.4 and 1.2.3.5) are particularly valid for strong couplings. Furthermore, there exist approaches by Refs. [61–63] that describe hadronization processes (and processes of decay of the newly formed bound states) within the QGP medium. This thesis will rather adopt the notion that hadronization occurs outside of the medium: At

---

[10] This is a particular type of (curved) space-time with a negative cosmological constant.

the very least the incident hard partons are considered at momentum scales that are sufficiently high to allow for multiple perturbative parton branchings before hadronization processes that occur on rather long time scales may happen. More importantly, in this thesis mostly media with temperatures $T \gg T_c$ are considered. Thus, one can argue that bound states do not form inside these media, much in contrast to media where $T \sim T_c$.

Merely with regard to the number of different approaches to parton-energy loss in the medium, it is necessary to search for observables that put constraints on these models. Since the models also emphasize different phenomena, one could learn, by means of these kinds of conditions, about the relative importance of the contributions to in-medium energy loss, and in particular about the role of collisional and radiative processes. To this end, the next subsection is centered around a combination of the observables R_{AA} and v_2.

1.2.4 Comparisons

As a short motivation of the work of this thesis results for both R_{AA} and v_2 obtained from different theoretical models of in-medium energy loss – based on either collisional or a combination of collisional and radiative processes – are shown in Fig. A.2 as functions of p_T in comparison to experimental values [64].

The experimental data for R_{AA} show a steep decrease for $p_T < 5$ GeV. For $p_T > 5$ GeV the suppression is stronger ($R_{\mathrm{AA}} < 0.5$), with only slight variations. This qualitative behavior is reproduced quite well, by almost all of the theoretical models considered, except for the results by WHDG [65, 66] and Vitev et al. [61], where only R_{AA} values for $p_T > 3$ GeV, or, respectively $p_T > 4$ GeV is shown. Fig. A.2 shows for the experimental data of v_2 small, positive values up to $p_T = 11.5$ GeV (the only remaining data point would allow for vanishing elliptic flow as well). Most of the depicted theoretical results exhibit a maximum around $p_T \approx 3$ GeV and decrease for higher p_T – a qualitative behavior that is consistent with the experimental data. However, the WHDG and POWLANG [32] results show rather a monotonous increase of v_2 with p_T than a clear maximum.

For a quantitative comparison between theory and experiment, many sources for theoretical uncertainties need to be considered: Notably, there does not exist an universal consensus among the different approaches about the treatment of heavy quarks at small energy and momentum scales. Thus, the ignorance about the precise hadronization mechanisms has been recognized as an important contribution to theoretical uncertainties, at least by the URQMD [67], DUKE [68], and POWLANG approaches. For the URQMD approach, e.g. differences between R_{AA} and v_2 values obtained with a coalescence model for hadronization or the phenomenological Peterson fragmentation function can be as large as 20% for D-meson production in Au-Au collisions at $\sqrt{s} = 200$ GeV. Another source of uncertainty is the interaction with the medium at small energy scales. In particular, models based on HTL calculations, such as MC@sHQ+EPOS2, BAMPS [69–72], the corresponding version of POWLANG, and the calculations by Djordjevic et al. [37, 73]. use an infrared regulator for the propagators of effective thermal gluons that are exchanged between the hard probes and the medium. This regulator has the dimension of a mass and is of the order of the Debye mass of the medium. Its numerical value is an important source of theoretical uncertainty, as Ref. [27] notes. Other important theoretical uncertainties are, e.g. the running of the coupling α_s (cf. [27]), in particular the scale of the coupling (cf. [32]), the uncertainties of shadowing effects (TAMU [74–76], and DUKE [68]), uncertainties in the PDFs [69–72] [11] . The resulting theoretical uncertainties

---

[11] Furthermore, some aspects, such as the consideration of hydrodynamic evolution of the medium (e.g. [68], [67], [68], [27]), shadowing ([68, 74–76]), or the running of the coupling ([27, 37, 69–73]), differ among the various models.

are of the order of magnitude of $\approx 0.1 - 0.2$ for R_{AA} and of $\approx 0.01 - 0.05$ for v_2.

One can observe a general tendency that models that produce sizable values for R_{AA}, or even overestimate the experimental results, yield too small v_2 values: Thus, if one focuses only on p_T values below 10 GeV/c, no model produces v_2 values above the central values, with the only exception of BAMPS for elastic energy loss[12]. However, many of these models overestimate R_{AA} in the same p_T region. It can be concluded, that the combination of both observables, R_{AA} and v_2, can serve as constraints of the available theoretical models. Considering the sizable experimental errors, as well as the aforementioned theoretical uncertainties, most of the theoretical approaches agree reasonably well with the available R_{AA} data. Furthermore, most of the models for purely collisional energy loss also reproduce the experimental data for v_2. Among the theoretical models that consider both radiative and collisional energy loss, only the MC@sHQ+EPOS2 approach reproduces the v_2 data for small as well as larger p_T values. If one considers, however, that the sources of uncertainty mentioned in Ref. [70], can amount to differences in v_2 as large as 0.05, one can argue that also the radiative and elastic BAMPS results are within a reasonable vicinity of the experimental data, at least for small p_T values. Since both, the MC@sHQ+EPOS2 as well as the BAMPS also produce reasonable R_{AA} and v_2 values if they consider collisional energy loss mechanisms alone, one has to conclude that qualitatively considerably different models might lead to comparable results for R_{AA} and v_2.

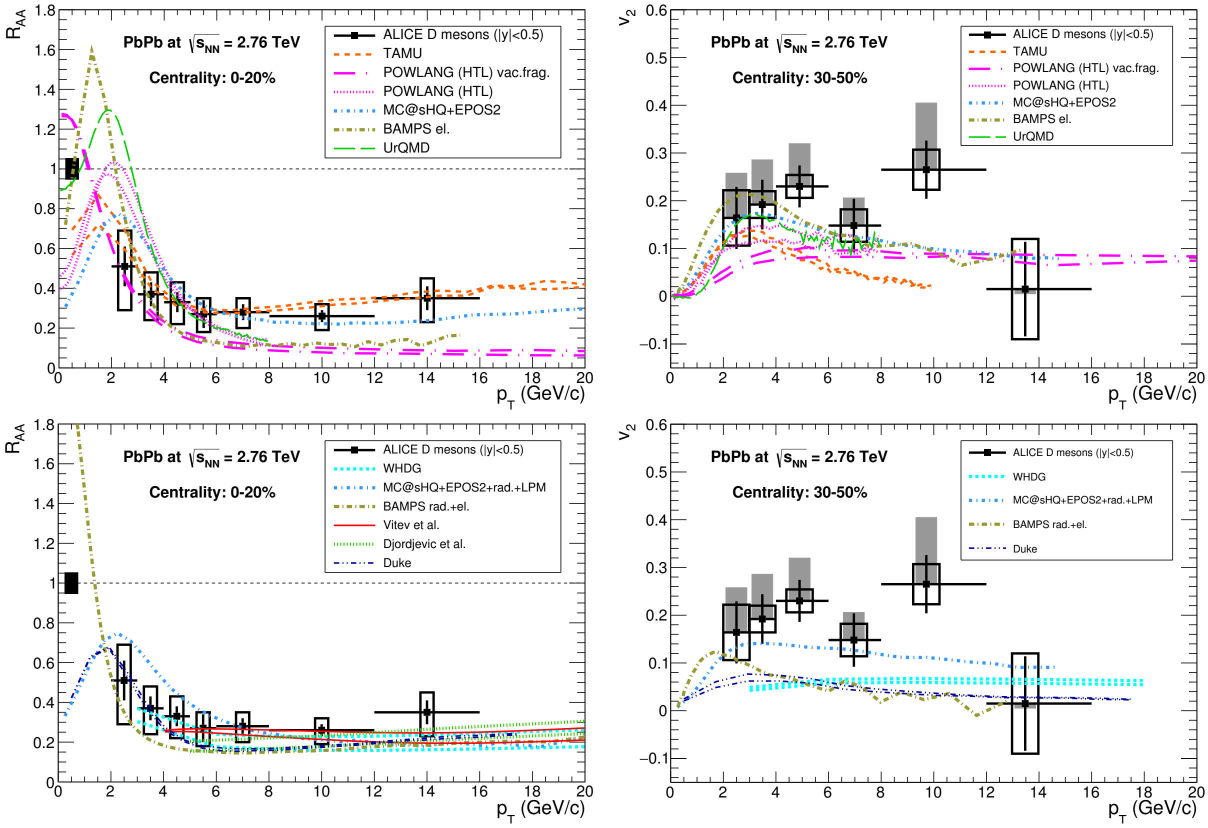

Figure 1.6: Nuclear modification factor (left panels) and elliptic flow (right panels) as functions of the averaged prompt D-mesons from Pb-Pb collisions in comparison with different theoretical model approaches, that use either solely collisional (upper panels) or collisional as well as radiative energy loss. Plots taken from Ref. [19].

---

[12] However, BAMPS was also calibrated to reproduce the elliptic flow.

In conclusion, it is mandatory to search for further, discriminative observables, in order to distinguish between the different energy-loss models. It can be argued that correlations between two particles that are radiated in the same heavy ion collision and can be expected to stem from the same hard process are a suitable choice of observable. In particular, this argument applies to the correlations between two jet particles: First of all, the number of particle pairs depends on the number of radiated particles inside the jet. Thus, one can expect that results from models that include processes of induced radiation are considerably different from those that neglect these types of processes. Secondly, it is, in principle, possible to generate the necessary experimental data at detector at RHIC or the LHC, because they obtain from individual heavy ion collisions multiple signals in different bins (of directions given via the azimuthal angle ϕ and the pseudorapidity η) which can be correlated among one another. Lastly, some first results, as e.g. for the azimuthal correlations shown in Fig. 1.8, already exist.

1.3 Correlations between heavy mesons and light hadrons

As it was shown in the previous sections (cf. subsections 1.2.1 and 1.2.2), the QGP-medium can be studied by means of observables that are constructed from large sets of individual particles. Examples are the nuclear modification factor R_{AA} and the elliptic flow v_2. An alternative to these kind of observables consists in two particle correlations, which are observables constructed from sets of particle pairs of so called trigger and associated particles.

The trigger is a particle that satisfies a certain condition, e.g. its p_T lies within a certain range and one considers the leading particle (i.e. the one with the highest p_T). Alternatively, one can also use heavy mesons (i.e. mesons with valence c or b quarks) as trigger. The advantage of this choice is, that one tags at the same time a heavy quark, which is most likely created in the initial hard processes following the heavy ion collision, due to its large mass. The heavy particle can be created in hard collision processes together with a corresponding antiparticle emitted in the opposite direction (back-to-back). Also the trigger particle can radiate further (light) particles while passing through the medium, due to both bremsstrahlung and induced radiative processes – and, thus, form a heavy quark jet. In all of these cases, there exists a correlation between the trigger particle and associate particles in the event. The corresponding particles are selected in the experiment by consideration of either anti-mesons or light hadrons (e.g. pions), respectively, as associated particles.

Angular correlations can be obtained from the directions of the trigger and associate particle 3-momenta, which are specified by the pseudorapidity η and the azimuthal angle ϕ. Thus, one can construct, e.g., a bi-dimensional distribution

$$\frac{1}{N_{\text{trig}}} \frac{d^2 N_{\text{assoc}}}{d\Delta\eta d\Delta\phi}, \tag{1.14}$$

of the number of associated particle N_{assoc} (N_{trig} is the number of trigger particles) over the respective differences $\Delta\eta$ and $\Delta\phi$ in pseudorapidities and azimuthal angles between a trigger and an associated particle. An example is given in Fig. 1.7: These kind of correlations show a ridge structure in the $\Delta\eta$ direction as well as a double peak structure (in case of two-jet events) in the $\Delta\phi$ direction (cf. also Refs. [78, 79]). The so-called azimuthal angular correlations are then a contribution

$$\frac{1}{N_{\text{trig}}} \frac{dN_{\text{assoc}}}{d\Delta\phi}, \tag{1.15}$$

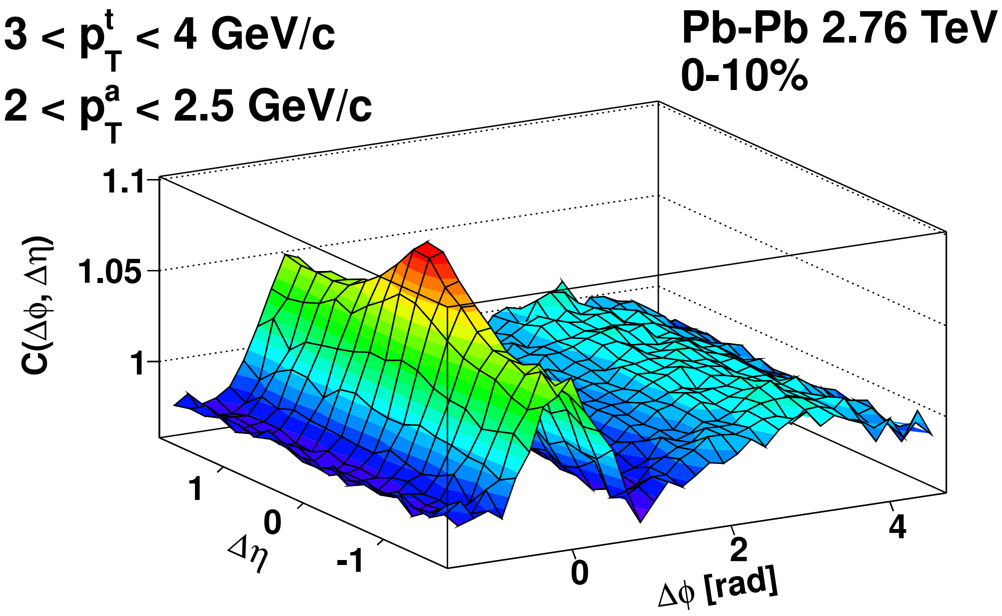

Figure 1.7: Distribution $C(\Delta\phi, \Delta\eta)$ over the differences in the pseudorapidities $\Delta\eta$ and azimuthal angles $\Delta\phi$ between trigger and associated particles (with transverse momenta p_T^t and p_T^a, respectively). As it is defined in Ref. [77], the distribution $C(\Delta\phi, \Delta\eta)$, is proportional to the bi-dimensional distribution of Eq. (1.14). The data was obtained from the 10% most central Pb-Pb collisions with $\sqrt{s} = 2.76$ TeV. This figure was taken from Ref. [77].

from a selected range in $|\Delta\eta|$ around $\Delta\eta = 0$. With regard to this distribution the peak – as well as the corresponding particles in these directions – around $\Delta\phi = 0$ is also called the "near side", while the one around $\Delta\phi = \pi$ is referred to as the "away side".

Studies of azimuthal angular two-particle correlations are often (cf. e.g. Ref. [80]) viewed as a valuable tool in order to further constrain the mechanisms of in-medium parton energy loss: Correlations between two particles created in a hard back-to-back emission allow to gain insight on the total in-medium energy loss, as well as on its dependence on the in medium path length. Examples are the angular correlations between D-$\bar{D}$ pairs (for a theoretical approach cf. Ref. [81]) or the azimuthal angular correlations between a heavy D-meson and a light hadron radiated in the away side.

Investigations on the near side of azimuthal angular correlations allow to specify the medium modifications on the propagations of individual jets, e.g. angular jet-broadening and increased intra-jet radiations.

The correlations between two heavy particles can be described by the individual propagation of each of the two particles. Since light particles – once radiated – do not play a role in the evolution of the heavy particles, it can be completely ignored, whether the D and $\bar{D}$ mesons are part of heavy quark jets. For the description of the correlations between a heavy – trigger – D-meson associated to any of the light hadrons of a jet, however, all sufficiently hard light partons in the jet need to be considered. Therefore, one needs a description for the formation of jets. While the correlations of a pair of two heavy mesons depend on the deflection and energy loss of the heavy particles, correlations of a heavy-light particle pair also depends on the number of light particles, which is expected to be larger for radiative than for collisional energy loss. Correlations between heavy and light particles represent, thus, a promising tool to distinguish between these different energy-loss mechanisms.

Fig. 1.8 shows measurements from ALICE on azimuthal angular 2 particle correla-

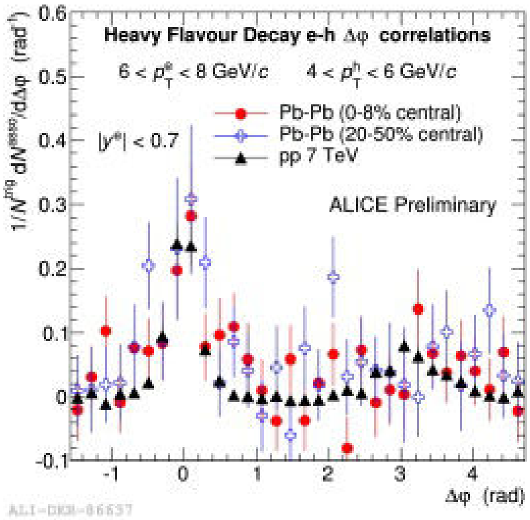

Figure 1.8: Azimuthal angular two particle correlations between electrons from heavy flavor decays acting as triggers and associated charged hadrons h obtained from pp collisions as well as Pb-Pb collisions in two centrality classes. The plot represents preliminary ALICE data from Ref. [80].

tions between D-mesons, represented via electrons from the heavy flavor decay and light hadrons. The data are obtained either from pp or Pb-Pb collisions. In the latter case data is shown for 2 different centrality classes, corresponding to the 8% most central as well as to semi-peripheral collisions. In the data shown in Fig. 1.8 results from pp and heavy ion collisions overlap within uncertainty bars, as Ref. [80] notices. Thus, it is not yet possible to draw conclusions about medium effects on azimuthal correlations from these results, mainly due to insufficient statistics on the heavy ion collisions.

1.4 Heavy- and light-quark jets

As it was pointed out before in subsection 1.1.3 as well as outlined in the previous two sections 1.2 and 1.3, the study of heavy quark production in heavy ion collisions can be a useful tool in order to understand the mechanisms of parton-energy loss inside the QGP medium. The data on heavy meson R_{AA} and v_2 still allow for various qualitatively different models of parton-energy loss, based on either purely collisional processes, or combinations of collisional and radiative processes inside the medium, as it was demonstrated in Fig. A.2 in subsection 1.2.4. As it was mentioned in the previous section 1.3, two-particle correlations between a heavy and a light particle represent promising alternative observables to further constrain the mechanisms of in-medium energy loss.

However, in order to obtain theoretical results for these observables, one needs to be able to describe the production of correlated particle pairs and their in-medium propagation. To this end, this section will summarize theoretical approaches to jet-production[13]. While some of the presented methods apply to jets that contain only light partons, the main focus of this section is the description of heavy quark jets, which contain the heavy-light particle pairs that need to be described in order to calculate the corresponding heavy-light two-particle correlation. The approach that this work takes in order to de-

---

[13] Due to the topic of this thesis, this overview on the theoretical approaches to jet-production is mainly motivated by their possible applications to two-particle correlations. There exist, however, many further observables that cannot be described only by the production of individual particles. Examples are event-shape observables, such as the thrust (cf. subsection 2.2.1).

scribe jets, in vacuum and medium, will be detailed in the subsequent Chaps. 2 and 3.

1.4.1 Heavy-quark production

Inclusive production of a hadron H with heavy quark content in hard processes that occur, e.g., in pp or pA collisions (with corresponding cross-section σ^{H+X}) can be factorized into the inclusive production of a parton k (with cross-section σ^{k+X}) and a fragmentation function D_k^H that describes the production of the hadron H from the parton k [14],

$$\sigma^{H+X} = \sigma^{k+X} \otimes D_k^H \,. \tag{1.16}$$

wherein the symbol "$\otimes$" is a short notation for a convolution of the form

$$\sigma^{H+X} = \sum_k \int dz \sigma^{k+X}(p_T, z, \mu) D_k^H(z, \mu) \,, \tag{1.17}$$

where the hadron H carries a fraction z of a component of the momentum of parton k. In the example above, this component is p_T, the part of the 3 momentum of k that is transverse to the beam axis. While both, σ^{k+X} as well as D_k^H depend on a certain factorization scale μ, the cross-section σ^{H+X} is independent of μ.

The production of parton k can be further factorized into the hard collision of partons i and j that yields k (represented by the cross-section $\sigma_{ij \to k+X}$) and into the productions of these partons i and j in the collisions of hadrons A and B, i.e.:

$$d\sigma^{k+X} = \sum_{i,j} f_i^A \otimes f_j^B \otimes d\sigma_{ij \to k+X} \,. \tag{1.18}$$

Therein, the parton distribution functions (PDF) f_i^A (f_j^B) are the number densities of parton i (j) inside of hadron A (B).

The above general description of factorization applies to the production of hadrons without heavy quark content as well. The remainder of this section focuses specifically on the production of heavy quarks and their subsequent hadronization.

There exist different approaches (cf. Ref. [19]) towards heavy quark production, which rely on factorization in the form of Eq. (1.18): The fixed flavor number scheme (FFNS) assumes that the heavy quark Q that yields the heavy hadron H is not an active quark. The cross-section of its production from the incident partons i and j, $\sigma_{ij \to Q+X}$ is calculated at fixed order in pQCD. Using Eq. (1.18) for the factorization of the heavy quark production (i.e.: for $k = Q$ in Eq. (1.18)), one obtains

$$\begin{aligned} &d\sigma^{Q+X}(s, p_T, y, m_Q) = \\ &\sum_{i,j} \int dx_i \int dx_j f_i^A(x_i, \mu_F) f_j^B(x_j, \mu_F) d\sigma_{ij \to Q+X}(x_i, x_j, s, \mu_F, m_Q, p_T, y, \mu_R) \,, \end{aligned} \tag{1.19}$$

with the Mandelstam-variable s of the collision, m_Q the rest mass and y the rapidity of the emitted heavy quark. The incident partons i and j carry fractions x_i and x_j of the momenta of hadrons A, or, respectively, B. The short distance cross-section $\sigma_{ij \to Q+X}$ is calculated with a coupling constant given at a certain renormalization scale μ_R. The PDFs are given at a certain factorization scale μ_F.

The short distance cross-section depends on logarithms of the ratios between μ_F and the hard scales p_T and the heavy quark mass m_Q. These logarithms appear at all orders of the coupling constant in the pQCD calculation of $\sigma_{ij \to Q+X}$. In the FFNS the short

---

[14] Thus, D_k^H contains, in general also non-perturbative hadronization processes.

distance cross-section is calculated at a fixed order in pQCD. Thus, the logarithms are included to this order. Therefore, the FFNS approximation is valid if the factorization scale μ_F is close to the hard scales. Then, its error is proportional to an inverse power of one of the hard scales. Hadronization can be included by means of a scale independent fragmentation function $D_Q^H(z)$ that is obtained from phenomenological considerations.

In case $p_T \gg m_Q$, contributions from logarithms of the p_T to m_Q ratio become large. Then, instead of the FFNS, one needs an approach that resums these logarithms at all orders. It is possible to include these terms in the fragmentation functions and PDFs, which have to fulfill renormalization group equations, the Dokshitzer Gribov Lipatov Altarelli Parisi (DGLAP) equations (Refs. [82, 83], cf. also Sec. 1.4.2).

Thus, one considers also the heavy quark as an active particle that can undergo fragmentation processes. An approach that accounts for the perturbative evolution of the heavy quark is the variable flavor number scheme (VFNS), where it is assumed that both the heavy quark and the light partons undergo a perturbative evolution, governed by the DGLAP equations, until a certain transition scale μ_T is reached. Then, only the light partons evolve further. Usually, for the transition scale the heavy quark mass is assumed.

For large enough heavy quark transverse momenta p_T it is reasonable to neglect the heavy quark mass. In this zero mass VFNS (ZM-VFNS), the error of the cross-section with regard to calculations that consider the quark mass explicitely is of the order $\mathcal{O}\left(\frac{m_Q^2}{p_T^2}\right)$ (cf. Eq. (4) of Ref. [19]). The general mass VFNS (GM-VFNS) includes mass effects in the fragmentation functions and is thus valid for all the p_T ranges from $p_T \ll m_Q$ to $p_T \gg m_Q$. However, in the GM-VFNS [84, 85] cited in Ref. [19], quark masses are only considered in the processes of heavy quark production, while they are neglected in the branchings of heavy quarks.

An approach that is valid from $p_T \ll m_Q$ to $p_T \gg m_Q$ are fixed order next to leading-logarithm (FONLL) [86] calculations. They match the cross-sections for the production of massive quarks (obtained in the FFNS approach) with those of massless quarks (obtained in the ZM-VFNS approach). Both of the matched cross-sections are calculated up to NLO accuracy.

From the discussion above it can be concluded that for high scales of heavy quark momenta, i.e.: $p_T \gg m_Q$, or, equivalently $Q \gg m_Q$, the fragmentation of a massive quark can be treated in the same way as for massless quarks. A formal argument, at least for fragmentation functions calculated at next to leading order (NLO) accuracy, is given in Ref. [87]. The paper gives the cross-sections for massive quark production in e^+-e^- collisions. However, it is argued that a factorization theorem can be applied. Thus, the entire process can be split in a hard part that contains the e^+-e^- collision and depends on the details of the collisional process and a soft part, represented by the heavy quark fragmentation function, that is process independent. The cross-section of the entire collision is calculated for large virtuality scales $Q \gg m_Q$ as an expansion up to the first order in the coupling constant $\alpha_s(Q)$ (with, however, a mass and scale dependent first order coefficient). An analogous expansion can be made for the cross-section of the hard subprocesses. In both cases, terms of order m_Q^2 are neglected. In case of the total process, the collinear singularities are cut off by the quark mass, which leads to collinear logarithms of the form $\log\left(\frac{Q^2}{m_Q^2}\right)$. For the hard subprocess, the $\overline{\text{MS}}$-scheme is used as a renormalization prescription. Both cross-sections are matched according to the factorization theorem. The dependencies on the heavy quark mass can then be included in the fragmentation function, while the cross-section for the hard subprocess is completely mass-independent. Consequently, the fragmentation functions have to fulfill DGLAP equations as renormalization group equations. The corresponding splitting functions are mass-independent as Ref. [87] shows, and were calculated up to NLO accuracy therein.

To Conclude: Using factorization theorems it is possible to separate the emission of partons from nuclei, their hard collisions and subsequent factorization into heavy quark jets, represented via the corresponding PDFs, cross-sections, and fragmentation functions, respectively. They are matched at certain factorization scales. Thus, while the total result has to be independent of these scales (which is the case if they fulfill the respective renormalization group equations), the functions that represent the subprocesses depend on them. Consequently, the cross-section for the hard heavy quark production, σ^{k+X}, depends on both, a hard scale, given, e.g. by p_T (cf. Eq. (1.17)), and the factorization scale μ. The remaining fragmentation process of the heavy quark (including its hadronization) can be described via the μ dependent fragmentation function D_k^H. For heavy quarks, where $p_T \gg m_Q$ or $Q \gg m_Q$, the quark masses can be neglected in the description of the heavy quark fragmentation, as it is done, e.g. in the ZM-VFNS. There exist also approaches, which consider the quark mass explicitly at momentum scales $p_T \sim m_Q$ or $p_T \ll m_Q$, but neglect it for $p_T \gg m_Q$, e.g. the GM-VFNS of Refs. [84, 85] or FONLL.

Furthermore, it has been demonstrated (cf. Refs. [88–90], also Ref. [87]) that the quark mass can be neglected (at leading order) in the evolution of a heavy quark at scales $Q \gg m_Q$. The quark mass independent evolution of the heavy quark fragmentation functions is governed by corresponding DGLAP equations.

Following the line of argumentation outlined above, in the work of this thesis heavy quark mass effects are neglected for the evolution of heavy quark jets. For the generation and evolution of jet-particles in vacuum Chap. 2 outlines an algorithm, which is a Monte-Carlo approximation towards the –coupled– DGLAP equations of massless quarks and gluons.

1.4.2 Evolution of parton fragmentation by the DGLAP equations

The DGLAP-equations [82, 83] are based on the assumption that the cross-section σ_{n+1} of a process that emits a certain number $n+1$ of partons can be factorized into the cross-section σ_n of a process for the emission of n partons and an additional probability density for the branching of one of these n particles, the so called splitting function P (cf. Eq. (5.28) of Ref. [91]), i.e.:

$$d\sigma_{n+1} \simeq d\sigma_n \frac{dQ^2}{Q^2} dx \frac{\alpha_s}{2\pi} P(x)\,, \tag{1.20}$$

with momentum fraction x. This probabilistic approach is valid, if the virtuality scales of the parton that undergoes the additional splitting is small compared to the scales of the subprocess, represented by σ_n. Chap. 2 examines this justification in more detail. The non-vanishing splitting functions at leading order in pQCD are the branchings of a quark into a quark and a gluon, and those of a gluon into either a gluon pair or a quark and an anti quark, cf. Ref. [91] for their derivation.

In the following paragraphs it is tried to motivate the DGLAP-equations as a means to describe the evolution of parton fragmentation functions with virtuality. To this end the following factorization theorem is assumed for the cross-section $\sigma(Q_\uparrow, x)$ of a process that emits partons with momentum fractions x of the total momentum of the incident particles and with intermediate states with maximal virtualities $Q_\uparrow$ (cf. Ref. [87])

$$\frac{d\sigma(Q_\uparrow,\, x)}{dx} = \sum_i \int \frac{d\hat{\sigma}_i(Q_\uparrow,\, Q,\, z)}{dz} D_i\left(\frac{x}{z},\, Q,\, m\right) \frac{dz}{z}\,, \tag{1.21}$$

where $\hat{\sigma}_i$ is the cross-section of a hard subprocess that produces a parton i of virtuality Q with fragmentation function D_i. Making use of the initial hypothesis of Eq. (1.20), $\hat{\sigma}_i(Q_\uparrow, Q)$ can be expressed as

$$d\hat{\sigma}_i(Q_\uparrow, Q, z) \simeq \\ \sum_j \int \frac{dy}{y} d\hat{\sigma}_j(Q_\uparrow, Q', \frac{z}{y}) \left(\delta(1-y)\delta_{ij} + \frac{\alpha_s}{2\pi} \ln\left(\frac{Q'^2}{Q^2}\right) P_{ij}(y) + \mathcal{O}(\alpha_s^2) \right) , \tag{1.22}$$

with $Q' > Q$.

The above Eq. (1.22) has an interesting form: If one understands the cross-section $\hat{\sigma}_i(Q_\uparrow, Q, z)$ as a measure of the probability to find a parton with momentum fraction z at a virtuality scale Q, the right hand side can be interpreted as its contribution from processes that produce at a virtuality scale Q' a parton that

1. is already emitted with a momentum fraction z (the first, delta-function-dependent term),
2. or has a larger momentum fraction $\frac{z}{y}$, and, thus, undergoes an additional splitting (described in the second term by means of the splitting function $P_{ij}(y)$), in order to produce the particle with momentum fraction $\frac{z}{y}y = z$, by emission of a particle with momentum fraction $\frac{z}{y}(1-y)$,
3. and contributions of higher order in α_s.

Eq. (1.22) can be iterated to obtain the cross-sections at scales smaller than Q. Inferring from the interpretation of Eq. (1.22) in the list above, such a development of the cross-section represents processes of multiple consecutive parton branchings, i.e.: partonic cascades. Chap. 2 will outline a corresponding Monte-Carlo algorithm for the simulation of parton cascades.

This chapter however deduces the analytic evolution equations of the parton fragmentation functions, the DGLAP equations. To this end, one has to remember that the total cross-section $\sigma(Q_\uparrow, x)$ needs to be independent of the chosen factorization scale Q. Therefore, one can insert Eq. (1.22) into Eq. (1.21) and differentiate with regard to $\ln(Q^2)$ (cf. explanations in Chap. 4 of Ref. [91]). A comparison of the first orders in $\ln(Q^2)$ yields

$$\frac{\partial D_i(x, Q, m)}{\partial \ln(Q^2)} \simeq \sum_j \int \frac{dz}{z} D_j(\frac{x}{z}, Q, m) P_{ij}(z) \,. \tag{1.23}$$

This equation is the general form of the DGLAP equations: They describe for partons of a certain type (e.g. partons $i, j \in \{q, \bar{q}, G\}$) the virtuality evolutions of their fragmentation functions. Thus, for a given incident particle of a certain virtuality Eq. (A.3) allows to obtain the parton number distribution with regard to momentum fraction x at smaller virtuality scales. A Monte-Carlo approximation of the DGLAP-equations for the parton fragmentation functions allows to simulate the creation of particle showers from a single incident parton.

Several event generators for the simulation of particle cascades from pp, pA, or AA collisions, use Monte-Carlo algorithms of the DGLAP equations. However, they mostly differ with regard to how they generate the incident partons, how they interact with a medium (if such a medium is present), and how hadrons are formed by the cascade partons. Hadronization processes occur at low virtuality and momentum scales and, thus, perturbative calculations in QCD can no longer be applied. Different models exist.

1.4.3 Monte-Carlo simulation of particle showers and hadronization

This subsection gives, together with the two examples of PYTHIA and HERWIG, a short overview on Monte-Carlo event generators that simulate jet production in pp collisions.[15]

Many of these programs exploit the fact that the described processes can be factorized into subprocesses. Then, one can identify in the corresponding Monte-Carlo algorithms at least the following parts:

1. Production of hard particles: The jets are generated in the interactions of multiple hard partons. The incoming partons of these processes stem from the colliding hadrons. In the initial stages of the collisions the partons are bound within the incoming protons. Since a solution of QCD has not been found and perturbative approaches are not suitable for bound states one has to resort to phenomenological model approaches, e.g.: The parton momenta are given by means of the respective parton-distribution functions (PDFs). Also PYTHIA and HERWIG take this approach.
2. Initial state radiation: The extracted particles can undergo additional branching processes that can be described in a perturbative approach in a space-like particle cascade. Since the particles in the cascade follow a space-like evolution, their momentum scales become increasingly harder.
3. Collisions between the incoming hard particles: These processes happen at hard momentum scales, so that a pQCD treatment is reasonable, e.g.: one can use the corresponding pQCD matrix-elements and cross-sections to simulate the momenta of the outgoing hard particles.
4. Final state radiation: The outgoing hard particles of these collisions evolve in time-like particle cascades. Since these cascades follow a time-like evolution, the momentum scales of their partons decrease.
5. Hadronization: At small momentum scales the produced partons form hadronic bound states. Again, as before in step 1, one encounters processes that are not solvable neither exactly nor perturbatively, but which can be treated within phenomenological approaches, so called hadronization models.

1.4.3.1 PYTHIA [92, 93]

This short sub-subsection on the event generator PYTHIA focuses on its hadronization model, since this is a part that qualitatively differs from HERWIG, the other event generator that is discussed in sub-subsection 1.4.3.2 below.

This hadronization model is the so called Lund string-fragmentation model [94, 95], which was first implemented in the JETSET program that later-on was merged with PYTHIA. It is based on the assumption that the confining attraction between two partons follows approximately a potential that is linearly rising with the distance between the particles: This is described by means of a string with a constant energy per length (typically of the order of 1 GeV/fm) that connects two confined partons, e.g. a $q\bar{q}$ pair. If the q and the $\bar{q}$ move relative to one another, the energy of the string increases linearly

---

[15] Often, these Monte-Carlo event generators allow to simulate e^+e^- or e^-p collisions as well. Examples are PYTHIA and HERWIG (which are also described in this subsection). Due to the context of this thesis only pp collisions will be discussed in this subsection.

with the distance between those two partons. If a critical value of the string energy is reached the string breaks into two pieces. The newly obtained endpoints are interpreted as quark q_1 and anti-quark $\bar{q}_1$ with the corresponding strings between the pairs $q\bar{q}_1$ and $q_1\bar{q}$, respectively. During the parton propagation this procedure of string breaking is then iterated multiple times – whenever the string energy is large enough – until one obtains states, where the relative parton momenta do not allow for further string breaking. These states are then interpreted as hadrons, in the case of a confined quark anti-quark pair as a meson (Ref. [93] notes that more complex sets of partons, which are connected via strings, are possible. Some of them allow also for baryon production.).

1.4.3.2 HERWIG [96–99]

HERWIG [96, 97], as well as its newer implementation HERWIG++ [98, 99][16] use the cluster hadronization model [100].

In this model, after the parton cascades have evolved perturbatively down to their infrared cut-off, decays of the gluons into pairs of quarks q and antiquarks $\bar{q}$ are simulated. From the so obtained sets of (anti)di-quarks and (anti)quarks, clusters of color-singlet states are formed. The momenta of these clusters are given as the sum of the momenta of its parton constituents. In subsequent steps massive clusters can decay into daughter clusters, that are again, color neutral. In a final Monte-Carlo step, pairs of hadrons are selected from the individual clusters: For a cluster $(q_1, \bar{q}_2)$ consisting of the parts q_1 and $\bar{q}_2$, this final step corresponds to the creation of an antiquark-quark or antidiquark-diquark pair $(q, \bar{q})$ in the vacuum, the creation of new clusters $(q_1, \bar{q})$ and $(q, \bar{q}_2)$ which then form hadrons. These hadronic bound states inherit conserved properties, such as spin and flavor from the preexisting clusters.

1.4.4 Medium effects on jets

Subsection 1.2.3 gave a briefly outlined some of the many different theoretical approaches to the in-medium energy loss of single hard particles. This subsection is intended to give an overview on the different theoretical approaches that are used to describe interactions of jet-particles with the hot and dense medium of QGP, in particular those approaches that were implemented as a Monte-Carlo code for the simulation of jets in the medium.

Many of these models for parton-energy loss involve the following two different mechanisms:

1. radiative energy loss, induced by jet-medium interactions. These radiative processes occur in addition to both, the parton-branching processes that already happen for partons propagating in the vacuum, as well as

2. collisional energy loss, due to the scatterings of jet-particles off medium particles. In case it can be assumed that this collisional process can be decoupled from the rest of the evolution of the jet, it can be described as the elastic scatterings between jet and medium particles. Energy loss of jet-particles can then be associated to an energy transfer to the medium. Thus, this thesis also refers to these processes as elastic energy loss.

In order to provide some general insight into the mechanisms of parton-energy loss in the different model approaches mentioned in this subsection, Tab. 1.1 specifies for each

---

[16] The former was programmed in FORTRAN, the latter in C++, hence the two versions are named differently.

of them, whether elastic energy loss or induced radiation (or both of them) is implemented. Besides approaches to jet-medium interactions that have been implemented in a Monte-Carlo code, there exist other theoretical approaches, e.g.: based on a path integral formalism [107]. By means of this type of approach also the importance of color coherence effects on gluon radiation, and color decoherence in the medium can be studied, cf. Ref. [108]. Another approach also studies medium effects on color coherence, however by means of a generating functional for the probability of multiple gluon radiation [109]. Jet evolution in the medium can also be described analytically by means of kinetic equations [110–112] for a gluon number distribution, which allows to include processes of both collisional as well as radiative energy loss.

Medium model(s)	Monte-Carlo	collisional	radiative
BDMPS	Q-PYTHIA [101]	No	Yes
pQCD+AMY	MARTINI [102]	Yes	Yes
pQCD+Gunion-Bertsch+BDMPS	JEWEL [103, 104]	Yes	Yes
continuous effective force	YaJEM [105, 106]	No	Yes

Table 1.1: Non-exhaustive list of Monte-Carlo event-generators for parton cascades in the medium.

1.4.5 Medium modified parton cascades

The models described in the following paragraphs treat the jet-evolution in medium by means of parton cascades in a probabilistic approach analogous to the DGLAP evolution of jets in the vacuum, however with different probability distributions for the processes involving jet particles.

Although not meant to describe jet evolution, the BDMPS approach introduces various scales and regimes that should also apply for jet evolution. Thus, several Monte-Carlo algorithms use the BDMPS approach: Q-PYTHIA [101] uses a medium correction to the splitting functions in the vacuum that reproduces the BDMPS radiation-spectrum. In JEWEL 2.0.0 (cf. Ref. [104] for the physics, for the manual consider Ref. [113]) probability densities for both, elastic scatterings as well as for jet-medium interactions with induced radiation, are used to select the properties of the outgoing particles in each subprocess (in addition to the probability densities for the branchings already present in the vacuum). If a process involves gluon radiation processes on top of multiple $2 \to 2$ particle collisions, the number of scattering centers ν is calculated. Following Eq. (1.11), the probability for the induced radiation process and the ν scattering processes is recalculated. In a final rejection step it is then decided, whether the subprocess is kept in the particle cascade, or rejected. PYQUEN [114] allows for coherent medium-induced gluon radiation that follows an energy-loss described in Refs. [115, 116] which is based on the BDMPS formalism.

1.4.5.1 Q-PYTHIA [101]

This approach is a Monte-Carlo algorithm based on PYTHIA [92, 93]. It assumes that in the medium the same processes of gluon radiation as in the vacuum, described by the DGLAP splitting functions P_{vac}, still occur. However, jet-medium interactions lead to additional processes of induced radiation, which are accounted for by a term ΔP which leads to the following total splitting function

$$P_{\text{tot}}(x) = P_{\text{vac}}(x) + \Delta P(x, Q, \hat{q}, L, E)\,, \tag{1.24}$$

which describes the radiation of a gluon with energy $(1-x)E$ from a branching parton with energy E. The virtuality of the radiating parton is Q.[17] L is the length of the medium, which exerts a transfer of momentum $\vec{p}_T$ transverse to the direction of the incident parton 3-momentum $\vec{p}$. This transfer is described by the transport coefficient $\hat{q} = \|\dot{\vec{p}}_T\|$. The splitting functions $P_{\text{vac}}(x)$ used by Q-PYTHIA are an approximation of the DGLAP splitting functions in the limit of soft gluon radiation, where x is close to 1. The medium modifications $\Delta P(x, Q, \hat{q}, L, E)$ are deduced from the medium induced gluon-radiation spectrum in the BDMPS approach.

1.4.5.2 MARTINI [102]

This algorithm performs a Monte-Carlo simulation of the so called McGill-AMY formalism [117–119], a coupled set of Fokker-Planck-type rate equations. Thus, the evolution of jet-momentum distribution $P(p)$ over time is governed by the transition rates $\frac{d\Gamma(p,k)}{dk}$ for processes, where a parton of energy p loses the energy k.

The transition rates represent both processes of elastic scattering with medium particles as well as induced radiation. For the elastic processes the transition rates used are calculated from the matrix elements in pQCD for elastic scattering of a hard jet-parton off medium particles, and the distribution functions for partons in the medium, where either a Bose-Einstein or Fermi-Dirac distribution was assumed. For the radiative processes the Arnold, Moore, and Yaffe (AMY) [120–122] formalism is used. This approach allows for the analytic calculation of the transition rates of induced radiation for hard partons in a medium of asymptotical temperatures, due to the strongly ordered scale $T \gg gT \gg g^2T$. The temperature dependence of the AMY formalism is given via both, the Bose-Einstein and Fermi-Dirac distributions of medium-particles, as well as via thermal masses (and, thus, thermal parton momenta). In addition MARTINI implements also the conversion of quarks into gluons and vice versa, due to Compton scattering and, furthermore, also considers processes involving photon radiation.

1.4.5.3 JEWEL [103, 104]

In its first version [123], JEWEL describes elastic scattering as follows: Cross-sections σ_{el} for $2 \to 2$ parton scattering processes are calculated. The momentum distribution of medium partons, n is assumed via a Bose-Einstein or Fermi-Dirac distribution. The times Δt between two subsequent splittings are estimated from the virtuality and energy of the intermediate particles and it is furthermore assumed that the intermediate parton behaves like a free particle that propagates with velocity β. Then the time $\tau \leq \Delta t$ between the splitting and a (tentative) scattering with a medium parton is determined in a Monte-Carlo selection step from the probability $P_{no\,scatt}$ that no scattering occurs during time τ_1, i.e.[18]:

$$P_{no\,scatt} = \mathrm{e}^{-\sigma_{el} n \tau_1 \beta} \,. \tag{1.25}$$

This selection can be iterated for the times $\tau_2, \tau_3, \ldots$ of subsequent scatterings during the remaining times $\Delta t - \tau_1$, $\Delta t - \tau_1 - \tau_2$, etc. Once the sum of the τ_i exceeds Δt no further scatterings are simulated for this intermediate particle – however, the process is repeated for the particles that are created in the splitting of the intermediate particle.

---

[17] The notations Q and x were used here for the parton virtuality and energy fraction, respectively, instead of following the notation t for the virtuality and z for the energy fraction used in Ref. [101]. This choice was made purposely, because it is consistent with the notation used in Chap. 2.

[18] It shall be noted that Eq. (1.25) represents only the simplest form of $P_{no\,scatt}$, i.e. when the parton distributions in the medium, and the cross-section are time-independent. However for the sake of conciseness, this should be the only version that is quoted in this thesis.

In order to describe the inelastic medium effects Ref. [123] increases the splitting function by multiplication with a constant (greater than 1).

Further effects are included in later versions of JEWEL. The version presented in Ref. [104] describes medium-induced radiation via a Gunion-Bertsch type of formalism [124]. Also the LPM-effect has been included.

1.4.5.4 YaJEM [105, 106]

An early version of YaJEM [105] effectively simulates jet-medium interactions by modifications of the four-momenta of cascade-partons: As for JEWEL the time Δt between two subsequent splittings is estimated. During this time, parton virtuality is increased. This virtuality transfer is dependent on the path of a cascade parton in the medium, and is obtained from a hydrodynamic calculation. Since the estimate for Δt also depends on parton virtuality both quantities need to be determined in a self-consistent way. This virtuality increase will lead to additional splittings in the parton-cascade, and, thus, can be used to simulate the effects on jets by medium-induced radation. The effective models of jet-medium interactions used in this work are based on YaJEM in the form given by Ref. [105].

Later versions of YaJEM contain additional effects, e.g. in Ref. [106] the virtuality threshold for parton splittings is parametrized as a function of a length- and an energy-scale. Due to this parametrization, values for the nuclear-modification factor can be obtained that agree with data from the CMS collaboration [23].

1.5 Conclusions and Perspectives

This chapter was intended as a motivation for studies on the QGP phase of quasi-free asymptotic partons in general, and the studies of this thesis on the mechanisms of heavy quark in-medium energy loss in particular.

In many theoretical models the incident particle loses energy in collisions with medium particles, either by transfer to the medium or by subsequent, induced radiation or by combinations of both effects. Interference effects, e.g. due to the long formation time of soft gluons, lead to the suppression of radiation. The relative importance of these two mechanisms might depend on the momenta of the incident (heavy) particles as well as on the temperature scales and evolution inside the medium.

In order to obtain phenomenological constraints on the different models, one can study combinations of the observables of the nuclear modification factor and the elliptic flow. One can observe a general tendency that theoretical models that overestimate R_{AA} underestimate v_2. However, there exist numerous models that reproduce both observables reasonably well and, thus, it would prove useful to find additional observables to constrain the energy-loss mechanisms.

Possible candidates are correlations between heavy and light particles, since they represent observables related to the gluon emission from heavy quarks and are thus sensitive to the relative contribution of induced radiation to in-medium energy loss. In order to obtain the necessary particle pairs, event generators, which simulate particle cascades produced in heavy ion collisions, can be used.

For the vacuum these tools represent Monte-Carlo simulations of the DGLAP equations, combined with a hadronization mechanism for the finally obtained partons and a production mechanism for the initial particles of the cascade. The algorithm used for the work of this thesis is detailed in Chap. 2.

For the parton propagation in the medium it was outlined that there exist various types of algorithms, representing different descriptions of collisional and/or radiative processes. In a pragmatic approach one can implement effective models that subject incident cascade particles to continuous forces that can be tuned to mimic both radiative or collisional energy loss corresponding to given temperature profiles. Medium modifications of the Monte-Carlo algorithm outlined in Chap. 2 in these kind of effective approaches are given in Chap. 3: The algorithm for radiative energy loss is based on the YaJEM approach. For collisional energy loss a similar model will be introduced, as well as a third, hybrid model. These are three simplistic, yet generic, effective models for the medium modification of parton propagation. It is, thus possible to change the relative contributions from either radiative or collisional processes to parton in-medium energy loss within a consistent framework, and to study the influence of these contributions on jet-observables.

In particular, this thesis systematically explores the effect of considering different types of energy loss mechanisms on correlation observables. Thus, Chap. 4 studies if energy loss mechanisms can indeed be constrained by their respective results on two particle correlations.

Chapter 2

The Monte-Carlo algorithm for parton cascades in the vacuum

This chapter summarizes an approach towards the (virtuality) evolution of parton fragmentation, represented in the current thesis work by Monte-Carlo simulations of parton showers– as it was done in numerous studies before, e.g. [103, 105, 113], and in particular for event generators, used to describe proton-proton collisions[1], e.g. [92, 98, 125]. The evolution of the corresponding fragmentation functions are described by the DGLAP-equations [82, 83]. The description introduced is a probabilistic approximation that considers the probability for each parton branching as being independent from the other sub-processes within the shower. This assumption requires that subsequent parton branchings are strongly ordered in virtuality. The DGLAP-equations, and thus the Monte-Carlo algorithm used, describe merely processes of collinear parton branchings, a type of emission that is however dominant at high enough parton energies.

Furthermore, the current version of the algorithm neglects heavy quark masses and assumes all parton masses to be 0. Following the reasoning of Sub-subsection 1.4.1, this kind of simplifying assumption is justified, if the momentum scales of the fragmenting heavy quarks are considerably larger than the quark masses. This constraint is mostly fulfilled for the hard heavy quark jets on which this thesis mainly focuses.

After a brief introduction of the variables used to describe individual partons, the overall structure of the Monte-Carlo algorithm used will be outlined, which further necessitates a description of its major components, the probability densities for individual parton branchings, followed by a discussion of their constraints in the particle phase space, as well as the implementations of these constraints in the algorithm. After discussion of some tests of the Monte-Carlo algorithm, results of the constructed program are used to give descriptions on the space and time development of different kinds of parton showers in the vacuum. To this end, an estimation of the temporal and spatial propagation of individual partons was considered.

2.1 Description of the algorithm

This section outlines the Monte-Carlo algorithm that is currently implemented, in order to simulate hard parton cascades in the vacuum.

To this end, subsection 2.1.1, will first of all define all the variables that are necessary in order to determine the degrees of freedom of the cascade. In particular, the reference frame in which the parton cascades are defined will be specified.

---

[1] Medium-modifications to the Monte-Carlo algorithm that is discussed in this chapter will be introduced in Chap. 3.

Subsection 2.1.2 explains the global structure of the algorithm. Its physical legitimization is discussed afterwards, by detailing its parts: Subsection 2.1.3 gives the probabilities/probability distributions for the selection of the emitted partons and their four momenta, with great emphasis on the relation of the resulting jet to the DGLAP evolution ([82, 83], cf. also Sec. 1.4). Then, the phase-space boundaries of the individual parton splittings are derived in subsection 2.1.4. In particular, the reference-frame dependencies that these constraints imply will be stressed.

2.1.1 Definitions of variables used in the algorithm

In the Monte-Carlo algorithm employed, partons i are described by their 4-momenta p_i. Vertices differ for quarks and gluons, and thus, possible splitting probabilities. Therefore, it needs to be specified for any parton in the cascade, whether it is a quark or a gluon (In this thesis, wherever necessary, quarks and gluons are distinguished by indices q and G, respectively; The implemented program code uses an additional variable.)[2]

The particle initiating a partonic cascade is defined by its virtuality $Q_1 = \sqrt{p_1^\mu \cdot p_{1\,\mu}}$ as well as the remaining 3 independent components of its 4 momentum p_1, which in addition also specifies the reference frame for the entire cascade. Assuming –in the algorithm– a 4 momentum p_1 of the form

$$p_1 = \left(E_{\text{ini}}, 0, 0, \sqrt{E_{\text{ini}}^2 - Q_1^2}\right) , \tag{2.1}$$

where $E_{\text{ini}} \geq Q_1$ is the initial jet energy, the 4 momentum p_i^μ ($\mu = 0, 1, 2, 3$) of any other parton of the cascade is specified relative to the first parton via the following 4 quantities

$$\begin{aligned} x_{i\text{tot}} &= \frac{p_i^0}{p_1^0} , & Q_i^2 &= p_i^\mu \cdot p_{i\,\mu} , \\ p_{i\,\perp} &= \sqrt{(p_i^1)^2 + (p_i^2)^2} , & \varphi_i &= \arcsin\left(\frac{p_i^2}{p_{i\,\perp}}\right) , \qquad \varphi_i \in \left[-\frac{\pi}{2}, \frac{\pi}{2}\right] . \end{aligned} \tag{2.2}$$

As an alternative to the description via energy fractions x_{tot}, we also considered a description using light-cone-energy fractions

$$z_{i\text{tot}} = \frac{p_i^+}{p_1^+} , \qquad \text{with } p_i^+ := p_i^0 + p_i^3 . \tag{2.3}$$

Equivalently to using the total (light cone) energy fractions, the 4-momenta of the cascade particles can be specified by the fractions

$$z = \frac{p_b^+}{p_a^+} , \qquad x = \frac{p_b^0}{p_a^0} , \tag{2.4}$$

between the (light cone) energies of a parton a that emits a parton b (and parton c with corresponding fractions $1 - z$ or $1 - x$, respectively). Both, x and z are ratios of components to parton momenta, and are, thus, reference frame dependent. In the remainder of this thesis, the convention is adopted that x and z assume the relations Eq. (2.4) in the same reference frame, in which the parton cascade is simulated, i.e. the one specified by Eq. (2.1). In other reference frames the dependencies of x and z on the

---

[2] An explicit description of particles in color space has not been implemented so far, since for parton branchings in tree-level pQCD, the color part of the matrix-elements is known to be given by the numbers C_F, C_A, and T_R in the splitting functions.

components of the four-momenta of particles a and b is different: Sub-subsection 2.1.4.3 sheds some light on this question. Since equivalent algorithms can be formulated with either choice of fractions x or z, the following description of the algorithm will refer to the general case of a momentum fraction χ, except if it is noted otherwise explicitly. Later on in subsection 2.1.4, the choices of particular momentum fractions $\chi = x$ and $\chi = z$ will be made, in order to specify the implementation of phase-space boundaries in the Monte-Carlo program.

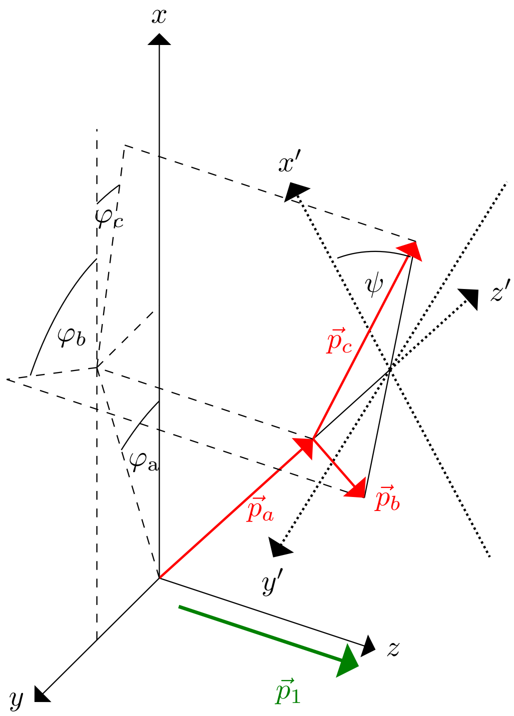

Figure 2.1: Illustration of the definitions of angles φ_a, φ_b, φ_c, and ψ: $\vec{p}_1$, $\vec{p}_a$, $\vec{p}_b$, and $\vec{p}_c$ are the three-momenta of the initial parton of the cascade, a branching parton a, and its decay-products b and c. A global orthogonal coordinate system (x, y, z) with its z-direction parallel to $\vec{p}_1$ and a local orthogonal coordinate system (x', y', z') with its z' direction parallel to $\vec{p}_a$ are defined. The angles φ_a, φ_b, and φ_c are defined as azimuthal angles of the momenta $\vec{p}_a$, $\vec{p}_b$, and $\vec{p}_c$ in the (x, y)-plane. A construction of these angles via orthogonal projection of the three momenta on the (x, y) plane is illustrated (dashed lines). ψ is defined as the azimuthal angle of momenta $\vec{p}_b$ and $\vec{p}_c$ around the z' axis (i.e.: in the (x', y') plane.

It follows, that in a Monte-Carlo simulation of partonic cascades, where each parton splitting is selected individually, a suitable algorithm has to give at least the following information for each splitting of a parton a into particles b and c:

1. information on the nature of the splitting products of a parton a: If parton a is a quark, it emits a gluon ($q \to q + G$). If it is a gluon, there are, at lowest order in α_s, 2 possibilities ($G \to G + G$ and $G \to q + \bar{q}$). Then it needs to be determined, whether the resulting partons b and c are quarks or gluons (so far no distinction between quarks and antiquarks has been made in the algorithm),
2. the virtualities Q_b and Q_c of the produced partons b and c ,
3. momentum fraction χ,
4. transverse momenta $p_{b\perp}$ and $p_{c\perp}$,

5. the azimuthal angles φ_b and φ_c.

For each splitting process, the incoming four-momentum is conserved. Further constraints in phase space are introduced later. Thus, from the two four-momenta, only four components are independent. In the implemented algorithm these four degrees of freedom are determined via the parton virtualities Q_b and Q_c, the momentum fraction χ, and an azimuthal angle ψ around the direction of the three momentum of parton a, which specifies the plane in which the momenta of partons b and c lie. In order to avoid confusion between the azimuthal angles φ_i in the global coordinate system around the direction of the three momentum of the initial parton of the cascade, $\vec{p}_1$, defined in Eq. (2.2) and the azimuthal angle ψ in the local coordinate system around $\vec{p}_a$, Fig. 2.1 illustrates both definitions.

2.1.2 The overall structure of the algorithm

In this subsection an algorithm for the simulation of parton cascades is shortly outlined, while its parts will be explained in more detail in the subsequent subsections. The particle showers are generated in a time-like process: They represent an approximation to the large sets of particles emitted as final state radiation in pp or heavy ion collisions. Sec. 1.4 briefly introduced some of the Monte-Carlo event generators that can be used to simulate these particle showers. Rather than using one of these sophisticated algorithms that consider many different phenomena, one can argue that it serves the purpose of this thesis at least as well to focus entirely on cascades generated via final state radiation and to implement a simplistic Monte-Carlo tool, which, however, can very easily be adapted to effectively simulate medium effects (cf. Chap. 3 for medium modifications).

The algorithm implemented for this thesis represents a Monte-Carlo simulation of DGLAP equations – an approach to final state radiation that has been already taken numerous times before, e.g. in PYTHIA [92, 93] or HERWIG [98, 99]. The algorithm described in this subsection was reconstructed from Refs. [103, 123].

Starting with the first splitting process, parton showers are simulated by the currently used Monte-Carlo algorithm in the following manner:

0. At first, for the initial particle, its maximal virtuality $Q_\uparrow$ is fixed, together with its energy E_{ini}. The latter quantity fixes also the reference frame of the parton cascade.

1. For the first parton in a parton shower, one selects the virtuality Q_1 – see subsection 2.1.3 for details – at which the parton splits. For all other partons in the shower, the sets of variables that define the individual partons a – containing the set of variables $\{Q_a, \chi_{a,\,\mathrm{tot}}, p_{a\perp}, \varphi_a, \mathrm{q\ or\ G}\}$ – are used for further splittings of parton a into partons b and c.[3]

2. If Q_a lies below a certain threshold $Q_\downarrow$, it is assumed, that no splitting occurs in fact, otherwise a splitting will be simulated. Physically, such a cut-off for small virtualities can be motivated by a transition from perturbative splitting processes to non-perturbative hadronization processes.

3. If a splitting process occurs, the type of the splitting is chosen via a Monte-Carlo selection, i.e.: It is specified, whether the produced partons are a quark and an antiquark, 2 gluons, or a quark and a gluon.

---

[3] Here, $\chi_{a,\,\mathrm{tot}}$ represents the momentum fraction relative to the initial parton of the cascade, while in step 4 of the algorithm the selected value χ represents the momentum fraction between the radiated and decaying particles of the last parton branching.

4. The 4 momenta of partons b and c are generated by means of a rejection loop A, that creates the virtualities Q_b and Q_c, together with the momentum fraction χ
    (a) The virtualities Q_b and Q_c of the produced partons are chosen via a M.-C. selection. This happens inside of a new loop B, that is repeated, until the condition $Q_a^2 \geq Q_b^2 + Q_c^2$ is satisfied.
    (b) For the current $\{Q_a, Q_b, Q_c\}$ candidate the momentum fractions χ of the produced partons are chosen via a M.-C. selection.
    (c) The component $k_\perp$ of the 3 momenta of parton b and c that is orthogonal to the 3 momentum of a is calculated as a function of Q_a, Q_b, Q_c, and χ.
    (d) Once $(k_\perp)^2 \geq 0$ is satisfied, the loop terminates, otherwise the steps of the loop A are repeated.
5. The azimuthal angle of the plane of scattering, with regard to the direction of the incoming parton a, ψ, is selected.
6. The transverse momenta of the produced partons, $p_{b\perp}$ and $p_{c\perp}$, and the azimuthal angles φ_b and φ_c around the longitudinal direction are calculated using $k_\perp$ and ψ together with the four momentum of parton a, p_a, given via Q_a, $p_{a\perp}$, and $\chi_{a,\mathrm{tot}}$.
7. The algorithm restarts at 1., this time using the produced partons b and c instead of parton a. The algorithm simulates the splittings one generation after another, i.e.: the algorithm is carried out from 1. to 6. for every parton produced after n consecutive splittings from the initial parton. For the so produced $n+1$ th generation this procedure is repeated. The algorithm terminates, if it is not possible for any particle in an entire generation to undergo a further splitting.

For each splitting the 4 momenta of the outgoing partons b and c are determined as follows: $\vec{k}_\perp$ ($-\vec{k}_\perp$ for particle c) is considered as the component of the 3-momentum $\vec{p}_b$ of particle b transverse to the 3 momentum $\vec{p}_a$ of the incident parton a with ψ ($\psi + \pi$) the azimuthal angle around the direction of $\vec{p}_a$. The remaining component of $\vec{p}_b(\vec{p}_c)$ parallel to $\vec{p}_a$ can then be calculated, since also the parton virtualities and a momentum fraction are known. Thus, the 3 momenta $\vec{p}_b$ and $\vec{p}_c$ are obtained in a cylindrical coordinate system, where the polar axis is parallel to $\vec{p}_a$. These momenta are then transformed via an Euler rotation in a global coordinate system of the shower. In this global coordinate system, the component orthogonal to the polar axis is projected out, and referred to as $\vec{p}_{b\perp}$ and $\vec{p}_{c\perp}$, respectively. φ_b (φ_c) are the corresponding azimuthal angles. So far, the direction of the momentum of the initial parton (i.e.: the jet axis for cascades in vacuum) $\vec{p}_1$ was used as polar axis.[4]

2.1.3 Probability distributions for the parton splittings

This subsection explains, why the Monte-Carlo algorithm of subsection 2.1.2 is suitable for the simulation of partonic cascades, and presents the deduction of the probability distributions necessary to implement in the algorithm the steps 1 and 4a to select the virtualities Q_a, Q_b, and Q_c, the step 3 to select the types of the produced partons, and the step 4b to select the momentum fraction χ.

---

[4] Alternatively, in p-p or heavy-ion collisions, the beam axis is often used as polar axis and directions orthogonal to this axis are referred to as transverse. Throughout this thesis, they will be labelled with an index T instead of $\perp$, in order to avoid confusion with the coordinate system implemented in the algorithm. For the first calculations of 2 particle correlations in Chap. 4 it will be assumed that the initial particle of the jet is emitted orthogonal to the beam axis, i.e., in this notation, $\vec{p}_1 = \vec{p}_{1T}$.

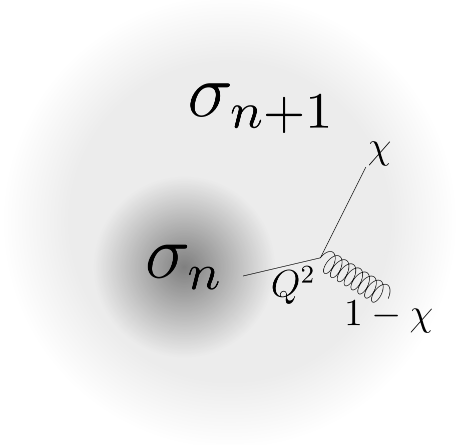

Figure 2.2: Schematics of how splitting functions relate an n particle process, with cross-section σ_n, to an $n+1$ particle process, with cross section σ_{n+1}. The picture demonstrates the case, where the n and $n+1$ particle processes differ in the emission of a gluon from a quark line.

In order to simplify calculations of the cross sections for parton cascades in pQCD, one can resort to a probabilistic approximation (cf. Ref. [91]), where the probability for a cascade with a certain number $n+1$ of parton branchings factorizes into the probabilities for an n-particle subprocess and the probability for an additional parton branching, as is schematically depicted in Fig. 2.2, i.e. a factorization theorem of the form of Eq. (1.20).

In subsection 1.4.2 it was demonstrated that from this kind of factorization theorem a DGLAP-evolution of the corresponding parton fragmentation functions can be deduced. This subsection shows how a Monte-Carlo algorithm can be deduced for processes of parton fragmentation that allow factorization in the form of Eq. (1.20) for all subprocesses. By means of such an algorithm large sets of parton cascades can be generated. Number distributions of all the simulated particles can be obtained. It can be argued that these distributions represent approximations to the fragmentation functions that evolve along the DGLAP equations.

To this end, the factorization theorem Eq. (1.20) is written in the following form:

$$d\sigma_{n+1}(Q,\chi,\Phi_n) = d\sigma_n(\Phi_n)\frac{dQ^2}{Q^2}d\chi\frac{\alpha_s(F(\chi,Q))}{2\pi}P_{a\to b,\,c}(\chi)\,, \tag{2.5}$$

where σ_i is the cross-section and Φ_i the phase-space volume for a process with i final particles, Q is the virtuality of the parton that produces the additional parton in the $n+1$-particle process, χ is the momentum fraction for its decay products. $P_{a\to b,\,c}(\chi)$ are splitting functions that serve as a measure for the probability of the additional branching of the virtual particle a into particles b and c. For the Monte-Carlo algorithm implemented, the splitting functions for collinear splitting of leading order (LO) in pQCD were used

$$\begin{aligned} P_{q\to q\,,G} &= C_F\frac{1+x^2}{1-x}\,,\\ P_{G\to G\,,G} &= C_A\left(\frac{1-x}{x}+\frac{x}{1-x}+x(1-x)\right)\,,\\ P_{G\to q\,,\bar{q}} &= T_R\left(x^2+(1-x)^2\right)\,, \end{aligned} \tag{2.6}$$

where x is defined as an energy fraction via Eq. (2.4) in the global reference frame of the cascade, given via Eq. (2.1)[5]. In this reference frame the assumption of a collinear splitting of parton a translates into the assumption of a hard parton a, i.e.: $E_a \gg Q_a$. The argument of the coupling constant α_s is assumed to have some dependence on χ and Q, symbolically represented here by a function F: As was mentioned in Ref. [87] a dependence of the form $\alpha_s(k_\perp^2) \approx \alpha_s(z(1-z)Q^2)$ leads to a resummation of soft (collinear) branchings.

In the current implementation of the M.-C. algorithm, only the LO-approximation $\alpha_s(F(\chi,Q)) = \frac{1}{b_0 \ln\left(\frac{\mathrm{F}(\chi,\mathrm{Q})^2}{\Lambda^2_{\mathrm{QCD}}}\right)}$ was considered. The cross-section σ_n has been written without any dependence on Q and χ, as by assumption it factorises from the splitting process.

The approximation described above works reasonably well, provided the following constraints are met (cf., e.g., Ref. [91]):

- Q is much smaller than the virtuality of any particle in the n-particle subprocess. There are 2 reasons for this approximation: For sufficiently small virtualities Q (in comparison to the virtualities occurring in the internal structure of the n-particle sub-process) the n-particle sub-process can be described suitably well as a process of n outgoing on-the-mass-shell particles, represented by the corresponding cross section, σ_n. Secondly, for the same sets of $n+1$ outgoing particles, different processes, represented by various different amplitudes and Feynman diagrams are possible. Thus, in the corresponding matrix elements one would need to also consider interference terms. However, since amplitudes of the processes involved introduce virtuality dependencies by the denominator of their propagators, i.e.: contain factors of the form $\frac{1}{Q^2}$, these interference terms will be subdominant in comparison to the squared amplitude of a process with sufficiently small virtuality Q of its intermediate particle. There, the propagators introduce a factor $\frac{1}{Q^4}$, which dominates over contributions to the matrix element from any of the other amplitudes. In such a case, a probabilistic approximation, like the DGLAP-approach, is justified.

- For simplicity, it is assumed that the branching angle (i.e.: the angle between the respective directions of the 3 momenta of the emitted partons) is very small. This assumption of collinear emission is not necessarily implied by the assumption of small Q values – which also allows for soft emissions: However, for the highly energetic jets considered in this thesis, collinear branching appears to be justified.

Trying to interpret Eq. (2.5), one could understand the part $\frac{\alpha_s(F(\chi,Q))}{2\pi} P_{a\to b,c}(\chi)$ as the probability density for a splitting at given values of $\log(Q^2)$ and χ. One can argue in favour of this kind of interpretation, due to the following argumentation:

One can define $\sigma_{n+1}\left(Q \in [Q_\downarrow, \tilde{Q}], \chi \in [\chi_-, \tilde{\chi}]\right)$ as the contributions to σ_{n+1} stemming from splittings with $Q \in [Q_\downarrow, \tilde{Q}]$ and $\chi \in [\chi_-, \tilde{\chi}]$, where $Q_\downarrow$ and χ_- are some (arbitrary) threshold values. Then, by integrating Eq. (2.5), one obtains:

---

[5] The splitting functions of Eq. (2.6) are only valid for $0 < x < 1$ and run into singularities – corresponding to soft and collinear radiation – for $x = 1$ (or $x = 0$ as well, in the case of the splitting of gluons into gluon pairs). These singularities can be treated explicitly via the so called "+ prescription" (cf. Ref. [91]). This thesis, however, takes a different approach (as it was already done by other Monte-Carlo algorithms, e.g. [103]): Due to phase-space boundaries of the parton branchings, the energy fractions are constrained to the region $x \in [x_-, x_+]$, where $0 < x_- < x_+ < 1$ (This will be discussed in subsection 2.1.4.). Thus, the cases $x = 1$ and $x = 0$ do not occur and parton branchings can be described via the splitting functions of Eq. (2.6) alone.

$$\sigma_{n+1}\left(Q\in[Q_\downarrow,\tilde{Q}]\,,\chi\in[\chi_-,\tilde{\chi}]\right)=\sigma_n\int_{Q_\downarrow^2}^{\tilde{Q}^2}\frac{d(Q^2)}{Q^2}\int_{\chi_-}^{\tilde{\chi}}d\chi\frac{\alpha_s(F(\chi,Q))}{2\pi}\sum_{a\to b\,,c}P_{a\to b\,,c}(\chi)\,. \tag{2.7}$$

With the use of an accurate normalisation, the quantities $\sigma_{n+1}\left(Q\in[Q_\downarrow,\tilde{Q}]\,,\chi\in[\chi_-,\tilde{\chi}]\right)$ and σ_n measure the probabilities of their corresponding processes. Thus, one may argue that

$$p\left(\text{split. for }Q\in[Q_\downarrow,\tilde{Q}]\,,\chi\in[\chi_-,\tilde{\chi}]\right):=\int_{Q_\downarrow^2}^{\tilde{Q}^2}\frac{d(Q^2)}{Q^2}\int_{\chi_-}^{\tilde{\chi}}d\chi\frac{\alpha_s(F(\chi,Q))}{2\pi}\sum_{a\to b\,,c}P_{a\to b\,,c}(\chi)\,, \tag{2.8}$$

is the probability for a splitting to happen in the ranges $Q\in[Q_\downarrow,\tilde{Q}]$ of virtualities and $\chi\in[\chi_-\,,\tilde{\chi}]$ of momentum fractions. On the other hand, if one was given Eq. (2.8) as the splitting probability in the corresponding ranges of virtuality and momentum fraction, the relation Eq. (2.5) follows, after approaching the limit of infinitesimal ranges of momentum fractions and virtualities and multiplying the so obtained conditional probability (density) with the n-particle cross-section which yields the $n+1$-particle cross-section.

In order to investigate some possible consequences of the reasoning above, $\sigma_n(Q^2)$ is redefined as the cross section of a n-parton subprocess of a partonic cascade that terminates at a given virtuality Q. The probability (density) that a splitting occurs for a (squared) virtuality of $Q^2\in[Q^2-dQ^2,Q^2]$ is then given via

$$\frac{\sigma_{n+1}(Q^2-dQ^2)}{\sigma_n(Q^2)}=\frac{d(Q^2)}{Q^2}\int_{\chi_-}^{\chi_+}dz\frac{\alpha_s(F(\chi,Q))}{2\pi}\sum_{a\to b\,,c}P_{a\to b\,,c}(\chi)\,, \tag{2.9}$$

where it was assumed, that the z values have to lie inside the range $\chi\in[\chi_-\,,\chi_+]\subset[0\,,1]$. One can argue that the fraction $\frac{\sigma_{n+2}(Q^2-dQ^2)}{\sigma_n(Q^2)}$ is of the order of $\mathcal{O}((dQ^2)^2)$, and for subprocesses, where more than $n+2$ partons are produced, the order in dQ^2 is even higher. One can then infer, that the number of subprocesses, that have no splitting in the range $Q^2\in[Q^2-dQ^2,Q^2]$ of virtualities is measured via: $\sigma_n(Q^2-dQ^2)=\sigma_n(Q^2)-\sigma_{n+1}(Q^2-dQ^2)$. Inserting this relation into Eq. (2.9) and applying a Taylor expansion of $\sigma_n(Q^2-dQ^2)$ for infinitesimal steps dQ^2 around Q^2 and finally comparing the coefficients of dQ^2, one obtains the following differential equation:

$$\frac{d\log(\sigma_n(Q^2))}{d\log(Q^2)}=\int_{\chi_-}^{\chi_+}d\chi\frac{\alpha_s(F(\chi,Q))}{2\pi}\sum_{a\to b\,,c}P_{a\to b\,,c}(\chi)\,. \tag{2.10}$$

Integrating this probability over a certain range[6] of virtualities $Q^2\in[Q_a^2\,,Q_{a\uparrow}^2]$ gives the following evolution:

$$\sigma_n(Q_a^2)=\sigma_n(Q_{a\uparrow}^2)\exp\left(-\int_{Q_a^2}^{Q_{a\uparrow}^2}\frac{dQ^2}{Q^2}\int_{\chi_-}^{\chi_+}d\chi\frac{\alpha_s(F(\chi,Q))}{2\pi}\sum_{a\to b\,,c}P_{a\to b\,,c}(\chi)\right)\,. \tag{2.11}$$

Thus, the cross-sections $\sigma_n(Q_{a\uparrow}^2)$ and $\sigma_n(Q_a^2)$ for n particle processes including intermediate particles of virtualities $Q_{a\uparrow}$ and Q_a, respectively, are related by the factor

$$S_a(Q_{a\uparrow},Q_a)=\exp\left(-\int_{Q_a^2}^{Q_{a\uparrow}^2}\frac{dQ^2}{Q^2}\int_{\chi_-}^{\chi_+}d\chi\frac{\alpha_s(F(\chi,Q))}{2\pi}\sum_{a\to b\,,c}P_{a\to b\,,c}(\chi)\right)\,, \tag{2.12}$$

---

[6] Here, the notation $Q_{a\uparrow}$ is introduced for the – yet to be determined – maximum value of possible virtualities of a particle a, while the notation $Q_\uparrow$ is still used for the maximum value of possible virtualities of the first particle of the cascade, which is for the sake of simplicity, up to now, selected by hand in step 0 of the algorithm given in subsection 2.1.2, but which can be expected to depend on the parton distributions inside the colliding particles, initial state radiation, and the hard collision that produces the first particle of the cascade.

which measures the probability, that no splitting of parton a occurs in the range of virtualities $Q \in [Q_{a\uparrow}, Q_a]$. $S_a(Q_{a\uparrow}, Q_a)$ is also called the Sudakov (form-)factor.

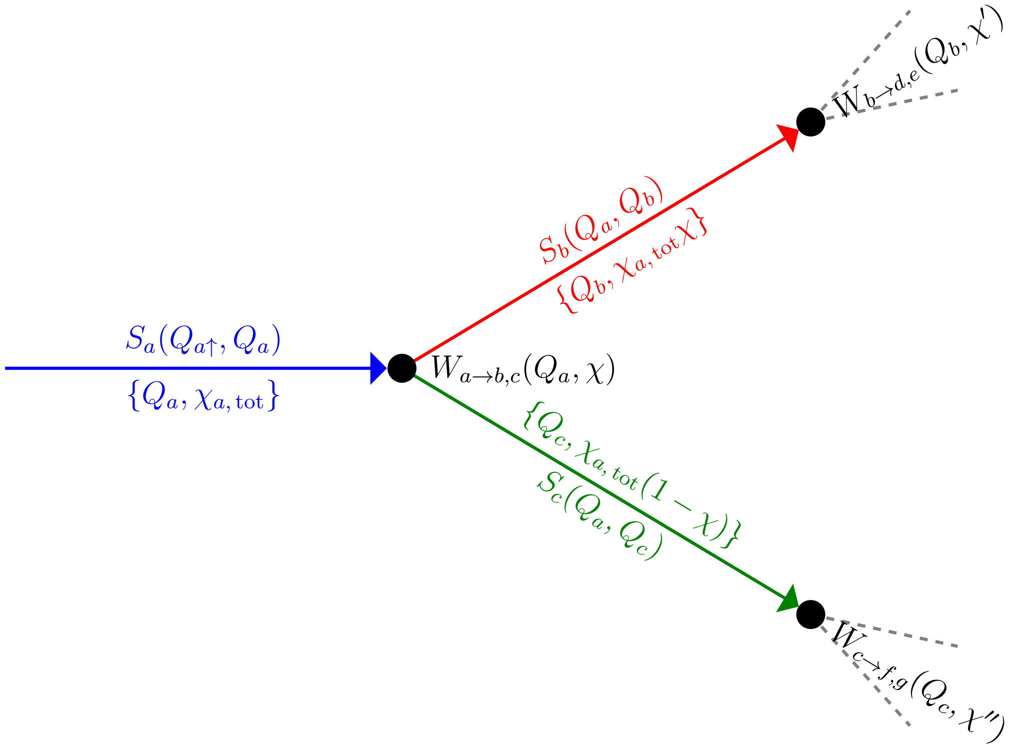

Figure 2.3: Partition functions (up to normalization constants) for both, the parton virtualities (at the lines) as well as the momentum fractions (at the vertices/blobs). In curly brackets: Parton virtualities and momentum fractions with respect to the total momentum of the system. $\chi_{a,\text{tot}}$ is the momentum fraction of the branching parton a with regard to the initial parton of the cascade. At the splitting of parton a, momentum fraction χ is selected for the distribution of the momentum of parton a among its decay products b and c by means of the partition function $W_{a\to b,c}(Q_a, \chi_a)$. Then, parton b carries the total momentum fraction $\chi_{a,\text{tot}}\chi$, and parton c carries $\chi_{a,\text{tot}}(1-\chi)$, respectively. The two blobs on the right side could represent further parton splittings: The dashed lines symbolize their possible branching products.

The probability (density) that a parton splits at exactly this virtuality Q_a is the probability, that the parton does not split at a higher virtuality than Q_a, times the probability (density) to split exactly at Q_a. This probability density is thus given by[7]

$$S_a(Q_{a\uparrow}, Q_a) \int_{\chi_-}^{\chi_+} d\chi \left(\frac{\alpha_s(F(\chi, Q^2))}{2\pi} \sum_{a\to b,c} P_{a\to b,c}(\chi) \right) = \frac{dS_a(Q_{a\uparrow}, Q_a)}{d\log(Q_a^2)} \,. \tag{2.13}$$

Thus, the Sudakov factor $S_a(Q_{a\uparrow}, Q_a)$ is the partition function for possible virtualities Q_a. The Monte-Carlo algorithm outlined in subsection 2.1.2 uses the Sudakov factor $S_a(Q_{a\uparrow}, Q_a)$ to determine the virtuality Q_a of the splitting parton a in step 4a. Also the virtuality Q_1 of the initial parton is determined in step 1 of the algorithm via a Sudakov factor $S_1(Q_\uparrow, Q_1)$.

---

[7] The integration boundaries $\chi_\pm$ are determined by the phase-space constraints of the parton cascade, and will be determined later.

The probability density $p\,(Q_a,\,\chi)$ for a splitting of parton a into partons b and c with a particular momentum fraction χ at a certain virtuality scale Q_a is obtained as

$$S_a(Q_{a\uparrow}\,, Q_a)\left(\frac{\alpha_s(F(\chi, Q^2))}{2\pi}P_{a\to b,c}(\chi)\right) = p\,(Q_a,\,\chi)\ . \tag{2.14}$$

For a parton cascade with several splittings, its probability density can be calculated by considering analogous distributions for the emitted partons and their products, etc. and by multiplying all of these distributions.

The probability density for the production of a particular parton cascade from a single parton can, thus, be written as

$$\begin{aligned}&\left(S_1(Q_\uparrow\,, Q_1)\frac{\alpha_s(F(\chi_1, Q_1^2))}{2\pi}P_{1\to 2,3}(\chi_1)\right)\times \\ &\left(S_2(Q_1\,, Q_2)\frac{\alpha_s(F(\chi_2, Q_2^2))}{2\pi}P_{2\to 4,5}(\chi_2)\right)\times \\ &\left(S_3(Q_1\,, Q_3)\frac{\alpha_s(F(\chi_3, Q_3^2))}{2\pi}P_{3\to 6,7}(\chi_3)\right)\ldots S_{l_1}(Q_{l_1}\,, Q_\downarrow)\ldots S_{l_N}(Q_{l_N}\,, Q_\downarrow)\,,\end{aligned} \tag{2.15}$$

where an initial particle (labeled with the number 1) with virtuality Q_1 distributes its momentum, according to the fraction χ_1, among two newly created particles (labeled 2 and 3) with virtualities Q_2 and Q_3 that split again, distributing their momenta according to fractions χ_2 and χ_3, etc. until finally the particles labeled l_1,..., l_N are obtained, which do not decay further.[8] For the first particle $Q_\uparrow$ was set as the maximum of its range of possible virtualities. In all further splittings, the virtuality of the branching particle was assumed to be the largest possible virtuality for each of its decay products. This constraint is always true for a time-like cascade.[9]

In order to be able to simulate these probability densities by means of Monte-Carlo simulations, one can express Eq. (2.14) in the following form:

$$\begin{aligned}p\,(Q_a,\,\chi) = &\left(S_a(Q_{a\uparrow}\,, Q_a)\sum_{a\to b,c} W_{a\to b,c}(Q_a, \chi_+)\right)\left(\frac{W_{a\to b,c}(Q_a, \chi_+)}{\sum_{a\to b,c} W_{a\to b,c}(Q_a, \chi_+)}\right)\times \\ &\left(\frac{1}{W_{a\to b,c}(Q_a, \chi_+)}\frac{\alpha_s(F(\chi, Q^2))}{2\pi}P_{a\to b,c}(\chi)\right)\ ,\end{aligned} \tag{2.16}$$

with

$$W_{a\to b,c}(Q_a, \chi) := \int_{\chi_-}^{\chi} d\tilde{\chi}\left(\frac{\alpha_s(F(\tilde{\chi}, Q_a^2))}{2\pi}P_{a\to b,c}(\tilde{\chi})\right)\,, \tag{2.17}$$

the partition function for a splitting with momentum fraction χ. The term in the first bracket in Eq. (2.16) is the probability density that parton a has virtuality Q_a and therefore splits – in a not further specified splitting: The notation $\sum_{a\to b,c} W_{a\to b,c}(Q_a, \chi_+) :=$

---

[8] Of course it is also possible, with probability $S_1(Q_\uparrow, Q_\downarrow)$, that an initial particle does not split at all, or, with probability (density) $\left(S_1(Q_\uparrow\,, Q_1)\frac{\alpha_s(F(\chi_1, Q_1^2))}{2\pi}P_{1\to 2,3}(\chi_1)\right) S_2(Q_1\,, Q_\downarrow)S_2(Q_3\,, Q_\downarrow)$, that it only splits one time.

[9] However, due to, e.g., additional phase-space constraints, the actual maximum virtuality $Q_{b\uparrow}$ for a product particle b in the splitting of particle a might be lower than Q_a, i.e. $Q_b \le Q_{b\uparrow} \le Q_a$. In the Monte-Carlo algorithm one can take care of this problem by running a rejection loop over the selection of Q_b candidates via the Sudakov form-factor $S_b(Q_a, Q_b)$. This loop terminates only, if a Q_b canditate is found that fulfills $Q_b \le Q_{b\uparrow}$. Thus, the distribution of virtualities is 0 in the range $[Q_{b\uparrow},\, Q_a]$. By consequence, the Sudakov factor is also modified to a new distribution function $\tilde{S}_b$ with $\tilde{S}_b(Q_a, Q_b) = \tilde{S}(Q_{b\uparrow}, Q_b)$. For this modified Sudakov factor Eq. (2.15) holds as well.

$W_{a\to q,\bar{q}}(Q_a,\chi_+)+W_{a\to G,G}(Q_a,\chi_+)+W_{a\to q,G}(Q_a,\chi_+)$ indicates that all types of LO parton splittings are considered, integrated over the range of all possible momentum fractions $\chi \in [\chi_-\,,\chi_+]$. Therefore, the term in the second bracket gives the (conditional) probability that the parton splitting is of a particular type $a \to b,c$. The term in the third bracket gives then the probability density that the splitting exhibits a particular momentum fraction χ. Thus, one can apply the following Monte-Carlo algorithm to the individual simulations of parton splittings, where the virtuality Q_a of the incident parton is known[10] (cf. Fig. 2.3):

I If parton a is a quark, then there is only the possibility of splitting into a quark and a gluon. If parton a is a gluon, a random number $\mathcal{R}' \in [0,1]$ is selected and compared with

$$p(G \to G,G) = \frac{W_{G\to G,G}(Q,\chi_+)}{W_{G\to q,\bar{q}}(Q,\chi_+)+W_{G\to G,G}(Q,\chi_+)}\,. \tag{2.18}$$

If $\mathcal{R}' \le p(G \to G,G)$ the gluon a splits into 2 gluons, otherwise into a quark and an antiquark.

II The virtualities of the produced partons b and c are selected, using as partition functions $\frac{1}{N_b}S_b(Q_a,Q_b)$ and $\frac{1}{N_c}S_c(Q_a,Q_c)$, respectively, where the normalization $N_{q,G} = S_{q,G}(Q_a,Q_\downarrow)$ is used. Note that now the virtuality of the branching particle, Q_a is considered as maximal virtuality instead of $Q_\uparrow$, which was used in the selection of Q_a. This choice of maximal virtuality corresponds physically to the assumption of timelike parton cascades and allows for iteration of the simulation of parton splitting, then with the maximal virtualities Q_b, Q_c, etc.

III The momentum fraction χ between the momenta of one of the partons (e.g.: b) with parton a is selected, using $W_{a\to b,c}(Q_a,\chi)$ as partition function.

IV Using the values of Q_a, Q_b, Q_c, and χ constraints on the allowed values of the 3 kinematical variables Q_b, Q_c, and χ is constructed. If these constraints are met by Q_a, Q_b, Q_c, and χ simultaneously, Q_b, Q_c, and χ are selected, otherwise, those values are rejected and the algorithm starts again at the first step using the same value for Q_a.

The above algorithm (given by steps I to IV) for the individual parton splittings corresponds to steps 3 and 4 of the algorithm for the simulation of a parton cascade, presented in subsection 2.1.2 (the steps can be identified as follows: I$\hat{=}$3, II$\hat{=}$4a, III$\hat{=}$4b, and IV$\hat{=}$4c+4d). The phase-space constraints that give in step IV as rejection conditions are explained in detail in the next subsection.

The parton energy distributions for the simulated cascades can be described via fragmentation functions that follow the virtuality evolutions given by the DGLAP-equation (alternatively to a direct derivation from the factorization theorem Eqs. (1.20) or (2.5) the Sudakov form-factor and its Monte-Carlo implementation can also be derived directly from the DGLAP-equations, cf. Ref. [91].).

2.1.4 Phase-space boundaries

In this subsection, the phase-space constraints on parton splitting are presented. Their physical motivation and mathematical form is given in sub-subsection 2.1.4.1. Then, their

---

[10] If the virtuality Q_a is not known, i.e.: for the first splitting (of parton 1), it is determined by solving the equation $\frac{1}{N_1}S_1(Q_\uparrow\,,Q_1) = \mathcal{R}$ for a random number $\mathcal{R} \in [0,1]$ (the normalization N_1 is explained in the paragraph below).

implementation in the Monte-Carlo Algorithm is shortly discussed in sub-subsections 2.1.4.2, 2.1.4.3, and 2.1.4.4: These considerations describe steps 1 and 4 of the overall algorithm of subsection 2.1.2 in more detail. First, the implementation of steps 4b to 4d is discussed in sub-subsection 2.1.4.2. To this end, one needs to make a select a particular definition for the momentum fraction χ: To understand how the choice of an energy fraction can be transformed into light-cone-energy fraction and vice versa (a procedure currently implemented in the algorithm) further explanations are necessary in sub-subsection 2.1.4.3. Sub-subsection 2.1.4.4 finally explains how the phase-space constraints are implemented for the selection of parton virtualities, which corresponds to steps 1 and 4a of the algorithm of subsection 2.1.2. Possible effects of the phase-space constraints on the Sudakov form-factors given in the previous subsection 2.1.3 are examined as well at the end.

As phase-space boundaries, the same two constraints as in, e.g.: [103, 123], are used:

- It is assumed that the virtualities of any off-the-mass-shell cascade parton is above a scale Q_0. Otherwise, partons are considered as on-shell.
- The component of the 3-momenta of emitted partons b and c transverse to the decaying parton a, $\vec{k}_\perp$, need to satisfy the condition $k_\perp^2 > (\zeta\Lambda_{QCD})^2 \geq 0$ (with a positive constant ζ). For simplicity $k_\perp^2 \geq 0$ (i.e. $\zeta = 0$) was chosen in all simulations, unless stated otherwise.

As shown later, the combination of these 2 conditions implies that in practice partons have a virtuality above a value $Q_\downarrow$, where $Q_\downarrow \geq 2Q_0$ (for $\zeta = 0$: $Q_\downarrow = 2Q_0$).

2.1.4.1 Consequences and mathematical form of the constraints

For the produced partons in each splitting the component of their 3 momentum that is orthogonal to the 3 momentum of the branching parton, $k_\perp$, assumes a real value: Using light-cone-energy fractions[11] z as the momentum fractions, one can express this relation as

$$\vec{k}_\perp^2 = z(1-z)Q_a^2 - (1-z)Q_b^2 - zQ_c^2 \geq (\zeta\Lambda_{\mathrm{QCD}})^2 \geq 0\,. \tag{2.19}$$

This condition implies boundaries for the integrations over the momentum fractions in both, the partition functions for the momentum fractions as well as the Sudakov form-factor.[12] Thus, one obtains maximal and minimal values for the momentum fractions, z_+ and z_-, respectively

$$z_\pm(Q_a, Q_b, Q_c) = \frac{1}{2Q_a^2}\left(Q_a^2 + Q_b^2 - Q_c^2 \pm \sqrt{Q_a^4 + (Q_b^2 - Q_c^2)^2 - 2Q_a^2(Q_b^2 + Q_c^2 + 2(\zeta\Lambda_{\mathrm{QCD}})^2)}\right)\,. \tag{2.20}$$

These are the constraints for the light-cone-energy fractions z in case of a parton branching in the general case of three different virtualities Q_a, Q_b, $Q_c \geq Q_0$ above the minimal virtuality Q_0. In the limit $Q_b = Q_c = Q_0$ one obtains

$$z_\pm(Q_a, Q_\downarrow) = \frac{1}{2}\left(1 \pm \sqrt{1 - \frac{Q_\downarrow^2}{Q_a^2}}\right)\,, \tag{2.21}$$

---

[11] One should note here that in all these relations z is defined as light-cone energy fraction only in the reference frame where $p_{a\perp} = 0$.

[12] Then, for the Sudakov factors the boundaries of the outer integration over the virtualities automatically fulfill the condition $\vec{k}_\perp^2 \geq 0$, since the inner integration over the momentum fractions only allow such values. Thus, one might argue: If the condition $\vec{k}_\perp^2 \geq 0$ is translated into an integration boundary for the momentum fractions, no constraints on the virtualities, except $Q_b\,, Q_c \geq Q_0$ have to be satisfied.

with

$$Q_{\downarrow} = 2\sqrt{Q_0^2 + (\zeta\Lambda_{QCD})^2}\,. \tag{2.22}$$

Thus, only partons with virtualities Q_a above the threshold $Q_{\downarrow}$ are allowed to split. Eq. (2.21) represents weaker constraints on the momentum fractions than Eq. (2.20). In the integration over the momentum fractions in the exponent of the Sudakov factor (cf. Eq. (A.5)) the weaker conditions Eq. (2.21) were used instead of the stronger ones, because the Sudakov factor $S_a(Q_{a\uparrow},\, Q_a)$ of a parton a can be interpreted as the probability that no splitting occurs for virtuality values inside the range $[Q_a,\, Q_{a\uparrow}]$. Consequently, momentum fractions that lie inside these integration boundaries correspond to candidate splittings of parton a that are rejected in the selection process of Q_a. In order to exclude all possible candidate splittings of parton a, the least restrictive constraints on the momentum fractions are used. These conditions are given by Eq. (2.21), which includes the range (given by Eq. (2.20)) of possible light-cone energy fractions for any splitting, where partons b and c with virtualities above the minimal virtuality Q_0 are created. The stronger conditions on the momentum fractions, Eq. (2.20), constrain the light-cone energy fraction z for a given combination of virtualities Q_a, Q_b, and Q_c to the kinematically allowed region given by Eq. (2.19), and give, therefore, the lower boundary in the integration over the momentum fraction in Eq. (A.4) of the partition function $W_{a\to b,c}$, used for the selection of the momentum fractions[13]

Expressed in terms of energy fractions x the momentum fraction constraints of Eq. (2.20) take the form

$$x_{\pm}(Q_a, Q_{\downarrow}, E_a) = \frac{1}{2}\left(1 \pm \sqrt{\left(1 - \frac{Q_{\downarrow}^2}{Q_a^2}\right)\left(1 - \frac{Q_a^2}{E_a^2}\right)}\right)\,, \tag{2.23}$$

where E_a is the energy of the incident parton. Since the splitting functions do not depend on the parton energies explicitly, only on the energy fractions, the Sudakov factors become independent of the parton energies E_a in the high-energy limit $E_a \gg Q_a$. This limit was implemented in version 1 of the code, assuming $\frac{Q_a}{E_a} = 0$ in Eq. (2.23). Version 1 already corresponds to a resummation at leading-log accuracy. The general, energy – and thus reference frame – dependent Sudakov factor was later implemented (version 2).

From now on always version 2 will be used, if not stated otherwise: It will be shown later on in sub-subsection 2.1.4.4 that the correction that yields version 2 is essential to obtain strongly virtuality ordered parton cascades, which is necessary condition for the validity of a DGLAP based approach, as it was explained in subsection 2.1.3. By consequence one will obtain, in general, cascade particles at high velocities and, thus, strongly focused cascades, as it will be shown in some examples in subsection 2.3.2.

2.1.4.2 Implementation of the phase space-constraints for the selection of momentum fractions

In the next few paragraphs the part of the Monte-Carlo algorithm that is used in order to obtain the momentum fractions χ is described, together with its implementation. This part corresponds to steps 4b) to 4d) of the algorithm outlined in subsection 2.1.2.

Following the considerations in subsection 2.1.1, energy fractions x as well as light-cone-energy fractions z can be used as momentum fraction χ. Either choice, together

---

[13] In the algorithm, this is however implemented differently: First, the momentum fractions are selected from a partition function that uses the weaker conditions, Eq. (2.21). Then, candidate splittings that do not fulfill Eq. (2.19) (and, thus, Eq. (2.20)) are rejected and a new candidate is searched until the condition is met. This procedure is called "rejection loop A" in step 4 of subsection 2.1.2 and is described in more detail in the next subsection.

with the particle transverse momenta, azimuthal angles, virtuality, and the (light-cone) energy of the initial particle, allow to uniquely describe the momentum of each particle inside the cascade. The currently implemented algorithm adopts both choices in different parts of the code:

- The energy fraction x is used, when the momentum fractions $\chi = x$ are selected from the functions $W_{a\to b,c}$, which was defined in Eq. (A.4), because the splitting functions there – given in Eq. (2.6) – have an especially easy form: In particular, they do not depend on the energy E, and are, thus, reference frame independent. One can then exchange in Eq. (A.4) the energy-dependent boundary x_- from Eq. (2.23) with the boundary z_- from Eq. (2.21) in order to obtain a energy- and, thus, reference-frame independent function $\tilde{W}_{a\to b,c}$ that overestimate the interval of kinematically possible momentum fractions. In a later step, particles that do not fulfill the phase-space constraints will be rejected.
- The light-cone-energy fraction z is used ($\chi = z$) for the implementation of the phase-space constraints that stem from the condition $\vec{k}_\perp^2 \geq 0$, because these conditions, Eq. (2.19), assume a particularly easy, energy independent form, if $\vec{k}_\perp^2$ is expressed in terms of z and the parton virtualities.

The proposed algorithm only needs to involve the reference-frame dependence of the parton cascades, when the selected energy fractions x are transformed into light-cone-energy fractions z, which will be explained in the next sub-subsection 2.1.4.3.

If parton a has a virtuality $Q_a > Q_\downarrow$ and the type of branching into partons b and c is known, the following algorithm can be used in order to determine the virtualities and momentum fractions of the produced partons:

1. The virtualities Q_b and Q_c are selected.[14]
2. The energy-fraction x is selected.
3. Using the energy of the initial parton of the cascade, E_{ini}, the energy fraction x, and virtualities Q_a, Q_b, and Q_c, the light-cone-energy fraction z is calculated.
4. Using the virtualities and z, the transverse momentum components $\vec{k}_\perp^2$ is calculated via Eq. (2.19).
5. If the condition $\vec{k}_\perp^2 \geq 0$ is satisfied, the variables Q_a, Q_b, Q_c, and z are kept and the parton branching is, therefore, determined. Otherwise, this algorithm is repeated until a combination of virtualities and momentum fractions satisfies the condition.
6. The four-momenta of particles b and c, p_b and p_c are reconstructed from Q_a, Q_b, Q_c, and z (explained as well in the next sub-subsection 2.1.4.3).

In order to obtain a faster algorithm and to prevent non-terminating loops (due to numerical inaccuracies), the loops are also terminated after a fixed number of repetitions. The corresponding cascades are deleted from the final results. In the simulations performed so far, the relative number of rejected cascades lies below 1 per mill. The condition $\vec{k}_\perp^2 \geq 0$ constrains the momentum fractions within the boundaries given via Eq. (2.20).

---

[14] In this step, the phase-space constraints need to be applied also on the Sudakov factor, which is explained later on.

2.1.4.3 Relation between x and z

Here, the relation between the energy-fraction x and the light-cone energy fraction z is documented. The relation obtained is reference frame dependent. One of its possible derivations is the following (where however the assumption $\vec{p}_{a\perp} = \vec{0}$ was made; without this restriction, the obtained relation is more complicated, because then $\vec{p}_{b\perp}$ depends on both $\vec{p}_{b\perp}$ as well as $\vec{k}_{\perp}$.):

$$\begin{aligned} x p_a^0 &= \frac{1}{2}\left(z p_a^+ + \frac{\vec{k}_\perp^2 + Q_b^2}{z p_a^+} \right) , \\ \Leftrightarrow x \left(p_a^+ + \frac{Q_a^2}{p_a^+} \right) &= z p_a^+ + \frac{z(1-z)Q_a^2 + zQ_b^2 - zQ_c^2}{z p_a^+} , \\ \Leftrightarrow x \left(1 + \tilde{t}_a \right) &= z + (1-z)\tilde{t}_a + \tilde{t}_b - \tilde{t}_c \, , \\ \Leftrightarrow z &= \frac{x\left(1+\tilde{t}_a\right) - \left(\tilde{t}_a + \tilde{t}_b - \tilde{t}_c\right)}{1 - \tilde{t}_a} , \end{aligned} \tag{2.24}$$

with the definition $\tilde{t}_i = \frac{Q_i^2}{(p_a^+)^2}$. For the dominant soft and collinear contributions, where $\tilde{t}_a \to 0$, this rule simplifies to:

$$z = x(1 + \tilde{t}_a) - (1-x)\tilde{t}_a + \mathcal{O}(\tilde{t}_a^2). \tag{2.25}$$

In the derivation shown above it was one of the basic assumptions that in a particular reference frame it is possible to define $x := \frac{p_b^0}{p_a^0}$ simultaneously with $z := \frac{p_b^+}{p_a^+}$. In the above reference frame one obtains

$$\vec{k}_\perp^2 = z(1-z)Q_a^2 - (1-z)Q_b^2 - zQ_c^2 \, , \tag{2.26}$$

$$\vec{p}_{b\perp} = +\vec{k}_\perp \, , \tag{2.27}$$

$$\vec{p}_{c\perp} = -\vec{k}_\perp \, . \tag{2.28}$$

Thus, using Eqs. (2.26)-(2.28) with a light-cone energy fraction z obtained from the energy fraction x via Eq. (2.24) one can deduce the transverse momenta $\vec{p}_{b\perp}$ and $\vec{p}_{c\perp}$ and thus obtain the 4-momenta p_b and p_c from p_a.

For the implementation of the phase-space constraints in the Monte-Carlo algorithm, which is explained in the next sub-subsection, one needs to generalize this transformation for the reference frame of the entire cascade, where $\vec{p}_{a\perp} \neq \vec{0}$. Currently, this is done in the following way:

1. The four-momentum p_a is transformed into the reference frame, where the transverse component of the momentum of parton a vanishes. Since this transformation is a rotation R, the energy fraction x remains the same as in the previous reference frame.

2. The light-cone energy fraction in this reference frame, z, is obtained via Eq. (2.24).

3. In the same reference frame, using Eqs. (2.26)-(2.28), the transverse components, and, thus, finally, the four-momenta of partons b and c are obtained.

4. Via application of the inverse rotation R^{-1} the four-momenta p_b and p_c can be obtained in the desired reference frame.

2.1.4.4 Implementation of the phase space-constraints for the virtuality selection

In order to impose the constraints on the momentum fractions $x_\pm$ on the selection of virtualities, the boundaries on the integration over momentum fractions in the exponent of the Sudakov factor in Eq. (A.5) needs to be changed to $x_\pm(Q_\uparrow, Q)$. These changes affect, thus, the steps 1 and 4a of subsection 2.1.2 that are used to select the parton virtualities, and, therefore, the calculation of the Sudakov form factor given in Sec. 2.1.3. The integration boundaries $x_\pm$ are energy, and thus, reference-frame dependent. In order to avoid the more complicated implementation of a reference-frame dependent Sudakov form-factor, we used the veto-algorithm (cf. Ref. [93] for a description).

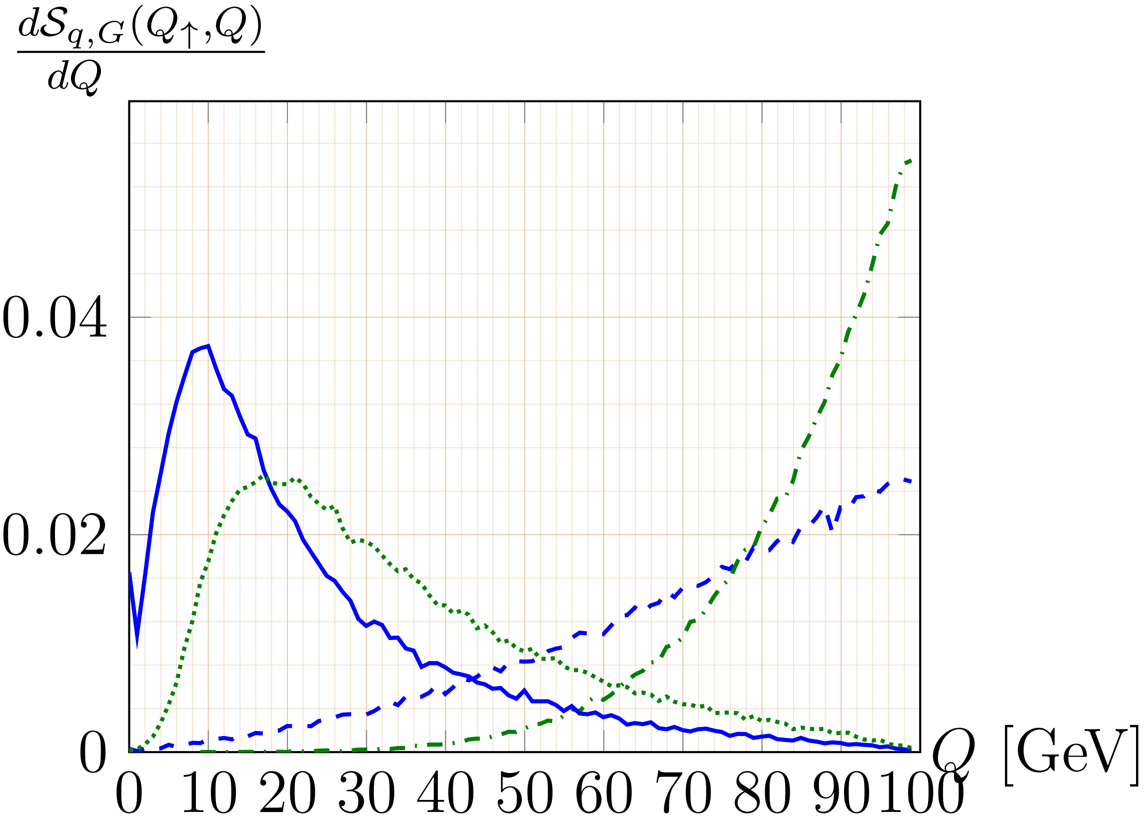

Figure 2.4: Distribution of the virtualities selected for a quark (blue/solid or dashed) or a gluon (green/dotted or dashed dotted) of energy $E = 100$ GeV between a virtuality threshold $Q_\downarrow = 1$ GeV and a maximal virtuality of $Q_\uparrow = 100$ GeV. The momentum-fraction boundaries of the leading-log version 1 were used for the dashed and dash dotted curves. The reference-frame dependent corrections of these boundaries, implemented in version 2 are also shown (solid and dotted curves).

The veto algorithm treats Monte-Carlo processes, where a variable t has to be selected, obeying a partition function S_a of the form

$$S_a(t, t_0) = \exp\left(-\int_{t_0}^{t} f(t')dt'\right), \tag{2.29}$$

for some particular non-negative function $f(t')$. Provided, it is possible to find another function $g(t) \geq\ f(t)\ \forall t \in [t_0,\, t_{\max}]$ one can construct a function

$$\tilde{S}_a(t, t_0) = \exp\left(-\int_{t_0}^{t} g(t')dt'\right), \tag{2.30}$$

and select the t values according to the S_a from Eq. (2.29) using the following algorithm:

1. Start with $i = 1$ and the threshold t_0.
2. Select (in a Monte-Carlo step) t_i following the partition function $\tilde{S}_a(t_i, t_{i-1})$.
3. Create a new random number $R \in [0,\, 1]$.
4. If $\frac{f(t_i)}{g(t_i)} \leq R$, add 1 to i and go back to step 2. Otherwise use t_i as the new value for t.

The following function represents the function f in the current version of the Monte-Carlo algorithm (cf. Eq (A.5)):

$$f(Q,E) = \int_{x_-(Q,E)}^{x_+(Q,E)} dx \frac{\alpha_s(x(1-x)Q^2)}{2\pi} \sum_{a\to b,c} P_{a\to b,c}(x)\,. \tag{2.31}$$

In the expression for $f(Q,E)$ it can be noted, that the integrand is non-negative, and thus also $f(Q,E)$. For further reference, the integration boundaries for the version 1 of the algorithm, which are given in Eq. (2.20), will be called $\tilde{x}_\pm(Q)$. It follows that

$$[x_-(Q,E),\, x_+(Q,E)] \subset [\tilde{x}_-(Q),\, \tilde{x}_+(Q)]\ . \tag{2.32}$$

Thus, $g(Q) \geq f(Q,E)$ is satisfied for the choice

$$g(Q) = \int_{\tilde{x}_-(Q)}^{\tilde{x}_+(Q)} dx \frac{\alpha_s(x(1-x)Q^2)}{2\pi} \sum_{a\to b,c} P_{a\to b,c}(x)\,. \tag{2.33}$$

With these choice for f and g, the requirements for the application of the veto algorithm are met. The corresponding function $\tilde{S}_a$ is represented via the Sudakov factor of the leading-log approximation in the current implementation of the veto algorithm.

Thus, the outlined veto algorithm allows to select the parton virtualities by means of a Sudakov factor with the boundaries $z_\pm(Q, Q_\downarrow)$ for the integration over the energy fractions. Due to the subsequently applied rejection condition, the finally obtained virtualities follow a distribution $\frac{dS_a}{dQ}$, with a Sudakov factor that imposes the stronger constraints $x_\pm(Q, E, Q_\downarrow)$ on the energy fractions.

Fig. 2.4 shows the virtuality distributions of quarks and gluons, $\frac{dS_{q,G}}{dQ}$, for both, Sudakov form-factors that employ the conditions $z_\pm(Q, Q_\downarrow)$, as well as the Sudakov form-factors that impose the stronger conditions $x_\pm(Q, E, Q_\downarrow)$ on parton momentum fractions, obtained with the Veto-algorithm. For small virtualities, both kind of distributions rise monotonously with increasing virtuality. Due to the dependencies of the stronger conditions $x_\pm(Q, E, Q_\downarrow)$ on an expression $(1-\frac{Q^2}{E^2})$, cf. Eq. (2.23), the curves obtained with these constraints start to decrease again at higher virtualities, while the distributions that were obtained with the weaker conditions $z_\pm(Q, Q_\downarrow)$ continue to increase. As a consequence the parton cascades that obey the stronger constraints of will Eq. (2.23) exhibit a strong ordering in virtuality, a necessary prerequisite for the validity of an evolution following the DGLAP equations.

2.1.5 Summary and Comparison

In this section an algorithm for the simulation of parton cascades that propagate in vacuum was presented. It represents a Monte-Carlo approximation of the DGLAP equations and can serve as an approach to the final state radiation of hadronic collisions (in particular pp collisions, where there is not a QGP medium assumed). Correspondingly, similar algorithms can be found in Monte-Carlo event-generators (cf. Sec. 1.4), in particular in the parts that specify final state radiation. It can be noted (cf. Ref. [93]) that – apart from the mere translation of the DGLAP-evolution of a (probability) distribution into Monte-Carlo-selection steps of parton variables – some steps in the algorithm could be selected differently in other algorithms:

1. The reference frame in which parton momenta, energies, and momentum fractions are expressed: A global reference frame, defined by the momentum of the initial parton $\vec{p}_1$ was chosen.
2. The choice of the evolution variable: In the algorithm of this thesis, the evolution variable is the virtuality Q.
3. The choice of momentum fraction: An energy fraction x was selected via parton splitting functions.
4. The constraints in the momentum fraction: The condition Eq. (2.23) was used.
5. The cut-off scale of the evolution variable: This scale is given by the lower virtuality threshold $Q_\downarrow$ that is related to the residual virtuality Q_0 by Eq. (2.22). These virtuality scales are the same for quarks and gluons.

These choices are mainly the same as in Refs. [103, 123], except that $Q_\downarrow = 2Q_0$ ($\zeta = 0$ in Eq. (2.22)) was chosen, and that the conditions Eqs. (5.17) and (5.18) of Ref. [123] that were used to assure angular ordering in the first version of JEWEL, were not implemented in the algorithm of this thesis – a choice that will be discussed in the next section.

PYTHIA (in the version presented in Ref. [93]) uses the same reference frame and momentum fraction as the Monte-Carlo algorithm of this thesis. Its evolution variable is the squared parton mass, which can be identified with parton virtuality for off-the-mass-shell partons. However, due to this choice, different cut-off scales for quarks and gluons, cf. Eqs. (10.7) and (10.8) in Ref. [93], are considered: These cut-offs are interpreted as effective quark and gluon masses and are, thus, higher than the kinematical parton masses (0 in case of the gluon, but non-vanishing for light and heavy quarks, cf. subsection 13.2.1 of Ref. [93]). In this thesis, all explicit mass effects were neglected, as subsection 1.4.1 explains, and are, for the sake of consistency, also ignored in this case. PYTHIA uses two different conditions on the momentum fraction: The first one, documented in Eq. (10.9) in Ref. [93], puts the same constraints on the selection of momentum fractions as Eq. (2.20) (there however expressed in terms of light-cone energy fractions, instead of energy fractions as in Ref. [93]). The second one (cf. the explanations after Eq. (10.10) in Ref. [93]) allows for additional branchings. PYTHIA also implements angular ordering as an additional constraint on momentum fractions, as well as on parton masses, via the Veto-algorithm.

An alternative, also discussed in Ref. [93], consists in using the transverse momentum components (of the radiated particle with regard to the momentum of the branching particle) as evolution variables.[15]

Furthermore, also for the Monte-Carlo algorithm of this thesis two different versions (cf. the discussion in subsection 2.1.4) were found, corresponding to two versions for the

---

[15] A remark on the different notations: What Ref. [93] calls $p_\perp^2$ corresponds to the absolute value of $\vec{k}_\perp$ in this thesis. What is called Q_0 in the descriptions of PYTHIA [93] and the first version of JEWEL [103, 123] is called $Q_\downarrow$ in the notation of this thesis.

constraints on the momentum fractions, Eq. (2.21) for version 1 and Eq. (2.23) for version 2. Version 1 represents the high energy limit of version 2. Both versions simulate parton cascades with leading-log accuracy. Whenever it is referred to the Monte-Carlo algorithm of this thesis, automatically version 2 is meant, unless stated otherwise. In addition to the similar description of partonic final state radiation, programs such as JEWEL or PYTHIA also contain hadronization models. While the current version of the algorithm lacks an explicit hadronization mechanism, the virtuality threshold can be adjusted in a way that allows to effectively simulate hadronization effects on certain observables, in particular the so called humped-back plateau distribution, which is examined in the next section, together with another observable.

2.2 Code validation and calibration

2.2.1 Thrust

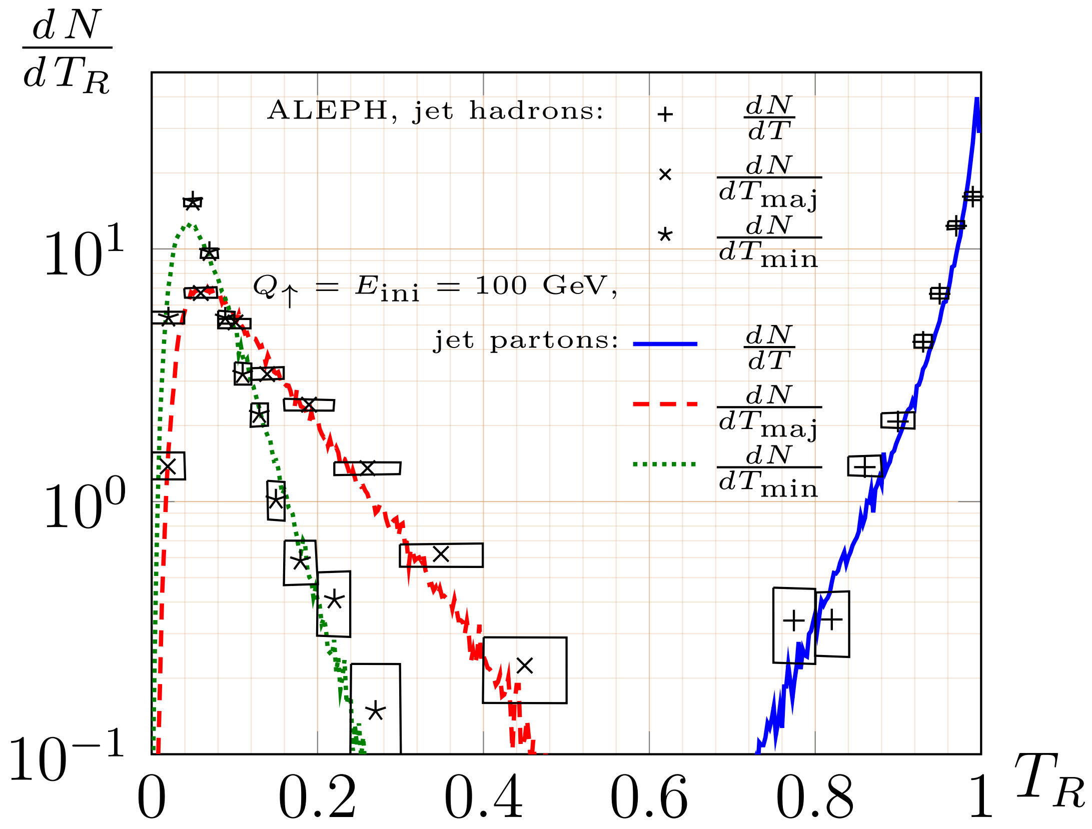

Figure 2.5: T, T_{maj}, and T_{min} obtained from Monte-Carlo simulations for jets with total energy and maximal virtuality of 100 GeV, in comparison to ALEPH-data [126] for $e^+ + e^-$ collisions with $\sqrt{s} = 200$ GeV.

In order to validate the Monte-Carlo algorithm implemented, we verify the same observables as Ref. [123]. Infrared-safe event-shape variables, such as the thrust T, thrust major T_{maj}, and thrust minor T_{min} are by definition not sensitive to changes at small virtuality and energy scales, and, thus, do not change significantly under the different choices for cut-off scales $Q_\downarrow$ and the hadronization process.[16] However, they are considerably affected by changes of the energies and (maximal) virtualities of the initial parton.

---

[16] Furthermore, T T_{maj}, and T_{min} are also ”collinear safe”, i.e.: if instead of a single particle a with

These jet-shape observables are defined as

$$T = \max_{\vec{n}} \frac{\sum_i |\vec{p}_i \cdot \vec{n}|}{\sum_i \|\vec{p}_i\|} \,, \qquad T_{\text{maj}} = \max_{\substack{\vec{n}_2 \\ \vec{n}_2 \cdot \vec{n} = 0}} \frac{\sum_i |\vec{p}_i \cdot \vec{n}_2|}{\sum_i \|\vec{p}_i\|} \,, \qquad T_{\text{min}} = \frac{\sum_i |\vec{p}_i \cdot \vec{n}_3|}{\sum_i \|\vec{p}_i\|} \,, \tag{2.34}$$

with $\vec{n}_3 = \vec{n} \times \vec{n}_2$. With these definitions one can describe a system, where the particle momenta are distributed without a preferred direction as $T = T_{\text{maj}} = T_{\text{min}} = \frac{1}{2}$, a system where all particle move in the same direction as $T = 1$, $T_{\text{maj}} = T_{\text{min}} = 0$. Systems where one particular momentum component in direction $\vec{n}$ is on average larger than the others will satisfy $T > T_{\text{maj}}, T_{\text{min}}$, with $T_{\text{maj}} > T_{\text{min}}$ if one of the other 2 momentum components is on average larger than the other and $T_{\text{maj}} = T_{\text{min}}$ otherwise.

Fig. A.4 shows the distributions of T, T_{maj}, and T_{min} for parton cascades initiated by quarks of energy and maximal virtuality of 100 GeV. As cut-off scale $Q_{\downarrow} = 0.6$ GeV was used, however it was also verified by comparison (not shown in Fig. A.4) with results for $Q_{\downarrow} = 1$ GeV that the particular choice of the $Q_{\downarrow}$ value has very small effects on the distributions – as it is expected for infrared-safe observables. The distributions of T, T_{maj}, and T_{min} were compared in Fig. A.4 with experimental data for e^+e^- collisions at $\sqrt{s} = 200$ GeV from ALEPH. The experimental data are reproduced reasonably well, which should be especially emphasized as the currently implemented Monte-Carlo algorithm does not include a hadronization mechanism. Thus, the T, T_{maj}, and T_{min} distributions can only be slightly affected by possible hadronization mechanisms. This observation can be already obtained from Fig. 5.4 in Ref. [123], which shows the corresponding results from JEWEL, on the parton level, as well as on the hadron level. Both of these curves are rather similar to one another (as well as to the ALEPH data). The Monte-Carlo algorithm of subsection 2.1.2 is also able to reproduce the corresponding results from Ref. [123] at the parton level (not shown in Fig. A.4).

2.2.2 Humped-back plateau and angular ordering

In addition, Fig. A.5 shows the so called humped-back plateau distribution, particle-number density $\frac{dN}{d\xi}$ with regard to the variable ξ, for which the definition

$$\xi = -\ln\left(\frac{\|\vec{p}_{\text{particle}}\|}{E_{\text{total}}}\right) \,, \tag{2.35}$$

is used, throughout this thesis (with $\vec{p}_{particle}$ the 3 momentum of a cascade particle and E_{total} the total energy of the particle cascade). In contrast to event-shape variables the humped-back plateau distributions largely change if the infrared cutoff given via Q_0 is lowered and, thus, additional radiation at lower virtuality and energy scales is allowed. In Fig. A.5 it is shown that the maximum of the humped-back plateau distribution for a virtuality threshold given by $Q_0 = 0.3$ GeV is almost 2 times as high as the maximum of the corresponding distribution for simulations with a threshold given by $Q_0 = 0.5$ GeV ($Q_{\downarrow} = 0.6$ GeV and $Q_{\downarrow} = 1$ GeV, respectively). The distribution for the larger threshold scale is also centered around smaller ξ – i.e.: higher energy – values. The Monte-Carlo simulation that was used for the reconstruction of Fig. A.4, however, can not reproduce neither the corresponding experimental data from ALEPH in Fig. A.5, left panel: For large values of $Q_{\downarrow}$ too few soft particles are radiated, i.e. the distribution at high ξ values is underestimated. On the other hand, the distribution is then overestimated in low ξ region. For small values of $Q_{\downarrow}$ the distribution at large ξ values is better approximated,

---

three-momentum $\vec{p}_a$ two particles b and c move in the same direction, with momenta $\vec{p}_b + \vec{p}_c = \vec{p}_a$ and $\vec{p}_a \| \vec{p}_b \| \vec{p}_c$, the observables remain the same.

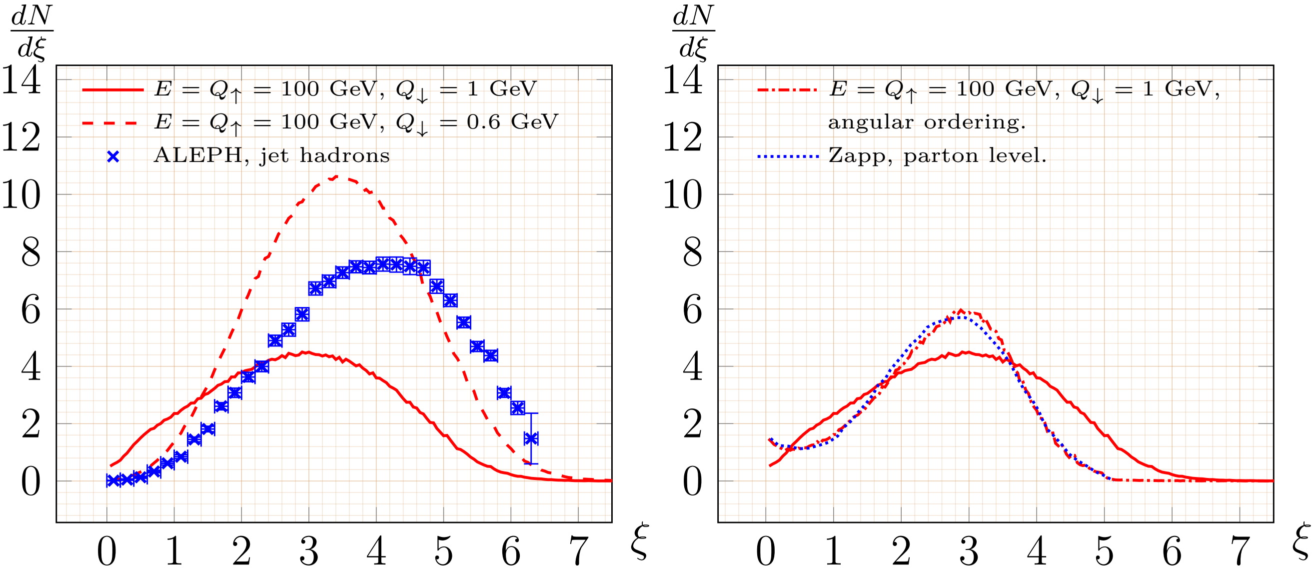

Figure 2.6: Humped-back plateau distribution of the variable $\xi = -\log(\|\vec{p}_{\text{particle}}\|/E_{\text{ini}})$. Left: Monte-Carlo simulations for jets with total energy and maximal virtuality of 100 GeV, for different lower virtuality cut-offs in comparison to ALEPH-data [126] for $e^+ + e^-$ collisions with $\sqrt{s} = 200$ GeV. Right: results for $Q_\downarrow = 1$ GeV with and without angular ordering (solid red, dashed dotted red) in comparison to corresponding results by Zapp [123].

but the number of produced particles per cascade is too large, which results, in particular, in an overestimation of the distribution at its peak.

One can attribute the bad agreement to experimental data to the following reasons:

1. As stated in Ref. [123], for the reproduction of the experimental data a reliable hadronization model for the virtuality scales below 1 GeV is necessary.

2. Alternative to hadronization models, a calculation that relies on local parton-hadron duality (LPHD) instead, the modified leading log approximation (MLLA) [127, 128] reproduces the humped-back plateau distribution pretty well [129]. MLLA consistently resums soft emissions under the assumption that subsequent parton branchings are angularly ordered.

In the right panel of Fig. A.5 the results for the humped-back plateau distribution of parton cascades with $Q_\downarrow = 1$ GeV are shown in comparison to results by Zapp (Fig. 5.7 of Ref. [123]). The results from Ref. [123] were obtained from partons in their final states – before the application of a hadronization model via Monte-Carlo simulation of particle cascades, where angular ordering was implemented. The results obtained from the currently implemented Monte-Carlo algorithm, where angular ordering was not enforced, disagree considerably with the parton level results from Ref. [123]. However, if angular ordering is implemented, the results for the humped-back plateau distribution agree reasonably well with the ones from Ref. [123]. In the currently implemented Monte-Carlo algorithm, angular ordering can be achieved by the following modifications [123, 130] Eqs. (5.17) and (5.18) of Ref. [123] (the former equation as a constraint in the momentum fraction selection, the latter as an additional rejection condition for entire vertices, i.e. in steps 4.b) and 4.d) were used as additional phase-space constraints. For $\vec{k}_\perp^2$ the expression in Eq. (5.8) of Ref. [123] was used. The condition $\vec{k}_\perp^2 > (\zeta\Lambda_{\text{QCD}})$ was replaced by $xE_a > \zeta\Lambda_{\text{QCD}}$ (with $\zeta = 1.1$ in that case).

It can be observed that angular ordering generally shifts the contributions to the humped-back plateau distributions from large ξ values towards smaller ξ values. For simplicity in the rest of this thesis angular ordering was never enforced (Only the phase-space constraints outlined in subsection 2.1.4 were implemented.).

2.3 Estimations on cascade evolution

2.3.1 Numbers of particles and parton branchings

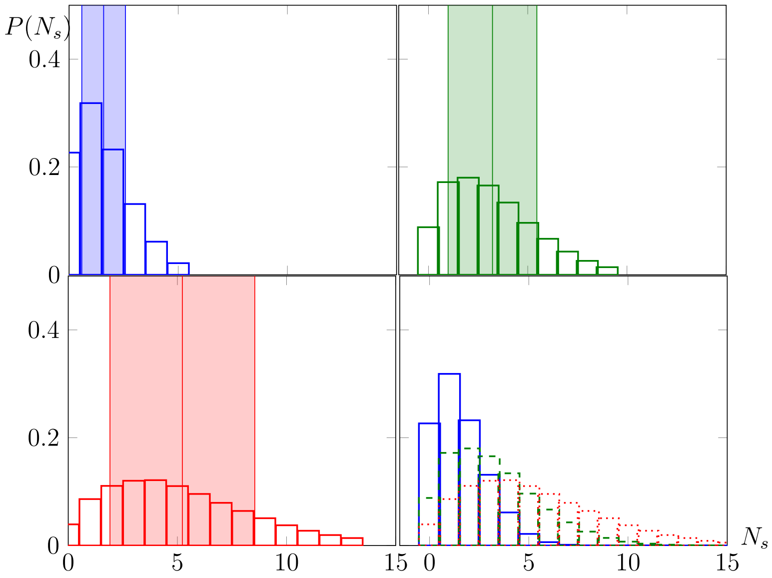

Figure 2.7: Probability $P(N_s)$ that a parton cascade exhibits N_s splittings for $E_{ini} = Q_\uparrow = 10$, 25, 50 GeV (upper left, upper right, and lower left panel, respectively) and $Q_\downarrow = 1$ GeV. The lower right panel compares the 3 cases. The vertical lines represent the mean number of splittings and the corresponding colored bars their deviations.

The number of parton branchings per cascade N_s was examined for 3 different types of cascades, where $E_{\text{ini}} = Q_\uparrow = 10$, 25, 50 GeV. Fig. 2.7 shows the corresponding probability distributions $P(N_s)$, Tab. 2.1 the corresponding average values of N_s. It can be seen that for the virtuality scales considered, the average parton cascade splits up to $N_s = 5$ times, until the virtualities of the particle reach the threshold $Q_\downarrow = 1$ GeV.

$Q_\uparrow$ [GeV]	$\langle N_s \rangle$	ΔN_s
10	1.582 2	1.000 0
25	3.223 6	2.236 1
50	5.228 5	3.316 6

Table 2.1: Mean number of splittings $\langle N_s \rangle$ and deviations ΔN_s for different maximal virtuality scales $Q_\uparrow$.

2.3.2 Time evolution of parton cascades in the vacuum

In preparation for the studies of jet evolution in a medium, it was necessary to obtain a notion of the ”life time” between the creation and annihilation (due to subsequent

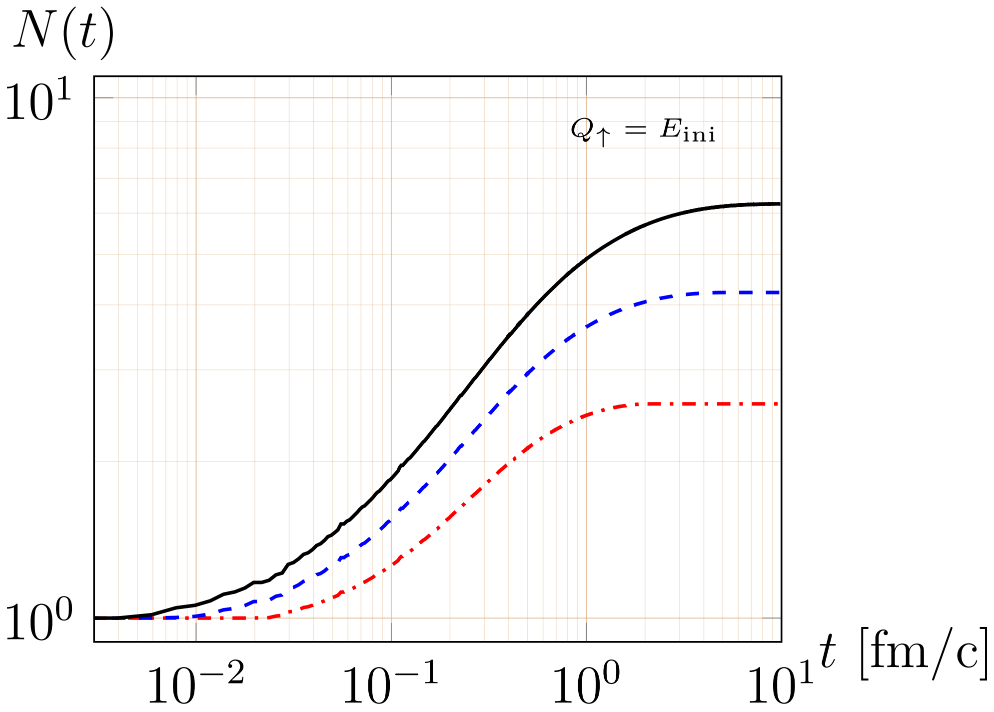

Figure 2.8: Mean number of partons radiated per cascade as functions of time for parton cascades with initial energy and maximal virtuality scales of $Q_\uparrow = E_{\rm ini} = 10$, 25, 50 GeV (red dash dotted, blue dashed, and black solid curves, respectively). The lower virtuality threshold is given as $Q_\downarrow = 1$ GeV.

splittings) of the jet particles considered. Furthermore, being able to analyze the time evolution of parton cascades – even in the vacuum – allows to estimate the time scales at which most splittings happen, or which contribute the most to particular jet-observables. In the current Monte-Carlo algorithm parton cascades were simulated using leading order splitting functions, i.e. following probability distributions calculated in momentum space. It follows from the uncertainty principle that an exact determination of the parton life-times (or the distances traveled by the partons during those lifetimes) is not possible.[17] However, one could estimate the lifetime $\Delta\tau$ of a jet-particle in its own rest frame due to the uncertainty principle to

$$\Delta\tau \approx \frac{1}{Q}\,, \tag{2.36}$$

an approach considered previously also by (at least), cf. [105, 123]. Applying a Lorentz boost to the laboratory frame (for the implemented M.-C. algorithm this reference frame is defined as the frame, where the initial parton of the cascade has the energy $E_{\rm ini}$ and moves along the z-axis), one obtains the corresponding life times Δt,

$$\Delta t \approx \frac{E}{Q^2}\,, \tag{2.37}$$

which is the estimation of particle life-times that is currently used in the M.-C. algorithm. Other, similar variations of this estimation – which, therefore, consider time scales of the same order of magnitude – have also been used in other event generators [103, 105]. E.g., Eq. (2.37) was also considered [113] as estimation for the average particle life-time $\langle\Delta t\rangle$,

---

[17] An alternative would consist in the use of Wigner distributions, i.e.: probability distributions for both, the particle positions/times as well as particle momenta.

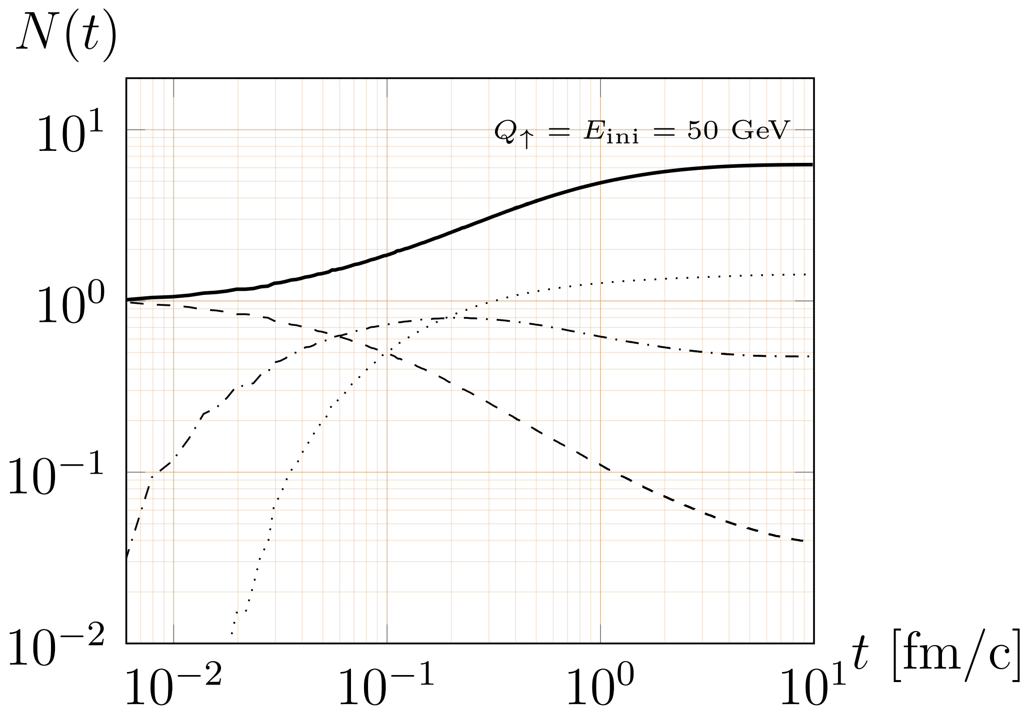

Figure 2.9: The number of partons per cascade as a function of time for $Q_\uparrow = E_{\mathrm{ini}} =$ 50 GeV, and $Q_\downarrow = 1$ GeV, together with its contributions from partons that have splitted in total 0 (dashed), 1 (dash dotted), and 2 times (dotted), throughout their whole time-evolution within the cascade, until time t.

whereas the actual life time was selected from a probability distribution that follows an exponentially decay of the form $\frac{1}{\langle \Delta t \rangle} \mathrm{e}^{-\frac{\Delta t}{\langle \Delta t \rangle}}$. An extensive study of the times between two splittings – also estimated via the uncertainty principle and an exponentially decaying distribution – has been performed in Ref. [131]. Therein, the obtained time scales were used, furthermore, in comparisons with the time scales of interaction with the medium. Since this different approach uses the same average time scales, it can be argued that also the average time evolution for jets will be identical.

In order to study the time evolution of jets in the vacuum, the time evolution of the number of partons per cascade $N(t)$(number of all particles simulated at time t averaged over the number of cascades) was studied. Some sample results are shown in Fig. 2.8: $N(t)$ is shown for 3 different types of cascades with $E_{\mathrm{ini}} = Q_\uparrow = 10, 25, 50$ GeV, where it can be seen that the number of finally obtained partons per cascade increases with $Q_\uparrow$. After the parton cascades are initiated by a single parton and a few first parton branchings, $N(t)$ exhibits an increase following a power law between approximately 0.1 and 1 fm/c, followed by a saturation of $N(t)$ between 1 and 10 fm/c. Radiation starts at smaller time scales for larger $Q_\uparrow$, but also lasts on average longer until all particles are on-the-mass-shell, i.e. until the aforementioned saturation of $N(t)$ is reached. Fig. 2.9 shows for cascades with $E_{\mathrm{ini}} = Q_\uparrow = 50$ GeV the contributions from the initial partons together with the partons produced in the first or second splitting. It can be seen that the number of initial partons decreases almost like a power law in t for most of the studied time span, filling the number of partons present after the first splitting: This curve increases up to its maximum at 0.2 fm/c, when the number of second splittings starts to dominate over the number of first splittings (however a significant number of partons produced in the first splitting are already on the mass shell, so that a saturation is visible below 10 fm/c).

The number of partons produced in the second splitting increases until 10 fm/c, when a flattening of the curve is visible.

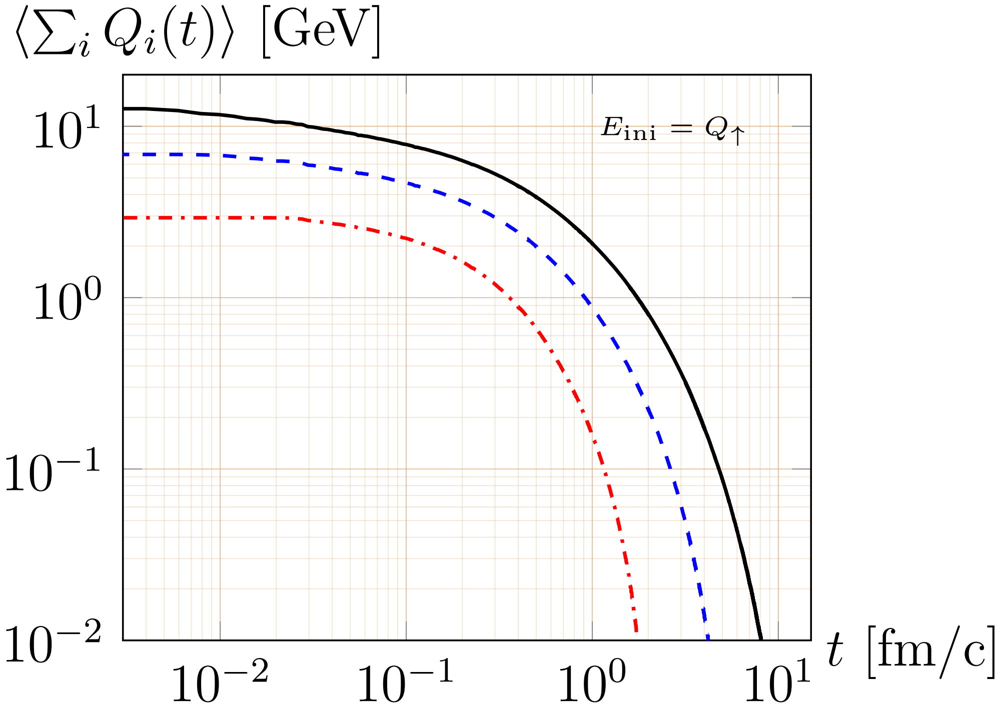

Figure 2.10: Mean values of the sum of the virtualities of all off-shell particles per cascade, averaged over all cascades as functions of time for parton cascades initiated by a quark of $E_{\text{ini}} = Q_\uparrow = 10$, 25, 50 GeV (red dash dotted, blue dashed, and black solid curves, respectively) and lower virtuality threshold $Q_\downarrow = 1$ GeV.

Alternatively, one can also study the time scales on which partonic cascades are produced via the time evolution of parton virtualities. As a result Fig. 2.10 shows the time evolution of the sum of the virtualities of all off-shell particles $\langle\sum_i Q_i(t)\rangle$, and Fig. 2.11 the time evolution of the virtuality of the initial parton of the cascade, $\langle Q_{HF}(t)\rangle$ (again, these averages are taken over the entirety of simulated cascades). $\langle\sum_i Q_i(t)\rangle$ decreases on longer timescales than $\langle Q_{HF}(t)\rangle$. However, both variables exhibit a strong decrease. For the 3 different types of cascades simulated, $\langle\sum_i Q_i(t)\rangle$ reaches the virtuality threshold of $Q_\downarrow = 1$ GeV in the range of 0.4 to 2 fm/c, and $\langle Q_{HF}(t)\rangle$ between 0.2 and 0.9 fm/c. These behaviors demonstrate that for the types of cascades considered parton splittings terminate on average on time scales of the order of magnitude of 1 fm/c in the vacuum. If the partons produced in these cascades would have to pass through a QGP medium, this time scale indicates, that the creation of the parton cascade and its propagation through the medium are 2 processes that overlap in time.

The M.-C. algorithm simulates the parton cascades as Markovian type of processes, a behavior that can be verified, e.g., in Fig. 2.11, by comparing curves for different values of $Q_\uparrow$: The initial quark has an average virtuality $\langle Q_1\rangle \leq Q_\uparrow$ and starts splitting at time $\langle t_1\rangle$. The same value $\langle Q_1\rangle$ will be reached for a cascade with higher $Q_\uparrow$ at a later time $t_1 + \Delta t$. Thus, if one compares the curves for $\langle Q_{HF}(Q_\uparrow = 50 \text{ GeV}, \text{t})$ to the curves $\langle Q_{HF}(Q_\uparrow = 10, 25 \text{ GeV}, \text{t} + \Delta\text{t})\rangle$, the 3 curves should coincide, if the M.-C. algorithm simulates a genuine Markovian process. This appears not to be the case in Fig. 2.11 in the comparison of the (shifted) curves for $Q_\uparrow = 10, 25$ GeV to the curve for $Q_\uparrow = 50$ GeV. However, if one merely shifts the curves for $\langle Q_{HF}(t)\rangle$ by a certain time difference Δt,

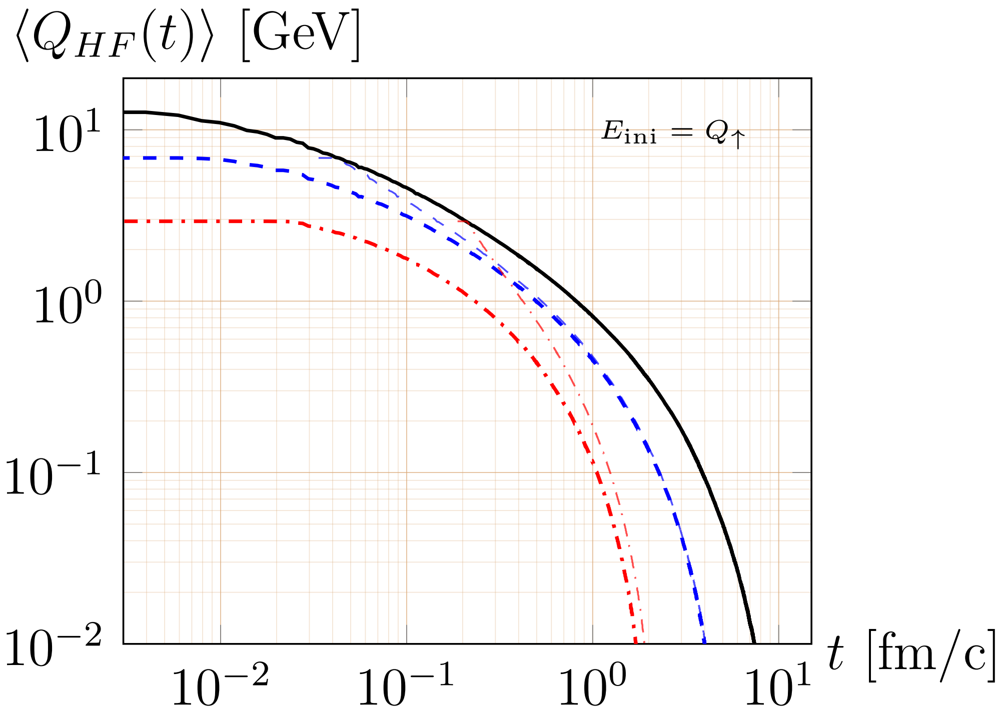

Figure 2.11: Mean virtualities of the initial quark, tagged during further splittings, averaged over all cascades as functions of time for parton cascades initiated by a quark of $E_{\text{ini}} = Q_\uparrow = 10,\ 25,\ 50$ GeV (red dash dotted, blue dashed, and black solid curves, respectively) and lower virtuality threshold $Q_\downarrow = 1$ GeV.

one ignores the dependencies of the corresponding curves on the energies of their initial quarks. After calculating the average energy for the initial quark at time $t_1 + \Delta t$ for the cascades with $Q_\uparrow = 50$ GeV, one obtains

$Q_\uparrow$ [GeV]	$t_1 + \Delta t$ [fm/c]	$\langle E\rangle$ [GeV]
25	0.0434	43.14
10	0.2092	33.31

Calculating cascades for the systems with $Q_\uparrow = 25$ GeV, $E_{\text{ini}} = 43.14$ GeV, and $Q_\uparrow = 10$ GeV, $E_{\text{ini}} = 33.31$ GeV, respectively (instead of $Q_\uparrow = E_{\text{ini}} = 25,\ 10$ GeV) one can make a suitable comparison with the curve for the cascades, where $Q_\uparrow = E_{\text{ini}} = 50$ GeV, as can be seen in Fig. 2.12. A comparison of Figs. 2.11 and 2.12 shows that the ratio between energy and virtuality is not constant throughout the time evolution of the parton cascade, and that in different reference frames (with different E_{ini} values) the parton virtualities evolve differently with time, due to the influence of reference frame dependent integration boundaries for the momentum fractions, $x_\pm(Q, E, Q_\downarrow)$, cf. Eq. (2.23).

The time dependence of the average ratio $\frac{Q}{E}$ between parton virtuality and energy is shown directly in Fig. 2.13: While the left panel shows the average ratio with contributions from all partons present at time t, the right panel shows only the contribution of partons above the virtuality threshold $Q_\downarrow = 1$ GeV. Partons that do no longer undergo further splittings were attributed a residual virtuality of $Q_0 = 0.5$ GeV (where $Q_0 = Q_\downarrow/2$ is obtained from Eq. (2.22), since the parameter ζ was set to zero, $\zeta = 0$, in the simulations for Fig. 2.13), which explains, why the curves in the left panel do not fall off to an average of $\frac{Q}{E} \approx 0$, but stabilize at values between 0.2 and 0.3. For off-shell particles the ratios stay mostly below a value of 0.5, except for the contributions from off-shell particles at

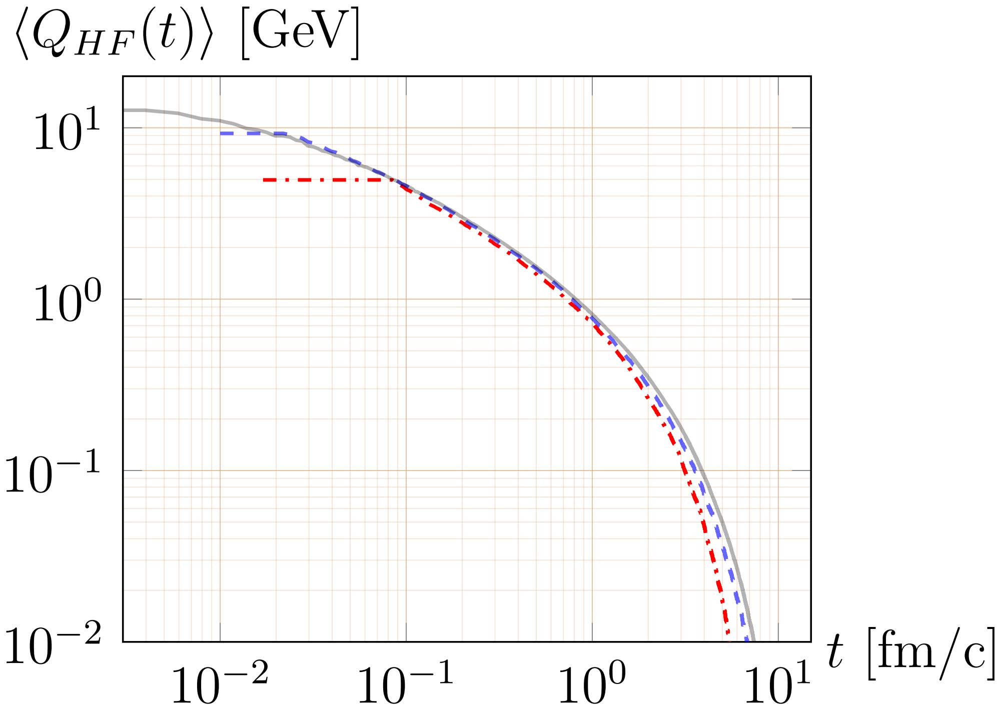

Figure 2.12: Average virtuality $\langle Q_{HF}(t)\rangle$ for parton cascades with $Q_{\uparrow} = E_{\text{ini}} = 50$ GeV (solid, gray) in comparison to the average virtualities $\langle Q_{HF}(t + \Delta t)\rangle$ for partonic cascades with $Q_{\uparrow} = 25\,,10$ GeV and $E_{\text{ini}} = 43.14\,,33.31$ GeV (blue dashed, and red dashed dotted curve, respectively) shifted by the respective time spans of $\Delta t = 0.01\,,0.017$ fm/c to the right.

later time scales (after 2 fm/c): However, from Fig. 2.14, which shows the time evolution of the parton numbers for off shell partons, one can estimate that there exist only few off shell particles at these time scales. The ratio $\frac{Q}{E}$ can serve as a measure for particle velocities β,

$$\beta = \sqrt{1 - \left(\frac{Q}{E}\right)^2}\,. \tag{2.38}$$

Ratios below 0.5 would, thus, correspond to velocities above $\beta = \sqrt{\frac{3}{4}} \approx 0.866$. Therefore, it has been verified (for the parton cascades simulated) that the assumption of relativistic cascade particles is valid. The resulting parton showers are strongly focussed in forward direction, since the branching angles $\theta \propto \frac{Q}{E}$ are also proportional to the ratios $\frac{Q}{E}$. Thus, it has been also verified numerically that collinear splitting is given for all the partons throughout the entire evolutions of the showers, a necessary prerequisite for the validity of the DGLAP-approach to parton fragmentation (cf. Ref. [91]).

Furthermore, the constraints $x_{\pm}$ for the energy fractions used in the Sudakov factor, Eq. (A.5), as well as in the selection of momentum fractions, Eq. (A.4), are proportional to the parton velocities β: These constraints directly lead to the observed suppression of particles with small velocities β, i.e. high ratios $\frac{Q}{E}$. It can be inferred from Figs. 2.13 and 2.14, that the reference frame dependence in the constraints $x_{\pm}$ for the momentum fractions are mainly relevant in the initial stages of the evolution of the partonic cascades. For the parton cascades simulated the relevant time span is of the order of 1 fm/c, starting from the creation of the initial parton.

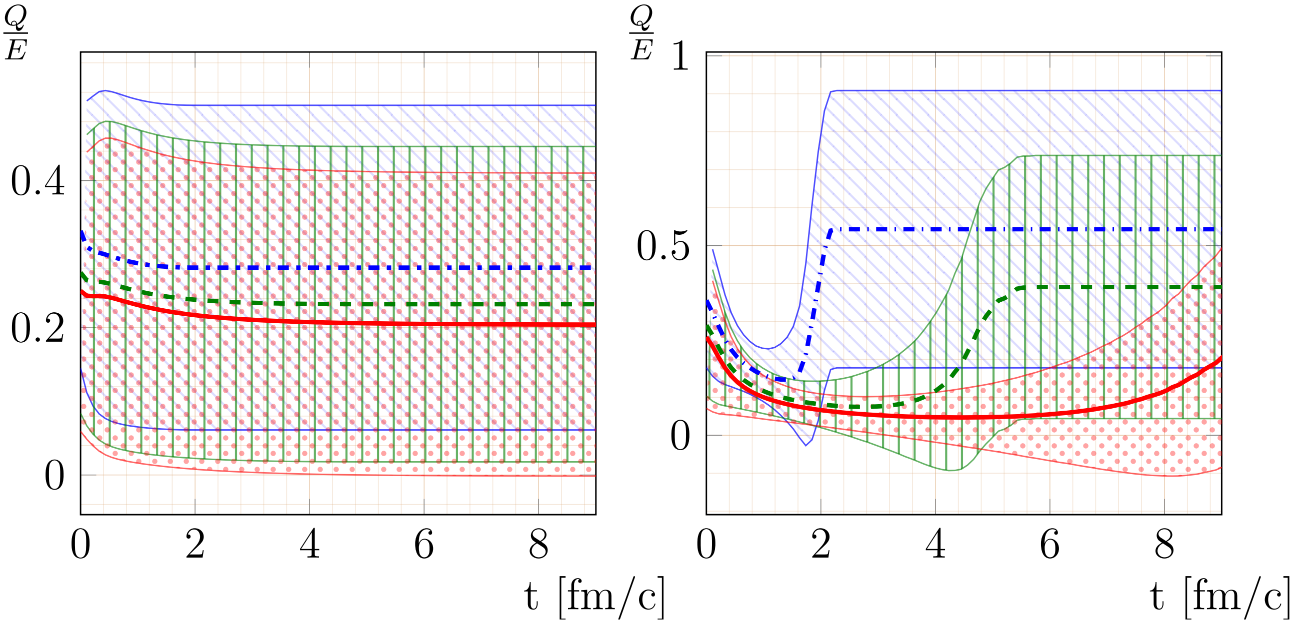

Figure 2.13: Average ratio $\left\langle \frac{Q}{E}(t) \right\rangle$ of parton virtuality Q to energy E as a function of time t for partonic cascades in the vacuum initiated by a quark of energy E_{ini} and maximal virtuality $Q_{\uparrow}$ of $E_{\text{ini}} = Q_{\uparrow} = 50, 25, 10$ GeV (solid red, dashed green and dashed dotted blue curves, respectively) and a minimal virtuality $Q_{\downarrow} = 1$ GeV, together with the corresponding standard deviation in the distributions of $\frac{Q}{E}(t)$ (dotted red, vertical green, and diagonal blue patterns). The average is taken over the total number of partons that contribute to the distributions of the ratios $\frac{Q}{E}$ at time t. Left panel: ratios for off- and on-shell particles, where on-shell particles retain the minimal virtuality $Q_{\downarrow}$. Right panel: ratios for off-shell particles ($Q > Q_{\downarrow}$).

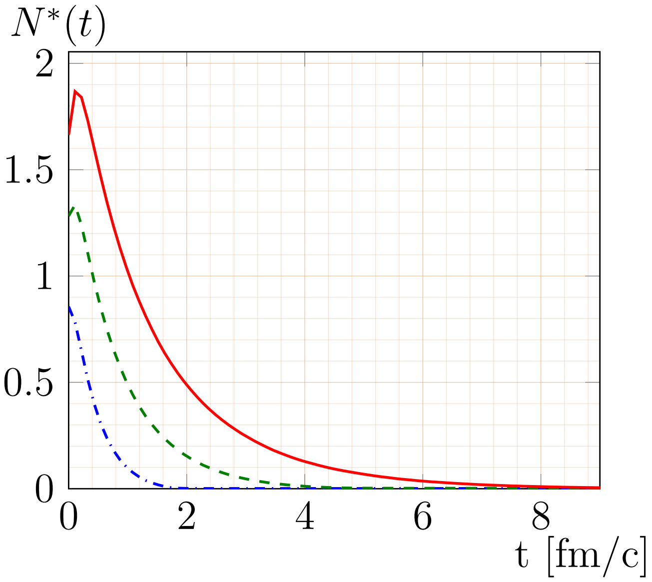

Figure 2.14: Average number $N^*(t)$ of partons per cascade above the minimal virtuality $Q_{\downarrow} = 1$ GeV, as a function of time t for the same types of parton cascades as in Fig. 2.13.

Chapter 3

Medium models

This chapter describes the different effective models of jet-medium interaction that are used in this thesis.

In general, interactions with the hot and dense QGP medium are assumed to depend on a spatially varying temperature[1] T. This is due to a temperature dependent particle density and, furthermore, T is also expected to set the scales for the momenta and energies of thermalised particles, which is often expressed by attributing an effective thermal mass to jet particles in the medium [27, 28, 132, 133]. Different models for the spatial dependence of the temperature exist, e.g.: hydrodynamical calculations.

In addition to parton branchings as in the vacuum, jet particles passing through a medium scatter both elastically (i.e.: they collide with a medium particle without radiating an additional particle. However, four-momentum is transferred to the medium particle) and inelastically (i.e.: additional radiation from the jet-particle is induced by the scattering) with medium particles. The aim of this thesis work is to study how these different types of jet-medium interactions affect the structure of the resulting jets expressed by observables such as two-particle correlations and vice versa to investigate jet-medium interactions via their effects on two-particle correlations. For this purpose effective models of in-medium parton-energy loss are introduced in Secs. 3.1 to 3.3. These models simulate the effects of jet-medium interactions by changing the four-momenta of cascade-partons during their propagation in the medium. These effects on the individual cascade particles are briefly summarized in Sec. 3.4. The phenomenology of (heavy quark) jets in the different effective models as compared to jets in the vacuum was studied in Sec. 3.5 by means of observables that were obtained from the number distributions of either individual cascade particles (in subsection 3.5.1) or heavy quarks (cf. subsection 3.5.2). Chap. 4 will continue the studies on jet-phenomenology: There, however, two-particle correlations, which are obtained from the number distributions of pairs of cascade particles will be studied instead.

It should be noted that the models for jet-medium interaction presented in this chapter are effective in the sense that the medium effects are mediated by continuous changes over time instead of the implementation of the interactions with the fundamental degrees of freedom of the medium, the partons. Furthermore, due to the lack of such a microscopic description the analogue of the LPM effect for a QCD medium [41–44] (cf. also sub-subsection 1.2.3.3) as additional interference effect in the medium, cannot be considered explicitly. It can be argued that one can account on average for the suppression of induced gluon radiation by adjusting the numbers of additionally emitted gluons in the medium model. Otherwise, one could introduce a minimal time span between 2 successive gluon emissions, e.g. cf. Ref. [113] . So far, neither of these approaches has been implemented.

---

[1] It is estimated that T is of the order of magnitude of $200 - 400$ MeV .

Trying to describe the in-medium evolution of parton cascades one has to account first of all for the in-medium loss of individual partons, but furthermore for additional medium effects, acting on the entire cascades. As it is often noted (cf. the introduction in Ref. [101]), at least the following phenomena can be expected from jets propagating in the medium:

1. An increased energy loss (in-medium parton-energy loss) compared to particles propagating in the vacuum,
2. A higher portion of particles radiated at large angles with regard to the jet axis (angular jet broadening),
3. An increased activity of the jet along the jet axis (larger intra-jet radiation),
4. and a (small) deflection of the jet axis due to collisions with the medium (jet deflection).

In this chapter, effective models of jet-medium interactions are proposed that aim at including all of these four medium effects on jet evolution.

3.1 Radiative Energy Loss

This section describes an effective model for in-medium energy loss of jet partons due to induced radiation.[2] The corresponding processes describe the evolution of cascade particles in addition to the branchings due to bremsstrahlung, already present in vacuum (cf. Chap. 2). While many different models for medium modifications of partonic cascades due to induced radiation exist (cf. Chap. 1), for this work an effective model based on an early version of YaJEM [105] was chosen[3]: Parton cascades evolve between an initial and final virtuality scale, $Q_\uparrow$ and $Q_\downarrow$, respectively, and follow the same splitting functions and Sudakov factors as in the vacuum case outlined in Chap. 2. However, during the lifetime Eq. (2.37) of a partons between to consecutive splittings, its virtuality is increased following a behavior of the form

$$\frac{d}{dt}Q^2 = \hat{q}_R\,, \tag{3.1}$$

where $\hat{q}_R$ is a time-dependent function (described below) that simulates the effects of four-momentum transfer from medium particles. Thus, $\hat{q}_R$ depends on typical energy and momentum scales of the medium particles and, thus, on the time-evolution of the temperature. Eq. (3.1) gives the increases of squared virtuality for quarks. In order to simulate the medium effects for gluons as well, $\hat{q}$ was multiplied by a factor $\frac{C_A}{C_F}$ in the currently implemented Monte-Carlo algorithm. Eq. (2.37) is solved self-consistently and, thus, the life-time of partons is shortened. Since parton virtuality is increased by $\hat{q}_R$, the number of parton branchings will increase as well.

This property of the model allows to effectively simulate the medium-modifications of parton cascades due to induced radiation and, thus, increased intra-jet-radiation. Furthermore, due to the additional branchings, individual partons passing through the medium

---

[2] The model will be referred to either as model for radiative energy loss, or "inelastic model". This name reflects the fact that the medium interactions lead to branchings, i.e. $1 \to 2$ processes in an effective model, corresponding microscopically to (multiple) collisions followed by a medium induced radiation, i.e.: $2 \to 2 \to \cdots \to 2 \to 3$ processes.

[3] The basic energy-loss mechanism in YaJEM of the version of Ref. [105] has the advantage that it is particularly easy to describe and also to implement. Thus, this section first explains this basic mechanism and only afterwards tries to justify the particular choice of model, vis-à-vis other approaches to radiative energy loss.

will on average lose more energy than in the vacuum. Also, the angles between the jet axis and the three momenta of the cascade particles in their final states is, on average, larger for cascades with additional induced branchings than for cascades in the vacuum. For the initial partons of the cascades this effect of angular broadening corresponds to larger deflections of their three-momenta from their original directions.

In order to properly describe the propagation of cascade particles in the medium, it is crucial to know, how their four-momenta change, in order to yield the virtuality increases over time described in Eq. (3.1). While different possibilities that correspond to the same $\hat{q}_R$ exist, this thesis attributes the virtuality increase to an increase in the cascade particle energy, i.e.: $\dot{E}^2 = \dot{Q}^2 = \hat{q}_R$. The reason for this choice is that it leaves the parton three-momenta unchanged during the particle propagation between two consecutive splittings – only parton branchings affect the three-momenta. Thus, this choice allows to simulate the effects of processes of induced radiation on parton cascades, while neglecting at the same time the effects of collisions with medium particles completely[4]. Since $\dot{E}^2 = \dot{Q}^2$ the energies of the partons in the cascade, and, thus, of the entire cascade is not conserved, but rather energy is transferred from the medium to the passing cascade. Due to the additional – induced – parton branchings the amount of energy radiated off a cascade particle is larger than the energy gains during its in-medium propagation, resulting in an overall energy loss for individual cascade particles, which is also larger than the energy lost in the branchings of vacuum cascades.

Compared to other models that describe induced radiation, the YaJEM model [105] has the particular advantage that it is simple to implement and to modify, allowing to simulate jet-medium interactions of different strength (i.e. corresponding to different temperature scales). Its main property is, that four-momenta of particles are changed due to an effective and continuous field, when the particles propagate through the medium. Thus, it is also easily possible to find an analogous model for in-medium energy loss due to purely collisional processes (cf. Sec. 3.2) or a combination of both collisional and elastic processes (cf. Sec. 3.3). It is then possible to study – consistently, within the same overall framework – the effects of the different energy-loss mechanisms on various observables, e.g. the ones shown in Sec. 3.5 (mostly for the purpose of calibrating the models), but, most importantly, two-particle correlations studied in Chap. 4.

In this work if a parton is produced with a virtuality below a fixed virtuality threshold $Q_\downarrow$ this parton will no longer undergo any splittings (as in the vacuum) or jet-medium interactions (and, thus, its virtuality will never rise above the threshold again), because at small virtuality scales a description of parton branchings that follows the DGLAP-equations is no longer valid. The reason is that if the incoming parton is almost on-shell the argument fails that the virtualities of cascade particles decrease strongly after (induced) branching – a necessary condition for the description of parton evolution via DGLAP-equations (cf. Chap. 2). Thus, it can be argued that descriptions of induced radiation, where the incident cascade-particle is already on-the-mass-shell, such as, e.g. Ref. [124, 134] are more suitable at this stage of the cascade evolution. On the other hand, for highly virtual particles it is assumed that branching processes as in the vacuum dominate the evolution of the cascades, with only slight modifications due to in-medium propagation. This work focuses on the initial highly virtual branching processes with particular emphasis on their effect on observables of the outgoing final jet particles, while neglecting later medium modifications.

An essential ingredient of the model is the dependence of $\hat{q}_R$ on time t. In general, the $\hat{q}_R$ that a particle experiences is a function of its trajectory $\vec{r}(t)$ and, thus, finally of

---

[4] The other extreme case of effective models for jet-medium interactions – a model for collisional processes that neglects induced radiation completely – is presented in the next section.

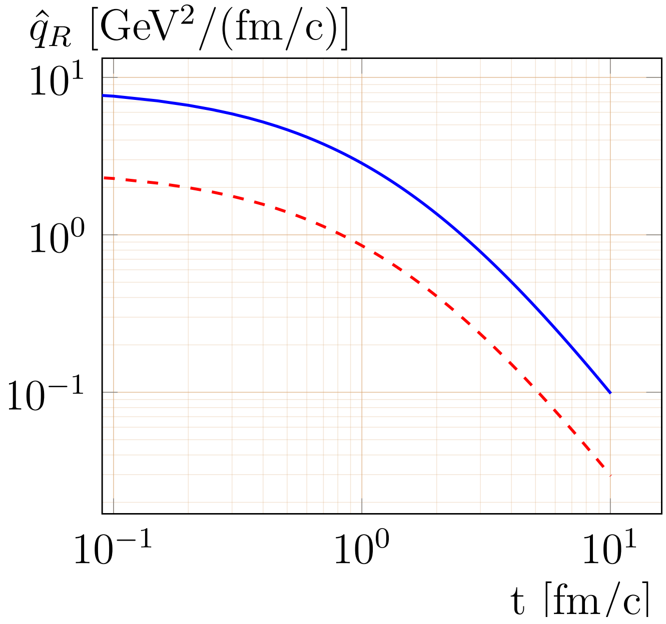

Figure 3.1: Virtuality transfer $\hat{q}_R$ as function of time t for media with $\Delta Q^2 = 10$ GeV^2 (blue, solid) and $\Delta Q^2 = 3$ GeV^2 (red, dashed).

time t. E.g. Ref. [105] calculates $\hat{q}_R$ in a hydrodynamical simulation. While principally other descriptions of $\hat{q}_R$ are possible, this thesis uses a fit [105] to the results of this hydrodynamical approach,[5]

$$\hat{q}_R(t) = \frac{a}{(b+t)^c} \,. \tag{3.2}$$

Ref. [105] mentions 3 scenarios for particle passing the medium. The one selected for calculations of this thesis corresponds to an initial particle created at the center of a medium extending until a length of $L = 10$ fm[6]. Accordingly, for the fit parameters the choices $b = 1.5$ fm/c, and $c = 2.2$ were made (thus, time t is also given in units of fm/c in the formula above). The parameter a is determined via a normalization of $\hat{q}_R$ to an overall squared virtuality increase ΔQ^2

$$\Delta Q^2 := \int_{t_0}^{t_f} \hat{q}_R(t)dt \,, \tag{3.3}$$

where $t_0 = 0$ and $t_f = L = 10$ fm/c was assumed, which yields $a \approx \frac{\Delta Q^2}{0.47}$. In the remainder of this thesis, ΔQ^2 is used as a measure for the strength of the jet-medium interactions. Fig. 3.1 shows examples for $\hat{q}_R(t)$ for the choices $\Delta Q^2 = 3$ GeV^2 and $\Delta Q^2 = 10$ GeV^2, which can be used to match both, energy loss in the RHIC and LHC experiment (while the actual coupling remains unknown).

Implementation of the model: The algorithm implemented discretizes time in small time intervals Δt and changes the cascade-parton virtuality Q and three-momentum

---

[5] It should be emphasized that this thesis focuses rather on a study of the mechanisms of jet-medium interactions and their relative dominances than on the evolution of the strength of these effects within the medium. Thus, once a reasonable time dependence of the strength of the jet-medium interactions is found, this description is used for all cascades in the medium, even if the relative importances of collisional and radiative processes varies among the corresponding systems.

[6] For simplicity – to avoid the simulation of $\hat{q}_R$ with a hydrodynamical model – it was assumed that the scenario for $\hat{q}_R$ holds for all cascade particles, even though it was originally fitted for a certain trajectory. By consequence, this simplification is valid for cascades where the particle trajectories lie in cones of small opening angles.

$\vec{p}$ per time step Δt in the following way

$$\begin{aligned} Q &\mapsto \sqrt{Q^2 + \Delta t\, \hat{q}_R(t)}\,, \\ \vec{p} &\mapsto \vec{p}\,, \end{aligned} \tag{3.4}$$

which results in a continuous increase in cascade-parton energy E,

$$E \mapsto \sqrt{E^2 + \Delta t\, \hat{q}_R(t)}\,. \tag{3.5}$$

3.2 Collisional energy loss

In contrast to the effective model for radiative parton-energy loss of the previous section, this section introduces an effective model for parton-energy loss that does not involve additional parton radiation, as compared to cascades evolving in the vacuum. Instead, parton-energy loss is attributed to elastic $2 \mapsto 2$ particle collisions (referred to as collisional energy loss) between cascade and medium particles, which lead to an energy transfer from the parton-cascade to the medium[7]

For such an effective model one can seek inspiration from genuine collisional models (cf. subsection 1.2.3) and, in particular the general approach to parton in-medium propagation via transport equations, cf. sub-subsection 1.2.3.1. Therefore, consider a cascade particle that is sufficiently long lived, so that the interaction with the medium can be described as a large number of elastic scatterings that only slightly change the momentum of the incident particle (i.e. the cascade particle is too hard and/or massive to thermalize, cf. discussion Chap. 1). There, the medium effects on the incident particle can be described by an effective and continuous force. Its effect on the three-momenta $\vec{p}$ of cascade partons can be described, transport equations as, e.g. the Fokker-Planck equation. The effective force contains, thus, components of a longitudinal drag forces and stochastic, transverse kicks. The longitudinal drag force $\vec{A}(t)$ can be defined as

$$\vec{A}(t) := -\frac{d}{dt}\langle \vec{p}_L \rangle\,, \tag{3.6}$$

where $\langle p_L \rangle$ is the average of the three-momentum component p_L in the direction of the three momentum of the incident cascade particle. As it can be seen in the definition in Eq. (3.6), the drag force $\vec{A}$ leads directly to a decrease of the absolute values of the cascade-parton three-momenta $\|\vec{p}\|$, and, thus, also to a cascade-parton-energy loss. Therefore, with a suitable description of $\vec{A}$ one can effectively account for the energy transfers from cascade-partons to medium partons in $2 \to 2$-particle collisions. This model will be extended to also include $2 \to 3$ processes in Sec. 3.3.

The effect of the stochastic force that acts transverse to the three-momenta directions of the incident partons can be expressed via a squared transverse momentum transfer $\hat{q}_C$, i.e.:

$$\hat{q}_C(t) := \frac{d\langle \vec{p}_\perp \rangle^2}{dt}\,. \tag{3.7}$$

---

[7] One can expect that during the in-medium propagation of jets, a combination of energy transfer to the medium as well as medium-induced radiation contribute to parton-energy loss. The main interest of introducing the two models of this section and the previous one lies in studying, later on (cf. Sec. 3.5 and Chap. 4), whether these two opposing effects can be identified in jet-observables. However, with the aim for a more realistic approximation to parton-energy loss, hybrid models that include collisional as well as radiative contributions are introduced in Sec. 3.3.

The stochastic and drag contributions to the effective force have to satisfy an Einstein relation ([135], also cf. Chap. 1, Subsection 1.2.3.1):

$$\hat{q}_C(t) = \kappa T A(t)\,, \tag{3.8}$$

with the proportionality constant κ and temperature T. One can obtain a more quantitative relation, by making use of two different types of transport cross sections, defined in Ref. [135]: The first one, σ_I^{tr}, is an approximation for the scatterings of relativistic particles with $\|\vec{p}\| \approx \|\vec{p}\,'\|$ (for the incident(outgoing) parton momentum $p(p')$), and only small changes $\Delta\vec{p}_\perp$ of transverse momenta. For collisions at a relative velocity v with medium particles that are distributed with a number density n σ_I^{tr} can be related to the average rate of transverse momentum transfer $\hat{q}_C$. In the ultrarelativistic case $v \approx 1$ one obtains

$$\sigma_I^{\mathrm{tr}} = \frac{\hat{q}_C}{2np^2}\,. \tag{3.9}$$

The other transport cross section, $\sigma_{II}^{\mathrm{tr}}$, can be used to describe the loss of the longitudinal momentum component, $\vec{p}_L$,

$$\sigma_{II}^{\mathrm{tr}} = \frac{A}{pnv}\,, \tag{3.10}$$

via the drag force A. For small parton energies E, the loss of longitudinal momentum is mainly due to potential scattering, where $\|\vec{p}\| = \|\vec{p}\,'\|$, leading to transverse momentum. If $E \ll \frac{T}{2}$ one can approximate $\sigma_I^{\mathrm{tr}} \approx \sigma_{II}^{\mathrm{tr}}$. If, however, $E \gg T$, the loss of longitudinal momentum is mainly due to energy transfers from jet to medium particles, which does not necessarily give rise to transverse momentum. It can be shown that in this case

$$\frac{\hat{q}_C}{A} \approx \frac{2E\sigma_I^{\mathrm{tr}}}{\sigma_{II}^{\mathrm{tr}}}\,. \tag{3.11}$$

Eq. (3.11) further implies $\sigma_I^{\mathrm{tr}} \ll \sigma_{II}^{\mathrm{tr}} \ll \sigma_{tot}$.

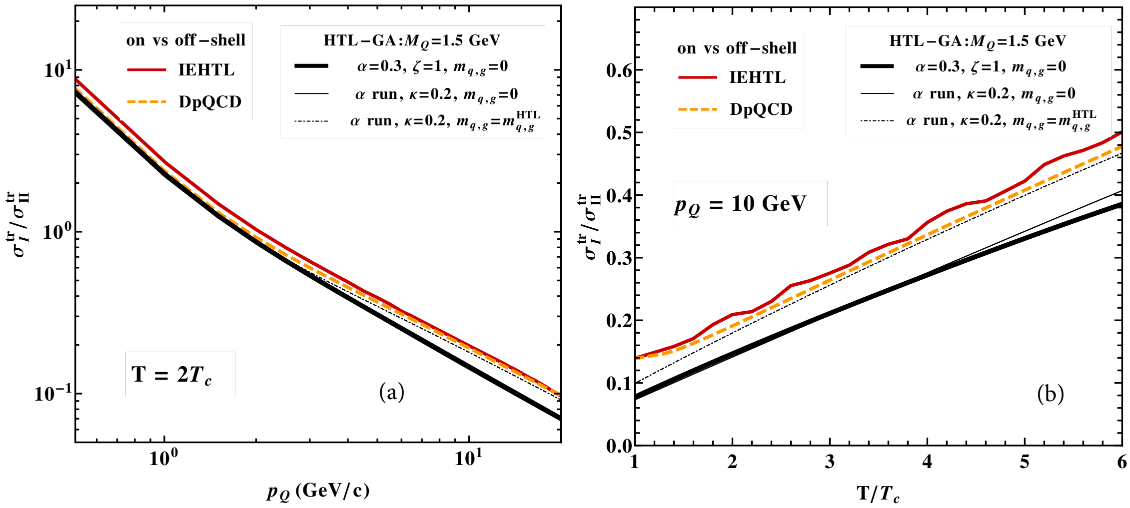

Figure 3.2: Figure taken from Ref. [135]: For the medium model of the current algorithm, the case of a non-vanishing thermal mass from an HTL approach (dashed dotted) was used.

As can be seen in Fig. 16 of Ref. [135] (cited as Fig. 3.2 in this chapter), the ratio between $\hat{q}_C$ and A is almost independent of the particle energy (cf. the left panel of the

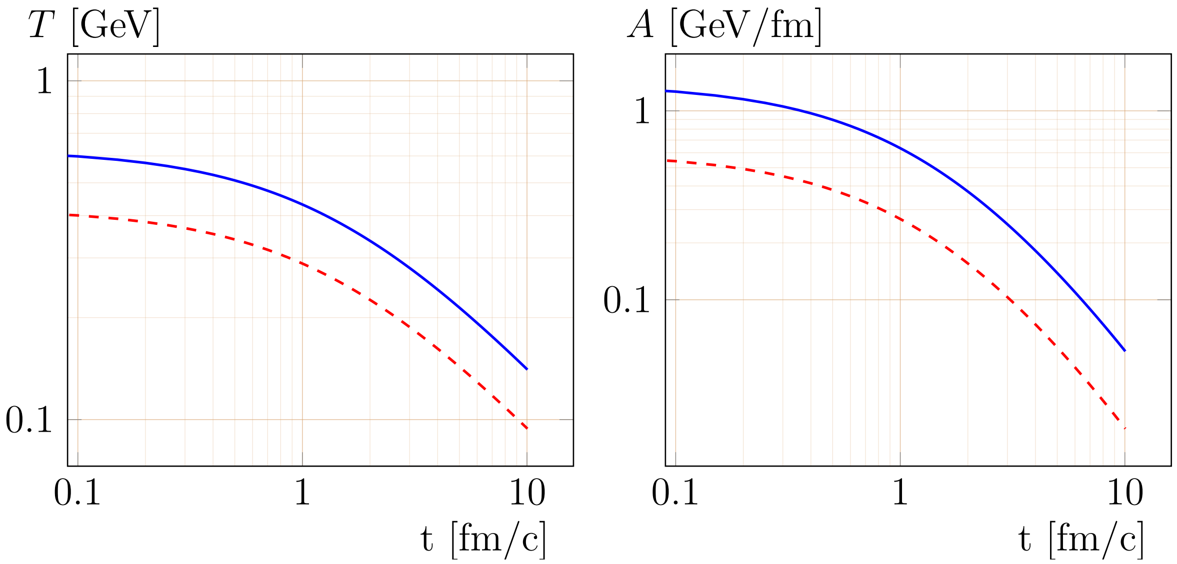

Figure 3.3: Temperature T (left panel), and drag force A (right panel) as functions of time t for media with $\Delta Q^2 = 10$ GeV^2 (blue, solid) and $\Delta Q^2 = 3$ GeV^2 (red, dashed).

figure), whereas it rises roughly linear with the temperature T. With this reasoning one can justify the following linear approximation (in units of GeV):

$$\frac{\hat{q}_C}{A} \approx 0.56 + 1.44\frac{T}{T_c}\,, \tag{3.12}$$

with the critical temperature $T_c = 0.158$ GeV.

Thus, using Eq. (3.12) one can determine the drag force $\vec{A}(t)$ from the transverse momentum transfers $\hat{q}_C$ and the temperature T. The jet collaboration has moreover determined [136] that $\frac{\hat{q}_C}{T^3}$ ≈const. Therefore, this thesis uses the parametrization

$$\hat{q}_C = 7T^3\,. \tag{3.13}$$

Consequently, once the transverse momentum transfer $\hat{q}_C$ is known for a given time t, so is the temperature T and the longitudinal drag force $\vec{A}$. For simplicity, the implemented model assumes $\hat{q}_C = \hat{q}_R$. Corresponding to the $\hat{q}_{C,R}(t)$ profile given in Fig. 3.1, Fig. 3.3 gives the time dependencies for $A(t)$ and $T(t)$[8]. As the behavior of Fig. 3.3 (left panel) suggests, one finds for the choices of $\hat{q}_{C(R)}$ with $\Delta Q^2 = 3$, 10 GeV^2 for the temperatures at the initial stages of the plasma evolution ($t \approx 0$) values of $T = 420$ MeV and $T = 627$ MeV, respectively. Therefore, these T scales, and, thus, the corresponding ΔQ^2 scales, will serve as a crude approximation of the expected scales at RHIC and LHC experiment in the remainder of this thesis. In an effective model for multiple 2 → 2 particle collisions between cascade and medium particles, two different medium effects play a role:

1. thermalization: The incident jet partons are slowed down by jet-medium interactions, due to the drag force $\vec{A}$. After a thermalization time t_T the absolute values of their momenta are entirely determined by the distribution of parton momenta within the medium.

---

[8] In the remainder of this thesis, the strength of the jet-medium interactions is denoted by a quantity that is labelled ΔQ^2, also in case of the effective model for elastic scattering, as well as for tentative hybrid models (with the induced radiation model). This quantity is defined in the model for collisional energy loss as $\Delta Q^2 = \int_0^L \hat{q}_C dt$ and corresponds, thus, to the in-medium gain in transverse momentum instead of virtuality.

2. isotropization: Due the stochastic transverse kicks on the incident particle, mediated by $\hat{q}_C$, the parton momenta are deflected, when cascade partons pass a medium. After an isotropization time t_I the directions of the cascade-parton momenta follow an isotropic distribution and are, thus, completely independent of the directions of the momenta at the production of the cascade partons in parton branchings.

In order clarify which one of the two processes dominates inside the jet-medium interactions, and at which stages of the cascade/medium evolution, one can estimate and compare the timescales t_T and t_I. From the definitions of the drag force in Eq. (3.6) and of the transverse momentum transfers in Eq. (3.7) one can calculate the absolute value of the total drag, p_D, (in the interval $[t_i, t_i + \Delta t]$) to

$$p_D = \int_{t_i}^{t_i+\Delta t} A dt \,, \tag{3.14}$$

and the absolute value of the accumulated momenta from transverse kicks, $p_{\text{stoc.}}$ to

$$p_{\text{stoc.}} = \sqrt{\int_{t_i}^{t_i+\Delta t} \hat{q}_C dt} \,. \tag{3.15}$$

In order to obtain t_T and t_I, it is assumed that the medium effects are approximately as large as the incident parton momenta, i.e.: $\|\vec{p}\| \approx p_D$ and $\|\vec{p}\| \approx p_{\text{stoc.}}$, respectively. Then $\Delta t = t_{T,I}$ in the above formulas can be determined. Under the further assumption of almost on-shell particles, i.e. $\|\vec{p}\| \approx E$, one can obtain the estimations

$$t_T = \frac{E}{A} \,, \qquad\qquad t_I = \frac{E^2}{\hat{q}_C} \,. \tag{3.16}$$

Results for the timescales t_T and t_I are shown for different ΔQ^2 values in Fig. 3.4. For the obtained curves, the values of t_T are smaller than the corresponding values of t_I, for high enough energies. Thus, it can be argued, that thermalization dominates over isotropization. Therefore, in comparison to transverse kicks to the momenta of the incident jet particles, a longitudinal drag force seems to be the more pertinent effect that needs to be included in a suitable description of jet medium interactions (at least in the case of scatterings implying energy transfer to the medium). Only at small parton energies, below 10 GeV, isotropization dominates.

However, while isotropization is in general of minor importance, compared to thermalization, it is important to note that certain observables are particularly sensitive to transverse forces and, thus, to isotropization, e.g. observables reflecting transverse momentum broadening (cf. sub-subsection 3.5.1.2). On the other hand, one can expect that observables that depend solely on the absolute values of particle momenta, such as, in particular, observables reflecting in-medium energy loss, can be suitably well described by a longitudinal drag force alone. The question of whether observables are sensitive to isotropization is revisited in Sec. 3.5, where also results for hybrid models (to be introduced in Sec. 3.3) will be shown.

3.2.1 Implementation of the model

The second model considered effectively simulates elastic scattering of jet particles and medium particles via a medium dependent force that continuously changes the particle 3 momenta $\vec{p}$, but does not affect the virtuality of the jet particle.

Since this thesis aims at calculating correlations between particles of highly energetic jets, $E \gg T$, and, thus, Eq. (3.12) can be assumed. Since it was the goal of this model to

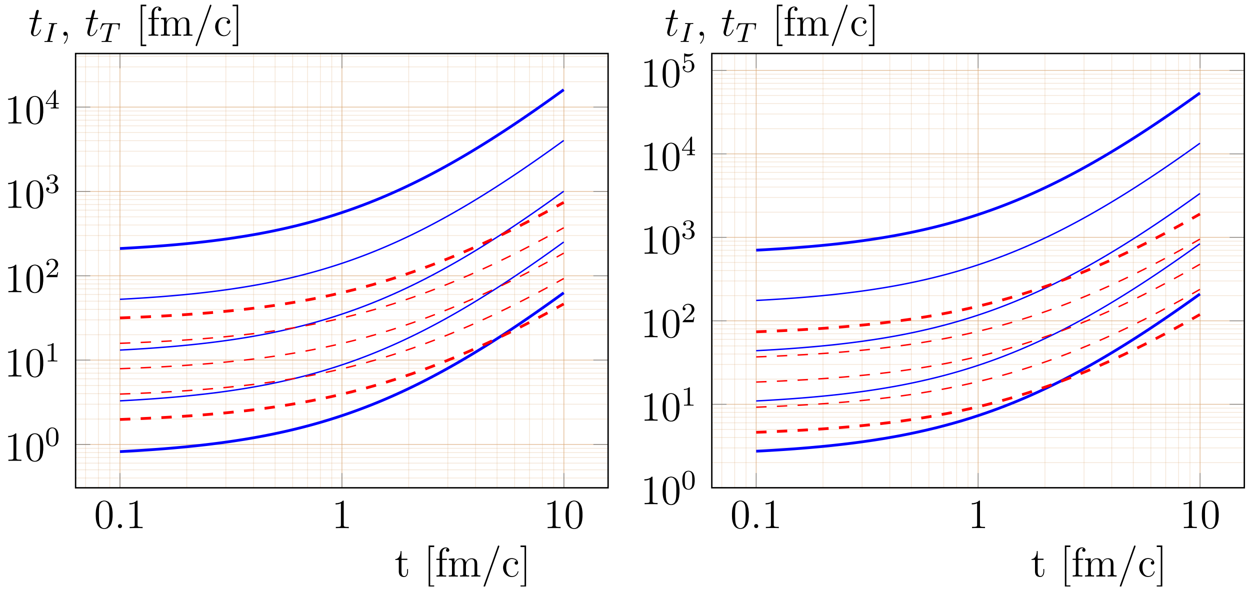

Figure 3.4: Isotropization times t_I (blue, solid) and thermalisation times t_T (red, dashed) in the implemented medium model, as a function of time t, defined via $\hat{q}$ and A, as shown in Figs. 3.1 and 3.3, for incoming particles of energies $E = 2.5$, 5, 10, 20, 40 GeV (from curves at the bottom to the top). Left panels: $\Delta Q^2 = 10$ GeV^2, Right panels: $\Delta Q^2 = 3$ GeV^2.

study the medium effects on 2 particle correlations that are merely due to elastic processes without induced radiation, the parton virtualities Q were set constant throughout the in medium propagation of partons between 2 successive splittings: By consequence, both the jet-particle 3-momenta, as well as the energies are affected by jet-medium interactions.

Thus, one obtains an algorithm, where for a cascade particle that propagates at time t for a small timespan Δt, the virtuality does not change, while the three-momentum is affected by the drag force $\vec{A}(t)$ and the stochastic transverse force, represented by $\hat{q}_C(t)$, i.e.:

$$\begin{aligned} Q(t) &\mapsto Q(t+\Delta t) = Q(t)\,, \\ \vec{p}(t) &\mapsto \vec{p}(t+\Delta t) = \vec{p}(t) - A(t)\Delta t \frac{\vec{p}(t)}{\|\vec{p}(t)\|} + \vec{n}(t)\sqrt{\hat{q}_C(t)\Delta t}\,, \end{aligned} \tag{3.17}$$

with unit vectors $\hat{p}(t)$ in direction of $\vec{p}(t)$ and $\vec{n}(t)$ in a direction transverse to the incident parton momentum $\vec{p}(t)$ (i.e.: $\vec{n}(t)\cdot\vec{p}(t) = 0$). In a thermalized medium the distribution of possible scattering centers is assumed to be (locally) isotropic around the incident jet particle. Correspondingly, the azimuthal angle that determines the direction of $\vec{n}(t)$ in the plane orthogonal to $\vec{p}(t)$ is selected from a uniform distribution in the Monte-Carlo algorithm implemented.

It follows directly from Eq. (3.17), that the cascade-parton energy $E(t)$ changes during a time step Δt of the particles in-medium propagation in the following way

$$E(t) \mapsto E(t+\Delta t) = \sqrt{E(t)^2 - 2\|\vec{p}(t)\|A(t)\Delta t + \hat{q}_C(t)\Delta t + \mathcal{O}\left(\Delta t^2\right)}\,. \tag{3.18}$$

Together with Eq. (3.12) one realizes that E decreases for

$$\|\vec{p}\| > \frac{\hat{q}_C}{2A} \approx 0.28 + 0.72\frac{T}{T_C}\,, \tag{3.19}$$

and increases for smaller parton momenta that do not fulfill the above condition (again the right-most part of the above relation is given in units of GeV). Regardless of the concrete numerical values in Eq. (3.19), this type of relation implies, that for cascade particles with momenta largely above the temperature of the medium, $\|\vec{p}\| \gg T$, the cascade-particle energies decrease, i.e.: energy is transferred to the medium. On the other hand, for momenta below a certain scale, which is of the order of the medium temperature T, the stochastic force dominates, which can result in an energy transfer from the medium to the cascade parton. In the implemented model, where the stochastic force only has components transverse to the momentum of the incident parton, the energy of the cascade parton always increases at these temperature scales.

The evolution of the three-momenta of partons subjected to the drag and stochastic forces can be described by a corresponding Langevin-equation, cf. Eq. (1.6) (the distribution of these momenta follow a Fokker-Planck equation). While these transport equations are often applied to on-the-mass-shell particles, one can argue that they are also valid for off-the-mass-shell particles, as they describe quite generally the action of drag and stochastic forces on a particle with certain three-momentum $\vec{p}$ – without an explicit dependence on the virtuality of this particle.

It is the purpose of the effective models in the studies of this thesis, to provide an overall framework that allows to consistently compare different types of jet-medium interactions between identical jet evolution scales (i.e.: virtualities $Q_\uparrow$ and $Q_\downarrow$ and E_{ini}) and for the same global medium parameters (initial temperature, medium evolution). Thus, the currently implemented version of the effective model for collisional energy loss does not consider any medium effects for cascade particles of virtualities smaller than the threshold $Q_\downarrow$, in order to allow for a consistent comparison between the results of this model with the one for radiative energy loss, which is outlined in Sec. 3.1.

For a more realistic description of in-medium parton-energy loss, of course, it can be even necessary to include also descriptions for the collisional energy loss of on-shell particles, as numerous – analytic – energy loss models suggest (cf. Chap. 1). An appendix will give a first such approach within the framework of the effective models shown in this chapter.

3.3 Hybrid model for collisional and radiative energy loss

Transfer of Energy and three-momentum between jet-partons and the medium, for which an effective model was introduced in the last Sec. 3.2, can be viewed as a generic feature of jet-medium interaction that can be found in processes of collisional as well as of radiative energy loss. In the latter case it can be argued that medium-induced radiation occurs only if jet and medium particles interact, which, in general, involves four-momentum exchanges. One can argue that the contributions to energy loss from induced radiation(for which an effective model was introduced in Sec. 3.1) and from momentum exchange with medium particles do not affect one another: Thus, if one suitably well combines the cascade-parton four-momentum changes of the two previous models, one should obtain more reasonable hybrid models that contain the contributions from both parton-energy loss due to momentum transfer to the medium as well as additional radiation. This section describes two of these effective hybrid-models.

3.3.1 Model with induced radiation and drag forces

This model allows for induced radiation as well as a longitudinal drag due to jet-medium interaction. In this first hybrid model approach forces transverse to incident cascade partons were neglected, because processes of thermalization can be expected to dominate over processes of isotropization, as it was argued in Sec. 3.2.

The parton momenta and virtualities change at time t during a small time-step Δt, in the following way

$$\begin{aligned} Q(t) &\mapsto Q(t+\Delta t) = \sqrt{Q(t)^2 + \Delta t \hat{q}_R(t)}\,, \\ \vec{p}(t) &\mapsto \vec{p}(t+\Delta t) = \vec{p}(t) - A(t)\Delta t \frac{\vec{p}(t)}{\|\vec{p}(t)\|}\,. \end{aligned} \tag{3.20}$$

In the concrete implementation of the model it is again assumed that $\hat{q}_R = \hat{q}_C$, which appears in the above relations only implicitly via the q_C dependence of the drag force A, given via Eq. (3.8).

As a consequence of Eq. (3.20), also the parton energy changes

$$E(t) \mapsto E(t+\Delta t) = \sqrt{E^2 + \Delta t(\hat{q}_R(t) - 2A(t)\|\vec{p}(t)\|) + \mathcal{O}(\Delta t^2)}\,. \tag{3.21}$$

These energy changes follow the same behavior that was previously observed for the effective model of purely collisional energy loss, i.e.: for momenta that fulfill Eq. (3.19)[9] the energy of the cascade particle decreases, due to the influence of the drag force $\vec{A}$, while it increases for smaller momenta, that do not satisfy Eq. (3.19), although this is now the outcome of virtuality increase.

3.3.2 Model with induced radiation, drag forces, and transverse forces

In contrast to the hybrid model of the previous subsection, now a model with a stochastic transverse force is introduced in order to allow a comparison of the two models and, thus, a study on the importance of this transverse force. The same parton-virtuality as in Eqs. (3.4) and (3.20) are considered in this model, in order to allow for a consistent comparison. Consequently, there are not any effects of the stochastic transverse force on the parton virtuality. Instead the stochastic transverse force affects the parton energy, as it was already the case for the elastic effective model in Eqs. (3.17) and (3.18).

Thus, one can write for the virtualities and parton three-momenta

$$\begin{aligned} Q(t) &\mapsto Q(t+\Delta t) = \sqrt{Q(t)^2 + \Delta t \hat{q}_R(t)}\,, \\ \vec{p}(t) &\mapsto \vec{p}(t+\Delta t) = \vec{p}(t) - A(t)\Delta t \frac{\vec{p}(t)}{\|\vec{p}(t)\|} + \vec{n}(t)\sqrt{\hat{q}_C(t)\Delta t}\,. \end{aligned} \tag{3.22}$$

It follows from these relations that the parton energies have to change according to

$$E(t) \mapsto E(t+\Delta t) = \sqrt{E(t)^2 + \Delta t(\hat{q}_R(t) + \hat{q}_C(t) - 2\|\vec{p}(t)\|A(t)) + \mathcal{O}\left(\Delta t^2\right)}\,. \tag{3.23}$$

Again, it can be stated that the parton energy decreases for parton momenta $\|\vec{p}\| \gg T$, but increases if

$$\|\vec{p}\| > \frac{\hat{q}_C + \hat{q}_R}{2A}\,. \tag{3.24}$$

---

[9] In this context it is implicitly assumed, that for the corresponding relation in the hybrid model $\hat{q}_C$ in Eq. (3.19) has to be exchanged for $\hat{q}_R$ (however, the drag force A is still derived from $\hat{q}_C$).

In comparison the Eq. (3.19) and the analogous relation for the hybrid model that does not contain the stochastic transverse force, the above relation contains contributions from both $\hat{q}_C$ and $\hat{q}_R$. For the choice $\hat{q}_R = \hat{q}_C$, which is used again in the implementation of the current effective model, this implies that the momentum scales that separate parton-energy decrease from increase is 2 times the corresponding scales of the elastic effective model or the previous hybrid model.

3.4 Summary on effective models

For the description of jet-medium interactions three models were considered, in order to study different possible medium effects on the evolution of partonic cascades in the medium: These are effective models that involve additional radiation (hereafter also referred to as radiative or inelastic model, or model A), a model where the primary –in-vacuum– radiation rate is unaffected, but where energy is transferred from the cascade to the medium due to a drag-force, and the cascade particles are subjected to stochastic kicks (hereafter also referred to as collisional, or elastic model, or model B), and two hybrid models that include both momentum exchange with the medium as well as additional radiation, where the first considers the medium-induced parton branchings and a longitudinal drag force but neglects transverse forces (hereafter also referred to as model C) and a second one that furthermore also involves a stochastic transverse force (hereafter referred to as model D).

In all of these models, the 4-momenta of the incident jet particles are changed by multiple interactions with the medium. Thus, the cascade evolution can be globally affected by additional splittings (due to increases of virtuality Q), as well as by forces acting on the cascade parton 3-momenta $\vec{p}$. These forces may include components in longitudinal, as well as transverse directions to the incident parton 3 momenta, $\vec{p}_{\parallel}$ and $\vec{p}_{\perp}$, respectively Tab. 3.1 shows, which components of the parton 4-momenta change, due to jet-medium interactions.

model	Q	$\vec{p}_{\parallel}$	$\vec{p}_{\perp}$	E
A (radiative/YaJEM-like)	$\uparrow$	$=$	$=$	$\uparrow$
B (collisional)	$=$	$\downarrow$	$\uparrow$	$\boldsymbol{\downarrow}\uparrow$
C (hybrid/no transverse force)	$\uparrow$	$\downarrow$	$=$	$\boldsymbol{\downarrow}\uparrow$
D (hybrid/transverse force)	$\uparrow$	$\downarrow$	$\uparrow$	$\boldsymbol{\downarrow}\uparrow$

Table 3.1: The 4-momentum components affected by jet-medium interactions in the various models. The symbol ↑ (↓) signifies that the corresponding component increases (decreases) due to medium effects, = that it remains the same. $\boldsymbol{\downarrow}\uparrow$ symbolizes that energy decreases due to medium effects for high $\|\vec{p}\|$, but increases for low $\|\vec{p}\|$. This is explained for model B in subsection 3.2.1 and for the hybrid models in Sec. 3.3.

From a study of these effective models via the resulting observables one can learn about the relative importance of different contributions to in-medium parton-energy loss: A comparison of the collisional and the radiative model would allow to determine how, and to which extent, these observables are sensitive to either four-momentum transfers to the medium or to the medium-induced parton-radiation. In the most ideal case it should then be possible to identify a set of observables that can be used as a tool to discriminate among different models to parton-energy loss (cf. subsection 1.2.3) and to learn to which extent collisional and radiative processes play a role.

If one wants to understand which one of the two contrary energy-loss mechanisms dominates, when both of them contribute to the jet-medium interactions one can compare model A and B with the hybrid models. Comparisons between the two hybrid models finally allow to determine whether there are still relevant contributions from processes of isotropization to certain jet-phenomena, like, e.g. transverse momentum broadening or angular broadening.

3.5 Observables

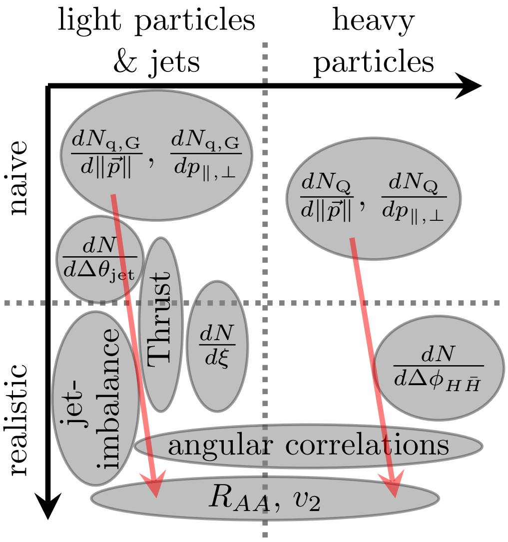

Figure 3.5: Schematic organization of jet observables. The red arrows show the main structure of the remainder of this chapter: To first produce some easily accessible ("naive") observables, in order to verify the presumed in-medium phenomenology, and then to produce more realistic (i.e.: experimentally accessible) observables. This approach is taken two times: First, to study the phenomenology of light particles and jets and a second time to learn about the medium effects on heavy particles.

Jet-medium interactions can be characterized qualitatively by the 4 properties of jet-broadening at large angles, in-medium energy loss, increased intra jet activity and small deflection of the initial particle of a jet/of the jet axis. In order to quantitatively access these behaviors of jets in the medium, numerous observables are considered in this section. Fig. 3.5 gives a (non-exhaustive) list: These observables are either obtained from (multiple) light particles in a jet or from individual heavy quarks/hadrons. The former type has the advantage, that they can be easily obtained from Monte-Carlo simulations of light parton cascades. The latter type gives access to the physics of heavy particles that do not thermalize in the medium and are, thus, a valuable probe for the QGP, as Chap. 1 explains, and one of the main subjects of this thesis work. Furthermore, observables in Fig. 3.5 were referred to as "naive", if they cannot be accessed directly by experiments. E.g. the distributions of parton momenta $\frac{dN_{q,G}}{dp_{\|,\perp}}$, $\frac{dN_{q,G}}{d\|\vec{p}\|}$ (or the related distribution $\frac{dN}{d\Delta\theta_{\rm jet}}$ of the angles $\Delta\theta_{\rm jet}$ of the parton momenta $\vec{p}$ with the jet axis) are not measurable quantities, because due to confinement, only the resulting hadrons can be detected. Observables that can in principle be measured by current heavy ion collision experiments, or which have already been studied experimentally (e.g.: R_{AA}, v_2, jet imbalances, angular correlations...) for genuine hadrons are referred to as "realistic". The remainder of this chapter will, thus, take the approach that is outlined in Fig. 3.5: First, some naive observables for light particles or the entire jet, respectively, are obtained with the jet-medium models of the previous Secs. 3.1, 3.2, 3.3. They are used to verify that the effective models lead to a qualitatively reasonable phenomenology of jet-medium interactions (i.e.: the aforementioned media-effects) and to study these medium modifications of the naive observables. Then more realistic observables will be constructed to further study the medium-effects from the different effective models and to produce results that can, in principle, be compared to experimental data. This approach (to first study naive and then more realistic observables), is repeated for the study of the medium effects on heavy quarks.

	Angular Broadening	Energy loss	Intra-Jet Radiation	Jet deflection
Thrust	×			
$\frac{dN_{q,G}}{dp_{\parallel,\perp}}$, $\frac{dN_{q,G}}{d\lVert\vec{p}\rVert}$	×		×	
$\frac{dN}{d\xi}$		×	×	
jet imbalance	×	×		
$\frac{dN}{d\Delta\phi_{H\bar{H}}}$			×	×
R_{AA}		×		
v_2		×	×	
angular correlations	×		×	

Table 3.2: List of several observables and the jet-phenomena they can possibly reflect (marked by the symbol ×).

Therefore, it is necessary to know which –qualitative– properties of jet-medium interactions are reflected by which observables. Tab. 3.2 gives an overview.

3.5.1 Light particle and jet observables

3.5.1.1 Thrust

By its definition (cf. Sec. 2.2) thrust is a suitable infra-red and collinear safe observable to study the isotropization or collimation of particle showers. The expected broadening in the directions of particle propagation due to medium effects would result in smaller values of T but larger T_{maj} and T_{min} values. On the other hand, due to the collinear safety of the observables, if the jet-medium interactions lead to large amounts of additional collinear radiation along the jet axis, this behavior does not necessarily affect the T, T_{maj}, and T_{min} values. It should be also noted that T, T_{maj}, and T_{min} represent naive observables in the sense that they consider the entirety of outgoing particles of an event. Thus, they do not distinguish between particle produced in hard collisions and remnants of the underlying event. The current version of the Monte-Carlo algorithm simulates parton cascades (considered as jets in the present context, without application of a jet-algorithm) from an initial quark, without the simulation of the underlying event. Thus, it is not yet evident whether the distributions of T, T_{maj}, and T_{min} that can be calculated from the Monte-Carlo simulations of jets correspond to measurable quantities and this would require further investigation.

Fig. 3.6 shows the distributions of T, T_{maj}, and T_{min} for parton cascades initiated by a quark with $Q_{\uparrow} = E_{\mathrm{ini}} = 20$ GeV which evolve down to scales $Q_{\downarrow} = 0.6$ GeV. Due to infrared safety of the observables, the distributions shown are largely unaffected by changes of $Q_{\downarrow}$, and one would get almost indistinguishable results for, e.g.: $Q_{\downarrow} = 1$ GeV.

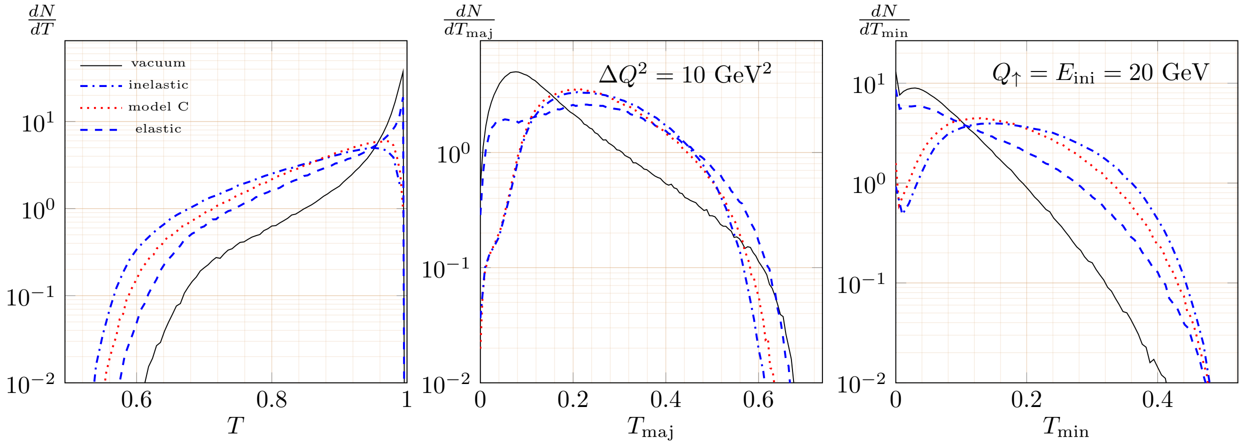

Figure 3.6: Results obtained from the Monte-Carlo simulations of cascades in the vacuum (solid) and the medium for thrust T (left panel), thrust major (middle panel), and thrust minor (right panel). Cascades in the medium were obtained within the three different effective models, the elastic (dashed), the inelastic (dash dotted), and the hybrid model C (dotted).

The distributions of the thrust T confirms the expectation that jet-propagation in the medium leads to angular broadening: For the effective models of both inelastic, and elastic scatterings as well as for the hybrid model C the number of cascades at smaller T values is larger than for cascades that propagate in the vacuum. On the other hand, the peak for "pencil-like" events at $T \approx 1$ is considerably diminished for cascades in the medium – even for purely elastic scatterings, where a sizable peak is still visible. Consequently, the largest angular broadening effect can be observed for the purely radiative model, and the smallest one for the purely collisional model. The distributions for T_{min} confirm these tendencies. However, at large T_{maj} values it appears that more vacuum than medium cascades can be found. This effect is more than overcompensated by the larger number of medium cascades that yield T_{maj} values at intermediate regions between 0.2 and 0.5. Thus, in comparison to vacuum cascades, the T_{maj} values are higher for most of the medium cascades.

3.5.1.2 Parton momenta distributions

In-medium parton-energy loss, as well as jet broadening can be considered as signal for jet-medium interactions. Consequently, this section investigates, for different types of jet-medium interactions, the distributions $\frac{dN}{d\|\vec{p}\|}$ (where $\vec{p}$ are the 3 momenta of individual jet particles) as a means to quantify the corresponding parton energy distributions. Furthermore, the components of $\vec{p}$ longitudinal and transverse to the jet axis, $p_{\parallel\, jet}$ and $p_{\perp\, jet}$, respectively, will be used to quantitatively understand jet broadening, in the implemented models of jet-medium interactions.

Fig. 3.7 shows the distributions $\frac{dN}{d\|\vec{p}\|}$ (normalized to the average number of particles produced per cascade)[10] for cascade particles in their final states obtained with the elastic or inelastic model, or the hybrid model C in comparison to the vacuum case. The most striking medium effect in these plots is the largely increased number of radiated particles – particularly for small $\|\vec{p}\|$ – that occurs for the models that include medium-induced radiation in comparison to the distributions for the elastic effective model or cascades in

---

[10] Unless stated otherwise, for any particle number distributions this type of normalization is used throughout the remainder of the thesis.

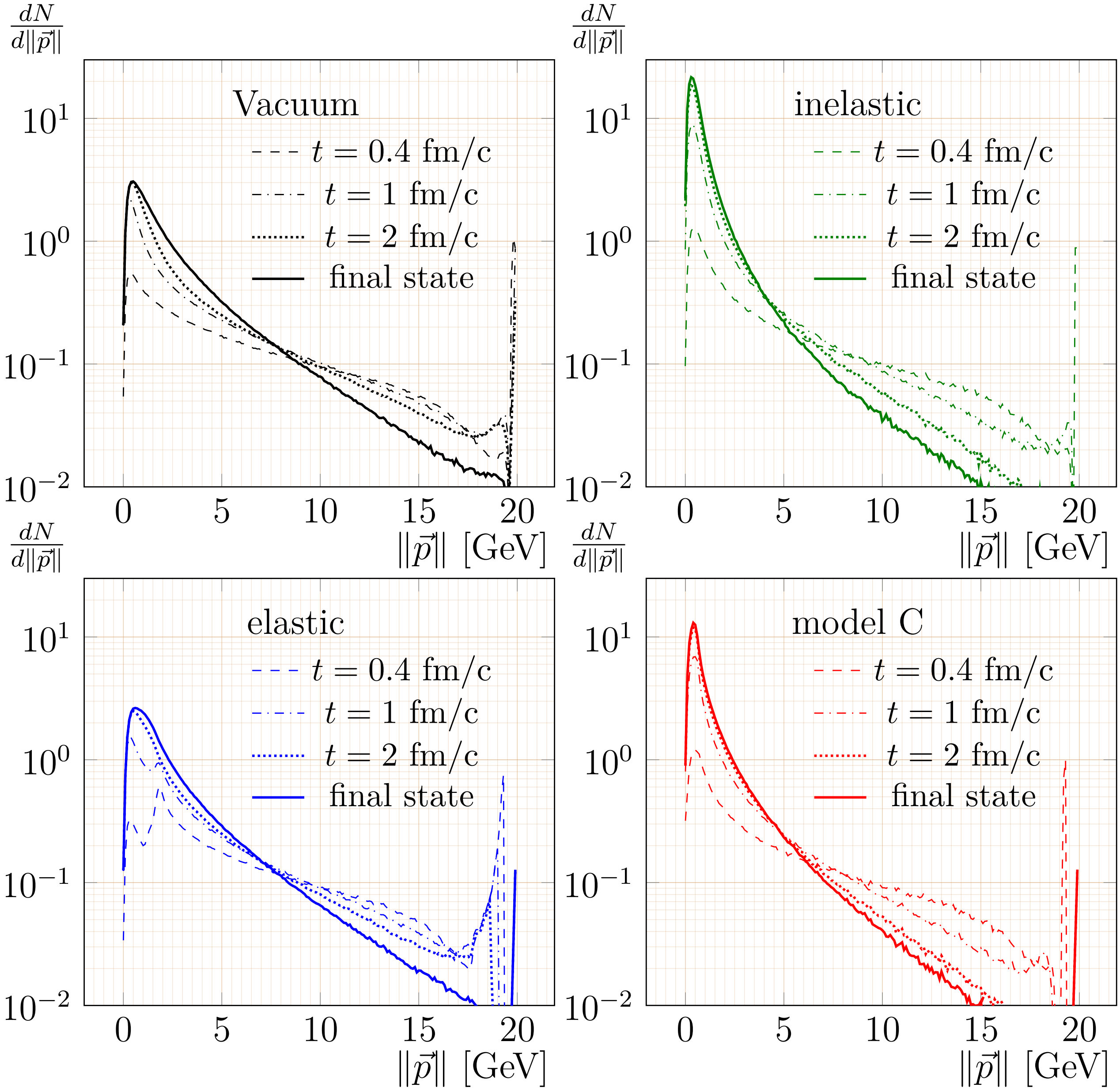

Figure 3.7: Distribution over the absolute values of jet-particle 3-momenta $\|\vec{p}\|$ for jet particles in the final states (solid) and at times $t = 0.4,\ 1,\ 2$ fm/c (dashed, dashed dotted, dotted) for the vacuum (upper left panel) and for inelastic (upper right panel) and elastic jet-medium interaction (lower left panel), as well as for model C (lower right panel). The corresponding cascades are initiated by a quark with $Q_{\uparrow} = E_{\text{ini}} = 20$ GeV, and evolve down to $Q_{\downarrow} = 0.6$ GeV. For the medium $\Delta Q^2 = 10$ GeV^2 was assumed.

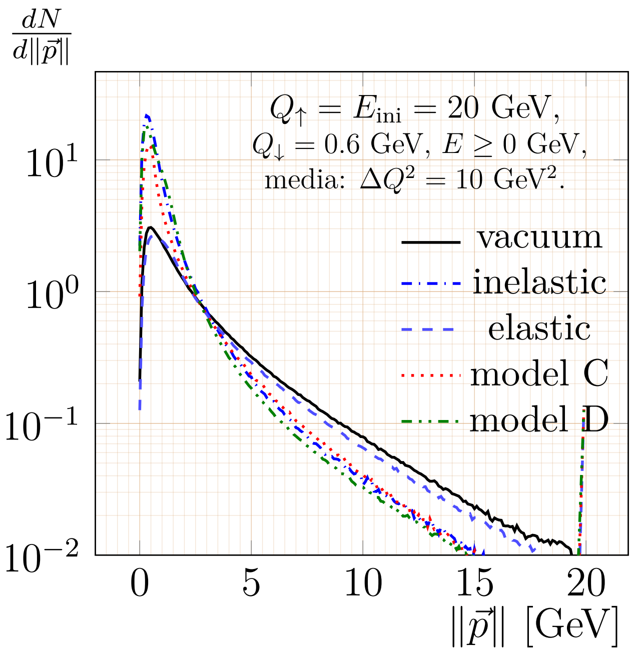

Figure 3.8: The distribution over the absolute values of jet-particle 3-momenta $\|\vec{p}\|$ for jet particles in the final states from Fig. 3.7 are shown here again in comparison to one another.

the vacuum. On the other hand the medium modifications of the elastic effective model appears to have little influence on the distribution, as compared to the distributions for cascades in the vacuum. Furthermore, Fig. 3.7 also depicts $\frac{dN}{d\|\vec{p}\|}$ for three different times t after the creation of the initial quark, in order to illustrate the time evolutions of these distributions. The different time scales were selected at early and intermediate stages of cascade evolution at $t = 0.4\,, 1$ fm/c, where several splittings have already happened, but a saturation of the number of produced particles is not yet visible, as well as at the onset of saturation at $t = 2$ fm/c. As it can be seen in the figure the distributions over $\|\vec{p}\|$ allow initially for larger contributions at higher momenta. Due to momentum loss caused by splittings or scatterings, this region is depleted over time, while radiation of soft partons is enhanced. From the large contributions at high momenta $\|\vec{p}\| \geq 10$ GeV in the distributions at time $t = 0.4$ fm/c the largest part is depleted at short time scales, below $t = 2$ fm/c in case the particles are allowed to produce induced radiation, like in the model for inelastic scatterings or model C. If these additional radiative processes are not present, as, e.g., for the vacuum cascades, as well as for the cascades that only undergo elastic scattering, the depletion of the initially present bump occurs at much larger time scales, so that most of it is still present at $t = 2$ fm/c. This observation indicates that the time evolution of parton cascades happens at much shorter time-scales, if cascade particles are also allowed to produce medium induced radiation.

Fig. 3.8 compares for the four models of jet-medium interactions, as well as for the vacuum, the distributions $\frac{dN}{d\|\vec{p}\|}$ of jet particles in their final states. These distributions exhibit, in general, a strong decrease with increasing values of $\|\vec{p}\|$. This kind of behavior implies that the majority of particles radiated are soft, i.e. have small energies. The distribution corresponding to the elastic energy loss model are slightly suppressed at large momenta, which is to be expected, if energy of the incident parton is transfered to the medium, due to the drag force $\vec{A}$. An even stronger depletion at large $\|\vec{p}\|$ values can be observed for the model of purely inelastic energy loss, where it can be explained by additional splittings of hard into soft partons. Therefore, the induced radiation is

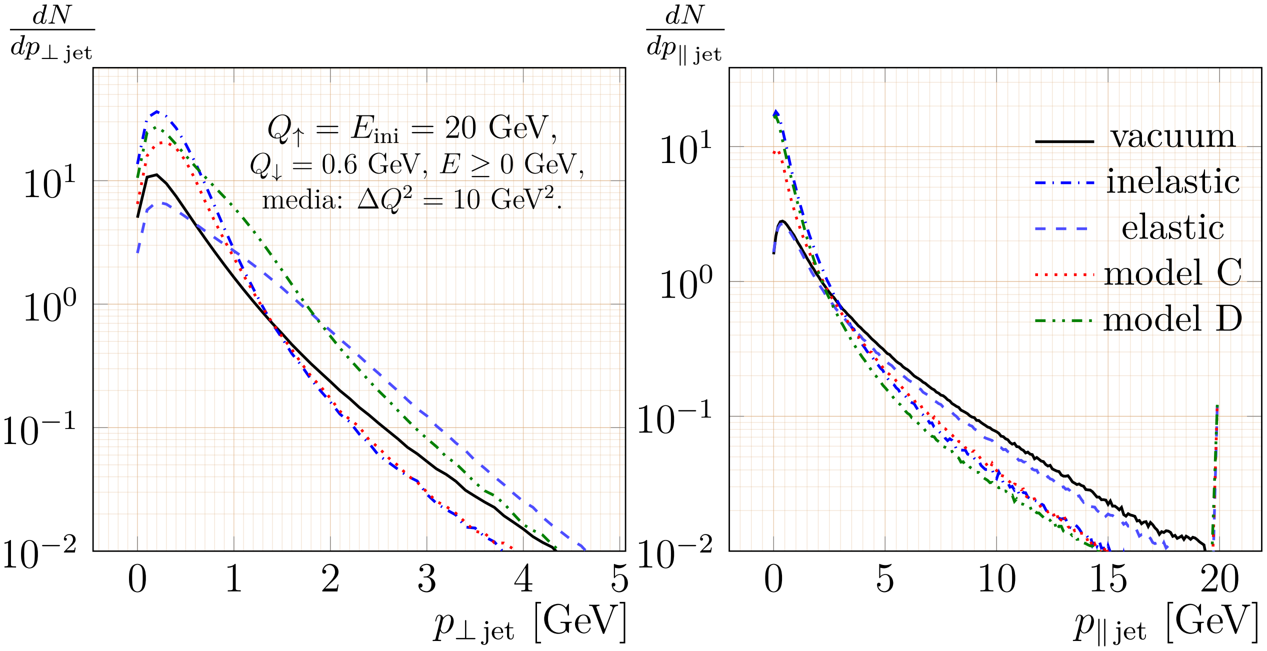

Figure 3.9: Distribution over parton momentum components transverse (left panel) as well as longitudinal (right panel) to the jet axis for particles in their final state. For these results, the same parton cascades as for Fig. 3.7 were used.

expected to occur at small $\|\vec{p}\|$ values. In fact, the peak at small momenta is of almost one order of magnitude larger than in the vacuum. For the hybrid models one observes behaviors similar to the one of the purely inelastic model, which should be reflected in the corresponding humped-back plateau distributions (to be studied in subsection 3.5.1.3).

Fig. 3.9 shows the distributions over the components transverse and longitudinal to the jet axis for the different models of jet medium interactions together with the vacuum. The remainder of this chapter adopts the notation $\vec{p}_{\|\,\mathrm{jet}}$ in order to specify for the three-momentum of a cascade particle its component parallel to the jet-axis.[11] For the three-momentum component orthogonal to the jet axis, the notation $\vec{p}_{\perp\,\mathrm{jet}}$ is adopted analogously.

For the distributions of $p_{\perp\,\mathrm{jet}} := \|\vec{p}_{\perp\,\mathrm{jet}}\|$ one observes a depletion at high values of $p_{\perp\,\mathrm{jet}}$ for cascade particles in the purely radiative effective model A and the hybrid model C, as compared to the corresponding distribution over cascade particles in the vacuum. However, for parton cascades in effective models that include a stochastic transverse force (i.e. models B and D) one observes an enhancement at large $p_{\perp\,\mathrm{jet}}$ values compared to the corresponding distribution for the vacuum[12]. The enhancements at large $p_{\perp\,\mathrm{jet}}$ values might be explained by the stochastic transverse force acting on incident cascade particles, because by definition, this force accounts for transvere momentum transfers to the incident cascade partons during small time steps, cf. Eq. (3.22) [13] . Furthermore, the hybrid models C and D differ in their construction only by the inclusion of the transverse

---

[11] In order to avoid confusion with the parallel component to the beam axis of the jet three-momentum, small letters p will always denote individual cascade particle momenta, while the global jet-momenta (if ever needed), will be denoted by capital letters P.

[12] The hybrid model D exhibits also an enhancement at small $p_{\perp\,\mathrm{jet}}$ values. However, this behavior can be attributed to medium induced radiation of soft particles and reflects, thus, the same physical effects as model A and C at these small scales of transverve momentum, which are discussed further below.

[13] For strongly collimated jets (i.e.: for high initial jet-energies E_{ini}) this stochastic transverse forces can be also viewed as forces that act mainly transverse to the jet axis, provided their cumulative effect on the propagation of the cascade partons is not too large, i.e. $\|\vec{p}\|^2 \gg \Delta Q^2$.

stochastic force (cf. Tab. 3.1), so that contributions from other effects can be excluded (the additional enhancement at small $p_{\perp\,\mathrm{jet}}$ is already present in model C).

For the distributions over $p_{\|\,\mathrm{jet}} := \|\vec{p}_{\|\,\mathrm{jet}}\|$, one observes qualitatively the same behavior as for the distribution of $\|\vec{p}\|$. Again, compared to jets in the vacuum the distribution is more depleted for large $p_{\|\,\mathrm{jet}}$ values in case of elastic jet-medium interactions, even more in case of inelastic scatterings and the hybrid models.

One of the most striking properties of these distributions of $p_{\|\,\mathrm{jet}}$ and $p_{\perp\,\mathrm{jet}}$ is the large enhancement of the peaks at small momentum scales for the effective models that include medium-induced radiation in comparison to the distributions of cascades in the vacuum. The overall shifts towards smaller momentum scales correspond to increases in soft parton radiation. The enhanced peaks at small $p_{\perp\,\mathrm{jet}}$, in particular, are a signal for either additional soft or collinear[14] radiation (the former if the $p_{\|\,\mathrm{jet}}$ corresponding to an individual particle is small, the latter, if $p_{\|\,\mathrm{jet}}$ is large). On the other hand, for the purely elastic model one does not observe any enhancement at small momentum scales, and, in case of the distribution of $p_{\perp\,\mathrm{jet}}$, even a slight suppression. It can, thus, be concluded that only in the effective models that allow for additional medium-induced radiation one can observe a narrowing of the inner core of the jets, while this is not true for the purely collisional effective medium model.

3.5.1.3 Humped-back plateau distribution

The humped-back plateau distributions $\frac{dN}{d\xi}$ also allows to study the distributions of the absolute values of cascade-parton momenta $\|\vec{p}\|$ that was already directly shown previously in Fig. 3.8. However, due to the definition $\xi := -\log(\|\vec{p}\|/E_{\mathrm{ini}})$, $\frac{dN}{d\xi}$ is particularly suitable to study the emission of soft particles. Consequently, in this sub-subsection, the humped-back plateau distributions are primarily used to discuss two aspects: the differences in the soft radiations of the models that include medium-induced radiation (which are hardly visible in Fig. 3.8, due to the display in a semilogarithmic scale) and the influence of $Q_{\downarrow}$ in the different effective models.

The distributions for the cascade particles in the medium have to be interpreted with care, as they likely cannot be translated directly into observable quantities at all ξ: For the chosen initial energy of $E_{\mathrm{ini}} = 20$ GeV, temperature scales of, e.g., $T \approx 200$ MeV or $T \approx 400$ MeV correspond to $\xi \approx 4.6$ and $\xi \approx 3.9$ respectively. Thus, contributions to $\frac{dN}{d\xi}$ at these ξ-values, or above, stem from particles that have most likely thermalized with the medium, and should, therefore, be ignored.

Fig. 3.10 shows corresponding results for parton cascades of light partons, initiated by a quark with $Q_{\uparrow} = E_{\mathrm{ini}} = 20$ GeV. In general, the distributions are depleted at low ξ (i.e.: hard particles), while they are filled at higher ξ scales. Thus, the average parton momenta and energies (represented by the ξ values) are smaller for medium cascade particles than for those that propagate in vacuum: This behavior of $\frac{dN}{d\xi}$ verifies an increased tendency to jet splitting in the medium.

In consistency with observations for Fig. 3.8 one notices in detail: The distributions for the purely elastic model are close to the corresponding distributions for the vacuum, except for an increase of the peak for $\Delta Q^2 = 10\ \mathrm{GeV}^2$ and $Q_{\downarrow} = 0.6$ GeV. On the other hand, for the models that involve medium-induced radiation one observes large enhancements at large ξ values and slight depletions at small ξ.

For the hybrid models one observes: Model C, whose only difference to the inelastic effective model A is the implementation of a drag force (cf. Tab. 3.1), is not as much enhanced (as compared to the distributions for cascades in the vacuum) as the inelastic

---

[14] i.e.: collinear to the jet axis.

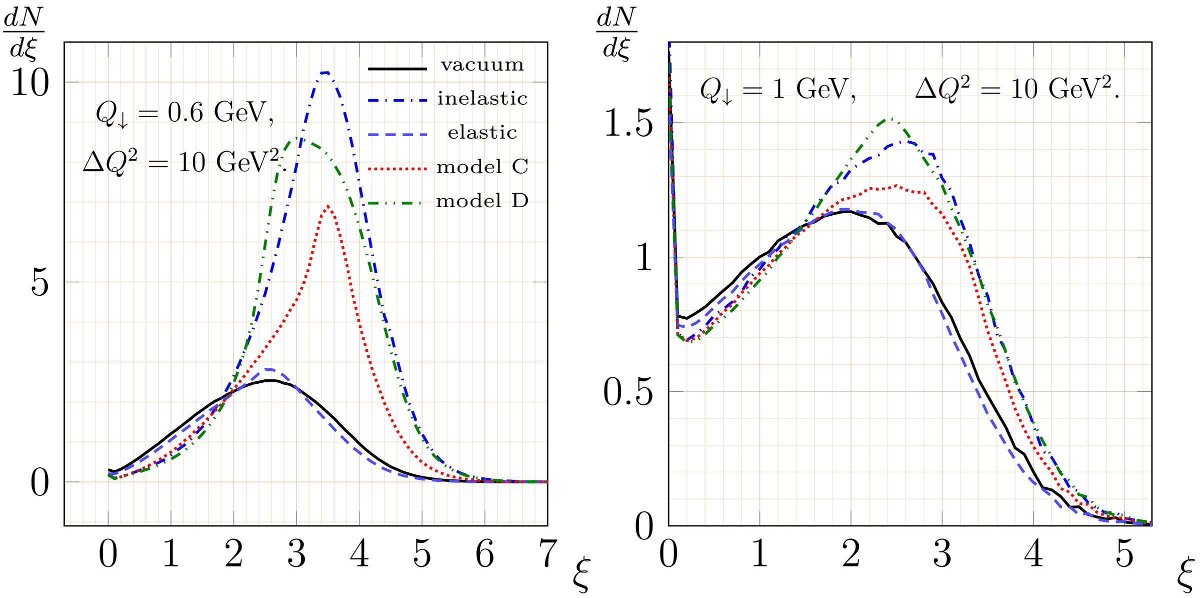

Figure 3.10: Humped-back plateau distribution of the variable $\xi = -\log(\|\vec{p}\|/E_{\text{ini}})$. For these results, parton cascades that evolve down to $Q_\downarrow = 0.6$ GeV (left panels) or $Q_\downarrow = 1$ GeV (right panels) and that are initiated by a quark with $Q_\uparrow = E_{\text{ini}} = 20$ GeV were simulated in the vacuum as well as in media with jet-medium interactions, described by the models for inelastic (dashed dotted), or elastic scattering (dashed), or the hybrid models C (dotted) and D (dash-dot-dotted).

effective model. The drag force yields an additional energy transfer to the medium (cf. Eq (3.21)), which decreases also the energies of possible decay products. Since the parton energies represent an upper limit to their virtualities, the number of radiated particles is expected to be on average smaller. This effect can be compensated by an additional stochastic transverse force, as it is shown by the corresponding distributions of model D. There one observes, furthermore, that the maxima of the distributions occur at slightly smaller ξ values, as compared to the inelastic effective model or model C. A tentative explanation is given via Eq. (3.23), which implies that the energy transfer to the medium is mitigated if a stochastic transverse force is implemented.

The distributions for cascades with $Q_\downarrow = 0.6$ GeV are shown in the left panels of Fig. 3.10, those for $Q_\downarrow = 1$ GeV are shown in the right panels. One observes that enhancement at large ξ for models that involve medium-induced radiation is several times larger for $Q_\downarrow = 0.6$ GeV than for $Q_\downarrow = 1$ GeV. It follows that most of the additional parton splittings, which occur in simulations with $Q_\downarrow = 0.6$ GeV, happen at small virtuality scales of the order of $Q_\downarrow$. From this comparison the idea emerges that the uncertainties due to different choices for $Q_\downarrow$ lies mainly in the amount of radiated soft particles (even though the behavior of the distributions and the changes due to medium effects are qualitatively the same for both choices of $Q_\downarrow$).

It has been noticed that hadronization can play a major role for the behavior of the humped-back plateau distributions, in particular at high ξ (cf. , e.g. , Ref. [123]). Furthermore, it has been observed that the strong enhancement due to radiative processes will be mitigated considerably, once hadronization is considered for both, cascades in the medium and the vacuum [101]. Analogously, one can expect that the large enhancements observed for models A, C, and D decrease, once a suitable hadronization model is applied to the Monte-Carlo Algorithm.

If one was to consider the humped-back plateau distribution of heavy quarks instead

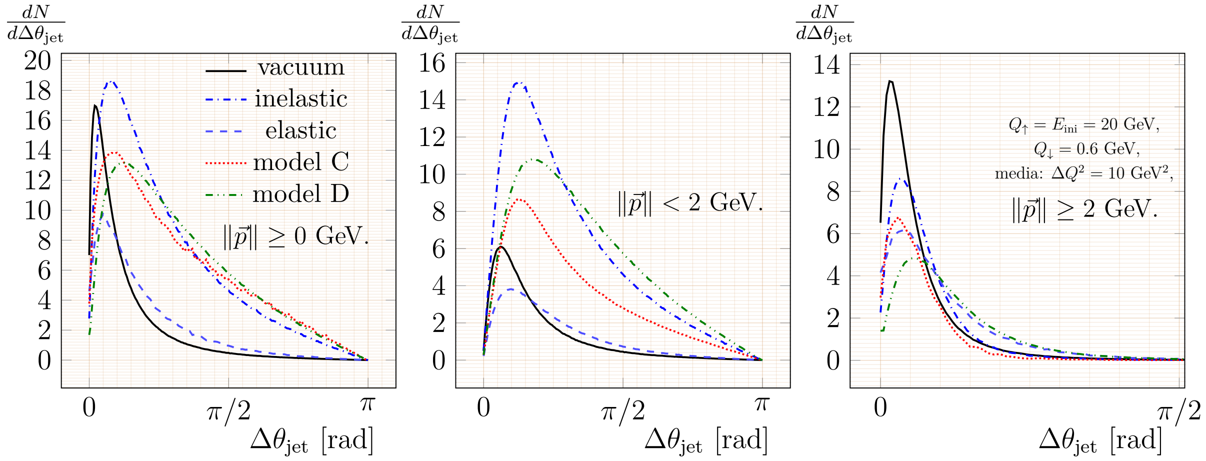

Figure 3.11: Distributions over the angle $\Delta\theta_{\text{jet}}$ between the parton three-momenta $\vec{p}$ and the jet axis for cascade partons in the different effective models of jet-medium interaction and the vacuum. For these results, the same parton cascades as for Fig. 3.7 were used.

that of light particles, one has to note that the heavy quark energy has to be at least as large as its mass. For charm quarks in the current system the mass scale $m_c \approx 1.5$ GeV corresponds to $\xi \approx 2.6$. In comparison with the light parton cascades it becomes evident that, if one neglects softer particles, much of the large differences in the peaks of the distributions at large ξ are neglected as well. Thus, one can argue that, while it is possible to distinguish the different energy loss mechanism for light quarks by means of the corresponding humped-back plateau distributions, the same cannot be stated automatically for the energy loss mechanisms of heavy quarks. In particular, if one considered also different temperature scales (represented by different ΔQ^2 values in the effective models) the distributions for hard particles might even become indistinguishable. However, these questions will not be studied in this sub-subsection, but in more detail later on, by means of estimations of the nuclear modification factor in sub-subsection 3.5.1.5 for the charged particles (where one can still argue that the different energy-loss mechanisms can be identified via their soft particle yield) and in sub-subsection 3.5.2.1 for heavy quarks.

3.5.1.4 Single angular distribution

In this sub-subsection the distributions over the angle $\Delta\theta_{\text{jet}}$, defined as the angle between the directions of cascade particle three momenta $\vec{p}$ with the jet axis are investigated. These distributions simultaneously reflect the medium effects on $p_{\parallel\,\text{jet}}$ and $p_{\perp\,\text{jet}}$ that were shown in Fig. 3.9. In particular, studying $\frac{dN}{d\Delta\theta_{\text{jet}}}$ permits to understand, whether the enhancement of $\frac{dN}{dp_{\perp\,\text{jet}}}$ that is observed for the models that include radiative energy loss at small $p_{\perp\,\text{jet}}$ values corresponds to additional soft or additional collinear radiation. Fig. 3.11 shows results of these angular distributions for the models of jet medium interaction, and the vacuum. While the left panel represents the distributions obtained from all particles in their final states, the middle panel considers only the ones with $\|\vec{p}\| < 2$ GeV, the right panel the remaining harder particles.

In general, for very small angles the distributions rise steeply, a behavior that originates from the $\sin(\Delta\theta_{\text{jet}})$ factor of the phase space volume element, peak at a small angle and decrease monotonously until π.

In particular in the left panel, one observes that the distribution for cascades in the vacuum reaches its maximum at the smallest angles, compared to the distributions for any of the three effective models of jet-medium interaction, and falls off the fastest. Therefore, for the models simulated, broadening of the jet cone, due to jet-medium interactions has been verified numerically.

As the distributions for (components of) parton momenta before, the angular distributions have been normalized to the mean number of particles produced per cascade $\langle n\rangle$, i.e.:

$$\int_0^{\pi} \frac{dN}{d\Delta\theta_{\text{jet}}} d\Delta\theta_{\text{jet}} = \langle n\rangle \,. \tag{3.25}$$

Thus, it is visible in the left panel, that, in general, more particles have been radiated in the inelastic model and in the hybrid models than in the vacuum, and that these enhancements occur at large angles (leading to angular broadening), as well as at small angles (increase of intra-jet radiation). On the other hand, for the elastic model, radiation is largely suppressed at small angles. In case of the inelastic model and hybrid models the additional radiation accounts also for the broadening of the distribution compared to the vacuum case, while for the purely elastic model such a broadening effect can – per definition of the model – only occur due to deflections of the cascade particles. Indeed, one observes that more particles are radiated at larger angles, while small angle radiation has been suppressed.

Particle cascades in the hybrid model C are subjected to both, medium-induced radiation as well as to a drag force, parallel to the incident parton momenta. Both effects lead to angular broadening: Due to the former effect, cascade partons undergo on average a larger number of successive splittings (as compared to the vacuum), which allow the accumulation of larger angles between the parton momenta and the jet axis. The latter effect of the drag force leads to a decrease in the parton three-momenta, cf. Eq. (3.20). Due to momentum conservation throughout parton branchings one can expect that components of the radiated partons parallel to the decaying partons are smaller than for the vacuum case, while the transverse components remain the same. By consequence, branching angles are large in models that contain a drag force. These behaviors of the hybrid model C are well reflected in the left panel of Fig. 3.11: For large angles one observes a larger enhancement of the vacuum distribution than for the purely elastic and the purely inelastic effective models alone. This behavior can be interpreted as a signal that radiative energy loss combined with a drag force add up to an even higher broadening effect. An even higher angular broadening can be achieved, if the jet-medium interactions contain, in addition to radiative energy loss and the drag force, also stochastic transverse force, as it can be seen from the angular distribution for model D.

If one studies the contributions to the angular distribution from either soft partons, where $\|\vec{p}\| < 2$ GeV (middle panel of Fig. 3.11), or hard partons, where $\|\vec{p}\| \geq 2$ GeV (right panel of Fig. 3.11) one observes for the three effective models that simulate radiative energy loss that most of the additionally radiated particles are soft, i.e.:$\|\vec{p}\| < 2$ GeV. In particular for models A and C, the enhancement at large angles is almost entirely due to soft particles – a behavior that is consistent with a picture of jet-shapes that has been deduced from experimental data [137, 138]. While for model D also the contributions to the angular distribution from hard partons are enhanced at large angles, for soft particles the enhancement is much larger. For the purely elastic model the discrepancies in the contributions to the angular distribution for soft and hard partons are not as large as for the models that simulate radiative energy loss. For hard partons a residual enhancement for larger angles can still be observed, while the distributions for model C lies even inside the distribution for cascades in the vacuum and those for the inelastic effective model are only slightly enhanced. However, as previously mentioned, the enhancement for model D is considerably larger than those for the purely inelastic model A and model C. Except for the different behaviors at small angles the distributions for model B and D are almost identical. These findings for the hybrid model D are consistent with the discussion of the $p_{\perp\ \mathrm{jet}}$ distribution shown in Fig. 3.9: Analogously it is argued now that at soft energy and momentum scales the number of radiated particles is largely increased, compared to the vacuum, similar to the behavior of cascades in the inelastic effective model, while for hard particles the angular distribution observes a broadening, similar to that observed for the elastic effective model.

Summarizing, one can deduce the following overall picture for the effects of the different effective medium models on the cascade evolutions in momentum space:

- In the effective models A and C the parton cascades contain a large amount of additional soft particles, radiated at all angles (in comparison to cascades in the vacuum). The harder the radiated partons, the more they are focused around the jet axis. However, the emission of hard particles is suppressed.

- In the effective model B for collisional energy loss (without medium induced radiation) parton cascades contain fewer soft particles than in the effective models for radiative energy loss. Due to numerous deflections within the medium, the generally harder particles are radiated at an on average larger angle towards the jet axis. Compared to cascades in the vacuum, directions close to the jet axis are depleted with particles that are redistributed towards directions with larger angles to the jet axis. This effect occurs at all of the investigated energy scales. Thus, the hard particles are less focused around the jet axis than it was the case for models A and C.

- Parton cascades in model D reflect a combination of both of the above behaviors: A large amount of additional soft partons is emitted at all angles, due to processes of medium-induced radiation. Thus, the production of hard particles is suppressed. The remaining hard partons are less focused around the jet-axis than those in models A and C or cascade partons in the vacuum.

3.5.1.5 Charged particle nuclear modification factor

A suitable observable for the study of the dependence of parton-energy loss in the medium is the nuclear modification factor R_{AA} (for the definition cf. Refs. [16, 17, 19] or subsection 1.2.1, which defines R_{AA} completely analogously for heavy quarks.). In this subsubsection an approximation for the nuclear modification factor of charged particles is obtained for the different effective medium models and subsequently used to study the dependence of the in-medium parton-energy loss on the parameter ΔQ^2, which characterizes the strength of jet-medium interactions. Using R_{AA} as a measure of in-medium parton-energy loss has the particular advantage that the systematic uncertainties in the particle yields obtained from either heavy ion or pp collisions can be expected to cancel each other in their ratio.

Since the parton cascade evolution has not yet been convoluted with the underlying events of hadronic collisions and, therefore, the incoming degrees of freedom are not known, it is not possible to obtain a nuclear modification factor that strictly follows the definition in Eq. (A.1). However, approximations to R_{AA} can be made nevertheless: It is assumed that in pp and heavy ion collisions parton cascades are produced, which are initiated by a quark of a certain maximal virtuality $Q_{\uparrow}$ and energy E_{ini}. In this simplifying approach it is also assumed that both scales are the same for cascades produced in pp and in heavy ion collisions. Thus, also initial state effects are neglected in this approach. Consequently, the nuclear modification factor R_{AA} can be approximated by the ratio of the particle yield of parton cascades in the medium to the one in the vacuum, which is referred[15] to as $R_{\mathrm{MV}}(\|\vec{p}\|)$ throughout the remainder of this thesis, and is defined as

$$R_{\mathrm{MV}}(\|\vec{p}\|) := \frac{\left(\frac{dN}{d\|\vec{p}\|}\right)_{\mathrm{medium}}}{\left(\frac{dN}{d\|\vec{p}\|}\right)_{\mathrm{vacuum}}} \,. \tag{3.26}$$

In this approximation the nuclear modification factor of charged particles is approached by considering every final particle in the medium and vacuum cascades. The parton momentum distributions $\frac{dN}{d\|\vec{p}\|}$ for the medium and the vacuum were used before in subsubsection 3.5.1.2 to directly study in-medium parton-energy loss. As indicated before, their ratio, Eq. (3.26), is independent of global normalization factors (an ambiguity/systematic uncertainty of the distributions $\frac{dN}{d\|\vec{p}\|}$). By its definition R_{MV} represents the medium effects on the $\|\vec{p}\|$ distributions, and allows to study in particular the importance of ΔQ^2.

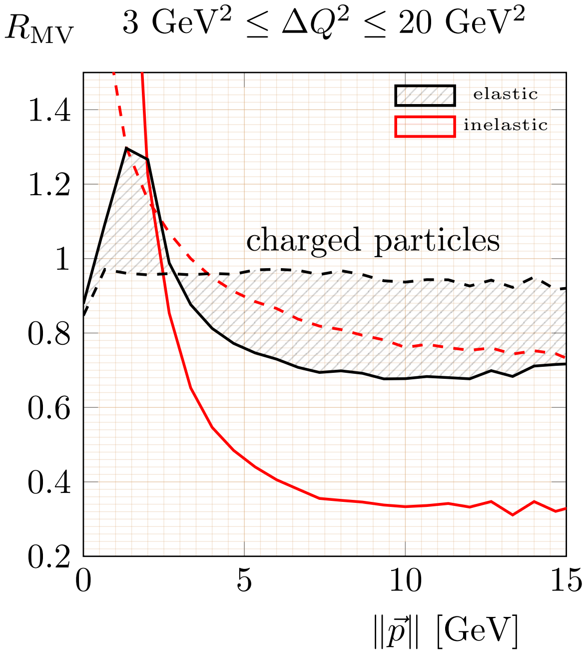

Figure 3.12: The approximation R_{MV} to the nuclear modification factor R_{AA}, for the cascade partons in their final state obtained from parton cascades simulated by Monte-Carlo implementations of (vacuum) parton branchings and the elastic and inelastic effective models of in-medium parton propagation. The cascades are initiated by a quark with $Q_{\uparrow} = E_{\mathrm{ini}} = 20$ GeV and evolve down to scales $Q_{\downarrow} = 0.6$ GeV. The results shown correspond to ranges in ΔQ^2 of different jet-medium interaction strengths between $\Delta Q^2 = 3$ GeV^2 (dashed lines) and $\Delta Q^2 = 20$ GeV^2 (solid lines).

Fig. 3.12 shows R_{MV} for different values of ΔQ^2, i.e.: 3 GeV^2 ≤ Q^2 ≤ 20 GeV^2. In general, one can observe a suppression, $R_{\mathrm{MV}} \leq 1$, for high $\|\vec{p}\|$ (in Fig. 3.12 this scale is around $\|\vec{p}\| \approx 3$ GeV) and an enhancement, $R_{\mathrm{MV}} \geq 1$ for small $\|\vec{p}\|$. For the same ΔQ^2 values the medium effects seem to be stronger for the inelastic effective model than for the elastic one. However, at large $\|\vec{p}\|$ the same R_{MV} values can be obtained from either the elastic or the inelastic effective model. Since the corresponding ΔQ^2 values are found

---

[15] The new notation R_{MV} – where the subscript stands just for "Medium to Vacuum" – is introduced, in order to distinguish this function from theoretical results that contain the aforementioned additional effects.

to be considerably different, this implies that the same R_{MV} values can be associated to different types of jet-medium interactions either $2 \to 2$ scatterings at high ΔQ^2 scales or medium-induced radiation at lower ΔQ^2 scales. This conclusion is consistent with corresponding observations above in sub-subsection 3.5.1.3 for the humped-back plateau distributions, where, at sufficiently hard parton-energy scales, the different mechanisms yield comparable results.

Especially the inelastic effective model (cf. Sec. 3.1) was mainly motivated by an early version of YaJEM [105]. In Refs. [105, 139] R_{AA} was obtained in models that used a transport coefficient $\hat{q}$ that was fixed up to a global multiplicative factor K[16]. This factor K was used to fit the R_{AA} results to experimental data from PHENIX [140]. Compared to the results from Refs. [105, 139] the results for R_{MV} obtained within the inelastic effective model shows the same qualitative behavior of small monotonous decreases for increasing scales of parton momentum above $\|\vec{p}\| = 5$ GeV. However, the results for R_{MV} are considerably larger than the results from Refs. [105, 139], and also larger than the experimental values from PHENIX. On the other hand, it should be emphasized that analogous to the fit by Renk, the nuclear modification factor can probably be reproduced by means of a fit with R_{MV} obtained from the inelastic effective model[17], where the parameter ΔQ^2 is used as a free parameter (instead of K).

3.5.2 Heavy particle observables

3.5.2.1 Heavy particle nuclear modification factor

This sub-subsection provides an approximation for the nuclear modification factor of heavy quarks (and the resulting mesons) that is obtained from the currently implemented Monte-Carlo simulations (in the vacuum and the effective medium models of Secs. 3.1, 3.2, and 3.3). As Ref. [28] notices, different types of jet-medium interactions can yield the same R_{AA} values for different scales of the coupling between heavy quark-jet and medium particles (i.e. the parameter ΔQ^2 in the context of the effective models of this thesis). Thus, it is the main goal of this chapter to learn about the dependence of heavy quark suppression on the parameter ΔQ^2 (cf. the previous sub-subsection 3.5.1.5 for the analogous study for charged particles) and to check within our framework, whether different effective models can yield comparable results for heavy flavour R_{AA}, if ΔQ^2 is varied.

As it was already shown in subsections 1.2.3 and 1.2.4 numerous models, based on both collisional as well as a combination of collisional and radiative energy loss, reproduce the R_{AA} reasonably well. Here, it is verified that the purely radiative model of Sec. 3.1, and the purely collisional model of Sec. 3.2 can yield the same estimation of R_{AA}.

As before for the estimation of the nuclear modification factor of charged particles in the previous sub-subsection 3.5.1.5 the heavy quark R_{AA} is approximated by a ratio R_{MV} of parton-momentum distributions in the medium and the vacuum, analogous to Eq. (3.26), with the only difference that instead of all final cascade partons, only heavy quarks contribute to the distributions $\frac{dN}{d\|\vec{p}\|}$[18]. Again, following the argument of subsection 1.4.1, the explicit dependencies of the cascade evolution on the heavy quark mass were neglected.

---

[16] While $\hat{q}$ relies on a hydrodynamical model and depends on the path of a particle in the medium, the function $\hat{q}_R$ (cf. Eq. (3.2)) represents a fit from Ref. [105] for a particular trajectory.

[17] The argument behind this statement is that both R_{MV} and R_{AA} behave qualitatively in the same way, also with regard to variations of the parameters ΔQ^2, or K, respectively.

[18] In this context, the present estimation of R_{AA} corresponds also to the study of heavy quark momentum distributions, which was suggested in the upper right quarter of Fig. 3.5.

Instead, parton cascades were initiated by quarks, which were considered as heavy quarks. In their final states these quarks were used for the calculation of R_{MV}.

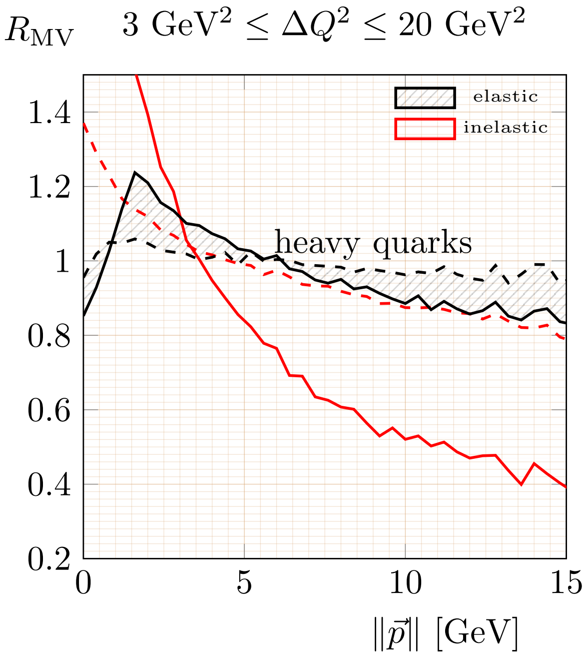

Figure 3.13: The approximation R_{MV} to the nuclear modification factor R_{AA}, for the initial quark in its final state obtained from parton cascades simulated by Monte-Carlo implementations of (vacuum) parton branchings and the elastic and inelastic effective models of in-medium parton propagation. The cascades are initiated by a quark with $Q_{\uparrow} = E_{\mathrm{ini}} = 20$ GeV and evolve down to scales $Q_{\downarrow} = 0.6$ GeV. The results shown correspond to ranges in ΔQ^2 of different jet-medium interaction strengths between $\Delta Q^2 = 3$ GeV^2 (dashed lines) and $\Delta Q^2 = 20$ GeV^2 (solid lines).

Fig. 3.13 presents some results for the heavy quark R_{MV} for both the purely elastic and inelastic models, each for ΔQ^2 values in the range 3 GeV^2 $\leq \Delta Q^2 \leq$ 20 GeV^2. Compared to experimental values of R_{AA} (cf., e.g., Figs. 1.3 and A.2), the R_{MV} values shown in Fig. 3.13 are too high. One can explain this difference by the fact that the currently employed effective models subject the cascade partons to interactions with the medium, only as long as they are off-the-mass-shell. Thus, the results in Fig. 3.13 represent the contribution to increased energy loss in the medium, stemming from off-shell particles, while a more realistic approximation of R_{AA} can be obtained, if one includes interactions between on-shell heavy quarks with medium particles (the same statement applies to the interactions of cascade and medium particles for the nuclear modification factor of charged particles).

The R_{MV} values for the effective model of collisional energy loss are, in general, higher than those for the effective model of radiative energy loss. However, for the collisional model with $\Delta Q^2 = 20$ GeV^2 and the radiative model with $\Delta Q^2 = 3$ GeV^2 the curves obtained for R_{MV} are close to one another for momentum scales above $\|\vec{p}\| \approx 5$ GeV. While the corresponding values of the modification factor R_{MV}, are more than twice as large as experimental values for R_{AA} one can argue that one would obtain more reasonable values, if one considered models that include also the jet-medium interactions of on-shell particles.[19] For small $\|\vec{p}\|$ values one obtains considerable differences between the results

---

[19] It is in fact possible to obtain quantitatively reasonable approximations to R_{AA} from the type of effective models presented in this chapter. However, these results demanded the constructions of new, but similar models. This is why these R_{AA} approximations are rather discussed in Chap. 5, for the sake of conciseness in this chapter.

from the different models, however, these scales are of the order of the charm mass of $m_C \approx 1.5$ GeV or below. The explicit effects of the quark mass in parton fragmentation might play a significant role at these small momentum scales, while they can be neglected at higher $\|\vec{p}\|$ values. The same statement can be made for the effects of thermalization within the medium and hadronization, which also have not yet been included in the Monte-Carlo algorithms.

3.5.2.2 Angular correlations $\frac{dN}{d\Delta\phi_{H\bar{H}}}$ of $Q\bar{Q}$ pairs in back to back emissions

In order to study the in-medium deflections of the initial quarks of jets one can investigate angular correlations between the three-momenta of heavy hadron pairs, originating from the back-to-back emission of heavy quark-antiquark pairs. Since, these initial quarks of the cascade represent leading particles of the cascades, which contain most of their energy and, thus, of the jet-momenta over long distances – a behavior that is even stronger for massive quarks, due to the additional suppression of parton radiation due to the deadcone effect– these heavy particle correlations also represent a measure of the deflection of the entire heavy quark jets.

The investigated correlations are $\frac{dN}{d\Delta\phi_{H\bar{H}}}$, where the $\Delta\phi_{H\bar{H}}$ are defined as the differences between the azimuthal angles ϕ_H of the hadron H originating from a heavy quark, and that of the hadron stemming from the corresponding antiquark $\phi_{\bar{H}}$. The azimuthal angles are defined as polar angles of the particle three-momentum projections on a plane orthogonal to the beam axis of the initially colliding heavy ion pairs.

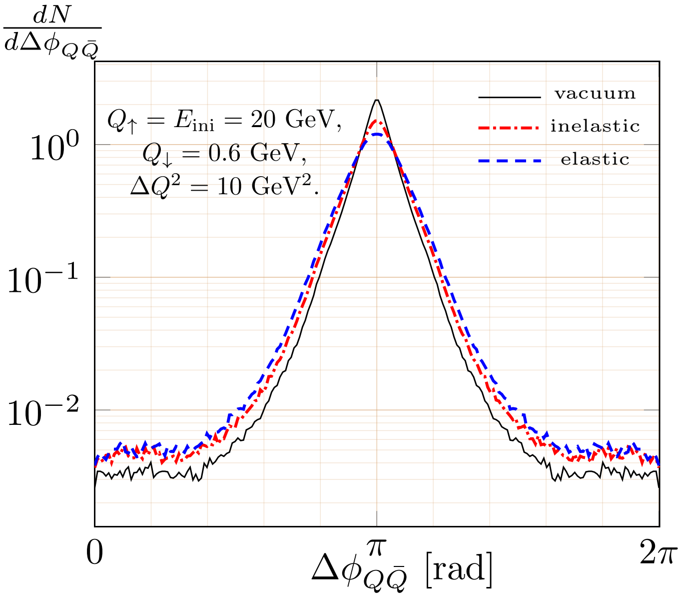

Figure 3.14: Distribution of the differences $\Delta\phi_{Q\bar{Q}}$ between the azimuthal angles of an initially back-to-back emitted quark antiquark pair after propagation of both of the partons of the pair in either the vacuum or a medium. Each of the initial quarks can form parton cascades as indicated on the left side of the legend. In the medium, they are also subjected to either collisional or radiative jet-medium interactions, as indicated on he right side of the legend.

Using the effective models of jet-medium interaction one can obtain estimations for the correlations $\frac{dN}{d\Delta\phi_{H\bar{H}}}$: From the simulated sets of parton cascades pairs were formed, where the initial quarks of the cascades propagate antiparallel to one another. Instead of the pair of heavy mesons H and $\bar{H}$, pairs of these initial quarks in their final states were correlated by calculation of the differences in their azimuthal angles $\Delta\phi_{Q\bar{Q}}$. The azimuthal angles were obtained in this estimation in the following way[20]: The momenta of the heavy quark and anti-quark, both in their final states were projected onto a plane parallel to the jet axis. The azimuthal angle $\Delta\phi_{H\bar{H}}$ was then defined as the angle between those directions. The jet axis was defined as parallel (anti-parallel) to the direction in which the initial heavy quark (anti-quark) of the cascade was emitted.

Some examples of the resulting distributions $\frac{dN}{d\Delta\phi_{Q\bar{Q}}}$ are shown in Fig. 3.14. Already for the particles in the vacuum there is a considerable number of parton pairs that are deflected from their initial back-to-back propagation, i.e.: $\Delta\phi_{Q\bar{Q}} = \pi$. The reason for this broadening are the parton branchings in vacuum. Nevertheless, one still observes a large peak around $\Delta\phi_{Q\bar{Q}} = \pi$. This behavior is only slightly affected by jet-medium interactions which amount to an additional suppression of the peak and a simultaneous broadening of the distributions. Thus, the overall behavior is that of a pair of leading particles that are only slightly deflected by jet-medium interactions. In Fig. 3.14 there cannot be observed large differences between the distributions obtained from cascades subjected to collisional and radiative energy loss. The broadening effect seems to be slightly larger for the elastic than for the inelastic effective model. The latter also leads to a larger peak at $\Delta\phi_{Q\bar{Q}} = \pi$. A tentative explanation of the differences could lie in the fact that in the elastic effective model (off-shell) jet-particles are always deflected by a stochastic transverse force, while in the additional parton branchings of the inelastic effective model a huge contributions stems from collinear parton splittings.

Some results for $\frac{dN}{d\Delta\phi_{H\bar{H}}}$ of $b\bar{b}$ and $c\bar{c}$ quark pairs, were also obtained in Refs. [81, 141]. There, a sizable peak around π – i.e.: back-to-back correlations was obtained for the higher parton momenta in the ranges [4, 10] GeV and [10, 20] GeV. However for small momentum scales below 4 GeV, the distribution around a maximum at π is completely flattened out and isotropized. These tendencies shown in Ref. [141] for $\frac{dN}{d\Delta\phi_{H\bar{H}}}$ have been verified also for the corresponding distributions obtained from the purely elastic and inelastic effective models via the currently implemented version of the Monte-Carlo Algorithm.

3.6 Conclusion and Perspectives

From the introduction in Chap. 1 it follows that there are up to now two main types of energy loss mechanisms for hard jet-partons (in particular heavy quarks) in the medium, collisional and radiative scattering processes. While both processes can act simultaneously on propagating partons in the medium, their contributions to the total energy loss has not yet been determined. Currently available experimental data (cf. Sec. 1.2.4) allow for numerous different possibilities to combine the two effects.

In order to clarify this issue, in Secs. 3.1 to 3.3 effective models for collisional and radiative energy loss, as well as a hybrid model were introduced. The main purpose of these models is to study directly, how different types of jet-medium interactions are reflected in observables and if it is possible to distinguish between their contributions. For a description of the medium modifications of jets, the models were discretized with regard to time and implemented on top of the already existing Monte-Carlo algorithm for cascades in the vacuum outlined in Chap. 2. The effective model of radiative energy loss is based on the YaJEM approach [105], which is then modified to account also for collisional energy loss (in the other models).

Before these effective models of jet-medium interactions are used in the study of the mechanisms of energy loss, it is necessary to verify, that they reproduce – at least qualita-

---

[20] This definition of the azimuthal angles is explained in more detail and justified later on in Sec. 4.1.

tively – the observed phenomenology of jets in the medium. To this end, parton cascades with $Q_{\uparrow} = E_{\text{ini}} = 20$ GeV were examined. The observed medium effects on the jet-phenomenology are not expected to change qualitatively for different values of $Q_{\uparrow}$ and E_{ini}, since the implemented effective jet-medium interactions do not depend explicitly on neither $Q_{\uparrow}$ nor E_{ini}.

	T, T_{maj}, T_{min}	$\lVert\vec{p}\rVert$, $p_{\parallel\,\text{jet}}$	$p_{\perp\,\text{jet}}$	$\Delta\theta_{\text{jet}}$	$\Delta\phi_{Q\bar{Q}}$
model A	$\longleftrightarrow$	$\boldsymbol{\uparrow}\downarrow$	$\boldsymbol{\uparrow}\downarrow$	$\uparrow\longleftrightarrow$	$\downarrow\uparrow$
model B	$\longleftrightarrow$	$\approx$	$\downarrow\uparrow$	$\downarrow\uparrow$	$\downarrow\uparrow$
model C	$\longleftrightarrow$	$\boldsymbol{\uparrow}\downarrow$	$\boldsymbol{\uparrow}\downarrow$	$\uparrow\longleftrightarrow$	
model D		$\boldsymbol{\uparrow}\downarrow$	$\uparrow\longleftrightarrow$	$\uparrow\longleftrightarrow$	

Table 3.3: Medium effects on distributions $\frac{dN}{dx}$, where x is one of the variables T, T_{maj}, T_{min}, $\lVert\vec{p}\rVert$, $p_{\parallel\,\text{jet}}$, $p_{\perp\,\text{jet}}$, $\Delta\theta_{\text{jet}}$, $\Delta\phi_{Q\bar{Q}}$ in the different effective models. ↑ symbolizes an increase, ↓ a decrease, and ≈ no apparent change of the distributions. $\boldsymbol{\uparrow}\downarrow$ ($\downarrow\uparrow$) means increases (decreases) of the distributions for small values of the variable with the opposite effect at large values. Broadening of the distributions is indicated by the symbols $\longleftrightarrow$. The effects on $\frac{dN}{d\xi}$ are here represented by the behavior of $\lVert\vec{p}\rVert$. For $\Delta\theta_{\text{jet}}$ large effects occur for models A, C, and D at small energy scales, but are strongly suppressed at large scales.

Medium effects on jet-phenomenology (expressed as the number distributions of observables for single cascade particles) have been summarized in Tab. 3.3: The thrust distributions of the cascades in the medium and the vacuum in Fig. 3.6 verify that the simulated parton cascades experience angular broadening in the purely elastic and inelastic models as well as the hybrid model C. Figs. 3.8 to 3.11 show that at small angles, radiation is enhanced in the models that contain radiative energy loss (while increased activity is also visible at higher angles). Fig. 3.10 verifies that, in general, in the medium the individual partons lose more energy during the cascade evolution than in the vacuum. This is true for the models that involve medium-induced parton branchings. For the elastic effective model, hard particles lose energy, while soft particles can also gain energy due to the transverse forces. Since, however, the latter phenomenon occurs at small energy scales of the order of the temperature T, cf. Eq. (3.19), the energy loss mechanism dominates for sufficiently hard cascade partons. Angular broadening (of cascade-parton three-momenta with regard to the jet axis) was shown in Fig. 3.11. Fig. 3.14 finally shows that the initial (heavy) quarks experience (compared to the initial quarks in the vacuum), in the medium a slight additional deflection with regard to their initial direction of propagation.

Sub-subsection 3.5.1.4 obtained the following qualitative image of jets that interact with the medium within the framework of the three effective models: Processes of medium-induced radiation account for an additional production of soft particles, that propagate at small as well as at large angles with the jet axis. While on average fewer hard particles remain, their directions of propagation are mostly the same as for cascades in the vacuum. On the other hand, if the jet-medium interactions are entirely described by the effective model for collisional energy loss, the number of emitted soft particles does not increase. However, the emission of hard particles is less focused and occurs also at larger angles.

After a study of the properties of the different effective models the following property was encountered in sub-subsection 3.5.2.1: For heavy particles the different energy loss mechanisms cannot necessarily be distinguished by the nuclear modification factor R_{AA}. For light cascade partons in the medium this problem did not occur, since Figs. 3.10 and 3.12 showed that for soft particles, sets of cascades undergoing additional radiative processes can be distinguished fairly well from jets subjected to collisional processes only.

However, as was argued in Chap. 1, heavy quark cascades would provide a more suitable probe for the medium of QGP, as heavy quarks do not thermalize throughout their in-medium propagation and due to the high energy threshold necessary to produce a heavy quark antiquark pair they are most likely created at the initial stages of heavy ion collisions. For the nuclear modification factor R_{AA} (in this chapter estimated via the factor R_{MV} cf. Eq. (3.26)), differences between effective models can be absorbed in the ΔQ^2 parameter. In particular, in some cases the same suppression behavior can be achieved either by means of radiative energy loss in a medium that is described via a small ΔQ^2 parameter, or by means of collisional energy loss in media with large ΔQ^2 values.

Consequently, the following chapter will perform a search for observables that allow to discriminate between the different mechanisms of (heavy) parton in-medium energy loss. This study will be focused mainly on two particle correlations between the initial quark of a (heavy) quark jet and a light parton. Not only can it be argued that the corresponding particle pairs are created in branchings inside the medium – and, thus, allow for further studies of the in-medium evolution of the jet; also the number of light partons that can be correlated with the initial quark largely depends on the type of model used. Therefore, two particle correlations are a quite promising tool to study jet-medium interactions.

Chapter 4

Two particle correlations

This chapter discusses two-particle correlations between a heavy and a light particle as a means to study medium effects on the evolution of heavy-quark jets. Particular emphasis will be laid on the phenomenon of angular broadening, which is investigated via angular correlations. In order to distinguish different mechanisms of in-medium parton-energy loss – more specifically elastic and inelastic jet-medium interactions, the dependencies of angular two-particle correlations on the absolute values of parton three-momenta $\|\vec{p}\|$ is studied in detail. The different types of jet-medium interactions were simulated via the effective models of the previous chapter 3.

4.1 Introduction of the Distributions used

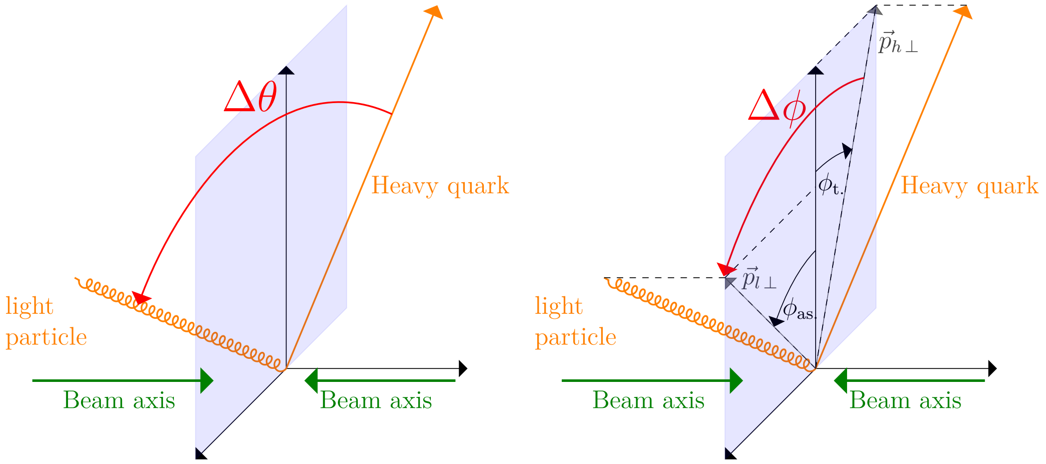

Figure 4.1: Angle $\Delta\theta$ (left panel, red arrow) and azimuthal angle $\Delta\phi$ (right panel, red arrow): They are given (in each case) via the three-momenta of a heavy trigger particle (orange line) and a light associated particle (orange spring). The vertical axis (black arrow) is the direction of the three-momentum of the initial heavy quark of the cascade, with angles (curved black arrows) $\phi_{\text{t.}}$, and $\phi_{\text{as.}}$ towards the projections (gray arrows in the right panel) $\vec{p}_{h\perp}$, and $\vec{p}_{l\perp}$ of the heavy (h) and light (l) parton momenta.

This section explains how two-particle correlations were extracted from the cascades simulated by the Monte-Carlo algorithm of Chaps. 2 and 3.

For the distributions of the two-particle correlations a definition is used that corresponds well to the experimental treatment of jets, where a trigger particle is associated to another particle (i.e. in the scope of heavy-light particle correlations, a heavy trigger particle and a light associated particle) that was produced in the pp or heavy ion collision (cf. Sec. 1.3). For the two-particle correlations shown in this chapter, parton cascades were initiated by a quark, which was identified as the heavy particle[1]. In its final state this initial quark is correlated with another (light) parton of the cascade, which is also considered only in its final – on-the-mass-shell – state.

Since they represent observables that are currently measured, or that will be obtained experimentally in the near future (cf. Sec. 1.3), and since they reflect directly the medium effect of angular broadening of the jet, this thesis particularly emphasizes angular two-particle correlations. They can be defined as the distribution

$$\frac{1}{N_{\mathrm{casc.}}}\frac{dN}{d\alpha}\,, \tag{4.1}$$

of the number of heavy-light particle pairs N over an angle α, which is given by the directions of the three-momenta of the heavy and the light particle, normalized by the number of simulated cascades[2] $N_{\mathrm{casc.}}$. The definitions for different choices of the angle α are illustrated in Fig. 4.1, for the angle $\alpha = \Delta\theta$ (left panel) and azimuthal angle $\alpha = \Delta\phi$ (right panel): The angle $\Delta\theta$ is defined as the angle between the directions of the three momenta of the heavy and the light particle, $\vec{p}_h$ and $\vec{p}_l$, respectively, i.e.:

$$\cos(\Delta\theta) := \frac{\vec{p}_h \cdot \vec{p}_l}{\|\vec{p}_h\|\|\vec{p}_l\|}\,. \tag{4.2}$$

Number distributions over $\Delta\theta$ show a behavior proportional to $\sin(\Delta\theta)$ at small angles.[3] This dependence is only due to the fact that the (infinitesimal) phase-space volume-elements of the heavy-light particle pairs are proportional to $\sin(\Delta\theta)$. In order to get rid of such a behavior of non-dynamic origins the distributions $\frac{1}{N_{\mathrm{casc.}}}\frac{dN}{d\cos(\Delta\theta)}$ can be considered instead of the distributions over $\Delta\theta$.

In the experiment, angles ϕ are obtained as azimuthal angles around the beam axis (cf., e.g., Refs. [142, 143]). The difference $\Delta\phi := \phi_{\mathrm{t.}} - \phi_{\mathrm{as.}}$ between the azimuthal angles of the trigger and associated particles, $\phi_{\mathrm{t.}}$ and $\phi_{\mathrm{as.}}$, respectively is then used to obtain the corresponding (azimuthal) angular two-particle correlations, following the definition of Eq. (4.1). In this chapter the angle $\Delta\phi$ was obtained from the Monte-Carlo simulated cascades by means of a projection of the three-momenta $\vec{p}_h$ and $\vec{p}_l$ on the plane orthogonal to the beam axis. From these projections, $\vec{p}_{h\perp}$ and $\vec{p}_{l\perp}$, respectively, one can then obtain the angle $\Delta\phi$, which is defined as

$$\cos(\Delta\phi) := \frac{\vec{p}_{h\perp} \cdot \vec{p}_{l\perp}}{\|\vec{p}_{h\perp}\|\|\vec{p}_{l\perp}\|}\,. \tag{4.3}$$

In contrast to the momenta $\vec{p}_h$ and $\vec{p}_l$, their projections $\vec{p}_{h\perp}$ and $\vec{p}_{l\perp}$ are distributed over a plane, rather than three-dimensional momentum space: Thus, there does not occur any additional – non-dynamical – dependence on the angle $\Delta\phi$ in its number distribution. Since the underlying heavy ion collision has not yet been simulated in the current version of the Monte-Carlo algorithm of Chaps. 2 and 3, the beam axis is not known for the simulated parton cascades. Thus, the simplifying assumption was made that the initial particle of a jet is emitted orthogonal to the beam axis (which is, in addition, always the

---

[1] Even though explicit mass dependencies were not included in the Monte-Carlo algorithm: cf. Sec. 1.4.1 for a justification of this approximation.

[2] For the current choice of trigger $N_{\mathrm{casc.}} = N_{\mathrm{trig.}}$. Thus, in Eq. (4.1) the same normalization is used as for the experimental results introduced in Sec. 1.3 (cf. Eq. (1.15).).

[3] The same behavior occurs for the distributions over the angle $\Delta\theta_{\mathrm{jet}}$ between parton three-momenta and the jet-axis, shown in Fig. 3.11, due to the same reasons as outlined in the current section 4.1.

same direction for all simulated cascades). With this assumption, a direction orthogonal to the three-momentum of the initial quark was randomly selected and considered as the beam axis for all of the simulated cascades.

4.2 Angular broadening

In this section, angular broadening is studied for jets that undergo the different types of jet-medium interactions that are effectively described by means of the four different models introduced in Secs. 3.1 to 3.3. It is the goal of this kind of investigation to determine observables that allow to distinguish between processes of radiative and collisional in-medium parton-energy loss.

Before studying angular two-particle correlations the overall suppression or enhancement of parton production of jets in the medium is investigated: To this end, the number of parton pairs per cascade that contain the heavy trigger quark, N is shown in Tab. 4.1 for the different models of jet-medium interactions and vacuum cascades. N is also chosen as the normalization of the angular two-particle correlations that are presented in this chapter. A cut in the absolute value of the parton momentum was used: Either all parton pairs of a cascade were considered in the calculation of N, i.e.: $\|\vec{p}\|_{\text{cut}} = 0$, or only those, where the absolute values of the parton momenta of both particles are larger than $\|\vec{p}\|_{\text{cut}} = 2$ GeV. From Tab. 4.1 one can see that for all of the effective models and for the vacuum, most of the produced particle pairs contain at least one soft particle, i.e. a particle with a momentum $\vec{p}$ that satisfies $\|\vec{p}\| \leq 2$ GeV. In comparison to the number of hard particle pairs, where the absolute values of both momenta lies above 2 GeV, the numbers of produced soft particles vary greatly among different models and the vacuum. While for models that also involve medium-induced radiation the number of additionally radiated particles is largely increased, as compared to the numbers for vacuum cascades (by roughly a factor of 2 for the hybrid model C in case $Q_\uparrow = E_{\text{ini}} = 20$ GeV and by roughly a factor of 3 in all other cases), the numbers of partons produced in the purely elastic effective model B are approximately the same as in vacuum.

	N for $Q_\uparrow = E_{\text{ini}} = 20$ GeV and		N for $Q_\uparrow = E_{\text{ini}} = 40$ GeV and	
	$\|\vec{p}\|_{\text{cut}} = 0$	$\|\vec{p}\|_{\text{cut}} = 2$ GeV	$\|\vec{p}\|_{\text{cut}} = 0$	$\|\vec{p}\|_{\text{cut}} = 2$ GeV
vacuum	6.07	1.68	9.80	3.84
inelastic	19.35	1.20	30.39	3.45
elastic	5.63	1.47	9.80	3.34
model C	11.90	1.08	27.70	2.48
model D	18.21	1.03	28.34	2.99

Table 4.1: Number N of correlated parton pairs used for the angular two-particle correlations. In all simulations $Q_\downarrow = 0.6$ GeV was assumed. For the medium models only the results for $\Delta Q^2 = 10$ GeV^2 are shown.

Angular broadening can be studied by means of the distributions over $\Delta\theta$. These distributions allow to study angular correlations and, thus, broadening at large angles. However, as mentioned before, at very small angles $\Delta\theta \to 0$ a suppressing factor $\sin(\Delta\theta)$ appears, which stems from the volume element in spherical coordinates. On the other hand, for the simulated sets of cascades, the distribution $\frac{dN}{d\cos(\Delta\theta)}$ exhibits a very steep increase for $\Delta\theta \to 0$. Thus, this section proceeds as follows: First, the effects of jet-medium interactions on angular two-particle correlations are studied in subsection 4.2.1 via $\frac{dN}{d\cos(\Delta\theta)}$ in order to determine their behavior at large angles. By means of the average angles $\langle\Delta\theta\rangle$

the overall angular broadening in the different models is investigated and an observable to distinguish the models is proposed. Then, in subsection 4.2.2, azimuthal correlations for the same sets of parton pairs are studied, in order to investigate the increases and suppressions at small azimuthal angles $\Delta\phi$, which reflect also the corresponding behaviors of the $\Delta\theta$ distributions.

4.2.1 Angular two-particle correlations over $\Delta\theta$

A first investigation verified the phenomenon of angular broadening of parton cascades due to medium effects by means of angular two-particle correlations in the form $\frac{dN}{d\cos(\Delta\theta)}$, where the angle $\Delta\theta$ is the angle between the directions of the three-momenta of the heavy quark and an associated light cascade particle. Some results are shown in Fig. 4.2 for the inelastic, and elastic model, as well as for the hybrid models, each simulated for two different temperature profiles, represented by the corresponding values $\Delta Q^2 = 3\,, 10$ GeV^2 and compared to the correlations in vacuum[4]. The cascades simulated for this study evolve down to a scale of $Q_\downarrow = 0.6$ GeV, and are initiated by a quark of energy E_{ini} and maximal virtuality scale $Q_\uparrow$ of either $E_{\text{ini}} = Q_\uparrow = 20$ GeV (left panels) or $E_{\text{ini}} = Q_\uparrow = 40$ GeV (right panels).

The distributions for cascades in the vacuum with $E_{\text{ini}} = Q_\uparrow = 20$ GeV and $E_{\text{ini}} = Q_\uparrow = 40$ GeV exhibit the same qualitative behavior of a monotonous increase towards smaller angles, and, in the vicinity of $\cos(\Delta\theta) \to 1$, rising considerably more steeply towards its maximum. Furthermore, for each of the investigated models these distributions show with increasing jet-medium interactions the analogous changes for $Q_\uparrow$ and E_{ini} scales[5]. Furthermore, the presented results for the angular 2-particle correlations were obtained after the application of a cut of $\|\vec{p}\| \geq 2$ GeV on the parton cascades simulated via the Monte-Carlo algorithm. In the case of purely inelastic jet-medium interactions the distributions shown are suppressed at large angles. However, for elastic scatterings the correlations at large angles increase together with ΔQ^2. This enhancement has to be compensated by a suppression at small angles, since the overall parton production is slightly suppressed, as compared to the vacuum, cf. Tab. 4.1. Analogous observations can be made for model D.

Such a behavior can be interpreted as a redistribution of partons towards 3-momenta that show large angles $\Delta\theta$ with the heavy quark 3-momentum, due to medium effects. It represents, thus, a verification of angular jet-broadening. For the hybrid model C, similar to the purely inelastic effective model, one observes a depletion at large angles. In conclusion, models B and D are enhanced at large angles, model A and C suppressed. Since model D differs from model C only by the inclusion of the stochastic transverse force, one can argue that a stochastic transverse force leads to an enhancement at large angles. On the other hand, from the behavior of the distributions of model A it follows that medium-induced radiation leads to a suppression at large angles.

In model A, the medium induced parton branchings are effectively simulated via the same parton splitting functions that were also used for the description of parton cascades in the vacuum. By construction medium induced radiation is, thus, predominantly soft, while more realistic descriptions, such as, e.g. those given via the BDMPS approach, may result in the radiation of harder partons. However, it can be argued that the qualitative behavior of the obtained angular correlations will be that same in those models, since

---

[4] These two values of ΔQ^2 were chosen as a rough estimate for the temperature scales at the experiments at RHIC and LHC.

[5] Thus, only the results for one of the two cases, $E_{\text{ini}} = Q_\uparrow = 20$ GeV, are shown in the remainder of this chapter. However, the results for $E_{\text{ini}} = Q_\uparrow = 40$ GeV have been studied for comparison as well.

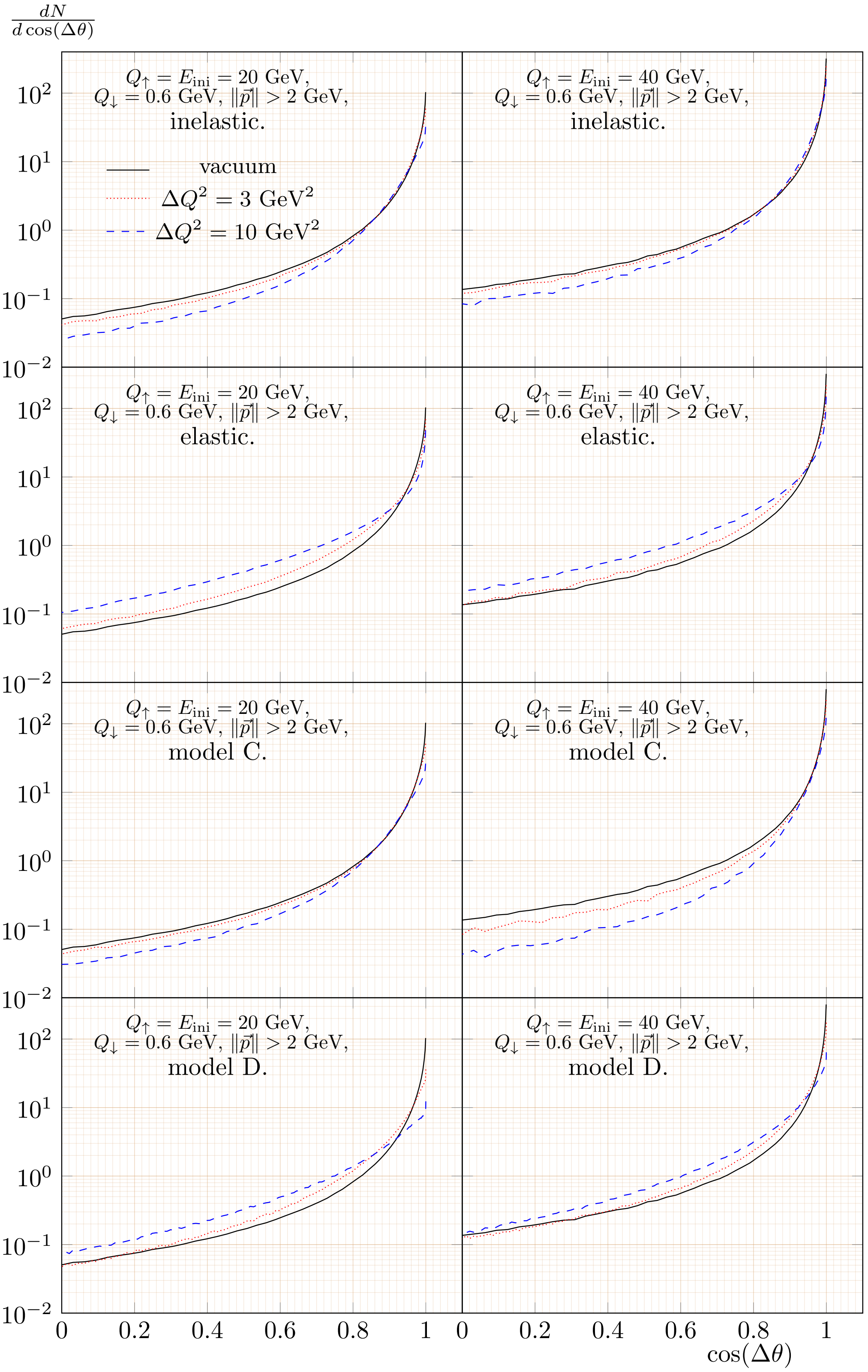

Figure 4.2: Angular correlations in the form of $\frac{dN}{d\cos(\Delta\theta)}$ between tagged heavy quarks and light partons from cascades initiated by the heavy quark of energy and maximal virtuality of either $E_{\text{ini}} = Q_\uparrow = 20$ GeV (left panels) or $E_{\text{ini}} = Q_\uparrow = 40$ GeV (right panels). Medium effects are shown for the inelastic (top panels), the elastic (middle panels), as well as the hybrid model C (bottom panels). Only angles between particles, where both particles satisfy $\|\vec{p}\| > 2$ GeV, were considered for the distributions shown.

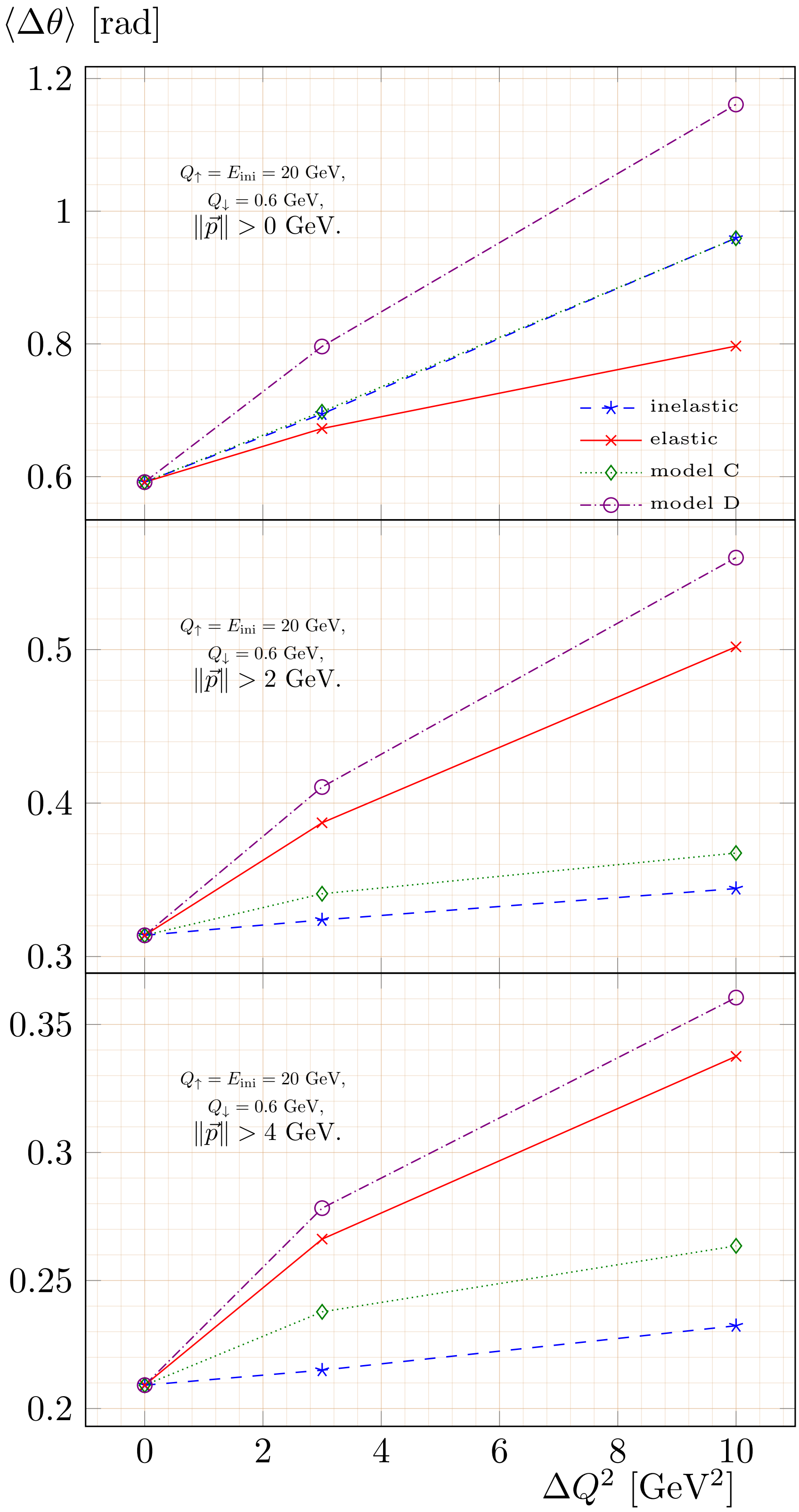

Figure 4.3: Mean values $\langle\Delta\theta\rangle$ of the angles $\Delta\theta$ between a heavy and a light cascade particle for $\Delta Q^2 = 0$, 3, and 10 GeV^2. For the results shown only those particle pairs were considered where both particles satisfy the conditions $\|\vec{p}\| > 0$, 2, and 4 GeV (upper, middle, and lower panel, respectively). The same cascades were used as for the $E_{\text{ini}} = Q_\uparrow = 20$ GeV results in Fig. 4.2.

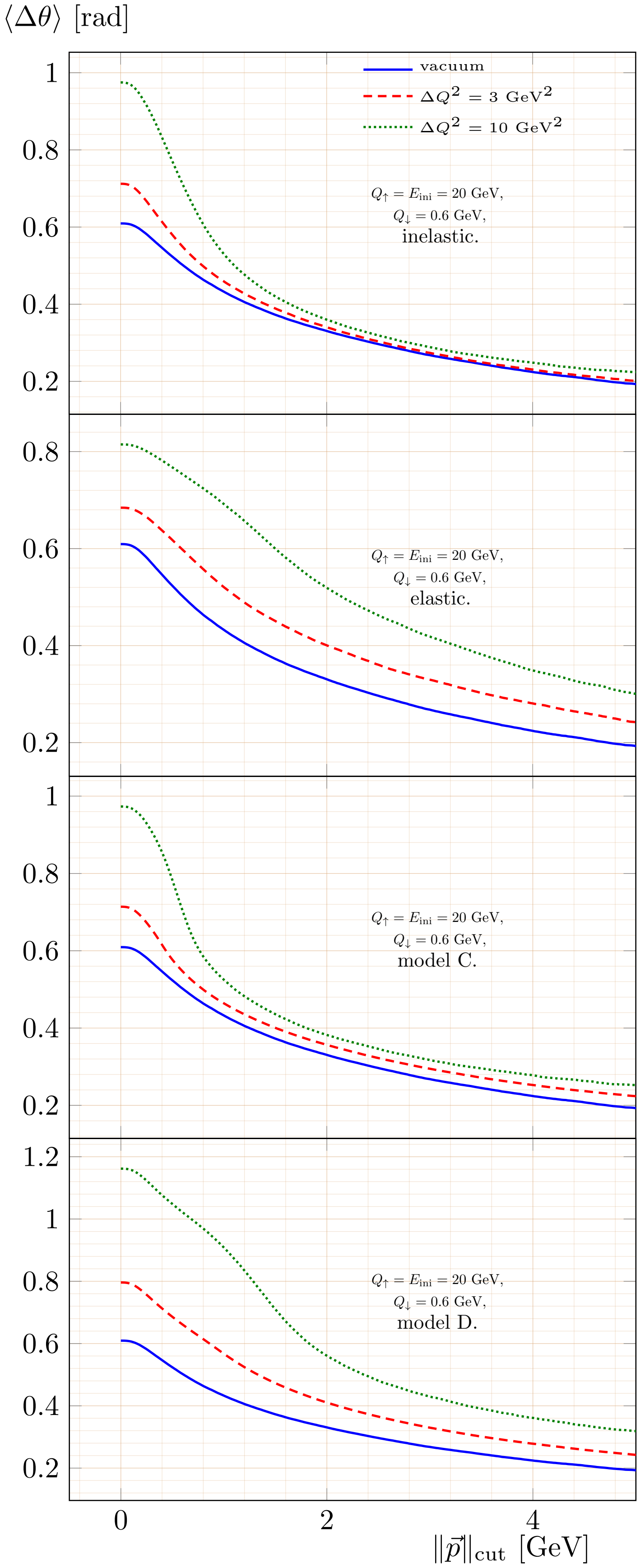

Figure 4.4: Evolution of the obtained mean angle $\langle \Delta\theta \rangle$ with the constraints imposed via the conditions $\|\vec{p}\| > \|\vec{p}\|_{\rm cut}$ on the parton cascades for the inelastic (top panel), elastic (middle panel), and hybrid model C (lower panel) and $\Delta Q^2 = 0,\ 3,\ 10$ GeV^2. The same cascades were used as for Fig. 4.3.

the principle of the radiative energy loss is a redistribution of the available jet-energy among more particles and an angular broadening due to additional branchings. Thus, angular correlations will be depleted at large angles, if a suitable cut in parton momenta is applied. On the other hand, for collisional jet-medium interactions that involve stochastic transverse kicks, such as models B and D, the same distributions are expected to be enhanced in the medium.

However, if one does not impose any constraints on the absolute values of the parton three-momenta, except $\|\vec{p}\| \geq 0$ GeV, one obtains for the angular correlations of all four medium models, enhancements at large angles (results not shown here).

Angular correlations were also studied for cascades, where the evolution was stopped at a threshold virtuality $Q_\downarrow = 1$ GeV for both $Q_\uparrow = E_{\text{ini}} = 20$ GeV and $Q_\uparrow = E_{\text{ini}} = 40$ GeV (not shown here). In this case considerably fewer particles are produced. Consequently, the angular correlations lie below the respective distributions for $Q_\downarrow = 0.6$ GeV, at least in case there is not any cut in $\|\vec{p}\|$ applied. Thus, these distributions remain small over a larger range in $\cos(\Delta\theta)$ but rise more rapidly at small angles, where $\cos(\Delta\theta) \to 1$. Since fewer partons are radiated in general, also the amount of particles produced due to medium-induced radiation is considerably smaller, and, therefore, also the associated contribution to angular broadening. Consequently, since the total jet-momentum is distributed among fewer particles, the distributions corresponding to the inelastic model, or the hybrid models, are less affected if a cut in $\|\vec{p}\|$ is applied, than the corresponding distributions for cascades with $Q_\downarrow = 0.6$ GeV. For the specific cut $\|\vec{p}\| \geq 2$ GeV the effect of angular broadening due to induced radiation and elastic scattering remain comparable. It should be noted that, nevertheless, whether one sets $Q_\downarrow = 0.6$ GeV or $Q_\downarrow = 1$ GeV, one can observe the same tendencies for the angular correlations in both cases:

1. If a cut in $\|\vec{p}\|$ is not applied, angular broadening can be observed for all four models of jet-medium interaction.

2. If a cut is applied, angular broadening is less apparent in angular correlations of all four models. However, the results from the elastic model and the model D are less affected by this kind of filter than the other two models, which do not include the stochastic transverse force.

Thus, the question arises, how – in each of the effective models – particles with different absolute values $\|\vec{p}\|$ of their three-momenta $\vec{p}$ contribute to angular two-particle correlations. To this end, the average values of $\Delta\theta$ as functions of ΔQ^2 were calculated for different cuts in $\|\vec{p}\|$, in each of the four models of jet-medium interaction. Some results can be seen in Fig. 4.3 for the cuts $\|\vec{p}\| \geq 0, 2$ and, 4 GeV (upper, middle, and lower panel, respectively). The mean angles $\langle\Delta\theta\rangle$ obtained from parton cascades without the use of a cut in $\|\vec{p}\|$ increase with ΔQ^2 in all of the models. This behavior can be seen as a verification of angular broadening, which was mentioned earlier for the distributions of the angular two-particle correlations. Furthermore, it can be seen that the values obtained for the purely inelastic model are practically indistinguishable from those of the hybrid model C and they exhibit a much stronger increase than the values for the elastic model, which contains the longitudinal drag and stochastic transverse forces alone, while the hybrid model D, which includes, in addition, also medium-induced radiation exhibits the strongest broadening effects of all of the four models.

However, for $\|\vec{p}\| \geq 2$ GeV and for $\|\vec{p}\| \geq 4$ GeV the values for both, the purely inelastic model, as well as the hybrid model C are much less affected to changes in ΔQ^2 than the steeply rising values corresponding to the elastic model (and model D). It follows, that for the purely inelastic model and the hybrid model C most of the contributions to the angular broadening that is observed in case no cut for $\|\vec{p}\|$ is applied can be attributed to soft particles, where $\|\vec{p}\| \leq 2$ GeV. On the other hand, there are sizable contributions to angular broadening from elastic scatterings (implemented in the purely elastic effective model B and model D), even for partons with $\|\vec{p}\| \geq 2$ GeV or $\|\vec{p}\| \geq 4$ GeV. More precisely, comparisons of the large angular broadening observed for model D with the corresponding results for models A and C show, that angular broadening due to processes of collisional energy loss receives its main contribution from a stochastic transverse force (representing transverse kicks by medium particles).

In order to quantify the dependence of angular broadening on $\|\vec{p}\|$, Fig. 4.4 shows $\langle\Delta\theta\rangle$ as a function of the cut for the four different models of jet-medium interactions. It can be seen that for the elastic model a considerable increase in $\langle\Delta\theta\rangle$ remains even for large cuts in $\|\vec{p}\|$. In the range 1 GeV $\leq \|\vec{p}\|_{\text{cut}} \leq$ 4 GeV, the angles $\langle\Delta\theta\rangle$ are approximately $\frac{5}{4}$ and $\frac{5}{3}$ times larger for $\Delta Q^2 = 3$ GeV^2 and $\Delta Q^2 = 10$ GeV^2, respectively, than for the vacuum. These relative increases are roughly the same for $\|\vec{p}\|_{\text{cut}} \geq 1$ GeV. Only, if all soft particles are considered for the calculation of $\langle\Delta\theta\rangle$, the relative increases are considerably smaller (by $\approx 10\%$ for $\Delta Q^2 = 3$ GeV^2 and by $\approx 25\%$ for $\Delta Q^2 = 10$ GeV^2). In sharp contrast to this behavior, one can observe for both models that allow for medium induced radiation that the angular broadening effects strongly decrease between $\|\vec{p}\|_{\text{cut}} = 0$ GeV and $\|\vec{p}\|_{\text{cut}} = 4$ GeV. This behavior is slightly more pronounced for the purely inelastic model in comparison to the hybrid model C, which still exhibits noticeable increases in $\langle\Delta\theta\rangle$ for $\|\vec{p}\|_{\text{cut}} = 2$ GeV and 4 GeV. Similarly, for model D one observes a steep fall-off with increasing $\|\vec{p}\|_{\text{cut}}$, while a considerable residual enhancement (comparable to the one of the purely elastic model B) for the angle $\langle\Delta\theta\rangle$ is observed at larger momentum scales. This behavior is consistent with the picture that in model D the medium induced radiation of soft particles contributes the most to angular broadening, however the smaller broadening effect from processes of elastic energy loss concerns hard particles as well as soft particles.

To Conclude: Elastic Collisions between jet and medium particles, described in the effective models by longitudinal drag and stochastic transverse forces lead to broadening effects at high as well as at low energy and momentum scales, while medium-induced radiation, described in the effective models by an increase of cascade-parton virtuality, leads to an angular broadening effect that relies predominantly on the emission of soft particles. Furthermore, comparisons of models C and D show that for the broadening effects due to mechanisms of collisional energy loss, the main contributions can be attributed to the action of a stochastic transverse force.

In order to distinguish collisional from radiative energy loss mechanisms the average angle $\langle\Delta\theta\rangle$ between the three-momenta of a heavy trigger quark and an associated cascade partons as functions of a momentum scale $\|\vec{p}\|_{\text{cut}}$ represents a suitable observable.

4.2.2 Azimuthal Angular Correlations

Azimuthal angular correlations between heavy and light mesons obtained from heavy quark jets created in heavy ion collisions are often studied experimentally as a tool to study jet-medium interactions, in particular angular broadening. The azimuthal correlations obtained for collisions that produce two heavy quark jets in back-to-back emissions exhibit, in general, a behavior with two peaks: one at $\Delta\phi = 0$ – the near side peak – and one at $\Delta\phi = \pi$ – the away side peak. Here, the direction corresponding to $\Delta\phi = 0$ is defined as the jet axis of the jet with the larger absolute value of its three-momentum. Judging from comparisons between the near and the away side contributions to azimuthal correlations

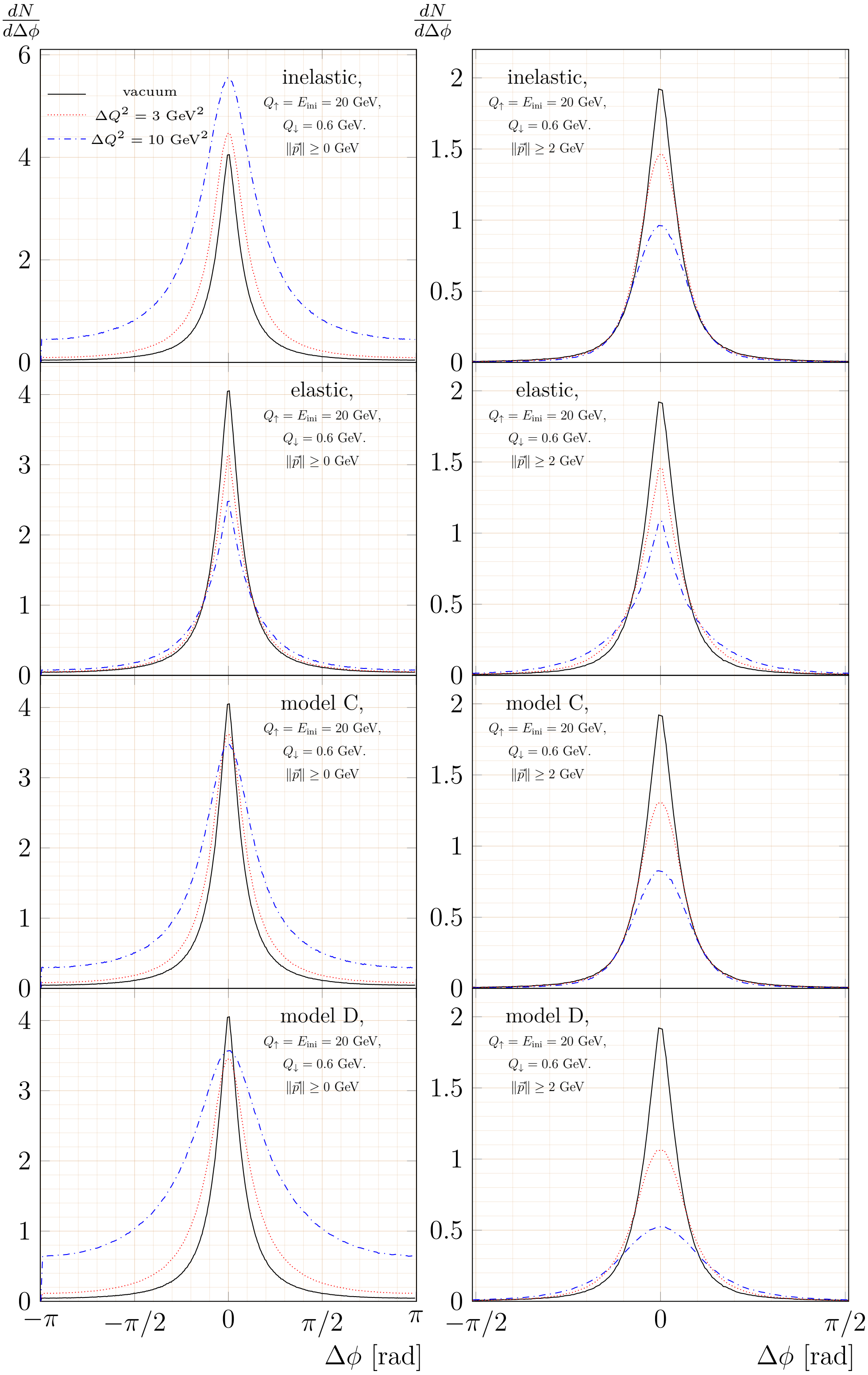

Figure 4.5: Azimuthal angular correlations between a tagged heavy quark and a light parton of partonic cascades initiated by a heavy quark with $E_{\rm ini} = Q_\uparrow = 20$ GeV for the inelastic (top panels), elastic (middle panels), and hybrid model C (lower panels), and for $\Delta Q^2 = 0,\ 3,$ and 10 GeV^2. For the results shown in the right panels only particle pairs were considered, where both particles satisfy the condition $\|\vec{p}\| \geq 2$ GeV, while for the cascades in the left panel there was not imposed any cut on the cascades.

or between azimuthal correlations obtained from p-p and heavy ion collisions, one can estimate that jet-medium interactions lead to both, a decrease in the height of the peaks, as well as increased contributions in the regions between the peaks. Such a behavior can be regarded as a consequence of angular broadening.

With the Monte-Carlo algorithm discussed in Chaps. 2 and 3 the near side contributions to azimuthal angular correlations can be studied. Results are shown in Fig. 4.5: Again, the simulations were made for heavy quark jets with $Q_\uparrow = E_{\text{ini}} = 20$ GeV, $Q_\downarrow = 0.6$ GeV, and again the vacuum behavior was compared to the 2 different temperature profiles represented by $\Delta Q^2 = 3,\ 10\ \text{GeV}^2$ in the four different models of jet-medium interaction. The left panels show the azimuthal angular correlations obtained directly from the simulated parton cascades, without prior application of a cut in $\|\vec{p}\|$. To the distributions shown, all possible pairs between the heavy quark and any other cascade particle (both in their final states and both from the same cascades) contribute. The obtained histograms were divided by the number of simulated cascades. Thus, the distributions shown are normalized to the average number of pairs of the heavy quarks with light partons per cascade $\langle N_{\text{h-l}} \rangle$. For the left panel such a normalization implies $\langle N_{\text{h-l}} \rangle = \langle N_{\text{S}} \rangle = \langle N_{\text{part}} \rangle - 1$, for the right panel $\langle N_{\text{h-l}} \rangle = \langle N_{\text{part, eff}} \rangle - 1$. Here, N_{part} is defined as the number of particles per cascade, and $N_{\text{part, eff}}$ as the number of particles that satisfy $\|\vec{p}\| \geq 2$ GeV for parton cascades, where also the heavy quark satisfies $\|\vec{p}\| \geq 2$ GeV.

In the left panel of Fig. 4.5, the large increase in the number of emitted partons in case of inelastic scattering is represented by the larger areas under the curves for $\Delta Q^2 = 3,\ 10\ \text{GeV}^2$ for the purely inelastic model, as well as for the hybrid models. For the purely inelastic model, radiation is enhanced at both small, as well as large azimuthal angles. In comparison to the purely inelastic model, the enhancement of the distributions is weaker for the hybrid models – a discrepancy that can be observed at all azimuthal angles. One can tentatively explain this kind of behavior by remembering (cf. Chap. 3) that the drag force $A(t)$ leads to a decrease in $\|\vec{p}\|$, associated to a transfer of energy from jet-particles to the medium[6]. Consequently, subsequent splittings will produce particles whose virtualities are constrained to smaller values and are thus, more likely to allow for more democratic branchings in parton energies, which corresponds to larger branching angles ϑ , due to the relation $\vartheta \approx \frac{Q}{E\sqrt{x(1-x)}}$. In sharp contrast to models that allow for induced radiation, the normalizations of the distributions exhibit much smaller changes in case of the elastic model, where parton production is slightly suppressed. With increasing values of ΔQ^2 contributions to the azimuthal correlations get more and more redistributed from the peak at small angles $\Delta\phi$ towards the minima at large angles. Such a behavior can be explained by particle pairs that would contribute to the large peak at $\Delta\phi = 0$, if the jet was propagating in the vacuum, but which experience transverse kicks in the medium that lead to an increasing isotropization with rising temperature.

As can be seen in the right panel of Fig. 4.5, for the elastic model the contributions to the azimuthal correlations from particles with $\|\vec{p}\| \geq 2$ GeV exhibit qualitatively the same behavior for increasing ΔQ^2 as in the left panel, where no cut was applied. However, it can be identified by the scales of the vertical axis, that the normalizations differ by a factor of ≈ 2: This indicates, that approximately only 50% of heavy-light particle pairs satisfy the constraints imposed by the cut, and were therefore considered. On the other hand, for the models which allow for sizable inelastic jet-medium interactions the ΔQ^2 dependence of the corresponding azimuthal angular correlations behaves qualitatively

---

[6] Since, also in model C, particle production is suppressed with regard to the purely inelastic effective model one can make this conclusion, because the only difference in the construction of models A and C lies in the inclusion of the drag force (cf. subsection 3.3.1).

considerably different, if a cut in $\|\vec{p}\|$ is applied: The maxima are smaller than in case of the vacuum, and the order of the curves for different ΔQ^2 values is, thus, opposite than for the results that include soft particles. Furthermore, the increased contributions at large angles, which are present in the plots in the left panels, do not appear, if the cut is applied, except for model D, where a small contribution occurs. For large values of $\Delta\phi$ the azimuthal correlations for in-medium propagation and for the vacuum become indistinguishable. In conclusion, the effect of angular broadening observed for the purely inelastic model and the hybrid model C obtains its major contributions from particle pairs, where at least one of the particles involved is soft, i.e. has a momentum of an absolute value smaller than 2 GeV. As stated previously in Sec. 4.2, the same observation can be made for model D, except that there, a residual broadening effect from processes of collisional energy loss can be observed for hard particles. This conclusion corresponds well with the previous discussion of Fig. 4.4, where, also, most of the increase of $\langle\Delta\theta\rangle$ with ΔQ^2 is found to disappear, if a cut of 2 GeV is applied. In addition, one can deduce from Fig. 4.5, that the remaining increases in $\langle\Delta\theta\rangle$ shown in Fig. 4.4 are, in fact, not due to a radiation of hard particles at larger angles to the hard quark, but rather due to the fact that fewer particles than in the vacuum propagate in directions collinear to the heavy quark.

4.3 Evolution of Emission angles

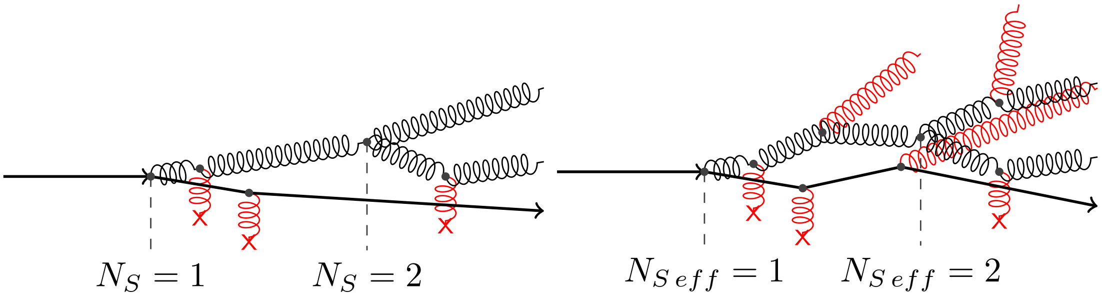

Figure 4.6: Examples of parton cascades in the medium. Jet-medium interactions are symbolized by a gluon exchange ending in an "x". The dashed gray lines indicate how N_S and $N_{S\,eff}$ are counted along the evolution of the cascade. Left diagram: cascade with a total number of $N_S = 2$ splittings in the medium. All splittings are counted. Right panel: cascade with a number of $N_{S\,eff} = 2$ splittings that produce partons that satisfy $\|\vec{p}\| \geq \|\vec{p}\|_{\text{cut}}$. Only those splittings are counted. Partons where $\|\vec{p}\| \leq \|\vec{p}\|_{\text{cut}}$, are drawn in red.

In order to understand how angular correlations and in particular the effect of angular broadening, both described in the previous section 4.2.2, are built up during the evolution of the parton cascade, the sets of parton cascades obtained from the Monte-Carlo simulations were filtered with regard to specific contributions.

In a first attempt, the cascades were selected and further investigated if they matched a certain type (referred to as "topologies" in the remainder of this chapter.): These topologies specify for every parton in the corresponding cascades, whether it is a quark or a gluon and whether it splits (and also for each of its splitting products, if any, whether they are quark or gluons and whether they split, etc.). Any of these topologies corresponds to cascades with a certain number of N_S splittings and thus $N_S + 1$ final particles. The left side of Fig. 4.6 shows a sketch of the example of a cascade with $N_S = 2$ and 2 final gluons radiated from an intermediate gluon.

There exist, however, some issues with regard to this approach:

1. N_S depends on the virtuality threshold $Q_\downarrow$. Therefore, if parton cascades are classified with regard to N_S, this distribution of cascades is not stable if $Q_\downarrow$ is changed.
2. N_S changes if additional soft particles are radiated, while the propagation of the remaining partons in the cascade might be only weakly affected. This behavior poses a problem specifically for the descriptions of inelastic jet-medium interactions, where the distribution in N_S is shifted, due to the production of induced radiation.
3. A more practical problem lies in the fact that a large number of different classes in N_S are produced, in particular in case of inelastic jet-medium interactions (see above): Thus, the study of certain types of topologies (e.g. the ones where $N_S = 2$) appear to be of limited value, since they represent only a few per mill of the total numbers of simulated cascades and are, therefore, not representative.

In order to obtain a more stable classification of parton cascades a cut in $\|\vec{p}\|$ was used: In this second approach parton cascades are identified with certain topologies, if they only differ via the emission of additional soft partons, where $\|\vec{p}\| < \|\vec{p}\|_{\text{cut}}$. A corresponding number of splittings that produce hard partons, $N_{S\,eff}$ was introduced. The right side of Fig. 4.6 gives an example for $N_{S\,eff} = 2$, and $N_S = 5$. In the second approach, the left and right side of Fig. 4.6 would be put in the same class, while the first approach distinguishes between the 2 diagrams.

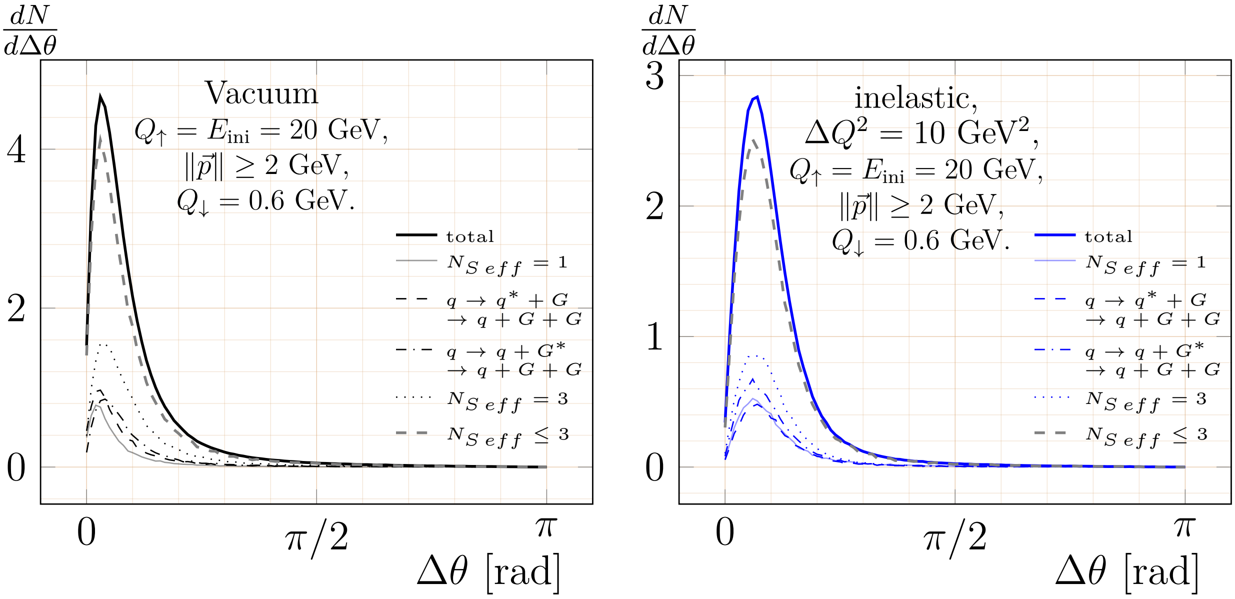

Figure 4.7: Angular 2-particle correlations in the form $\frac{dN}{d\Delta\theta}$ together with their contributions from several topologies with a particular $N_{S\,eff}$ as indicated, and the sum of all the contributions from cascades with $N_{S\,eff} \leq 3$ (dashed lines). left panel: distributions in the vacuum. right panel: distributions in a medium with $\Delta Q^2 = 10$ GeV^2, where jet-medium interactions are described in the purely inelastic model.

Fig. 4.7 verifies that for angular two-particle correlations (here in the form $\frac{dN}{d\Delta\theta}$) between sufficiently hard heavy and light partons the major contributions come from parton cascades with a small value of $N_{S\,eff}$. Therein, the results shown were obtained after application of a cut $||\vec{p}||_{\text{cut}} = 2$ GeV to vacuum cascades as well as cascades from the inelastic model of jet-medium interactions with $\Delta Q^2 = 10$ GeV^2. For $Q_\uparrow = E_{\text{ini}} = 20$ GeV cascades, where $N_{S\,eff} \leq 3$, amount to $\approx 75\%$ and $\approx 67\%$ of events in the vacuum and the medium. Cascades with $N_{S\,eff} = 2$ of the topology where two final gluons are radiated successively from the quark line ($q \to q^* + G \to q + G + G$) represent between 10% (purely inelastic model and model C, both for $\Delta Q^2 = 10$ GeV^2) and 16% (elastic model for $\Delta Q^2 = 10$ GeV^2) of cascades simulated.

It has to be noted that the application of a cut in $||\vec{p}||$ has the effect of a depletion of the angular correlations in particular – if induced radiation can occur – at large angles $\Delta\theta$, as it was discussed before in Sec.4.2. Furthermore, with rising values $||\vec{p}||_{\text{cut}}$, the absolute values of more and more cascade particle three momenta lie below the cut and are, consequently, neglected in the results. The corresponding cascades are then identified with topologies of smaller and smaller values for $N_{S\,eff}$. Less than 27% of all cascades are found with $N_S = N_{S\,eff} \leq 3$ in case $||\vec{p}||_{\text{cut}} = 0$, while for $||\vec{p}||_{cut} = 2$ GeV the majority of cascades are found to be represented by topologies, where $N_{S\,eff} \leq 3$.

The above investigation show that parton cascades with a small number $N_{S\,eff}$ are representative for the entire set of simulated parton cascades and, consequently the corresponding contributions for the overall results on angular two-particle correlations, provided a suitable cut in $||\vec{p}||$ is applied. This allows for a detailed investigation of the evolution of twoparticle correlations by means of studies on cascades with particular topology. To this end, one can study the branching angles ϑ_i, defined as the branching angle of the i^{th} consecutive splitting along the branch of a tree-like cascade that produces two partons with $||\vec{p}|| \geq ||\vec{p}||_{\text{cut}}$. For each of the two different topologies with $N_{S\,eff} = 2$ that produce two hard gluons and a hard quark, as well as for the cascades with $N_{S\,eff} = 3$ Fig. 4.8 shows the results for the average branching angles $\langle\vartheta_i\rangle$ ($i = 1,\, 2,\, 3$) as functions of ΔQ^2 for the purely inelastic model of jet-medium interactions.

One can determine in all three panels of Fig. 4.8 that $\langle\vartheta_1\rangle > \langle\vartheta_2\rangle > \langle\vartheta_3\rangle$. A similar ordering scheme was found in Ref. [144, 145], which shows that for successive splittings (here labeled as i and $i+1$, with the corresponding branching angles ϑ_i and ϑ_{i+1}, respectively.), branching angles that satisfy $\vartheta_i > \vartheta_{i+1}$ occur predominantly, while events where this ordering is broken are largely suppressed. This behavior is generally referred to as angular ordering. While this is an interference effect that applies, in general to consecutive branchings in individual cascades in the vacuum, Fig. 4.8 verifies with $\langle\vartheta_i\rangle > \langle\vartheta_{i+1}\rangle$ that on average the angles of those branchings that produce hard partons follow a similar ordering scheme. It has to be emphasized that, as was mentioned briefly in Chap. 2, in contrast to other algorithms, e.g. Refs. [103, 113] angular ordering ordering was never built in by hand – in the attempt to study, whether this principle is violated, due to multiple jet-medium interactions. The ordering found for the average branching angles can be explained by their proportionality to the ratio between virtuality and energy of the incident decaying parton i, i.e.: $\vartheta_i \propto \frac{Q_i}{E_i}$. This ratio can be shown to decrease strongly during the evolution of parton cascades, cf. e.g. Fig. 2.13 for the time evolution for $\frac{Q}{E}$ for vacuum cascades of different total energy and initial virtuality.

It was found for $N_{S\,eff} = 2$ that the average value of the first branching angle $\langle\vartheta_1\rangle$ is only slightly affected by increasing values of ΔQ^2 in comparison to more strongly rising values of $\langle\vartheta_2\rangle$. For $N_{S\,eff} = 3$, $\langle\vartheta_1\rangle$ decreases, while $\langle\vartheta_2\rangle$ only changes weakly, and $\langle\vartheta_3\rangle$ increases considerably. For the purely inelastic model the effect of angular broadening, observed in Fig. 4.3 for the average angles $\langle\Delta\theta\rangle$ of a heavy light particle pair, can be attributed to an overall increase in the branching angles ϑ_i, since the directions of the three-momenta are not changed during the propagation of an intermediate particle, in contrast to the elastic model of jet-medium interaction, where transverse momentum

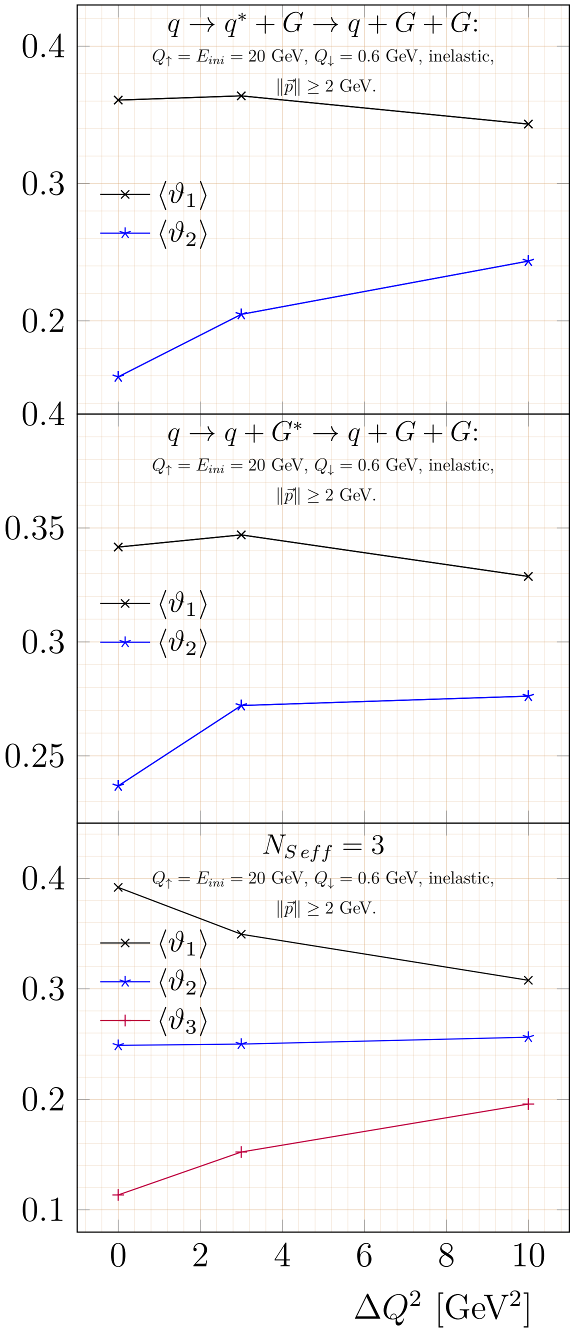

Figure 4.8: Average branching angles $\langle\vartheta_1\rangle$, $\langle\vartheta_2\rangle$, and –if present – $\langle\vartheta_3\rangle$ in cascades of different topologies for the respective first, second and third splitting, which produces parton pairs, where each parton individually fulfills the condition $\|\vec{p}\| \geq \|\vec{p}\|_{cut} = 2$ GeV, as a function of ΔQ^2 in the inelastic model of jet-medium interactions. Top panel: $N_{S\,eff} = 2$, final particles with $\|\vec{p}\| \geq 2$ GeV are a quark and two gluons, radiated from the quark. Middle panel: $N_{S\,eff} = 2$, final particles with $\|\vec{p}\| \geq 2$ GeV are a quark and 2 gluons, radiated both via a common intermediate gluon from the quark. Lowest panel: all cascades where $N_{S\,eff} = 3$.

transfers play a role. Thus, it can be concluded from the study of $\langle\vartheta_i\rangle$ as functions of ΔQ^2 that splittings that happen at a later stage in the evolution of the cascade contribute more to the effect of angular broadening in the medium. A tentative explanation is given via the fact that parton virtualities Q are found to strongly decrease in successive splittings (cf. Fig. 2.4 for virtuality distributions in vacuum.). Since for the life time of the particle an approximation proportional to $\frac{1}{Q}$ was used, cf. Eqs (2.36) and (2.37), the corresponding incident branching partons exist for longer time spans than the branching partons involved in earlier splittings. By consequence, their virtualities increase more due to their in-medium propagation. Since the branching angles are approximately proportional to $\frac{Q}{E}$ it follows, that medium effects are stronger for splittings that occur at later stages in the cascade evolution.

The average values of ϑ_i were also investigated for cascades with $\|\vec{p}\|_{\text{cut}} = 0$ (not shown here) in the same topologies as those shown in Fig. 4.8. As it was mentioned before the results obtained in this first approach correspond to fewer cascades as those from the second. However, for all branching angles investigated, there occurs in most cases (except for $\langle\vartheta_1\rangle$ for $N_S = 3$ and $q \to q^* + G \to q + G + G$ which are approximately constant) a large increase with ΔQ^2, which corresponds well to the overall behavior of a strong effect of angular broadening observed in the top panel of Fig. 4.8. As before one observes that splittings, which occur at a later stage in the cascade evolution, are more affected by jet-medium interactions than earlier ones. In contrast to the behavior for $\|\vec{p}\|_{\text{cut}} = 2$ GeV, for the additional soft particles that are considered, if $\|\vec{p}\|_{\text{cut}} = 0$ GeV is used, the differences in the increases of the average branching angles are large enough that the orderings of the average angles found for the vacuum, $\langle\vartheta_1\rangle \geq \langle\vartheta_2\rangle \geq \langle\vartheta_3\rangle$, are inverted for $\Delta Q^2 = 10$ GeV^2, i.e.: $\langle\vartheta_3\rangle \geq \langle\vartheta_2\rangle \geq \langle\vartheta_1\rangle$.

In conclusion of this section it can be summarized that Monte-Carlo simulated parton cascades can be grouped in different cascade topologies. Then, the evolution of the branching angles ϑ_i was studied in the vacuum and the medium, where it was found that the medium effects on the cascade increase during its evolution, which can result in a weakening of the ordering of the average branching angles $\langle\vartheta_i\rangle$ that is found in the vacuum. Ideally, one would then desire to search for cascade topologies in real jets that are produced in pp and heavy ion collisions. However, since in the experiments only the final jet-particles are known, it is not trivial to identify the branching angles ϑ_i among the angles between the momenta of these final particles. For given sets of simulated parton cascades one could try to obtain the conditional probabilities that certain sets of final particles correspond to particular cascade topologies, by means of a Bayesian approach. Instead of such a study, the present section should serve here as a motivation to investigate the evolution of angular jet-broadening for individual topologies, in order to better understand the behavior for all Monte-Carlo simulated parton-cascades. This will be done in the next section.

4.4 Distributions over two angles

Both collisional as well as radiative processes of jet-medium interaction may contribute to angular jet-broadening (in addition to their contributions to parton-energy loss), a phenomenon that was studied in Sec. 4.2.

The main goal of this section, however, is a better understanding of the underlying cumulative mechanisms that yield the effect of angular jet-broadening in the medium. A particular focus lies on the question, how much the (additional) radiation of light partons at large angles contribute to angular broadening in comparison to deflections of the incident heavy quark. To illustrate the problem, Fig. 4.9 depicts three angles that can be expected to increase due to jet-medium interactions (at least on average). These are: The angle between the three-momenta of a light and a heavy cascade particle, $\Delta\theta$, the angle between the three momentum of a light cascade particle and the jet-axis, $\Delta\theta_{\mathrm{jl}}$, and the angle between the the three momentum of the heavy quark and the jet-axis, $\Delta\theta_{\mathrm{jQ}}$[7].

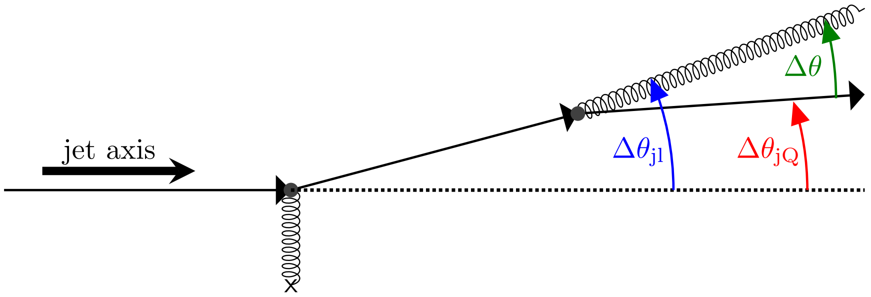

Figure 4.9: Illustration of the definition of the angles $\Delta\theta$, $\Delta\theta_{\mathrm{jQ}}$, and $\Delta\theta_{\mathrm{jl}}$ for a sample parton cascade that is initiated by a heavy quark.

In principle, it could be possible that one of these angles increases independently from the other two (and, thus, contributes to angular jet-broadening)[8]. Fig. 4.10 illustrates two different types of cascades, one, where both $\Delta\theta$ and $\Delta\theta_{\mathrm{jQ}}$ are increased simultaneously due to jet-medium interactions, and another one, where jet-medium interactions yield an increase of $\Delta\theta_{\mathrm{jQ}}$, while $\Delta\theta$ remains unchanged. In the first case (in the left panel of Fig. 4.10) the parton branching angle is increased, but there are no additional deflections. This kind of behavior can occur, if the virtuality of the decaying partons are increased due to jet-medium interactions, i.e. in the models that implement radiative energy loss. The other case can occur, if the decaying partons experience forces that change the directions of their three-momenta, i.e. in the models that describe collisional energy loss.

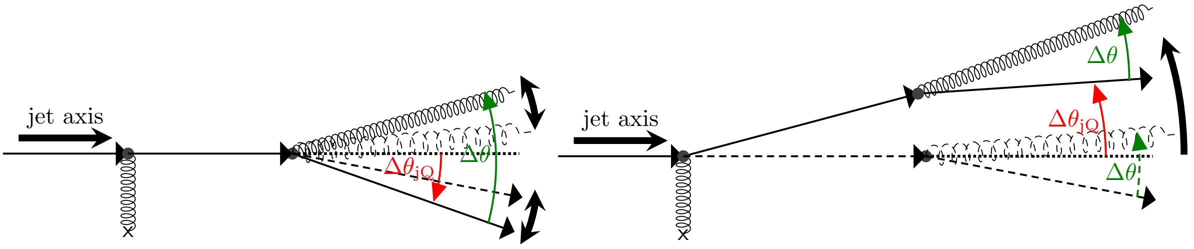

Figure 4.10: left panel: example of a cascade, where $\Delta\theta$ and $\Delta\theta_{\mathrm{jQ}}$ are simultaneously changed via jet-medium interactions due to an increase of the branching angles. right panel: example of a cascade, where the angle $\Delta\theta_{\mathrm{jQ}}$ is increased due to jet-medium interactions, while the angle $\Delta\theta$ is the same as in vacuum. In both panels: Jet-medium interactions are symbolized via a gluon line ending in "x". The resulting changes of the directions of parton momenta are symbolized with the bold arrows on the right side of each panel. Dashed quarks and gluons symbolize the partons one would obtain in a cascade in the vacuum.

In order to quantify, to which picture parton cascades that are subjected to different kinds of jet-medium interactions correspond the most, it is necessary to study the distributions for one angle (e.g.: $\Delta\theta_{jQ}$) for a fixed value of the other angle (in this example

---

[7] Since it is possible to reconstruct the direction of the jet axis from experimental data (e.g. by identifying a photon that was produced in the hard process of heavy quark production, or from the hadrons produced in pp or heavy ion collisions by means of a suitable jet algorithm, etc.), the angles $\Delta\theta_{\mathrm{jQ}}$ and $\Delta\theta_{\mathrm{lj}}$ represent quantities that are in principle experimentally measurable.

[8] The remainder of this section then focuses solely on the pair of angles $\Delta\theta$ and $\Delta\theta_{\mathrm{jQ}}$, thus, neglecting the other two equivalent possibilities.

$\Delta\theta$). This is why this section explores the distribution over the combinations of the two angles $\Delta\theta$ and $\Delta\theta_{\mathrm{jQ}}$, i.e.: $\frac{d^2N}{d\Delta\theta d\Delta\theta_{jQ}}$.

4.4.1 Results for the vacuum case

In order to identify medium effects in the distributions over two angles, it is necessary to study these distributions for cascades in the vacuum before. Some results are shown in Fig. 4.11. In order to understand the distribution for $N_{S\,eff} = 1$ (upper left panel), one can assume that the angle $\Delta\theta$ is approximately the same as the splitting angle ϑ_{bc} (for outgoing heavy quark b and gluon c) between the heavy quark and the produced gluon, $\Delta\theta \approx \vartheta_{bc}$, since subsequent soft processes are expected to only slightly affect the propagation of the hard partons. One can use the further approximation $\vartheta_1 \approx \frac{Q}{E\sqrt{x(1-x)}}$, with the virtuality Q and energy E of the splitting parton and x $(1-x)$ the energy fractions of the outgoing partons. Since $N_{S\,eff} = 1$, small virtualities Q are possible. They even can be supposed to represent the dominant scale for the corresponding splitting processes, because the Sudakov form factor is peaked at virtualities of ≈ 10 GeV (cf. Fig. 2.4) and, furthermore, higher values of Q in such a first hard splitting are more likely to allow subsequent further splittings. Therefore, one can assume a virtuality just above the threshold $Q_\downarrow$ of the algorithm, e.g. $Q \approx 1$ GeV, which yields $\frac{Q}{E} \approx 0.05$. The maximal value of $\sqrt{x(1-x)}$ is $x = \frac{1}{2}$, its minimal value is given by the most unequal energy distribution allowed, but since a cut of 2 GeV was imposed on the parton momenta, one obtains the constraints $0.1 \leq x \leq 0.9$. Thus, the angles between most pairs of a heavy and a light parton lie within the range of $\Delta\theta \approx \vartheta_{bc} \in [0.10, 0.15]$. As can be seen in the left upper panel of Fig. 4.11, this estimation approximates the relevant orders of magnitude reasonably well. The second angle $\Delta\theta_{jQ}$ can be approximated analogously as the angle between the momenta of the incident and outgoing heavy quark in the corresponding splitting process ϑ_b. Since $\vartheta_b = (1-x)\vartheta_{bc}$, one can estimate thus $\Delta\theta_{jQ} \approx (1-x)\Delta\theta$. Due to $x \in [0.1, 0.9]$, one obtains thus a distribution $\frac{d^2N}{d\Delta\theta d\Delta\theta_{jQ}}$ with its main contributions in the half of the plane below the first median. Furthermore, in quark splittings high energy fractions, $x \to 1$ dominate and consequently predominantly small values of $\Delta\theta_{jQ}$. Both tendencies can be verified in the figure.

Subsequently, the topologies for $N_{S\,eff} = 2$ were studied. Results for the radiations of 2 gluons from the heavy quark and an intermediate gluon are shown in the upper middle and right panel of Fig. 4.11, respectively. In an $N_{S\,eff} = 2$ topology one of the outgoing partons of the first branching (which creates 2 partons above the $\|\vec{p}\|$ cut) is an intermediate parton that splits again into 2 partons above the $\|\vec{p}\|$ cut. Thus, its typical virtuality is expected to be higher than that of the corresponding outgoing parton in the branching of the $N_{S\,eff} = 1$ topology. By consequence, the virtuality of the initial parton that has to create the intermediate parton in a splitting is supposed to be also larger than its equivalent in the $N_{S\,eff} = 1$.

Thus, in the case, where 2 gluons are emitted by the heavy quark, it follows from this observation that the first splitting angle is on average larger than in the $N_{S\,eff} = 1$ topology, yielding a larger value for $\Delta\theta$. On the other hand, for the second splitting, the analogous estimation to the $N_{S\,eff} = 1$ case can be made and, thus, for its contribution to the distribution in $\Delta\theta$ values comparable to those in the $N_{S\,eff} = 1$ case can be expected. The $\Delta\theta_{jQ}$ values will be larger than for the $N_{S\,eff} = 1$ topology, due to the larger splitting angle in the first branching. Furthermore, the additional second splitting accounts for a smearing effect, resulting in a broader distribution in the $\Delta\theta_{jQ}$ direction.

In case two finally obtained gluons are emitted from an intermediate gluon one observes

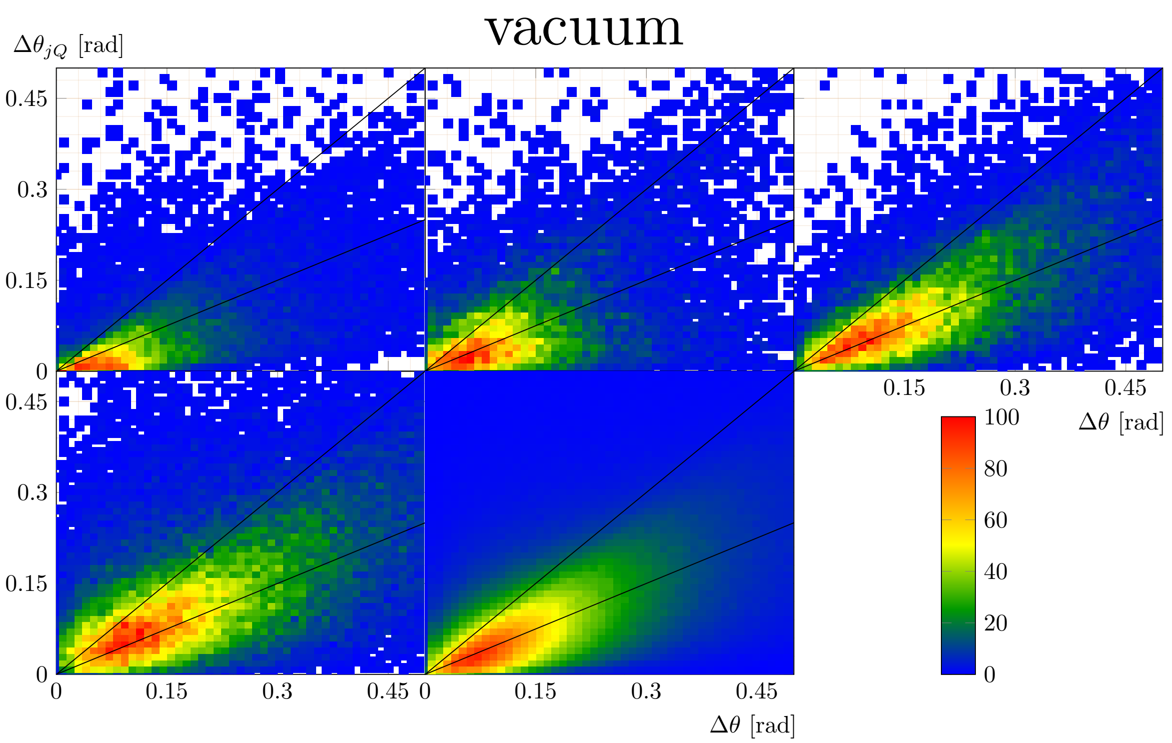

Figure 4.11: Distributions $\frac{d^2N}{d\Delta\theta d\Delta\theta_{jQ}}$ over the angle $\Delta\theta_{jQ}$ (vertical axes) and $\Delta\theta$ (horizontal axes) for parton cascades in the vacuum with $Q_\uparrow = E_{\text{ini}} = 20$ GeV, $Q_\downarrow = 0.6$ GeV (lower middle panel) together with its contributions from cascades with $N_{S\,eff} = 1$ (top left panel), $N_{S\,eff} = 2$ where the intermediate particle is either a heavy quark (top middle panel) or a gluon (top right panel), or $N_{S\,eff} = 3$ (lower left panel). The color bar on the lower right indicates the values of the plotted distributions in % of their respective values at the peaks. The lines $\Delta\theta_{jQ} = \Delta\theta$ and $\Delta\theta_{jQ} = \frac{1}{2}\Delta\theta$ are also shown in black.

a large distribution in a certain direction in the vicinity of the $\Delta\theta_{jQ} = \frac{1}{2}\Delta\theta$ line. This different behavior can be explained as follows: The intermediate gluon has to split into 2 gluons with $\|\vec{p}\|$ values above the cut. Consequently, one can expect that this particle is highly energetic. This constraint leads to a bias towards smaller energy fractions x in the first branching[9]. This bias competes with the overall tendency towards large x values in heavy quark splittings. It follows that for the selected cascades x peaks around a certain value x_{typ} (in Fig. 4.11 $x_{\text{typ}} \approx \frac{1}{2}$) that just allows for the 2 gluon production. The corresponding distribution $\frac{d^2N}{d\Delta\theta d\Delta\theta_{jQ}}$ is then mostly peaked around the direction $\Delta\theta_{jQ} = (1 - x_{\text{typ}})\Delta\theta$[10].

A qualitatively similar, albeit broader, distribution can be obtained for $N_{S\,eff} = 3$ (lower left panel of Fig. 4.11). The results from all cascade topologies are shown in the lower right panel of Fig. 4.11. For the cut $\|\vec{p}\| \geq 2$ GeV contributions from $N_{S\,eff} > 3$ play only a negligible role, as was shown in Fig. 4.7. Thus, the behavior of the distribution can be mostly explained by its already discussed $N_{S\,eff} \leq 3$ contributions.

---

[9] For the case of the emission of 2 gluons from the heavy quark, these considerations did not play a role since the quark splitting function leads already to a strong tendency towards large energy fractions $x \to 1$ of the heavy quark involved.

[10] With the splitting angle ϑ_{BC} of the first branching, one can argue that the distribution is peaked around $\Delta\theta_{jQ} = (1 - x_{\text{typ}})\vartheta_{BC}$. However, the direction of the 3 momenta of the gluons are –on average– distributed symmetrically around the 3 momentum of the intermediate gluon. Thus, two contributions to the distribution in $\Delta\theta$ from each cascade are on average distributed symmetrically around ϑ_{BC}. As a result one obtains a distribution with a smearing around a main ridge $\Delta\theta_{jQ} = (1 - x_{\text{typ}})\Delta\theta$.

4.4.2 Results for the elastic effective model

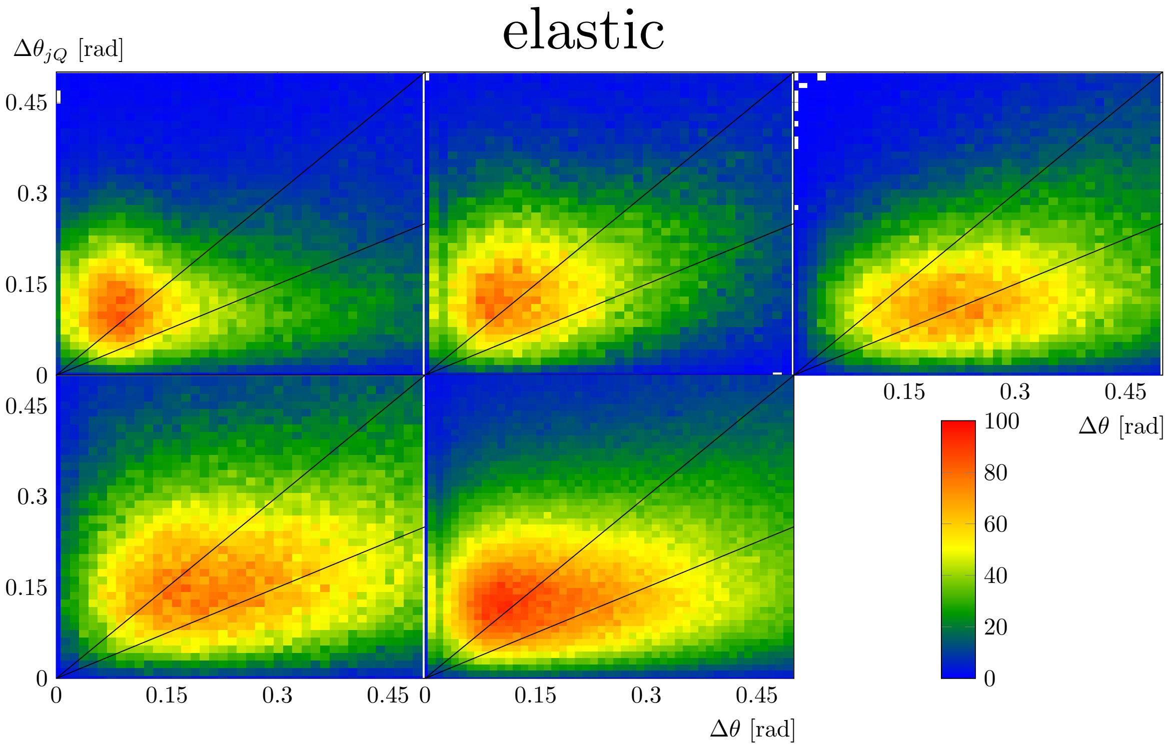

Figure 4.12: The same distributions as shown in Fig. 4.11 for cascades in the vacuum, now for parton cascades in a medium, with jet-medium interactions described by the elastic effective model with $\Delta Q^2 = 10$ GeV^2.

In comparison to the vacuum case one obtains for the effective model of elastic jet-medium interactions largely different results, both for the overall distributions as well as for its contributions from the $N_{S\,eff} < 3$ topologies, as can be seen in Fig. 4.12. In general, one observes distributions that are peaked at larger $\Delta\theta_{jQ}$ values, compared to the vacuum case, and with sizable contributions in the half of the plane, where $\Delta\theta_{jQ} > \Delta\theta$. The mean value $\langle\Delta\theta_{jQ}\rangle$ appears to be almost independent of $\Delta\theta$, which suggests a weakening of the correlation between the $\Delta\theta$ and $\Delta\theta_{jQ}$ values observed in Fig. 4.11. Furthermore, one observes a broad distribution of $\Delta\theta$ values. Since similar differences between vacuum and medium results occur in all of the investigated cases, one can try to understand the medium effects in the simplest case of $N_{S\,eff} = 1$: There, the virtuality of the branching parton is expected to be small, since only a single splitting occurs. By consequence, this initial quark exists for large timescales and, thus, experiences a corresponding amount of transverse momentum transfers. As a result, one obtains a broader distribution in $\Delta\theta_{jQ}$, with a higher average value $\langle\Delta\theta_{jQ}\rangle$. The direction of the 3 momentum of the branching heavy quark can be largely changed during the lifetime of this initial particle, while the angle $\Delta\theta$ depends only on its virtuality Q and energy E. By consequence, the correlation between $\Delta\theta$ and $\Delta\theta_{jQ}$ is weaker than in case of jets in the vacuum. In contrast to the transfers of transverse momentum to the incident splitting parton, where several momentum transfers can annihilate as well as enhance one another, the energy transfer to the medium is described in the model as an effect that accumulates over time. Since the elastic scattering processes do not directly affect the virtuality of the initial quark, the ratio $\frac{Q}{E}$ and, therefore, the branching angle $\vartheta_{bc} \approx \Delta\theta$ can be expected to be larger than in vacuum.

In the paragraph above the broadening of $\Delta\theta_{jQ}$ in the medium due to elastic scattering was explained by the long lifetime of the initial quarks: While this argument was made for the $N_{Seff} = 1$ topologies, it can be generalized to any type of parton cascade by acknowledging that for a series of heavy quark splittings, of all the intermediate heavy quarks the one involved in the last splitting has the smallest virtuality and, therefore, the longest lifetime. Thus, this last intermediate heavy quark contributes the most to the broadening of $\Delta\theta_{jQ}$. This behavior can be verified in the comparison of the two $N_{Seff} = 2$ topologies studied: In both cases the virtuality of the initial heavy quark is expected to be high. However, in case of gluon emission from the heavy quark, the heavy quark undergoes a second splitting. The intermediate particle in this additional branching accounts for a larger broadening effect of $\Delta\theta_{jQ}$ in comparison to the case of the emission of two gluons from an intermediate gluon, as can be seen in Fig. 4.12.

4.4.3 Results for the inelastic effective model

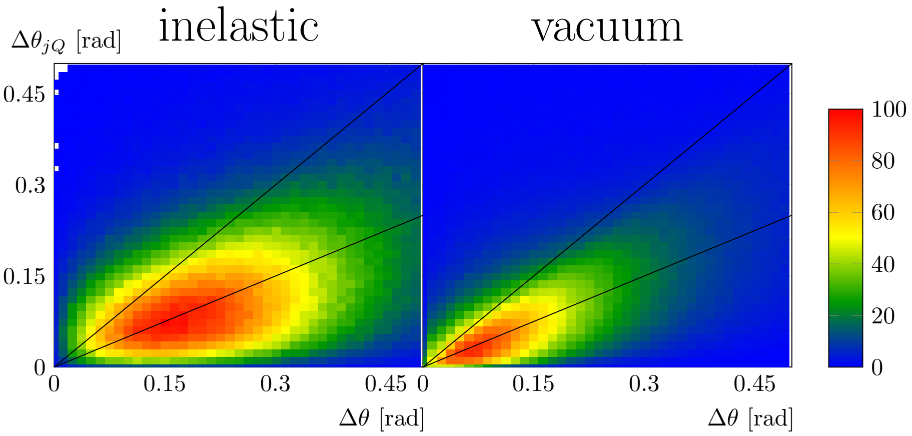

Figure 4.13: Distribution over the angles $\Delta\theta$ and $\Delta\theta_{jQ}$ as in the lower middle panels of Figs. 4.11 and 4.12, for parton cascades undergoing jet-medium interactions described by the inelastic effective medium model (left panel), in comparison to the distributions of parton cascades in the vacuum (right panel).

The $\frac{d^2N}{d\Delta\theta d\Delta\theta_{jQ}}$ distributions were also investigated in the effective model for purely inelastic scattering. There, it can be expected that a broadening in the distributions of $\Delta\theta$ as well as $\Delta\theta_{jQ}$ occurs. The reason for such a behavior is, that both angles are directly proportional to the virtuality, which increases due to the employed description of inelastic jet-medium interactions. On the other hand, the ratio between $\Delta\theta_{jQ}$ and $\Delta\theta$ is unaffected by interactions with the medium.

The results for the purely inelastic model of jet-medium interaction are shown in Fig. 4.13 (here without the additional investigation of $N_{Seff} \leq 3$ topologies). Indeed, this distribution exhibits a very similar behavior (with a ridge of maximal values along a line $\Delta\theta_{jQ} \approx \frac{1}{2}\Delta\theta$) as the corresponding distribution for the vacuum, shown in Fig. 4.11, except the fact, that it is broader in both directions.

Furthermore, it has to be emphasized that the distributions for the elastic and the purely inelastic model of jet-medium interactions (cf. Figs. 4.12 and 4.13) are considerably different: In comparison to the corresponding distribution for the elastic model, the one shown in Fig. 4.13 exhibits a stronger correlation between the angles $\Delta\theta_{jQ}$ and $\Delta\theta$ and a less apparent broadening in $\Delta\theta_{jQ}$ direction. In particular, the maxima of the distribution occurs for angles $\Delta\theta_{jQ} < \Delta\theta$, in contrast to the results obtained for the elastic model.

4.4.4 Results for the hybrid models

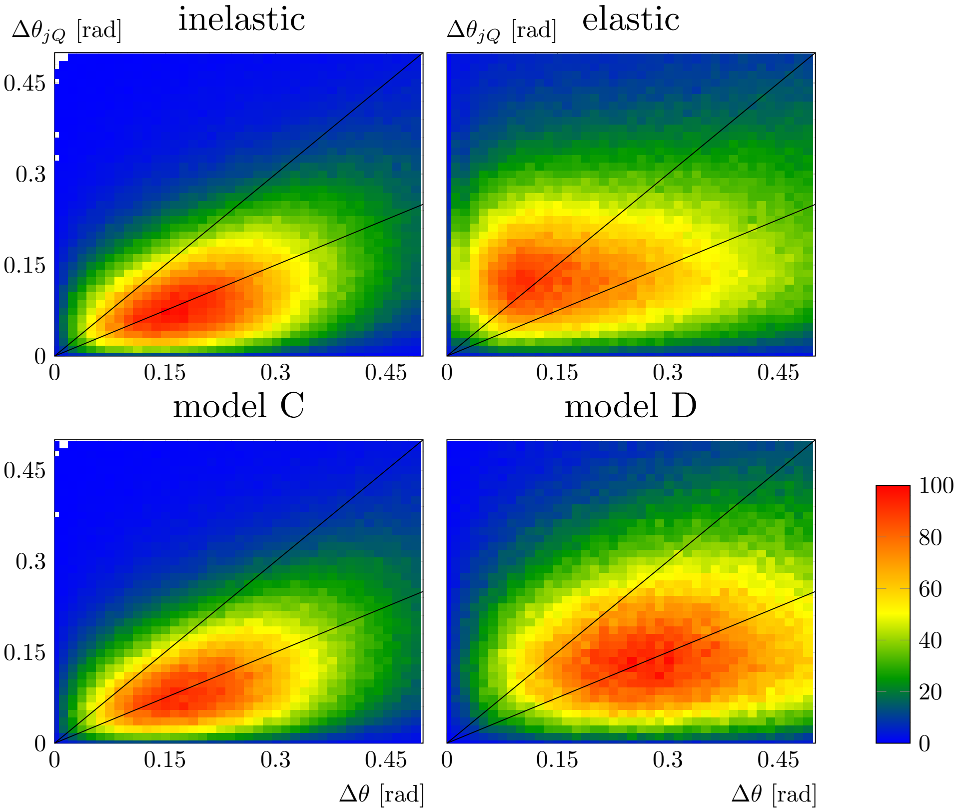

Figure 4.14: Distribution over the angles $\Delta\theta$ and $\Delta\theta_{jQ}$ for the two hybrid model C (lower left) and model D (lower right) compared to the corresponding distributions for the inelastic and elastic effective model (upper left and right, respectively). For the simulations, the same conditions as in the previous figures ($Q_\uparrow = E_{\text{ini}} = 20$ GeV, $Q_\downarrow = 0.6$ GeV) were used. The jet-medium interaction is parametrized by $\Delta Q^2 = 10$ GeV^2. A cut of $\|\vec{p}\| \geq 2$ GeV was applied.

In this subsection, the $\frac{d^2N}{d\Delta\theta d\Delta\theta_{jQ}}$ is studied for the two hybrid models in order to understand the effects of the longitudinal drag force and the stochastic transverse force. Results are shown in Fig. 4.14 in comparison to the corresponding distributions for the inelastic and elastic effective model, that were both already studied before.

It can be seen that the distribution for model C exhibits its maximal values along a ridge in the $\Delta\theta_{jQ} = \frac{1}{2}\Delta\theta$ direction, while the correlation between the two angles seems to disappear in the corresponding distributions for model D. Analogous differences in the medium effects occur in the distributions for the inelastic model and the elastic model. In that case, the disappearance of the correlation between the two angles can be attributed, at least, to processes of collisional energy loss. If one compares the distributions of model C and D, one can specify this observation: The stochastic transverse forces lead to the disappearance of the correlation of the two angles, since the effective models C and D only differ with regard to this single aspect (cf. Fig. 3.1).

Furthermore, in comparison to the elastic effective model – where the most of the largest values of the distribution occur in the $\Delta\theta_{jQ} > \Delta\theta$ part of the plane – the corresponding distribution for the model D appears to be shifted to the right – as the maximum values occur in the $\Delta\theta_{jQ} < \Delta\theta$ part of the plane. This behavior has to reflect the implementation of medium-induced radiation in model D, since this is the only aspect by which model D differs from the elastic model (cf. Fig. 3.1). Indeed the behavior is consistent with the observation (made in the previous subsection 4.4.3) that the ridge along the $\Delta\theta_{jQ} = \frac{1}{2}\Delta\theta$ direction is broader in the distributions of the inelastic effective model than in the vacuum case.

4.4.5 Comparison and Summary

In order to quantify the observations on the distributions over two angles made in the previous subsections 4.4.1 to 4.4.4, this subsection shows in Fig. 4.2 a list of parameters that define the combined and individual distributions over the two angles $\Delta\theta$ and $\Delta\theta_{jQ}$.

	$\frac{\mathrm{Cov}(\Delta\theta,\Delta\theta_{jQ})}{\sigma(\Delta\theta)\sigma(\Delta\theta_{jQ})}$	$\langle\Delta\theta\rangle \pm \sigma(\Delta\theta)$ [rad]	$\langle\Delta\theta_{jQ}\rangle \pm \sigma(\Delta\theta_{jQ})$ [rad]
vacuum	0.765	0.330 ± 0.350	0.200 ± 0.230
inelastic	0.709	0.360 ± 0.302	0.207 ± 0.200
elastic	0.554	0.518 ± 0.440	0.306 ± 0.265
model C	0.705	0.380 ± 0.325	0.213 ± 0.207
model D	0.473	0.560 ± 0.406	0.287 ± 0.238

Table 4.2: Parameters for the distributions in $\Delta\theta$ and $\Delta\theta_{jQ}$ for cascades in the vacuum or subjected to effective medium models (the same sets of cascades as for Figs. 4.11 to 4.14 and a $\|\vec{p}\|$-cut of 2 GeV was used), i.e.: Covariance $\mathrm{Cov}(\Delta\theta, \Delta\theta_{jQ})$ of the $\frac{d^2N}{d\Delta\theta d\Delta\theta_{jQ}}$ distribution divided by the standard deviations $\sigma(\Delta\theta)$ and $\sigma(\Delta\theta_{jQ})$ of the $\Delta\theta$ and $\Delta\theta_{jQ}$ distributions, respectively (left column), mean values $\langle\Delta\theta\rangle$ of the $\Delta\theta$ distribution together with their standard deviations $\sigma(\Delta\theta)$ (middle column), and mean values $\langle\Delta\theta_{jQ}\rangle$ of the $\Delta\theta_{jQ}$ distribution together with their standard deviations $\sigma(\Delta\theta_{jQ})$ (right column).

The mean values and standard deviations for the distributions over a single angle, $\Delta\theta$ or $\Delta\theta_{jQ}$, of two particles with three-momenta that satisfy $\|\vec{p}\| \geq \|\vec{p}\|_{\mathrm{cut}} = 2$ GeV reflect a rather small angular broadening for the models that do not contain a stochastic transverse force compared to the elastic effective model and the model D that do contain this kind of force. For the average values $\langle\Delta\theta\rangle$ this behavior is consistent with Fig. 4.4, where most angular broadening effects disappear for the inelastic effective model and model C at $\|\vec{p}\|_{\mathrm{cut}} = 2$ GeV, in contrast to the elastic effective model and model D.

In order to study the distributions over the two angles $\Delta\theta$ and $\Delta\theta_{jQ}$ correlation coefficients $\frac{\mathrm{Cov}(\Delta\theta,\Delta\theta_{jQ})}{\sigma(\Delta\theta)\sigma(\Delta\theta_{jQ})}$ were calculated. The behavior observed in Figs. 4.11 to 4.14 before is well reflected in these values: While for the cascades in the vacuum the angles $\Delta\theta$ and $\Delta\theta_{jQ}$ are strongly correlated and this correlation is still largely present (the correlation coefficients decrease by $\approx 8\%$) for the inelastic effective model as well as model C, which both do not contain a stochastic transverse force, for the elastic effective model as well as the hybrid model D, which both contain such a stochastic transverse force, the decrease in the correlation coefficient is much larger ($\approx 27\%$ for the elastic model and $\approx 38\%$ for model D).

To summarize: The distribution $\frac{d^2N}{d\Delta\theta d\Delta\theta_{jQ}}$ has been studied for cascades in the vacuum as well as the different medium models in order to better understand how the effects of parton radiation at larger angles (due to larger parton branching angles, as well as due to additional branchings) and of in-medium deflection of the heavy quark result in the behavior of angular jet-broadening. For cascades in the vacuum this deflection of the heavy quark is entirely due to those parton branchings that involve the heavy quarks.

The two angles $\Delta\theta_{jQ}$ and $\Delta\theta$ are correlated with peak values of the distribution $\frac{d^2N}{d\Delta\theta d\Delta\theta_{jQ}}$ around the direction $\Delta\theta = \frac{1}{2}\Delta\theta_{jQ}$. This correlation was also found for parton cascades that are subjected to processes of radiative energy loss alone (i.e. neglecting the three-momentum exchanges in collisions of jet and medium particles) or even a longitudinal drag force. However, it is a particular feature of models that contain a transverse stochastic force that the correlation between the two angles is weakened. This kind of behavior can be explained by large deflections of the heavy quark (resulting in larger $\Delta\theta_{jQ}$ values) before the radiation of gluons.

While angular jet-broadening is a phenomenon that can occur for both collisional and radiative energy-loss mechanisms and can be observed already via the $\frac{dN}{d\Delta\theta_{jQ}}$ and $\frac{dN}{d\Delta\theta}$ distributions, the weakening of the correlations of the two angles cannot be described by these two distributions alone. However, the $\frac{d^2N}{d\Delta\theta d\Delta\theta_{jQ}}$ distribution is a suitable observable to study it.

In order to quantify the weakening of the correlation between $\Delta\theta_{jQ}$ and $\Delta\theta$, correlation coefficients have been calculated, which are smaller for the elastic effective model and the hybrid model D than for the other models or for the vacuum.

4.5 Conclusions and Perspectives

This chapter has demonstrated that two-particle correlations can provide an additional means to distinguish different mechanisms of in-medium parton energy-loss, i.e. collisional and radiative scatterings off medium partons.

To this end, parton cascades were simulated within the effective models presented in Chap. 3 – starting from the same quark (i.e. same $Q_\uparrow$, E_{ini}) in all systems, and for media with the same space-time evolution of the temperature. Then, two-particle correlations were obtained from the four-momenta of two cascade particles, with systematic triggering on one particle of the pair. Usually this trigger particle was the initial quark of the cascade in its final state. Special emphasis was laid on investigations of angular correlations.

Sec. 4.2 investigated the angular correlations between such a trigger particle and any of the remaining final particles of the cascades – representing heavy-light meson pairs. In particular the average increase of the angle between the pairs of particles due to jet-medium interactions was studied. When filtering the final particles with regard to the absolute values of their three-momenta, $\|\vec{p}\|$, one observes that, not only is this angular broadening effect smaller for increasing momentum/energy scales, but also that this effect is considerably different for the effective models of collisional and radiative energy loss. Thus, it was found that for the effective model of radiative energy loss the angular broadening effects are mainly due to the emission of soft particles, while for the elastic effective model, the deflection of hard jet particles plays a considerable role. Consequently, the angular broadening effect for cascades subjected to only processes of collisional energy loss is more insensitive to the application of a cut in the parton momentum/energy scale. It was found that the dependencies of the average angle $\langle\Delta\theta\rangle$ on the cut $\|\vec{p}\|_{\text{cut}}$ shown in Fig. 4.4 provide a useful tool in order to distinguish between the different mechanisms of in-medium parton energy-loss.

Sec. 4.3 followed the ambitious goal to study the history of angular jet-broadening: To this end the sets of cascades that were obtained from the Monte-Carlo simulations were regrouped into different classes of cascade topologies. It was then studied in particular, how the average branching angles evolve in these topologies. Unfortunately, it was not possible to construct observables that would directly reflect individual branching angles. However, Sec. 4.3 motivated a search for observables (in the subsequent section 4.4) that allow to distinguish the contributions to angular jet-broadening by changes of the direction of the parton three-momenta over time, due to jet-medium interactions (in models that allow for processes of collisional energy loss) from the effects of the medium effects on parton-branching angles[11].

Sec. 4.4 complemented the studies of the angle $\Delta\theta$ of parton pairs by a simultaneous study of the angle $\Delta\theta_{jQ}$ between the heavy quark and the jet axis. By studying the distributions over the pairs of angles in Figs. 4.11, 4.12, and 4.13, one can obtain further, valuable insights that also allow to distinguish between the effective medium models: The two angles $\Delta\theta$ and $\Delta\theta_{jQ}$ are noticeably correlated for vacuum cascades but also for cascades subjected to radiative energy loss alone. The ridge of those angle pairs that give the maximal values of the distribution exhibit a characteristic linearly rising behavior. On the other hand, for parton cascades in the elastic effective model, not only are the maxima of the distributions shifted towards higher $\Delta\theta_{jQ}$, due to multiple deflections of the heavy quark in the medium, but also the aforementioned correlations between the two angles $\Delta\theta_{jQ}$ and $\Delta\theta$ are weakened.

Summarizing, one can conclude that this chapter identified the following characteristic behaviors of quantities that are, in principle, observable, which allow to discriminate between collisional and radiative energy loss:

1. The momentum scale dependence of the angular broadening, observed via the mean angle $\langle\Delta\theta\rangle$,
2. the (de)correlation of the angles $\Delta\theta_{jQ}$ and $\Delta\theta$ due to radiative (collisional) processes,

Of course, within the approaches taken towards two-particle correlation there are still a lot of issues and/or phenomena that need to be addressed in the future: They can be grouped into problems that demand changes and additions in the description of the cascade evolution (and also the underlying hard heavy-ion or pp collisions) and possible additional investigations in two-particle correlations.

The former part consists of issues such as: the missing description of a hard collision that creates the first particle of a (time-like) cascade, as well as initial state radiations and parton distributions of the colliding heavy ions/protons, the explicit consideration of quark-mass effects, a hadronization model, a microscopic description of the jet-medium interactions (with coherence effects) or an extension of the effective model beyond off-shell cascade particles, recoil effects, jet-particles that stem from thermalized medium particles, etc. They should be only mentioned here, but discussed in more detail in the next chapter, as they do not concern the main focus of this chapter, the construction of (new) observables to investigate and distinguish the mechanisms of in-medium energy loss.

Thus, the second part is more relevant here: As Fig. 4.4 – and Sec. 4.2 in general – shows, there is a clear correlation between the average angles $\langle\Delta\theta\rangle$ and parton energies. Studies of some joint distributions in angles and energies could provide a promising tool to further quantify the observations made within Sec. 4.2. Two-particle energy correlations or correlations between the momentum components transverse to the jet axis also have not yet been considered. A substantial improvement to the approaches taken would be the inclusion of jet algorithms (e.g.: [6–13]) and grooming algorithms (e.g.: [146]) in order to identify sub-jets. This would allow to translate the different topologies studied in Sec. 4.3 into observable and infrared- and collinear safe quantities. This would allow to investigate the in-medium *evolution* of the jets both experimentally as well as theoretically.

---

[11] A third aspect is of course the increased angular jet-broadening due to medium-induced radiation, which, however, has been studied before in Sec. 4.2.

Chapter 5

Conclusion and future work

This thesis proposed a strategy for studying the mechanisms of parton-energy loss in the medium of QGP by means of two-particle correlations.

In order to perform the necessary investigations on jets and their observables, a Monte-Carlo algorithm was implemented (cf. Chap. 2). This tool represents a Monte-Carlo simulation of the virtuality evolution of parton fragmentation that is given by the DGLAP equations. Thus, parton radiation via bremsstrahlung in the vacuum has been resummed with leading-log accuracy. This algorithm can be used to simulate parton cascades corresponding to the jets created in the final state processes of heavy quarks produced in pp collisions.

Several, qualitatively different effective models of jet-medium interaction were then introduced in Chap. 3. They where implemented as medium modifications of the Monte-Carlo algorithm. While the models are rather simplistic, they, however, do allow to systematically study, in a consistent overall framework, the consequences of different types of energy-loss mechanisms on single and multiple particle observables. In particular, the two complementary mechanisms of radiative and collisional energy loss were each studied within a corresponding effective model. While the first one leads to induced parton branching, and, thus, to a larger number of partons within the cascade, the second one corresponds to an energy transfer of cascade particles to the medium, both via a longitudinal drag-force and a transverse stochastic force. Under the assumption that both, collisional and radiative mechanisms are independent of one another, their combined effects were considered in the hybrid models C and a tentative model D was proposed. While the former effectively simulates induced radiation as well as a longitudinal drag force, but lacks the transverse stochastic force of the model for collisional energy loss, model D contains all three effects.

In a first study of some resulting observables, such as distributions over parton-momentum components or angles with jet axes, in Chap. 3, it was found that the collisional energy loss mechanisms lead to a momentum- and angular broadening for cascade partons at all of the investigated energy scales, while for radiative energy loss angular broadening is obtained via the emission of multiple soft particles. Furthermore, since these soft particles are obtained via parton branchings, particle distributions at high energies are depleted in the effective model for radiative energy loss in comparison to the vacuum case.

In order to further quantify this observation and to further discriminate between the different models, Chap. 4 developed a strategy using two-particle angular correlations as observables: Thus, angular correlations were studied in the form of distributions over angles $\Delta\theta$, which are the angles between the three momenta of the initial quark of a cascade (representing a heavy quark in a heavy quark jet) and of another, associated parton of the cascade in its final state. In particular the mean angle $\langle\Delta\theta\rangle$ was investigated:

First, Fig. 4.3 showed that this average angle increases with the strength of jet-medium interactions (expressed via a parameter ΔQ^2). Then, a tool to quantitatively discriminate between the collisional and radiative energy loss mechanisms was given via Fig. 4.4, which shows the mean angles $\langle \Delta\theta \rangle$ as functions of a cut in parton momenta $\|\vec{p}\|_{\text{cut}}$. For the model of collisional energy loss the mean angles $\langle \Delta\theta \rangle$ are considerably larger than for the vacuum case at all considered momentum cuts. For the model of radiative energy loss, such an increased $\langle \Delta\theta \rangle$ value can only be found at small momentum cuts, while for larger scales the $\langle \Delta\theta \rangle$ values drop steeply and approach the vacuum behavior. These different behaviors can be either explained via a redistribution of parton momenta over a large set of different directions due to elastic scattering processes in the medium, or by an additional amount of soft particle emitted due to processes of medium-induced radiation. By consequence, it can be argued, that the presented method to distinguish the different types of parton cascades rely on general physical properties of the respective collisional and radiative jet-medium interactions rather than on mere artifacts of the effective medium models presented in Chap. 3. This kind of studies can be complemented, among other investigations, with an additional examination of distributions over two angles $\Delta\theta$ and $\Delta\theta_{jQ}$ in Sec. 4.4. For the vacuum case, a correlation between the two angles has been found, which retains much of its original behavior, if the cascade particles are subjected to radiative energy loss. However, for cascades undergoing processes of collisional energy loss, much of the initial correlation between the two angles is lost. This different behavior is due to a large broadening of the corresponding angles, but mostly of $\Delta\theta_{jQ}$. It can be interpreted as a sign of the larger isotropization of the corresponding parton momenta due to the (stochastic) transverse forces they experience.

So far, Chap. 4 searched for two-particle observables that allow to distinguish types of cascades that are subjected to different kinds of jet-medium interactions. Therein, the sets of cascades that were compared, were obtained with simulations that used the same value of the parameter ΔQ^2. This model parameter corresponds to the strength of the jet-medium interaction and, thus, to the temperature scales of the medium. For the temperature profile given by Eqs. (3.2) and (3.13) (and the assumption that $\hat{q}_R = \hat{q}_C$) that was used in the effective models, the choices of $\Delta Q^2 = 3$ GeV^2 and $Q^2 = 10$ GeV^2 in Chap. 4 (and in most parts of Chap. 3) can serve as an estimation for the RHIC and LHC temperature scales, respectively.

However, in order to distinguish models that yield the same predictions for physical observables, one should rather compare different effective models that produce the same values for the nuclear modification factor instead. As the results for the approximations R_{MV} to the nuclear modification factor R_{AA}, obtained in Fig. 3.13 for both the collisional and radiative effective model, suggest, the ΔQ^2 values for different models that yield the same nuclear modification factor can be largely different as well. Thus, even higher discrepancies between the corresponding behaviors of the angular two-particle correlations (e.g. expressed via the curves analogous to the ones found in Fig. 4.4) can be expected.

The implemented effective models describe jet-medium interactions only for off-the-mass-shell particles of a virtuality above the threshold $Q_{\downarrow}$, while particles with smaller virtualities are assumed as final particles that are neither allowed to split nor to change their four-momenta. This restriction was made, since the range of possible momentum fractions is very restricted for partons with virtualities slightly above $Q_{\downarrow}$, cf. Eqs. (2.21) and (2.23). By consequence, if the effective model for radiative energy loss was modified in such a way that it allowed for on-the-mass-shell particles to regain virtuality and split once the virtuality is above the threshold, one would obtain an unreasonably high amount of partons produced in democratic branchings, where $x \approx z \approx \frac{1}{2}$. To avoid these kind of problems jet-medium interactions were turned off for virtualities $Q \leq Q_{\downarrow}$ in all of the effective models[1]. For an extension that includes medium effects of on-the-mass-shell particles one can argue as follows: The currently implemented algorithm relies on the DGLAP evolution of parton fragmentation. This approach is applicable, if the cascade partons are strongly ordered in virtuality. If the cascade partons effectively acquire virtuality due to scatterings off medium particles, the additional parton splittings can still be described via the same splitting functions as in the vacuum case, if the additionally acquired virtuality is small compared to the initial virtuality of the incident cascade parton. For incident partons that are already on-the-mass-shell, or at the threshold virtuality, this requirement is no longer satisfied. Thus, the collinear splitting functions need to be replaced at this scale with different probability densities that better apply to the domain of small virtualities. A suitable description of induced particle radiation might be obtained by the approach of Gunion and Bertsch [124], which calculates induced gluon radiation for incident on-shell particles (cf. in particular Ref. [134] for an application to on-shell heavy quarks in the medium).[2] In order to obtain more realistic predictions (both for the single particle observables, most notably the estimation R_{MV} of the nuclear modification factor as well as for angular correlations) the effective models established in this thesis should be modified to include the jet-medium interactions of cascade partons with virtualities smaller than $Q_{\downarrow}$. For the effective treatment of collisional energy loss, one merely has to apply the drag and stochastic forces on the particles with $Q \leq Q_{\downarrow}$ as they were applied before on particles with $Q > Q_{\downarrow}$, cf. Sec. 3.2.1. The presented strategy to distinguish radiative and collisional parton-energy-loss mechanisms via two-particle correlations will remain the same for tentative extended models, because it relies on the fact that parton-energy loss is either attributed to an energy transfer to the medium due to a parton three-momentum change or to an additional number of parton branchings (and, thus, a redistribution of energy), rather than on details of the specific models. However, since the extended models will involve additional jet-medium interactions one will obtain a larger energy-loss for the same ΔQ^2 scales. For the estimation R_{MV} of the nuclear modification factor (cf. Fig. 3.13) one can, thus, expect smaller values. Especially for the purely collisional model, which right now yields values that are too high (at ΔQ^2 scales that can be associated to reasonable temperature scales) compared to experimental data, one can expect reasonable values.

Up to now, cascades were initiated by a quark that was considered as a heavy quark. While such an approach can be justified by the fact that heavy quarks are automatically labeled as triggers among the other partons, due to their large masses, their interactions with the medium and spectra of radiated gluons might differ as well. However explicit heavy quark-mass effects have not yet been included in the current version of the Monte-Carlo algorithm. If the code would be adapted accordingly, one would, most notably, observe the so-called dead-cone effect [47] in the resulting data: Correspondingly, collinear parton branching would be suppressed and, by consequence, radiative energy loss would decrease as well. Furthermore, a proper inclusion of heavy quarks in the Monte-Carlo algorithm, will also give rise to $Q\bar{Q}$ production via gluon splitting at high energy and virtuality scales above $2m_Q$ These contributions can be simulated by implementing $G \rightarrow Q\bar{Q}$ splitting functions. By consequence, the production of heavy quarks at late stages of the cascade evolution should then be possible as well. Furthermore, the simplifying

---

[1] While the aforementioned problem does not appear for collisional energy loss in the effective models any jet-medium interaction was turned off for partons with $Q \leq Q_{\downarrow}$ in order to allow for a consistent comparison between the different models.

[2] Also, one should remember, that in the present algorithm, outlined in Chap. 2, the virtuality threshold $Q_{\downarrow}$ is motivated by the introduction of a minimum virtuality scale Q_0 of resolvable partons. One can argue that within this model such a virtuality scale is independent of the position of a possible splitting in space and time.

assumption of this thesis that only a single heavy quark is present per cascade has then to be dropped – with the result that corresponding two-particle correlations will be obtained from more that one trigger particle per jet.

Summarizing, one could modify the Monte-Carlo Algorithm in a way that considerably affects jet-phenomenology by allowing on-the-mass-shell jet-particles to interact with the medium. Indeed, it is planned right now to extend the part for collisional energy loss in the effective models to on-the-mass-shell partons. Considering the effective description of medium induced radiation, the main goal is to implement a different approach for gluon radiation off on-the-mass-shell cascade-particles, e.g.: using the formalism by Gunion and Bertsch. Then, it will be necessary to find a suitable transition between the high virtuality region where the emission of gluons can still be described via splitting functions for collinear splitting and the low virtuality region. In addition, for the heavy quarks, the quark mass should be included in the description of their evolution inside the parton cascade, in order to account for phenomena such as the Dead-Cone effect.

Finally, on the side of the observables, a considerable improvement in the applicability of the presented results could be achieved, if two-particle correlations were replaced by the correlations between two different parts of a jet, where at least one of the two is identified as a sub-jet: In contrast to individual particles sub-jets – that were obtained with a suitable jet-algorithm – are entities that are stable under additional soft or collinear parton branchings (cf. the discussion in, e.g., Ref. [8]). Thus, the choice of a virtuality threshold, or possible hadronization effects, would play a smaller role. Once, sub-jets have been identified via a suitable algorithm, an observable that represents a first direct test on the jet-structure is the jet-fragmentation function [147].

Bibliography

[1] H. Fritzsch, M. Gell-Mann, and H. Leutwyler. "Advantages of the color octet gluon picture". *Physics Letters B* **47**.4 (1973), 365 –368. URL: `http://www.sciencedirect.com/science/article/pii/0370269373906254`.

[2] Michael E. Peskin and Daniel V. Schroeder. *An Introduction to Quantum Field Theory*. Ed. by David Pines. The Advanced Book Program, Westview Press, A Member of the Perseus Book Group, 1995.

[3] Roland Katz. "A quantum approach to dynamical quarkonia suppression in high energy heavy ion collisions". PhD thesis. SUBATECH, Nantes, 2015. URL: `https://tel.archives-ouvertes.fr/tel-01278863`.

[4] http://www.itp.tuwien.ac.at/Fundamental_Interactions.

[5] C. Patrignani et al. "Review of Particle Physics". *Chin. Phys.* **C40**.10 (2016), 100001.

[6] Stephen D. Ellis and Davison E. Soper. "Successive combination jet algorithm for hadron collisions". *Phys. Rev.* **D48** (1993), 3160–3166. arXiv: `hep-ph/9305266 [hep-ph]`.

[7] S. Catani et al. "Longitudinally invariant K_t clustering algorithms for hadron hadron collisions". *Nucl. Phys.* **B406** (1993), 187–224.

[8] Matteo Cacciari, Gavin P. Salam, and Gregory Soyez. "The Anti-k(t) jet clustering algorithm". *JHEP* **04** (2008), 063. arXiv: `0802.1189 [hep-ph]`.

[9] Yuri L. Dokshitzer et al. "Better jet clustering algorithms". *JHEP* **08** (1997), 001. arXiv: `hep-ph/9707323 [hep-ph]`.

[10] M. Wobisch and T. Wengler. "Hadronization corrections to jet cross-sections in deep inelastic scattering". *Monte Carlo generators for HERA physics. Proceedings, Workshop, Hamburg, Germany, 1998-1999.* 1998, 270–279. arXiv: `hep-ph/9907280 [hep-ph]`. URL: `https://inspirehep.net/record/484872/files/arXiv:hep-ph_9907280.pdf`.

[11] S. Bethke et al. "Experimental investigation of the energy dependence of the strong coupling strength". *Physics Letters B* **213**.2 (1988), 235 –241. URL: `http://www.sciencedirect.com/science/article/pii/0370269388910325`.

[12] Gavin P. Salam and Gregory Soyez. "A Practical Seedless Infrared-Safe Cone jet algorithm". *JHEP* **05** (2007), 086. arXiv: `0704.0292 [hep-ph]`.

[13] Gerald C. Blazey et al. "Run II jet physics". *QCD and weak boson physics in Run II. Proceedings, Batavia, USA, March 4-6, June 3-4, November 4-6, 1999.* 2000, 47–77. arXiv: `hep-ex/0005012 [hep-ex]`. URL: `http://lss.fnal.gov/cgi-bin/find_paper.pl?conf-00-092`.

[14] R Aaij et al. “Study of J/ψ production and cold nuclear matter effects in pPb collisions at $\sqrt{s_{NN}} = 5$ TeV”. *J. High Energy Phys.* **02**.arXiv:1308.6729. LHCB-PAPER-2013-052. CERN-PH-EP-2013-156 (2013). Comments: 26 pages, 7 figures; Published in JHEP, 072. 25 p. URL: `http://cds.cern.ch/record/1596262`.

[15] Michael L. Miller et al. “Glauber modeling in high energy nuclear collisions”. *Ann. Rev. Nucl. Part. Sci.* **57** (2007), 205–243. arXiv: `nucl-ex/0701025 [nucl-ex]`.

[16] K. Aamodt et al. “Suppression of Charged Particle Production at Large Transverse Momentum in Central Pb-Pb Collisions at $\sqrt{s_{NN}} = 2.76$ TeV”. *Phys. Lett.* **B696** (2011), 30–39. arXiv: `1012.1004 [nucl-ex]`.

[17] Francesco Prino and Ralf Rapp. “Open heavy flavor in QCD matter and in nuclear collisions”. *Journal of Physics G: Nuclear and Particle Physics* **43**.9 (2016), 093002. URL: `http://stacks.iop.org/0954-3899/43/i=9/a=093002`.

[18] K Aamodt et al. “Charged-particle multiplicity density at mid-rapidity in central Pb-Pb collisions at $\sqrt{s_{NN}} = 2.76$ TeV”. *Phys. Rev. Lett.* **105** (2010), 252301. arXiv: `1011.3916 [nucl-ex]`.

[19] A. Andronic et al. “Heavy-flavour and quarkonium production in the LHC era: from proton–proton to heavy-ion collisions”. *The European Physical Journal C* **76**.3 (2016), 1–151. URL: `http://dx.doi.org/10.1140/epjc/s10052-015-3819-5`.

[20] J. Adam et al. “Inclusive, prompt and non-prompt J/ψ production at mid-rapidity in Pb-Pb collisions at $\sqrt{s_{\mathrm{NN}}} = 2.76$ TeV”. *Journal of High Energy Physics* **2015**.7 (2015), 51. URL: `http://dx.doi.org/10.1007/JHEP07(2015)051`.

[21] S. Chatrchyan et al. “Suppression of non-prompt J/ψ, prompt J/ψ, and Υ (1S) in PbPb collisions at $\sqrt{s_{\mathrm{NN}}} = 2.76$ TeV”. *Journal of High Energy Physics* **2012**.5 (2012), 63. URL: `http://dx.doi.org/10.1007/JHEP05(2012)063`.

[22] J. Adam et al. “Transverse momentum dependence of D-meson production in Pb-Pb collisions at $\sqrt{s_{\mathrm{NN}}} = 2.76$ TeV”. *Journal of High Energy Physics* **2016**.3 (2016), 81. URL: `http://dx.doi.org/10.1007/JHEP03(2016)081`.

[23] Serguei Chatrchyan et al. “Study of high-pT charged particle suppression in PbPb compared to pp collisions at $\sqrt{s_{NN}} = 2.76$ TeV”. *Eur. Phys. J.* **C72** (2012), 1945. arXiv: `1202.2554 [nucl-ex]`.

[24] Rudolf Baier et al. “Quenching of hadron spectra in media”. *Journal of High Energy Physics* **2001**.09 (2001), 033. URL: `http://stacks.iop.org/1126-6708/2001/i=09/a=033`.

[25] B. Abelev et al. “Azimuthal anisotropy of D-meson production in Pb-Pb collisions at $\sqrt{s_{NN}} = 2.76$ TeV”. *Phys. Rev. C* **90** (3 2014), 034904. URL: `http://link.aps.org/doi/10.1103/PhysRevC.90.034904`.

[26] B. Abelev et al. “D Meson Elliptic Flow in Noncentral Pb-Pb Collisions at $\sqrt{s_{NN}} = 2.76$ TeV”. *Phys. Rev. Lett.* **111** (10 2013), 102301. URL: `http://link.aps.org/doi/10.1103/PhysRevLett.111.102301`.

[27] P. B. Gossiaux and J. Aichelin. “Toward an understanding of the single electron data measured at the BNL Relativistic Heavy Ion Collider (RHIC)”. *Phys. Rev. C* **78** (1 2008), 014904. URL: `http://link.aps.org/doi/10.1103/PhysRevC.78.014904`.

[28] P. B. Gossiaux, R. Bierkandt, and J. Aichelin. “Tomography of quark gluon plasma at energies available at the BNL Relativistic Heavy Ion Collider (RHIC) and the CERN Large Hadron Collider (LHC)”. *Phys. Rev. C* **79** (4 2009), 044906. URL: `http://link.aps.org/doi/10.1103/PhysRevC.79.044906`.

[29] Kiyosi Ito. “On Stochastic Differential Equations”. *Memoirs of the American Mathematical Society* 4 (1951).

[30] A. Beraudo et al. “Transport properties and Langevin dynamics of heavy quarks and quarkonia in the Quark Gluon Plasma”. *Nucl. Phys.* **A831** (2009), 59–90. arXiv: `0902.0741 [hep-ph]`.

[31] W. M. Alberico et al. “Heavy-flavour spectra in high energy nucleus-nucleus collisions”. *Eur. Phys. J.* **C71** (2011), 1666. arXiv: `1101.6008 [hep-ph]`.

[32] W. M. Alberico et al. “Heavy flavors in *AA* collisions: production, transport and final spectra”. *Eur. Phys. J.* **C73** (2013), 2481. arXiv: `1305.7421 [hep-ph]`.

[33] Michel Le Bellac. *Thermal Field Theory*. Cambridge University Press, 2011. ISBN: 9780511885068, 9780521654777. URL: `http://www.cambridge.org/mw/academic/subjects/physics/theoretical-physics-and-mathematical-physics/thermal-field-theory?format=AR`.

[34] Magdalena Djordjevic and Miklos Gyulassy. “Heavy quark radiative energy loss in QCD matter”. *Nuclear Physics A* **733**.3 (2004), 265 –298. URL: `http://www.sciencedirect.com/science/article/pii/S0375947403019924`.

[35] M. Gyulassy, P. Levai, and I. Vitev. “Reaction operator approach to non-abelian energy loss”. *Nuclear Physics B* **594**.1 (2001), 371 –419. URL: `http://www.sciencedirect.com/science/article/pii/S0550321300006520`.

[36] Magdalena Djordjevic. “Theoretical formalism of radiative jet energy loss in a finite size dynamical QCD medium”. *Phys. Rev.* **C80** (2009), 064909. arXiv: `0903.4591 [nucl-th]`.

[37] Magdalena Djordjevic and Ulrich W. Heinz. “Radiative energy loss in a finite dynamical QCD medium”. *Phys. Rev. Lett.* **101** (2008), 022302. arXiv: `0802.1230 [nucl-th]`.

[38] Magdalena Djordjevic. “Collisional energy loss in a finite size QCD matter”. *Phys. Rev.* **C74** (2006), 064907. arXiv: `nucl-th/0603066 [nucl-th]`.

[39] Magdalena Djordjevic and Marko Djordjevic. “Generalization of radiative jet energy loss to non-zero magnetic mass”. *Phys. Lett.* **B709** (2012), 229–233. arXiv: `1105.4359 [nucl-th]`.

[40] J. I. Kapusta and Charles Gale. *Finite-temperature field theory: Principles and applications*. Cambridge University Press, 2011. ISBN: 9780521173223, 9780521820820, 9780511222801.

[41] L. D. Landau and I. Pomeranchuk. “Limits of applicability of the theory of bremsstrahlung electrons and pair production at high-energies”. *Dokl. Akad. Nauk Ser. Fiz.* **92** (1953), 535–536.

[42] A. B. Migdal. “Bremsstrahlung and Pair Production in Condensed Media at High Energies”. *Phys. Rev.* **103** (6 1956), 1811–1820. URL: `http://link.aps.org/doi/10.1103/PhysRev.103.1811`.

[43] R. Baier et al. “The Landau-Pomeranchuk-Migdal effect in QED”. *Nucl. Phys.* **B478** (1996), 577–597. arXiv: `hep-ph/9604327 [hep-ph]`.

[44] R. Baier et al. “Radiative energy loss of high-energy quarks and gluons in a finite volume quark - gluon plasma”. *Nucl. Phys.* **B483** (1997), 291–320. arXiv: `hep-ph/9607355 [hep-ph]`.

[45] V. M. Galitsky and I. I. Gurevich. “Coherence effects in ultra-relativistic electron bremsstrahlung”. *Il Nuovo Cimento (1955-1965)* **32**.2 (1964), 396–407. URL: `http://dx.doi.org/10.1007/BF02733969`.

[46] A. H. Sørensen. “On the suppression of the gluon radiation for quark jets penetrating a dense quark gas”. *Zeitschrift für Physik C Particles and Fields* **53**.4 (1992), 595–600. URL: `http://dx.doi.org/10.1007/BF01559735`.

[47] Yuri L. Dokshitzer and D. E. Kharzeev. “Heavy quark colorimetry of QCD matter”. *Phys. Lett.* **B519** (2001), 199–206. arXiv: `hep-ph/0106202 [hep-ph]`.

[48] Néstor Armesto, Carlos A. Salgado, and Urs Achim Wiedemann. “Medium-induced gluon radiation off massive quarks fills the dead cone”. *Phys. Rev. D* **69** (11 2004), 114003. URL: `http://link.aps.org/doi/10.1103/PhysRevD.69.114003`.

[49] M. Mannarelli and R. Rapp. “Hadronic modes and quark properties in the quark-gluon plasma”. *Phys. Rev. C* **72** (6 2005), 064905. URL: `http://link.aps.org/doi/10.1103/PhysRevC.72.064905`.

[50] D. Cabrera and R. Rapp. “T-matrix approach to quarkonium correlation functions in the quark-gluon plasma”. *Phys. Rev. D* **76** (11 2007), 114506. URL: `http://link.aps.org/doi/10.1103/PhysRevD.76.114506`.

[51] F. Riek and R. Rapp. “Quarkonia and heavy-quark relaxation times in the quark-gluon plasma”. *Phys. Rev. C* **82** (3 2010), 035201. URL: `http://link.aps.org/doi/10.1103/PhysRevC.82.035201`.

[52] E. Eichten et al. “Charmonium: The model”. *Phys. Rev. D* **17** (11 1978), 3090–3117. URL: `http://link.aps.org/doi/10.1103/PhysRevD.17.3090`.

[53] E. Eichten et al. “Erratum: Charmonium: The model”. *Phys. Rev. D* **21** (1 1980), 313–313. URL: `http://link.aps.org/doi/10.1103/PhysRevD.21.313.2`.

[54] Juan Martin Maldacena. “The Large N limit of superconformal field theories and supergravity”. *Int. J. Theor. Phys.* **38** (1999). [Adv. Theor. Math. Phys.2,231(1998)], 1113–1133. arXiv: `hep-th/9711200 [hep-th]`.

[55] Jacob D. Bekenstein. “Black Holes and Entropy”. *Phys. Rev. D* **7** (8 1973), 2333–2346. URL: `http://link.aps.org/doi/10.1103/PhysRevD.7.2333`.

[56] Steven S. Gubser. “Drag force in AdS/CFT”. *Phys. Rev. D* **74** (12 2006), 126005. URL: `http://link.aps.org/doi/10.1103/PhysRevD.74.126005`.

[57] Christopher P. Herzog et al. “Energy loss of a heavy quark moving through $\mathcal{N}$=4 supersymmetric Yang-Mills plasma”. *Journal of High Energy Physics* **2006**.07 (2006), 013. URL: `http://stacks.iop.org/1126-6708/2006/i=07/a=013`.

[58] P. Kovtun, Dan T. Son, and Andrei O. Starinets. “Viscosity in strongly interacting quantum field theories from black hole physics”. *Phys. Rev. Lett.* **94** (2005), 111601. arXiv: `hep-th/0405231 [hep-th]`.

[59] Steven S. Gubser. “Momentum fluctuations of heavy quarks in the gauge-string duality”. *Nuclear Physics B* **790**.1–2 (2008), 175 –199. URL: `http://www.sciencedirect.com/science/article/pii/S0550321307006633`.

[60] Dam T. Son and Derek Teaney. “Thermal noise and stochastic strings in AdS/CFT”. *Journal of High Energy Physics* **2009**.07 (2009), 021. URL: `http://stacks.iop.org/1126-6708/2009/i=07/a=021`.

[61] Azfar Adil and Ivan Vitev. “Collisional dissociation of heavy mesons in dense QCD matter”. *Phys. Lett.* **B649** (2007), 139–146. arXiv: `hep-ph/0611109 [hep-ph]`.

[62] Rishi Sharma and Ivan Vitev. “High transverse momentum quarkonium production and dissociation in heavy ion collisions”. *Phys. Rev.* **C87**.4 (2013), 044905. arXiv: `1203.0329 [hep-ph]`.

[63] Taesoo Song, Che Ming Ko, and Su Houng Lee. “Quarkonium formation time in quark-gluon plasma”. *Phys. Rev.* **C87**.3 (2013), 034910. arXiv: `1302.4395 [nucl-th]`.

[64] Betty Abelev et al. “Suppression of high transverse momentum D mesons in central Pb-Pb collisions at $\sqrt{s_{NN}} = 2.76$ TeV”. *JHEP* **09** (2012), 112. arXiv: `1203.2160 [nucl-ex]`.

[65] Simon Wicks et al. “Elastic, inelastic, and path length fluctuations in jet tomography”. *Nucl. Phys.* **A784** (2007), 426–442. arXiv: `nucl-th/0512076 [nucl-th]`.

[66] Simon Wicks et al. “Heavy quark jet quenching with collisional plus radiative energy loss and path length fluctuations”. *Nucl. Phys.* **A783** (2007), 493–496. arXiv: `nucl-th/0701063 [nucl-th]`.

[67] Thomas Lang et al. “Heavy quark transport in heavy ion collisions at energies available at the BNL Relativistic Heavy Ion Collider and at the CERN Large Hadron Collider within the UrQMD hybrid model”. *Phys. Rev.* **C93**.1 (2016), 014901. arXiv: `1211.6912 [hep-ph]`.

[68] Shanshan Cao, Guang-You Qin, and Steffen A. Bass. “Heavy-quark dynamics and hadronization in ultrarelativistic heavy-ion collisions: Collisional versus radiative energy loss”. *Phys. Rev.* **C88** (2013), 044907. arXiv: `1308.0617 [nucl-th]`.

[69] Jan Uphoff et al. “Heavy quark production at RHIC and LHC within a partonic transport model”. *Phys. Rev.* **C82** (2010), 044906. arXiv: `1003.4200 [hep-ph]`.

[70] Jan Uphoff et al. “Elliptic Flow and Energy Loss of Heavy Quarks in Ultra-Relativistic heavy Ion Collisions”. *Phys. Rev.* **C84** (2011), 024908. arXiv: `1104.2295 [hep-ph]`.

[71] Jan Uphoff et al. “Momentum imbalance of D mesons in ultra-relativistic heavy-ion collisions at LHC”. *Phys. Rev.* **C89**.6 (2014), 064906. arXiv: `1310.1340 [hep-ph]`.

[72] Jan Uphoff et al. “Elastic and radiative heavy quark interactions in ultra-relativistic heavy-ion collisions”. *J. Phys.* **G42**.11 (2015), 115106. arXiv: `1408.2964 [hep-ph]`.

[73] Magdalena Djordjevic and Marko Djordjevic. “LHC jet suppression of light and heavy flavor observables”. *Phys. Lett.* **B734** (2014), 286–289. arXiv: `1307.4098 [hep-ph]`.

[74] Min He, Rainer J. Fries, and Ralf Rapp. “Heavy Flavor at the Large Hadron Collider in a Strong Coupling Approach”. *Phys. Lett.* **B735** (2014), 445–450. arXiv: `1401.3817 [nucl-th]`.

[75] Min He, Rainer J. Fries, and Ralf Rapp. “Thermal Relaxation of Charm in Hadronic Matter”. *Phys. Lett.* **B701** (2011), 445–450. arXiv: `1103.6279 [nucl-th]`.

[76] Min He, Rainer J. Fries, and Ralf Rapp. “$\mathbf{D_s}$-Meson as Quantitative Probe of Diffusion and Hadronization in Nuclear Collisions”. *Phys. Rev. Lett.* **110**.11 (2013), 112301. arXiv: `1204.4442 [nucl-th]`.

[77] K. Aamodt et al. “Harmonic decomposition of two-particle angular correlations in Pb-Pb collisions at $\sqrt{s_{NN}} = 2.76$ TeV”. *Phys. Lett.* **B708** (2012), 249–264. arXiv: `1109.2501 [nucl-ex]`.

[78] B. I. Abelev et al. “Long range rapidity correlations and jet production in high energy nuclear collisions”. *Phys. Rev. C* **80** (6 2009), 064912. URL: `http://link.aps.org/doi/10.1103/PhysRevC.80.064912`.

[79] Georges Aad et al. “Measurement of the azimuthal anisotropy for charged particle production in $\sqrt{s_{NN}} = 2.76$ TeV lead-lead collisions with the ATLAS detector”. *Phys. Rev.* **C86** (2012), 014907. arXiv: `1203.3087 [hep-ex]`.

[80] Sandro Bjelogrlić. “Heavy-flavour correlations in pp, p–Pb and Pb–Pb collisions”. *Nuclear Physics A* **931** (2014). QUARK MATTER 2014XXIV INTERNATIONAL CONFERENCE ON ULTRARELATIVISTIC NUCLEUS-NUCLEUS COLLISIONS, 563 –568. URL: `http://www.sciencedirect.com/science/article/pii/S0375947414005235`.

[81] Marlene Nahrgang et al. “Heavy-flavor azimuthal correlations of D mesons”. *Journal of Physics: Conference Series* **509**.1 (2014), 012047. URL: `http://stacks.iop.org/1742-6596/509/i=1/a=012047`.

[82] G. Altarelli and G. Parisi. “Asymptotic freedom in parton language”. *Nuclear Physics B* **126**.2 (1977), 298 –318. URL: `http://www.sciencedirect.com/science/article/pii/0550321377903844`.

[83] Yuri L. Dokshitzer. “Calculation of the Structure Functions for Deep Inelastic Scattering and e+ e- Annihilation by Perturbation Theory in Quantum Chromodynamics.” *Sov. Phys. JETP* **46** (1977). [Zh. Eksp. Teor. Fiz.73,1216(1977)], 641–653.

[84] B. A. Kniehl et al. “Inclusive $D^{*\pm}$ production in $p\overline{p}$ collisions with massive charm quarks”. *Phys. Rev. D* **71** (1 2005), 014018. URL: `http://link.aps.org/doi/10.1103/PhysRevD.71.014018`.

[85] B. A. Kniehl et al. “Collinear subtractions in hadroproduction of heavy quarks”. *Eur. Phys. J.* **C41** (2005), 199–212. arXiv: `hep-ph/0502194 [hep-ph]`.

[86] Matteo Cacciari, Mario Greco, and Paolo Nason. “The P(T) spectrum in heavy flavor hadroproduction”. *JHEP* **05** (1998), 007. arXiv: `hep-ph/9803400 [hep-ph]`.

[87] B. Mele and P. Nason. “The fragmentation function for heavy quarks in QCD”. *Nuclear Physics B* **361**.3 (1991), 626 –644. URL: `http://www.sciencedirect.com/science/article/pii/055032139190597Q`.

[88] John C. Collins, Frank Wilczek, and A. Zee. “Low-Energy Manifestations of Heavy Particles: Application to the Neutral Current”. *Phys. Rev.* **D18** (1978), 242.

[89] John C. Collins and Wu-Ki Tung. “Calculating Heavy Quark Distributions”. *Nucl. Phys.* **B278** (1986), 934.

[90] John C. Collins. “Hard scattering factorization with heavy quarks: A General treatment”. *Phys. Rev.* **D58** (1998), 094002. arXiv: `hep-ph/9806259 [hep-ph]`.

[91] R. K. Ellis, W. J. Stirling, and B.R. Webber. *QCD and Collider Physics*. Ed. by T. Ericson and P. V. Landshoff. Vol. 8. Cambridge monographs on particle physics, nuclear physics and cosmology. Cambridge University Press, 1996.

[92] Torbjorn Sjöstrand et al. “An introduction to PYTHIA 8.2”. *Computer Physics Communications* **191** (2015), 159 –177. URL: `http://www.sciencedirect.com/science/article/pii/S0010465515000442`.

[93] Torbjorn Sjöstrand, Stephen Mrenna, and Peter Z. Skands. “PYTHIA 6.4 Physics and Manual”. *JHEP* **05** (2006), 026. arXiv: `hep-ph/0603175 [hep-ph]`.

[94] Bo Andersson et al. "Parton Fragmentation and String Dynamics". *Phys. Rept.* **97** (1983), 31–145.

[95] Bo Andersson. "The Lund model". *Camb. Monogr. Part. Phys. Nucl. Phys. Cosmol.* **7** (1997), 1–471.

[96] G. Corcella et al. "HERWIG 6: An Event generator for hadron emission reactions with interfering gluons (including supersymmetric processes)". *JHEP* **01** (2001), 010. arXiv: `hep-ph/0011363 [hep-ph]`.

[97] G. Corcella et al. "HERWIG 6.5 release note" (2002). arXiv: `hep-ph/0210213 [hep-ph]`.

[98] Manuel Bähr et al. "Herwig++ physics and manual". English. *The European Physical Journal C* **58**.4 (2008), 639–707. URL: `http://dx.doi.org/10.1140/epjc/s10052-008-0798-9`.

[99] J. Bellm et al. *Herwig++ 2.7 Release Note.* 2013. arXiv: `1310.6877 [hep-ph]`.

[100] B.R. Webber. "A QCD model for jet fragmentation including soft gluon interference". *Nuclear Physics B* **238**.3 (1984), 492 –528. URL: `http://www.sciencedirect.com/science/article/pii/055032138490333X`.

[101] Néstor Armesto, Leticia Cunqueiro, and Carlos A. Salgado. "Q-PYTHIA: a medium-modified implementation of final state radiation". English. *The European Physical Journal C* **63**.4 (2009), 679–690. URL: `http://dx.doi.org/10.1140/epjc/s10052-009-1133-9`.

[102] Bjoern Schenke, Charles Gale, and Sangyong Jeon. "MARTINI: An Event generator for relativistic heavy-ion collisions". *Phys. Rev.* **C80** (2009), 054913. arXiv: `0909.2037 [hep-ph]`.

[103] Korinna Zapp et al. "A Monte Carlo Model for 'Jet Quenching'". *Eur.Phys.J.* **C60** (2009), 617–632. arXiv: `0804.3568 [hep-ph]`.

[104] Korinna C. Zapp, Frank Krauss, and Urs A. Wiedemann. "A perturbative framework for jet quenching". *JHEP* **03** (2013), 080. arXiv: `1212.1599 [hep-ph]`.

[105] Thorsten Renk. "Parton shower evolution in a 3D hydrodynamical medium". *Phys. Rev. C* **78** (3 2008), 034908. URL: `http://link.aps.org/doi/10.1103/PhysRevC.78.034908`.

[106] Thorsten Renk. "Physics probed by the P_T dependence of the nuclear suppression factor". *Phys. Rev. C* **88** (1 2013), 014905. URL: `http://link.aps.org/doi/10.1103/PhysRevC.88.014905`.

[107] Jorge Casalderrey-Solana and Carlos A. Salgado. "Introductory lectures on jet quenching in heavy ion collisions". *Acta Phys. Polon.* **B38** (2007), 3731–3794. arXiv: `0712.3443 [hep-ph]`.

[108] Liliana Apolinário et al. "Medium-induced gluon radiation and colour decoherence beyond the soft approximation". *JHEP* **02** (2015), 119. arXiv: `1407.0599 [hep-ph]`.

[109] Jean-Paul Blaizot et al. "Probabilistic picture for medium-induced jet evolution". *JHEP* **06** (2014), 075. arXiv: `1311.5823 [hep-ph]`.

[110] Edmond Iancu and Bin Wu. "Medium-induced jet evolution: multiple branching and thermalization". *Proceedings, 7th International Conference on Hard and Electromagnetic Probes of High-Energy Nuclear Collisions (Hard Probes 2015): Montréal, Québec, Canada, June 29-July 3, 2015.* 2016. arXiv: `1510.04464 [hep-ph]`. URL: `http://inspirehep.net/record/1398053/files/arXiv:1510.04464.pdf`.

[111] R. Baier et al. ““Bottom-up” thermalization in heavy ion collisions”. *Physics Letters B* **502**.1–4 (2001), 51 –58. URL: `http://www.sciencedirect.com/science/article/pii/S0370269301001915`.

[112] Peter Brockway Arnold, Guy D. Moore, and Laurence G. Yaffe. “Effective kinetic theory for high temperature gauge theories”. *JHEP* **01** (2003), 030. arXiv: `hep-ph/0209353 [hep-ph]`.

[113] Korinna C. Zapp. “JEWEL 2.0.0: directions for use”. *Eur.Phys.J.* **C74** (2014), 2762. arXiv: `1311.0048 [hep-ph]`.

[114] I. P. Lokhtin and A. M. Snigirev. “A model of jet quenching in ultrarelativistic heavy ion collisions and high- p T hadron spectra at RHIC”. *The European Physical Journal C - Particles and Fields* **45**.1 (2006), 211–217. URL: `http://dx.doi.org/10.1140/epjc/s2005-02426-3`.

[115] R. Baier et al. “Angular dependence of the radiative gluon spectrum and the energy loss of hard jets in QCD media”. *Phys. Rev. C* **60** (6 1999), 064902. URL: `http://link.aps.org/doi/10.1103/PhysRevC.60.064902`.

[116] R. Baier et al. “Angular dependence of the radiative gluon spectrum”. *Phys. Rev. C* **64** (5 2001), 057902. URL: `http://link.aps.org/doi/10.1103/PhysRevC.64.057902`.

[117] Guang-You Qin et al. “Jet energy loss, photon production, and photon-hadron correlations at RHIC”. *Phys. Rev.* **C80** (2009), 054909. arXiv: `0906.3280 [hep-ph]`.

[118] Guang-You Qin et al. “Radiative jet energy loss in a three-dimensional hydrodynamical medium and high pT azimuthal asymmetry of pi0 suppression at mid and forward rapidity in Au+Au collisions at sNN=200 GeV”. *Phys. Rev.* **C76** (2007), 064907. arXiv: `0705.2575 [hep-ph]`.

[119] Guang-You Qin et al. “Radiative and collisional jet energy loss in the quark-gluon plasma at RHIC”. *Phys. Rev. Lett.* **100** (2008), 072301. arXiv: `0710.0605 [hep-ph]`.

[120] Peter Arnold, Guy D. Moore, and Laurence G. Yaffe. “Photon Emission from Ultrarelativistic Plasmas”. *Journal of High Energy Physics* **2001**.11 (2001), 057. URL: `http://stacks.iop.org/1126-6708/2001/i=11/a=057`.

[121] Peter Arnold, Guy D. Moore, and Laurence G. Yaffe. “Photon emission from quark-gluon plasma: complete leading order results”. *Journal of High Energy Physics* **2001**.12 (2001), 009. URL: `http://stacks.iop.org/1126-6708/2001/i=12/a=009`.

[122] Peter Arnold, Guy D. Moore, and Laurence G. Yaffe. “Photon and gluon emission in relativistic plasmas”. *Journal of High Energy Physics* **2002**.06 (2002), 030. URL: `http://stacks.iop.org/1126-6708/2002/i=06/a=030`.

[123] Korinna C. Zapp. “A Monte Carlo Model for Jet Evolution With Energy Loss”. PhD thesis. Combined Faculties for the Natural Sciences and for Mathematics of the Ruperto-Carola University of Heidelberg, Germany, 2008.

[124] J. F. Gunion and G. Bertsch. “Hadronization by color bremsstrahlung”. *Phys. Rev. D* **25** (3 1982), 746–753. URL: `http://link.aps.org/doi/10.1103/PhysRevD.25.746`.

[125] T. Gleisberg et al. “Event generation with SHERPA 1.1”. *Journal of High Energy Physics* **2009**.02 (2009), 007. URL: `http://stacks.iop.org/1126-6708/2009/i=02/a=007`.

[126] "Studies of QCD at e^+e^- centre-of-mass energies between 91 and 209 GeV". English. *The European Physical Journal C - Particles and Fields* **35**.4 (2004), 457–486. URL: `http://dx.doi.org/10.1140/epjc/s2004-01891-4`.

[127] Yuri L. Dokshitzer, Victor S. Fadin, and Valery A. Khoze. "Coherent Effects in the Perturbative QCD Parton Jets". *Phys. Lett.* **B115** (1982), 242–246.

[128] C. P. Fong and B. R. Webber. "Higher Order QCD Corrections to Hadron Energy Distributions in Jets". *Phys. Lett.* **B229** (1989), 289–292.

[129] Valery A. Khoze and Wolfgang Ochs. "Perturbative QCD approach to multiparticle production". *Int. J. Mod. Phys.* **A12** (1997), 2949–3120. arXiv: `hep-ph/9701421 [hep-ph]`.

[130] Korinna C. Zapp. Private Communication. 2016.

[131] Jorge Casalderrey-Solana, Jose Guilherme Milhano, and Paloma Quiroga-Arias. "Out of Medium Fragmentation from Long-Lived Jet Showers". *Phys. Lett.* **B710** (2012), 175–181. arXiv: `1111.0310 [hep-ph]`.

[132] Eric Braaten and Tzu Chiang Yuan. "Calculation of screening in a hot plasma". *Phys. Rev. Lett.* **66** (17 1991), 2183–2186. URL: `http://link.aps.org/doi/10.1103/PhysRevLett.66.2183`.

[133] Eric Braaten and Markus H. Thoma. "Energy loss of a heavy quark in the quark-gluon plasma". *Phys. Rev. D* **44** (9 1991), R2625–R2630. URL: `http://link.aps.org/doi/10.1103/PhysRevD.44.R2625`.

[134] Joerg Aichelin, Pol Bernard Gossiaux, and Thierry Gousset. "Gluon radiation by heavy quarks at intermediate energies". *Phys. Rev. D* **89** (7 2014), 074018. URL: `http://link.aps.org/doi/10.1103/PhysRevD.89.074018`.

[135] Hamza Berrehrah et al. "Dynamical collisional energy loss and transport properties of on- and off-shell heavy quarks in vacuum and in the Quark Gluon Plasma". *Phys. Rev.* **C90**.6 (2014), 064906. arXiv: `1405.3243 [hep-ph]`.

[136] Karen M. Burke et al. "Extracting the jet transport coefficient from jet quenching in high-energy heavy-ion collisions". *Phys. Rev.* **C90**.1 (2014), 014909. arXiv: `1312.5003 [nucl-th]`.

[137] Vardan Khachatryan et al. "Decomposing transverse momentum balance contributions for quenched jets in PbPb collisions at $\sqrt{s_{\mathrm{N\,N}}} = 2.76$ TeV". *JHEP* **11** (2016), 055. arXiv: `1609.02466 [nucl-ex]`.

[138] Vardan Khachatryan et al. "Measurement of transverse momentum relative to dijet systems in PbPb and pp collisions at $\sqrt{s_{\mathrm{NN}}} = 2.76$ TeV". *JHEP* **01** (2016), 006. arXiv: `1509.09029 [nucl-ex]`.

[139] Thorsten Renk. "Comparison study of medium-modified QCD shower evolution scenarios". *Phys. Rev. C* **79** (5 2009), 054906. URL: `http://link.aps.org/doi/10.1103/PhysRevC.79.054906`.

[140] M. Shimomura. "High- , η, identified and inclusive charged hadron spectra from {PHENIX}". *Nuclear Physics A* **774** (2006). {QUARK} {MATTER} 2005Proceedings of the 18th International Conference on Ultra-Relativistic Nucleus–Nucleus Collisions, 457 –460. URL: `http://www.sciencedirect.com/science/article/pii/S0375947406002971`.

[141] Marlene Nahrgang et al. "Azimuthal correlations of heavy quarks in Pb + Pb collisions at $\sqrt{s} = 2.76$ TeV at the CERN Large Hadron Collider". *Phys. Rev.* **C90**.2 (2014), 024907. arXiv: `1305.3823 [hep-ph]`.

[142] Jaroslav Adam et al. “Evolution of the longitudinal and azimuthal structure of the near-side jet peak in Pb-Pb collisions at $\sqrt{s_{\mathrm{NN}}} = 2.76$ TeV” (2016). arXiv: `1609.06667 [nucl-ex]`.

[143] Serguei Chatrchyan et al. “Studies of azimuthal dihadron correlations in ultra-central PbPb collisions at $\sqrt{s_{NN}} = 2.76$ TeV”. *JHEP* **02** (2014), 088. arXiv: `1312.1845 [nucl-ex]`.

[144] Alfred H. Mueller. “On the Multiplicity of Hadrons in QCD Jets”. *Phys. Lett.* **B104** (1981), 161–164.

[145] B. I. Ermolaev and Victor S. Fadin. “Log - Log Asymptotic Form of Exclusive Cross-Sections in Quantum Chromodynamics”. *JETP Lett.* **33** (1981). [Pisma Zh. Eksp. Teor. Fiz.33,285(1981)], 269–272.

[146] Andrew J. Larkoski et al. “Soft Drop”. *JHEP* **05** (2014), 146. arXiv: `1402.2657 [hep-ph]`.

[147] *Splitting function in pp and PbPb collisions at 5.02 TeV*. Tech. rep. CMS-PAS-HIN-16-006. Geneva: CERN, 2016. URL: `http://cds.cern.ch/record/2201026`.

Appendix A

Partie française de la thèse

L'un des buts principaux de la thèse est de trouver des moyens pour discriminer les mécanismes de la perte d'énergie des partons dans le milieu chaud d'un plasma de quarks et de gluons (PQG) avec des corrélations de deux particules comme observables principaux. Ci-dessous se trouve le résumé de la thèse en français. Nous commençons par éxpliquer les notions de base (Sec. A.1), ensuite la problèmatique (Sec. A.2), les méthodes utilisées (Sec. A.3), les résultats (Sec. A.4), ainsi que leur conséquences et des questions encore ouvertes (Sec. A.5).

A.1 Production de quarks lourds dans les collisions d'ions lourds

A.1.1 La théorie de l'interaction forte: La chromodynamique quantique

La matière peut être décrite par des particules différentes, par exemple des protons p et neutrons n. Ils constituent les noyaux des atomes et ils sont membres d'une plus grande famille des particules: les hadrons. Après la découverte d'un grand nombre d'hadrons différents, souvent groupés par leur masses en baryons (par exemple les p et n) et mésons (qui sont généralement plus légers; par exemple les pions π et les mésons D). On a cherché pour un procedé systematique pour classer tous ces particules. Finalement on a prouvé, que les hadrons sont eux-mêmes des états composés, constitués par des particules appelées quarks. Ces derniers sont confinés par l'interaction forte, qui est transmise par l'échange d'autres particules: les gluons. Pour des raisons historiques, les quarks et les gluons sont appelés les partons.

Les quarks ont une charge qui existe en trois variations différentes; cette propriété a été appelée couleur et on peut identifier des quarks "rouges", "verts", et "bleus". Les hadrons existent que dans la forme des états qui sont neutre en couleur, ou "blancs". La théorie qui décrit les hadrons comme des états composés de particules avec couleurs est appelée la chromodynamique quantique (CDQ), d'après le mot grec pour couleur "chroma". Il est une particularité de cette théorie, que les gluons qui transmettent le couleur portent eux-mêmes de la couleur. Par conséquent, les gluons peuvent interagir avec d'autres gluons, ainsi qu'avec des quarks. La CDQ connait donc les interactions suivantes:

En plus de la couleur, les quarks existent en plusieurs types, nommés "saveurs". Six saveurs sont connus: up (u), down (d), strange (s), charm (c), bottom (b), et top (t). Après chacunes de masses différentes les trois premières saveurs sont appelés les saveurs légères, tandis que les autres trois sont appelés les saveurs lourdes.

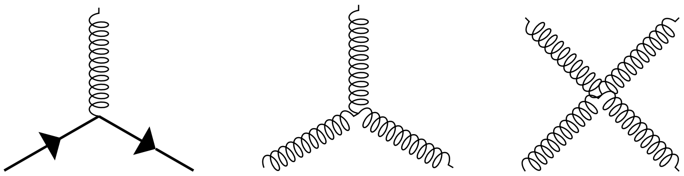

Figure A.1: Symbolisation des interactions fondamentales entre quarks (lignes droites avec des flèches) et gluons (spirales). La direction du temps dans ces diagrammes n'a pas été spécifié: Toutes les combinaisons de particules incidentes et sortantes possibles sont permites.

A.1.2 Les sondes dures pour le diagramme de phase

Le couplage entre les partons n'est pas une constante et dépend de la largeur des changements des impulsions que les partons subissent. A grande échelle le couplage devient faible, un comportement appelé liberté asymptotique.

Pour des cas de faible couplage, on peut s'imaginer un nouvel état de matière où les quarks et les gluons peuvent se propager à de grandes distances (i.e. plus grandes que les largeurs typiques des hadrons) quasiment libre. Les partons ne sont pas confinés mais interagissent plutôt par diffusion avec d'autres partons de ce milieu. Cet état est appelé le plasma de quarks et de gluons.

Pour comprendre dans quelless conditions ce PQG peut exister, on peut étudier le diagramme de phase de CDQ. A de faibles températures T et depotentielles chimiques μ, la matière est confinée dans les états liés des hadrons. A de grandes valeurs de T et/ou μ on suppose qu'il existe le PQG[1]. On suppose que la condition à grand T a eu lieu dans les premières millisecondes après la création de l'univers, tandis que les états de matière à grand μ peuvent être réalisés dans les étoiles à neutrons.

On peut essayer de récréer le PQG par des collisions d'ions lourdes. On possède des évidences, que le PQG se forme dans l'expérience des collisions à grandes énergies. Ce milieu n'existe que pour des temps et des extensions spatiales d'une échelle de quelques fm (fm/c).

Pour étudier les propriétés du PQG, on a besoin des sondes particulières, qui ne se thermalisent pas avec le milieu. Une possibilité est donnée par des quarks des saveurs lourdes, b et c, qui traversent le milieu de PQG et formeront des mésons lourdes. On pourrait également étudier les partons légers à hautes énergies, ce qui résulte dans des particules chargés. Les interactions de ces sondes dures s'expriment aussi par une perte d'énergie dans le milieu. Des observables additionnelles peuvent être obtenues, si on considère plusieurs particules corrélées. Si elles se propagent avec de grandes impulsions, très focalisées autour d'une direction commune, on parle de jets. Les sondes dures peuvent être créees dans les collisions d'ions lourds.

A.2 La problematique

Il existe plusieurs modèles qui décrivent la perte d'énergie avec des combinaisons de perte d'énergie collisionelles et radiatives. Jusqu'à présent, il n'a pas encore été clarifié quel(s) type(s) de processus domine(nt) les interactions d'une particule dans une gerbe avec le milieu de PQG. L'intérêt principal de cette thèse est de trouver des observables pour

---

[1] Par conséquence entre ces deux régimes on peut déduire qu'il doit exister soit une transition de phase (estimé autour d'une température critique $T_c \approx 170$ MeV pour le cas de petits μ), soit des milieux où les deux phases sont présentes en même temps (appelé un "cross-over" des phases).

pouvoir identifier les contributions des mécanismes collisionnels et radiatifs de la perte d'énergie d'une particule dans le milieu.

L'ignorance générale sur les mécanismes microscopiques de perte d'énergies se manifeste aussi dans les observables de collisions d'ions lourds. Un exemple qui est souvent discuté dans la littérature est donnée par la combinaison des observables du facteur de modification nucléaire R_{AA} et de l'ecoulement elliptique v_2. Le R_{AA} est défini comme:

$$R_{\mathrm{AA}} = \frac{N_{\mathrm{AA}}}{\langle T_{\mathrm{AA}} \rangle \sigma_{PP}}\,, \tag{A.1}$$

où N_{AA} est le nombre de particules produites dans les collisions d'ions lourds, $\langle T_{\mathrm{AA}} \rangle$ la fonction de recouvrement nucléaire, et σ_{PP}, la section efficace pour la production de particules dans les collisions de protons. Donc, le R_{AA} représente le ratio entre les nombres de particules produites (à un certain p_T, centralité donnée, etc.) dans les collisions d'ions lourds et de protons.

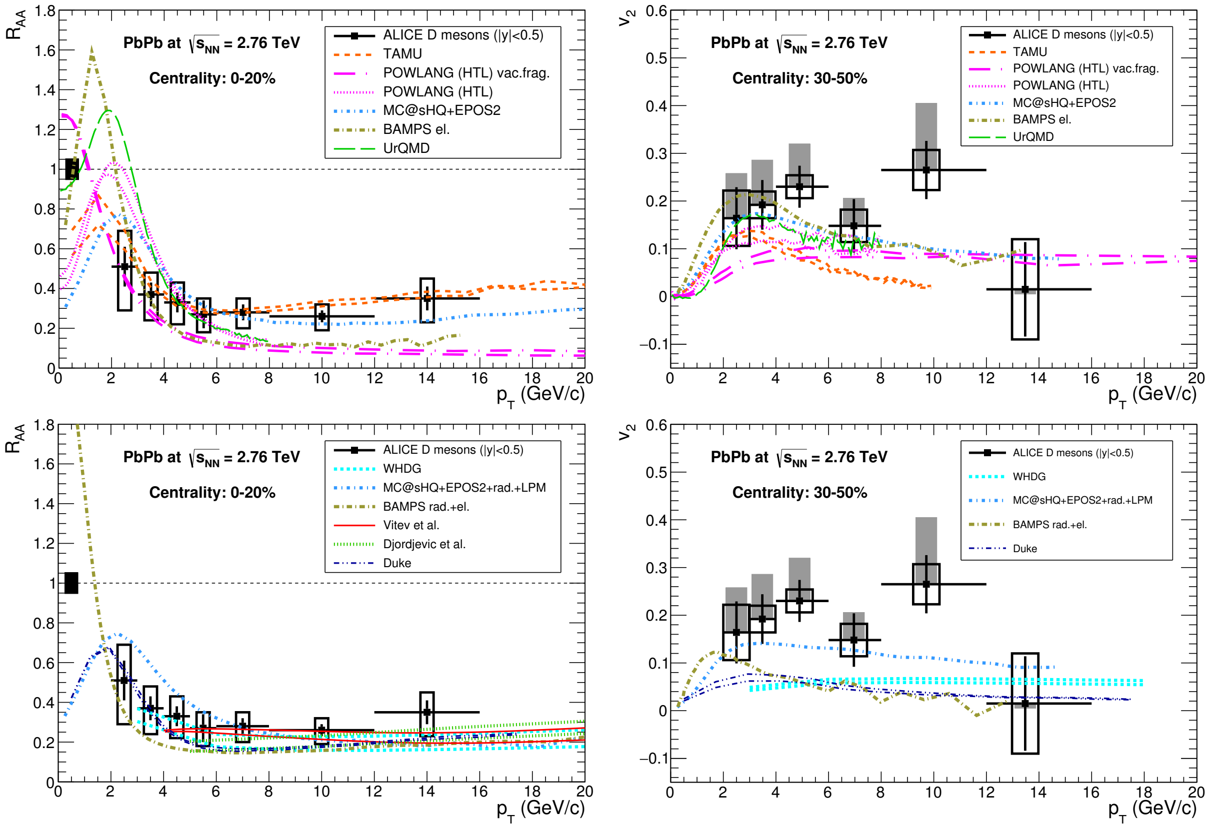

Figure A.2: Facteur de modification nucléaire (à gauche) et ecoulement élliptique (à droite) pour des mesons-D promptes, obtenues dans des collisions Pb-Pb en comparaison avec des modèles théoriques, qui utilisent seulement la perte d'énergie collisionnelles (en haut), ou une combinaison des mécanismes collisionels et radiatifs (en bas). La figure a été prise de la Ref. [19].

Le v_2 est défini comme le deuxième coefficient d'une évolution en série de Fourier de la distribution en angle azimutale ϕ (défini par rapport au plan d'évènement) des particules détectées après des collisions d'ions lourds, $\frac{d^2N}{dp_T d\phi}$. L'observation d'une anisotropie se fait par la mésure du v_2, car si $v_2 = 0$, les particules pourraient être émises dans tous les angles sur le plan d'évènement. Le v_2 positif à petit p_T peut être interprété comme un signal pour des effets collectifs d'un milieu (par exemple une expansion anisotrope). Des valeurs positives de v_2 à grand p_T peuvent indiquer que la perte d'énergie est anisotrope. La

Fig. A.2 montre la combinaison des observables R_{AA} et v_2 – des données expérimentales d'ALICE ainsi que des résultats théoriques des modèles basé sur des mécanismes de perte d'énergie radiative ou sur des combinaisons des mécanismes radiatifs et collisionels. On peut voir que la plupart des modèles peut reproduire une des deux observables plus précisément que l'autre. En générale, si les valeurs pour R_{AA} sont trop grandes, celles pour v_2 sont trop petites, et vice versa. Il suit de cette observation, que la combinaison des observables R_{AA} et v_2 est un moyen très dépendant aux modèles différentes de la perte d'énergie dans le milieu. On remarque que dans la Fig. A.2, il y a beaucoup de modèles qui reproduisent des valeurs pour R_{AA} et v_2 qui sont simultanément dans les barres d'erreurs. Donc, il est nécessaire de trouver des observables alternatives, qui permettraient de distinguer ces modèles plus précisément. Pour cela les corrélations entres des paires de particules de gerbes ont été proposées récemment. Le R_{AA} et le v_2 mesurent une multitude d'impulsions de particules individuelles. Tandis que les objets mesurés pour les corrélations de deux particules sont les impulsions de paires de particules. Même si on peut reproduire les mêmes taux de perte d'énergie avec des processus radiatifs, ainsi qu'avec des combinaisons de mécanismes radiatifs et collisionels. Le nombre de paires de particules augmente pendant les processus radiatifs tandis qu'il reste invariant pendant les collisions de deux particules initiales (de la gerbe et du milieu) vers deux particules finales. Cette argumentation est reprise dans cette thèse. Elle comprend les corrélations entre des particules lourdes et légères dans la gerbe – plus précisément les corrélations angulaires – comme moyens pour discriminer les mécanismes radiatifs et collisionnels dans le PQG.

A.3 Méthodes

Afin de pouvoir décrire les corrélations entre des paires des particules dans des sondes dures on est suivi la notion de trouver, tout d'abord, une méthode pour construire la gerbe des particules contenant les paires dont on déterminera les corrélations. Pour les processus considérés, les transferts d'impulsions (mesuré par les virtualités Q^2 dans la suite) sont très grands comparés à l'échelle de confinement de CDQ: $\Lambda_{\mathrm{QCD}} \approx 200$ MeV. Cependant, on peut appliquer des méthodes perturbatives de la chromodynamique quantique pour pouvoir décrire la création des particules de la gerbe. Il faut bien noter que les particules créées dans la gerbe sont mesurées comme des état liés hadroniques. La formation de ces états liés a lieu dans des processus de petite virtualité, de l'ordre de grandeur de Λ_{QCD}. Donc, elle ne peut pas être décrite par des méthodes perturbatives. Néanmoins, on peut décrire les gerbes de particules créées dans des collisions d'ions lourds avec bonne approximation, si on se concentre sur des processus perturbatives en négligeant l'hadronisation, en utilisant les règles suivantes:

- les particules dures, dont on veut connaitre les corrélations, sont créées dans les processus durs, perturbatifs, et sont juste soumises par la suite à des processus d'hadronisation.

- dans les processus d'hadronisation on peut argumenter que les impulsions de partons de la gerbe correspondent approximativement aux impulsions des hadrons, car on observe une conservation globale des impulsions dans ces processus. Puisque l'on se concentre sur des corrélations entre des impulsions pendant cette thèse on assume cet argument valide.

Si on considère les processus d'émission de partons par des autres partons de manière perturbative, on note que les mécanismes de rayonnement dominantes sont:

- le rayonnement de particules à basse énergies (”mous”)
- le rayonnement de particules à petite angle par rapport à la particule incidente (”colinéaires”).

Pendant l'évolution des partons, les processus de rayonnement mous et colinéaires se répètent plusieurs fois, menant à une cascade de partons. Afin de décrire ces cascades, on peut d'abord considérer des processus qui émettent (au moins) un parton, qui – soi-même – émet une autre parton dans un rayonnement colinéaire. On note que l'on peut factoriser ce processus en une partie qui décrit la création d'un parton intermédiaire, et en une partie qui décrit l'embranchement de ce parton en deux (cf. Fig. A.3). Donc, ce dernier processus peut être considéré indépendant du premier.

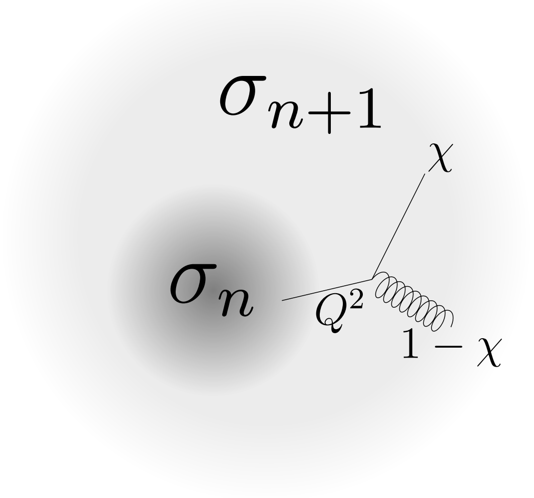

Figure A.3: Illustration d'un embranchement: factorisation de la section efficace, σ_{n+1}, d'un processus qui produit $n+1$ particules en la section efficace d'un processus qui produit n particules, σ_n, et un embranchement additionnel où les particules produites portent une fraction χ $(1-\chi)$ de l'impulsion de la particule qui se désintègre et possède une virtualité Q.

Une densité de probabilité

$$\frac{1}{Q^2}\frac{\alpha_s(F(\chi,Q))}{2\pi}P(\chi)\,, \tag{A.2}$$

est associée à cet embranchement, qui dépend de la virtualité Q de la particule intermédiaire, et de la fraction χ d'impulsion de la particule émise (cf. Fig. A.3). $P(\chi)$ est appelée la fonction de splitting. Dokshitzer, Gribov, Altarelli, et Parisi (DGLAP [82, 83]) ont trouvé que les embranchements colinéaires successifs peuvent être ressommés par des équations d'évolution en virtualité, les équations DGLAP:

$$\frac{dD(\chi,\,Q,\,m)}{d\ln(Q^2)} \simeq \int \frac{dz}{z} D(\frac{\chi}{z},\,Q,\,m)P(z)dz\,. \tag{A.3}$$

Les fonctions de fragmentation $D(\chi,Q^2)$ représentent les densités de nombres de partons rayonnés avec une certaine fraction d'impulsion à l'échelle Q^2 de virtualité carré.

Cette thèse utilise la méthode suivante: dans le vide, les équations DGLAP sont résolues par des simulations Monte-Carlo. C'est à dire que les fonctions de fragmentation sont approximées par des distributions sur un large nombre de partons dans un large nombre des gerbes différentes. On considère des particules incidentes à une certaine échelle d'énergie E_{ini} et à une virtualité maximale $Q_\uparrow$ qui peuvent créer des gerbes de particules. L'évolution en virtualité selon les fonctions de splitting est interprétée de manière suivante: les fonctions de splitting représentent une densité de probabilité d'embranchement, avec cette densité de probabilité on décide, si un parton peut se fragmenter ou non. Dans le milieu, des modèles effectives sont appliqués aux gerbes.

A.3.1 L'approche dans le vide

Pour les cascades dans le vide, on implémente l'algorithme suivant:

0. Pour la particule initiale, on fixe sa virtualité maximale $Q_\uparrow$ et sa énergie E_{ini}.
1. Pour cette particule initiale, on sélectionne sa virtualité Q_1. Puis on utilise les variables cinématiques qui décrivent la particule "a" qui peut se fragmenter – cidedans sa virtualité Q_a – pour décrire les embranchements suivantes.
2. Si la virtualité Q_a (ou Q_1) est plus grande que le seuil $Q_\downarrow$ ce parton se fragmente, autrement non.
3. S'il y a un embranchement, on en détermine les particules, i.e.: un quark plus un gluon, deux gluons, ou une paire quark antiquark.
4. Dans une boucle de réjection des quadri-impulsions pour des partons rayonnés, b et c sont déterminées: Les virtualités Q_b et Q_c sont sélectionnées, puis la fraction d'impulsion χ. Pour la combinaison des valeurs Q_a, Q_b, Q_c, et χ on calcule $k_\perp$, la composante des tri-impulsions les particules b et c qui est orthogonale par rapport à la tri-impulsion de la particule a. Un embranchement est accepté, si la condition $k_\perp^2 \geq 0$ est satisfaite. Autrement l'embranchement sera rejeté et la boucle recommence.
5. On sélectionne un angle azimutale des tri-impulsions des particules b et c par rapport à la tri-impulsion de la particule a.
6. On calcule les composantes manquantes pour pouvoir décrire les quadri-impulsions des particules b et c.
7. Les pas 1. à 6. sont répétés pour les particules b et c. Ainsi, l'algorithme est répété génération par génération. Par la suite on va appeler "génération n" toutes les particules qui sont créées à partir du particule initiale par n embranchements. Si toutes les particules d'une génération ont une virtualité plus basse que le seuil $Q_\downarrow$, l'algorithme se termine.

Cette algorithme sera répété plusieurs fois afin de créer un nombre de cascades suffisamment grand. Pour cette thèse des ensembles de 10^5 à 10^6 cascades ont été simulés.

Les fractions d'impulsion χ sont sélectionnées selon les fonctions de splitting comme densité de probabilité, ou selon la fonction de partition suivante:

$$W_{a\to b,c}(Q_a,\chi) := \int_{\chi_-}^{\chi} d\tilde{\chi} \left(\frac{\alpha_s(F(\tilde{\chi},Q_a^2))}{2\pi} P_{a\to b,c}(\tilde{\chi}) \right) , \tag{A.4}$$

Les virtualités Q_a sont sélectionnées selon la fonction de partition suivante

$$S_a(Q_{a\uparrow},Q_a) = \exp\left(-\int_{Q_a^2}^{Q_{a\uparrow}^2} \frac{dQ^2}{Q^2} \int_{\chi_-}^{\chi_+} d\chi \frac{\alpha_s(F(\chi,Q))}{2\pi} \sum_{a\to b,c} P_{a\to b,c}(\chi) \right) . \tag{A.5}$$

La fonction ci-dessus est aussi appelé le facteur de forme de Sudakov. Elle est interprétée comme la probabilité qu'il n'y a pas de splitting pour les virtualités dans l'intervalle $[Q_a, Q_{a\uparrow}]$. En ce qui concerne les bornes supérieures des virtualités (indiqué par la flèche $\uparrow$), on se rend compte que les gerbes que l'on considère sont des processus "timelike", c'est à dire des virtualités décroissantes. Cependant, on prend la virtualité de la particule qui se désintègrent comme borne supérieure pour les virtualités de ses produits, e.g.: $Q_{b\uparrow} = Q_{c\uparrow} = Q_a$. Pour les angles azimutales, on considère des distributions uniformes. Des corrélations entre des angles azimutales des embranchements successives existent, mais sont faibles (cf. Ref. [91], ch. 5).

A.3.2 Les approches dans le milieu

Pour le milieu, on cherche à trouver des modèles qui peuvent décrire soit des effets radiatives, soit des effets collisionnels, soit des combinaisons de ces effets.

L'approche de YaJEM [105] représente un modèle effectif qui simule la perte d'énergie radiative par des gains en virtualités carrés $\hat{q}_R$ que les particules intermédiaires de la gerbe accumulent pendant leur propagation dans le milieu. Cependant, le nombre des embranchements est augmenté car les intervalles de virtualités dans lesquelles il peut se passer un embranchement ont été élargis par rapport au vide plusieurs fois pendant l'évolution de la cascade.

Le principe simple du modèle YaJEM est que les effets du milieu sur l'évolution de la gerbe sont simulés par des changements des quadri-impulsions des particules de gerbes. Donc, on pourrait utiliser une approche analogue pour simuler les effets des processus de perte d'énergie collisionnel comme des actions des forces sur les particules de la gerbe, i.e.: des échanges tri-impulsions. Tandis qu'un modèle comme YaJEM, ou un modèle qui contient aussi des effets collisionnels inspiré par YaJEM, est très simpliste, le principe de changer dans le milieu que les quadri-impulsions des particules de gerbes permet d'étudier et puis comparer les effets du milieu d'une manière pertinente. C'est pour cette raison que l'on a choisi ce type de modèle.

En ce qui concerne la force effective, qui peut être construite pour un modèle,qui décrit des effets collisionnels, on a considéré deux types de forces:

- une force de frottement $\vec{A}$ longitudinale, qui fait décroitre la composante de l'impulsion longitudinale (i.e. parallèle à l'impulsion du particule incidente)
- une force transverse stochastique qui agit en direction orthogonale de l'impulsion du particule incidente.

Le transfert des impulsions transverses $\hat{q}_C$ a été relié à la valeur absolue de la force de frottement $\vec{A}$ par une ratio entre deux sections efficaces de diffusion pour des particules de la gerbe: une section efficace pour la diffusion ultra-relativiste dans un potentiel, une autre pour la perte de l'impulsion longitudinale dans un potentiel [135]. On a supposé que $\hat{q}_R = \hat{q}_C$ et on a utilisé un fit [105] du résultat d'un calcul hydrodynamique, qui parametrise $\hat{q}_R$ comme une fonction de temps t.

Pour cette thèse, on a considéré quatre modèles effectives, qui simulent des effets collisionnels et radiatifs:

- modèle A (appelé "inelastic"), qui simule la radiation induite par le milieu avec une augmentation du carré de la virtualité avec le temps, et est basé sur une version ancienne de YaJEM [105],
- modèle B (appelé "elastic"), qui simule les processus de la perte d'énergie collisionnelle,

- modèle C, qui est un modèle hybride et contient des effets radiatifs dans la façon dont il sont simulés dans le modèle A, ainsi que la force de frottement $\vec{A}$, mais qui ne contient pas la force transverse stochastique,
- modèle D, qui est aussi un modèle hybride, qui contient les effets radiatifs et la force de $\vec{A}$ également, mais aussi la force transverse stochastique.

Afin de mésurer pour le taux d'interaction entre les particules de la gerbe et du milieu, on reprend la notation de la Ref. [105]:

$$\Delta Q^2 := \int_{t_0}^{t_f} \hat{q}_R(t)dt\,, \tag{A.6}$$

ΔQ^2 est l'augmentation en virtualité carré d'une particule qui traverse le milieu du centre (on a utilisé $t_0 = 0$) jusqu'à l'extérieur du milieu (où on suppose que la frontière entre le milieu et son extérieur se situe à distance $t_f = L$ de son centre), sans avoir fait aucun embranchement. Pour le modèle élastique, cette définition ne fait pas de sens. Par conséquent, on a défini ΔQ^2 comme l'intégralle sur $\hat{q}_C$ au lieu de $\hat{q}_R$.

A.3.3 Validation, etalonnage, et tendances des observables

A.3.3.1 Dans le vide

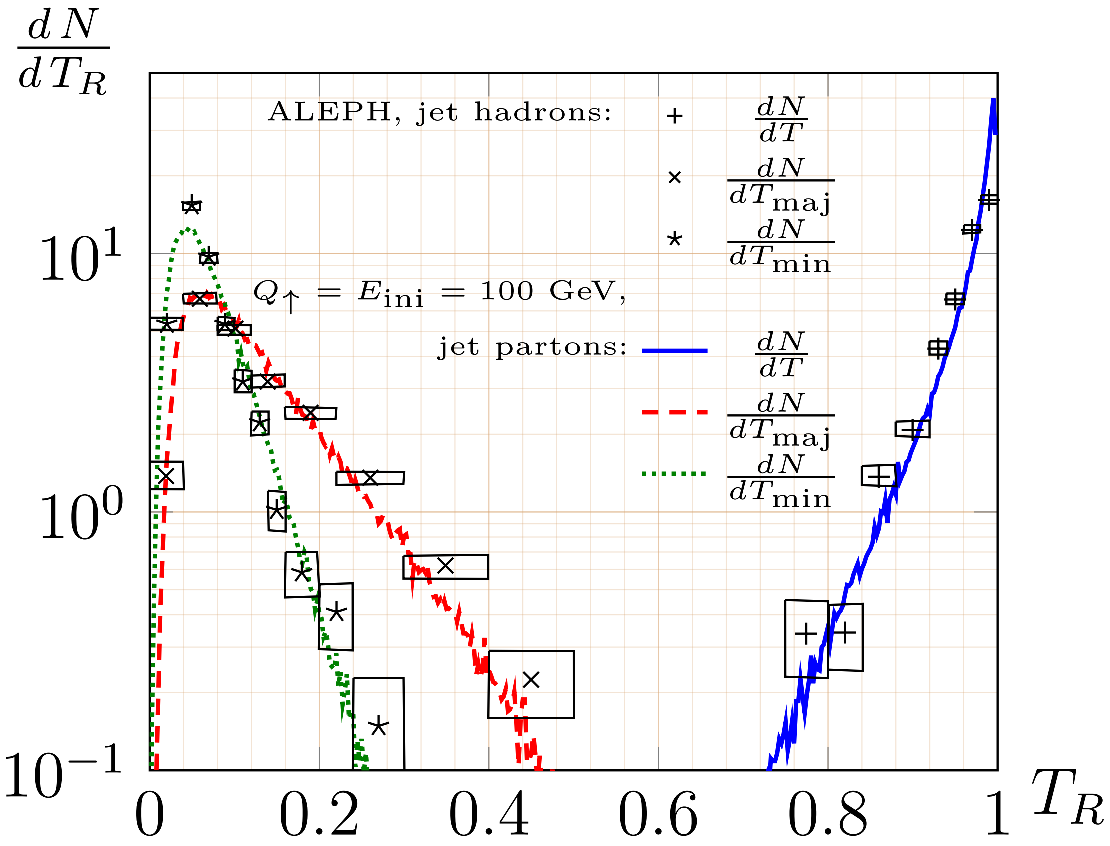

Figure A.4: T, T_{maj}, et T_{min}, obtenus par des simulations Monte-Carlo pour des jets avec une énergie totale et virtualité maximale de 100 GeV, en comparaison avec des données d'ALEPH [126] pour des collisions $e^+ + e^-$ avec $\sqrt{s} = 200$ GeV.

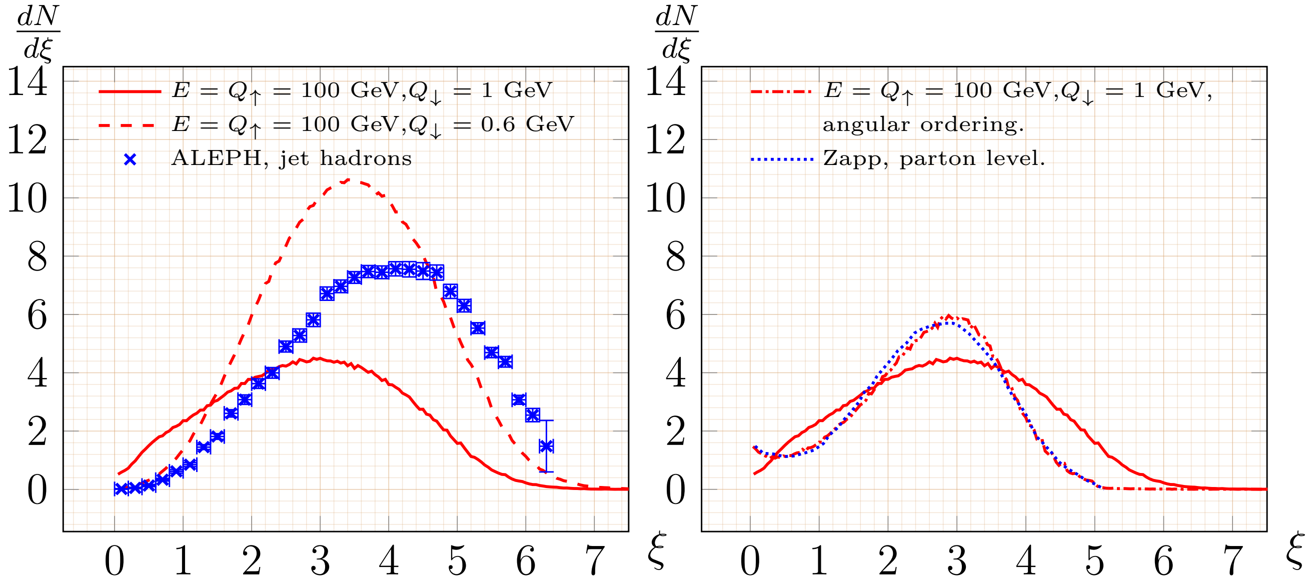

Figure A.5: Humped-back plateau distributions. A gauche: résultats des simulations Monte Carlo pour des jets avec une énergie totale et virtualité maximale de 100 GeV, en comparaison avec data d'ALEPH [126] pour des collisions $e^+ + e^-$ avec $\sqrt{s} = 200$ GeV. A droite: résultats pour $Q_\downarrow = 1$ GeV sans (rouge solide) et avec (rouge tirés-pointillés) ordonnancement angulaire en comparaison des résultats correspondantes par Zapp [123].

Pour gagner un image qualitatif des jets avec notre algorithme on suit la stratégie suivante; On considère un type d'observable, qui est très stable par rapport à la distribution moyenne des impulsions – c'est à dire, la forme globale des jets, négligeant des effets des rayonnements mous. Ensuite, on considère une autre observable qui est dépendant par rapport aux effets de la radiation molle. Pour le premier type on a considéré les variables des thrust T, thrust majeur T_{maj}, et thrust mineur T_{min}, pour le deuxième type on a utilisé la distribution appelé "humped-back plateau distribution", $\frac{dN}{d\xi}$.

T, T_{maj}, et T_{min} sont défini dans la façon suivante:

$$T = \max_{\vec{n}} \frac{\sum_i |\vec{p}_i \cdot \vec{n}|}{\sum_i \|\vec{p}_i\|}\,, \qquad T_{\mathrm{maj}} = \max_{\substack{\vec{n}_2 \\ \vec{n}_2 \cdot \vec{n} = 0}} \frac{\sum_i |\vec{p}_i \cdot \vec{n}_2|}{\sum_i \|\vec{p}_i\|}\,, \qquad T_{\mathrm{min}} = \frac{\sum_i |\vec{p}_i \cdot \vec{n}_3|}{\sum_i \|\vec{p}_i\|}\,, \tag{A.7}$$

Ces observables peuvent décrire la forme d'un ensemble des particules rayonnés dans un évènement, parce que les particules émises dans les mêmes directions, ou dos-à-dos représentent un évènement avec $T = 1$, $T_{\mathrm{maj}} = T_{\mathrm{min}} = 0$, tandis qu'un évènement où les particules sont émises uniformément dans toutes les directions correspond à $T = T_{\mathrm{maj}} = T_{\mathrm{min}} = \frac{1}{2}$. Si on considère tous les cas intermédiaires, on voit que ce type d'observable montre les ouvertures angulaires par rapport aux axes des jets, pondérés par leurs impulsions.

La Fig. A.4 montre les distributions en T, T_{maj}, et T_{min} pour des jets initialisés par des quarks de $Q_\uparrow = E_{\mathrm{ini}} = 100$ GeV comparés aux mesures de l'expérience ALEPH pour des collisions d'électrons et positons à une énergie dans le système de centre d'impulsions de 200 GeV. On peut voir, qu'il y a en générale un bon accord de manière qualitative entre les résultats théoriques (obtenu pour des partons) et expérimentaux (où on a mesuré des hadrons chargés). Par définition, T, T_{maj}, et T_{min} sont des observables, qui sont indépendents par rapport aux rayonnements des particules molles. Ce n'est pas une surprise car les effets de l'hadronisation ou le choix précis du seuil inférieur de virtualité, $Q_\downarrow$, ne jouent qu'un rôle négligeable.

La ”humped-back plateau distribution” est une distribution de nombres des particules avec une certaine valeur de ξ – une variable définie comme:

$$\xi = -\ln\left(\frac{\|\vec{p}_{\text{particle}}\|}{E_{\text{total}}}\right) . \tag{A.8}$$

$\frac{dN}{d\xi}$ représente une distribution en énergies de partons, mais élargit particulièrement les contributions des particules molles. Cependant, elle est très sensible par rapport aux seuils de virtualités $Q_{\downarrow}$ comme la partie gauche de la Fig. A.5 démontre. Une fois encore, nous avons comparé avec des données d'ALEPH, par contre on ne peut pas reproduire ces données. La Ref. [123] note que les processus de l'hadronisation, qui se passent à basses énergies, y jouent une grande rôle. On n'a pas implémenté un modèle d'hadronisation. Par contre, on peut comparer les résultats de l'algorithme de cette thèse avec des résultats pour les partons finaux (juste avant l'hadronisation), que la Ref. [123] a obtenu. Dans cette référence, un modèle d'hadronisation a été utilisé et les résultats d'ALEPH ont pu être reproduits. La partie droite de Fig. A.5 compare des résultats de la Ref. [123] et de l'algorithme de cette thèse: Si on n'utilise pas des conditions pour renforcer de l'ordonnancement angulaire, il n'y a pas de concordance avec les résultats de la Ref. [123]. Si on utilise les mêmes conditions pour implémenter l'ordonnancement angulaire [130], on peut reproduire les résultats de la Ref. [123][2]. Outre que cette comparaison avec la Ref. [123], on n'a jamais utilisé les conditions d'ordonnancement angulaire pour des raisons de simplicité.

A.3.3.2 Dans le milieu

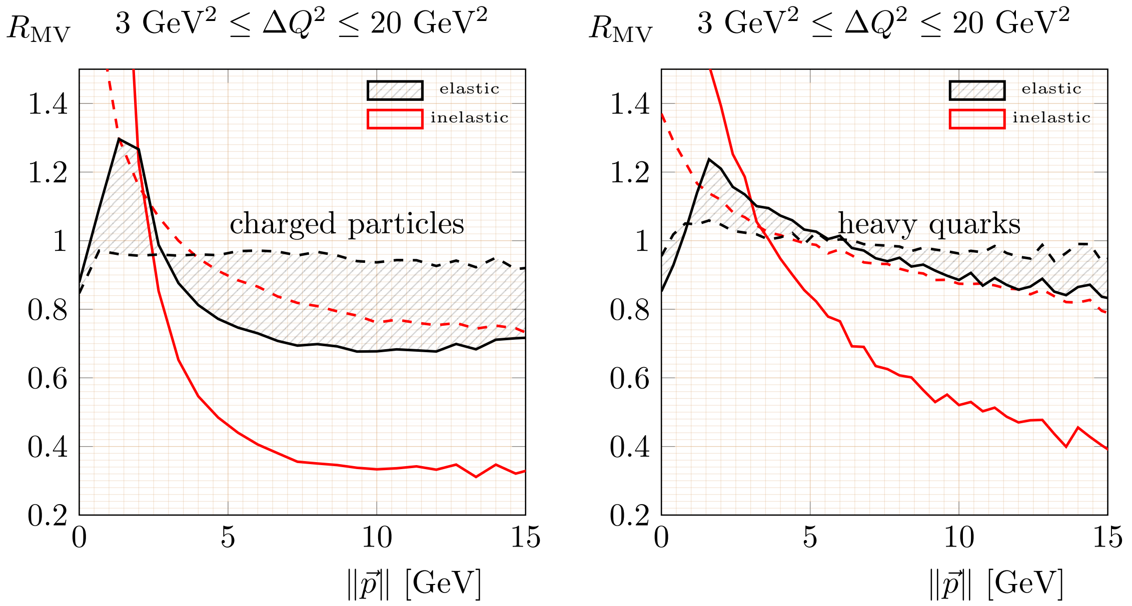

Figure A.6: Estimation R_{MV} de la facteur de modification nucléaire, R_{AA}, dans des milieux avec des ΔQ^2 entre 3 GeV^2 (tirés) et 20 GeV^2 (solides). A gauche: particules légers/chargés. A droite: Quarks lourds.

En principe, pour les cascades dans le milieu, les mêmes considérations jouent une rôle que dans le vide. Par contre, il faut séparer les particules des gerbes de leur arrière plan

---

[2] L'ordonnancement angulaire correspond à une effet d'interférence: On a trouvé que des types de cascades sont dominant, où l'angle de embranchement décroit d'embranchements successifs.

des hadrons, qui ont leurs origines dans les particules thermalisées du milieu. Ici nous n'avons pas affiché les résultats correspondants pour le milieu, mais plutôt les observables qui ont souvent été mesuré: les facteurs de la modification nucléaire, R_{AA}. On a estimé ce facteur par un ratio entre particules produites dans le milieu et dans le vide: R_{MV}. La Fig. A.6 donne des résultats pour R_{MV} de particules chargés (partie gauche) et de quarks lourds (partie droite) pour les modèles A et B. En comparaison avec l'expérience [140], les valeurs sont trop élevées. Dans la Ref. [105], les données de PHENIX ont été reproduites, par contre le taux d'interaction a été parametrisé à ces résultats. On trouve le même comportement des R_{MV} et les résultats dans la Ref. [105]. Donc, si on avait parametrisé ΔQ^2 sur des données de PHENIX on aurait pu le reproduire. Mais ce n'était pas le but de cette thèse.

Un fait plus intéressant est que les mêmes valeurs en R_{MV} peuvent être produites par différents modèles. Il y a des régions au delà de 3 GeV dans la Fig. A.6, où les courbes pour les modèles A et B sont très proches, voir identiques. Ce n'est pas un problème pour les particules légères, où l'on peut identifier les mécanismes différents par le comportement des courbes aux basses impulsions. Mais cela devient un problème pour les quarks lourds, où les impulsions sont fortement plus grandes que les masses, qui sont déjà élevées à $m_c \approx 1.5$ GeV. Ces observations correspondent à la problématique introduite dans la Sec. A.2.

A.4 Résultats

Cette thèse a étudié les corrélations à deux particules. En particulier, nous avons consideré des paires de particules dans les gerbes de quarks lourds créées avec l'algorithme Monte-Carlo. Dont le quark lourd initial (en état finale) appelé la particule "trigger" est associée avec n'importe quel autre parton final dans la même cascade. On a calculé les distributions sur des angles $\Delta\theta$, l'angle entre les quadri-impulsions du particule trigger et associé[3]. On a remarqué dans plusieurs phases de travaux sur les résultats de l'algorithme Monte-Carlo, que les énergies des particules émises à grands angles sont considérablement différentes selon les modèles effectifs. Maintenant, on va démontrer cette observation qualitative par les valeur moyennes de $\Delta\theta$: On a considéré une valeur minimale $\|\vec{p}\|_{\mathrm{cut}}$ pour les valeurs absolues des tri-impulsions des partons trigger et associés. Cependant, si chacune des deux particules d'une paire a une tri-impulsion avec une valeur absolue plus grande que $\|\vec{p}\|_{\mathrm{cut}}$, le paire des particule contribue dans le calcul de $\langle\Delta\theta\rangle$. La valeur $\Delta\theta$ est moyennée sur toutes les paires qui satisfassent la condition donnée par $\|\vec{p}\|_{\mathrm{cut}}$.

Fig. A.7 montre $\langle\Delta\theta\rangle$ en fonction de $\|\vec{p}\|_{\mathrm{cut}}$ pour les quatre modèles effectifs en comparaison avec les comportement dans le vide: Il semble que l'allure de la contribution additionnelle (par rapport au vide), dans le milieu n'est pas la même pour tous les milieux. Pour les modèles A et C, où les effets de milieu sont la radiation induite ou la combinaison d'une radiation induite et une force de frottement, il y a un grand élargissement angulaire à petits $\|\vec{p}\|_{\mathrm{cut}}$, i.e.: l'émission des particules molles représente une grande contribution à l'élargissement angulaire. A grand $\|\vec{p}\|_{\mathrm{cut}}$ on remarque des angles moyens proche aux valeurs pour le vide.

Pour les modèles B et D on aperçoit que l'élargissement angulaire est moins dépendant par rapport à la coupure $\|\vec{p}\|_{\mathrm{cut}}$. On note, que les modèles B et D sont aussi les deux modèles qui contiennent la force transverse stochastique. De ce fait, les contributions de la force transverse expliquent la plupart des différences entre les allures des modèles B et

---

[3] Parmi plusieurs autre résultats produits, on a juste mentionné les résultats pour les distributions en $\Delta\theta$, pour des raisons de brèveté de ce résumé, puisqu'il s'agit ici d'un des résultats principaux de la thèse.

D en comparaison des modèles A et C, car le modèle C contient tous les effets du milieu du modèle D, sauf la force transverse.

Les angles moyens $\langle \Delta\theta \rangle$ en fonction d'une coupure $\|\vec{p}\|_{\mathrm{cut}}$ peuvent être utilisés comme moyen pour distinguer les mécanismes de la perte d'énergie collisionnels et radiatives.

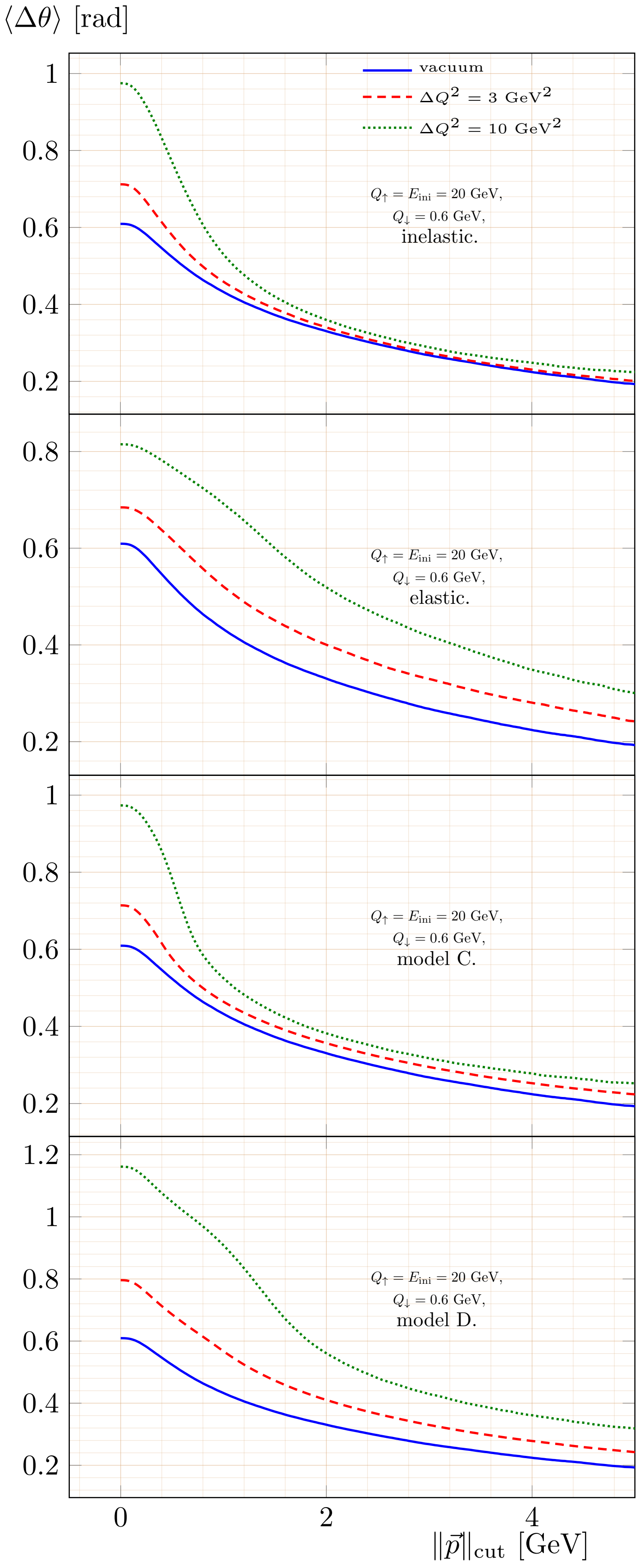

Figure A.7: Angles moyens entre quarks lourds et partons légers en fonction d'une coupure en valeur absolue d'impulsion de particule pour les modèles comme indiqués en comparaison avec le vide (courbes bleu solides).

A.5 Conclusion et travail futur

Afin de trouver un moyen d'identifier des différents mécanismes de la perte d'énergie dans le milieu du PQG par des observables, on a implémenté un algorithme Monte-Carlo pour simuler des gerbes dans le vide suivant des évolutions décrites par les équations DGLAP. Puis nous avons rajouté quatre modèles effectifs différentes pour définir le milieu. Ensuite, on a cherché dans les corrélations, entre des paires de particules finales de la gerbe, des observables qui permettent de discriminer les effets collisionnels des effets radiatifs dans les modèles effectifs. On a trouvé finalement que l'élargissement angulaire des gerbes dans le milieu dépend des échelles d'énergie et d'impulsion des partons suivant les modèles.

Une des tâches qui restent à faire est surtout de stabiliser les résultats par rapport aux processus qui se passent pour des échelles basses en énergies et impulsions, notamment la dépendance en $Q_\downarrow$. A l'échelle $Q_\downarrow$, des partons finales sont produits, sans introduction d'un modèle d'hadronisation. Une possibilité serait d'introduire de l'hadronisation. Une autre possibilité (qui n'introduit pas des dépendances explicites au modèle d'hadronisation) serait d'étudier plutôt des observables qui sont indépendentes des processus qui se passent aux échelles infrarouges. Des observables basées plutôt sur des sous-jets que des particules individuelles (ou paires des particules) représentent des exemples pour un tel type d'observable. Des expériences comme CMS ont déjà produits des premières données. Un deuxième aspect important négligé est l'effet explicite de la masse des quarks lourds. Tandis qu e l'on a toujours fait l'approximation que les effets de la masse ne jouent qu'un rôle négligeable dans la fragmentation des quarks lourdes à haute virtualité, $Q \gg M$, il y a tout de même des effets de la masse à petite virtualité. Dokshitzer a démontré, par exemple, qu'il existe une dépendance de la masse M à un angle minimale pour le rayonnement d'un gluon à partir d'un quark lourd, un phénomène appelé "dead-cone effect". Il serait intéressant de savoir comment les corrélations angulaires se changent si cet effet est inclus dans la phénoménologie des jets.

Références

Voir "Bibliography" dans la partie anglaise de la thèse.

UNIVERSITE
BRETAGNE
LOIRE

IMT Atlantique
Bretagne-Pays de la Loire
École Mines-Télécom

Thèse de Doctorat

Martin ROHRMOSER

Etude des corrélations des quarks lourds suppression dans les collisions d'ions lourds et de leur rôle dans la compréhension des mécanismes de perte d'énergie dans le plasma de quarks et de gluons

Study of correlations of heavy quarks in heavy ion collisions and their role in understanding the mechanisms of energy loss in the quark gluon plasma

Résumé

Contexte : La chromodynamique quantique (CDQ), théorie de l'interaction forte, prédit un nouvel état de la matière, le plasma de quarks et de gluons (PQG) dont les degrés de liberté fondamentale, les quarks et les gluons, peuvent bouger quasi-librement. Les hautes températures et densités de particules, qui sont nécessaires, sont supposées être les conditions de l'univers dans ses premiers moments ou dans les étoiles à neutrons. Récemment elles ont été recrées par des collisions de noyaux d'ions lourdes à hautes énergies. Ces expériences étudient le PQG par la détection des particules de hautes énergies qui traversent le milieu, notamment, les quarks lourds. Les mécanismes de leur perte d'énergie dans le PQG ne sont pas compris complètement. Particulièrement, ils sont attribués aux processus soit de radiation induite par le milieu, soit de collisions de particules de type 2 vers 2, ou des combinaisons.
Méthodes : Afin de trouver de nouvelles observables pour pouvoir distinguer les mécanismes de la perte d'énergie, on a implémenté un algorithme Monte-Carlo, qui simule la formation des cascades des particules à partir d'une particule initiale. Pour traiter le milieu, on a introduit des interactions PQG-jets, qui correspondent aux processus collisionnels et radiatifs. Les corrélations entre deux particules finales des cascades, dont une représente un quark trigger, ont été examinées comme moyen pour distinguer les modèles.
Résultats : La dépendance de l'ouverture angulaire pour des corrélations entre deux particules en fonction des énergies des particules peut servir comme moyen pour séparer les mécanismes collisionnels et radiatifs de la perte d'énergie dans le milieu.

Mots clés
Plasma des Quarks et des Gluons, Collisions d'ions lourds, Corrélations angulaires, Corrélations à deux particules, jets, fragmentations, Simulations Monte-Carlo

Abstract

Context: Quantum chromodynamics (QCD), the theory of the strong interactions, predicts a new state of matter, the quark-gluon plasma (QGP), where its fundamental degrees of freedom, the quarks and gluons, behave quasi-freely. The required high temperatures and/or particle densities can be expected for the early stages of the universe and in neutron stars, but have lately become accessible by highly energetic collisions of heavy ion cores. Commonly, these experiments study the QGP by the detection of hard probes, i.e. highly energetic particles, most notably heavy quarks, that pass the medium. The mechanisms of their energy-loss in the QGP are not yet completely understood. In particular, they are attributed to processes of either additional, medium induced radiation or 2 to 2 particle scattering, or combinations thereof.
Methods: In a theoretical, phenomenological approach to search for new observables that allow discriminating between these collisional and radiative energy-loss mechanisms a Monte-Carlo algorithm that simulates the formation of particle cascades from an initial particle was implemented. For the medium, different types of QGP-jet interactions, corresponding to collisional and/or radiative energy loss, were introduced. Correlations between pairs of final cascade particles, where one represents a heavy trigger quark, were investigated as a means to differentiate between these models.
Findings: The dependence of angular opening for two-particle correlations as a function of particle energy may provide a means to disentangle collisional and radiative mechanisms of in-medium energy loss.

Key Words
Quark Gluon Plasma, Heavy Ion Collisions, Angular Correlations, Two-Particle Correlations, Parton-Energy Loss, Jets, Fragmentation, Monte-Carlo Simulations

L'Université Bretagne Loire